$$
\left.
\begin{aligned}
f(i,j) &= f(x_i, y_j) \\
P(i,j) &= \sum_{l=1}^{\bar{N}} f(i,l)\bar{M}_j^l \\
Q(i,j) &= \sum_{k=1}^{N} f(k,j)M_i^k \\
R(i,j) &= \sum_{k=1}^{N}\sum_{l=1}^{\bar{N}} f(k,l)M_i^k \bar{M}_J^L
\end{aligned}
\right\} \quad i = 1 \ldots N,\ j = 1 \ldots \bar{N} \qquad (25.20)
$$

For $x < x_1$, $x > x_N$, $y < y_1$ or $y > y_{\bar{N}}$ we extrapolate by using respectively $S_{1,j}$, $S_{N-1,j}$, $S_{i,1}$, $S_{i,\bar{N}-1}$.

For one particular mesh the moments M_i^k and $\bar{M}_j^l$ of the cardinal splines have to be computed only once. The three sets of quantities P, Q, R have to be calculated once for each function f to be interpolated. (In our calculations we have six such functions: the dimensionless force and torque components). To any point (x,y) belongs a rectangle characterized by the numbers i and j, and the eight quantities A_i, B_i, C_i, D_i, $\bar{A}_j$, $\bar{B}_j$, $\bar{C}_j$, $\bar{D}_j$ can be computed for that point. Then S(x,y) as given by (25.19) yields the interpolated value for the function f at (x,y).

CHAPTER VI

WIND TUNNEL EXPERIMENTS.

§26 *Boomerang arms in uniform straight flow.*

The main part of this chapter is concerned with experiments on rotating boomerangs. This section, however, deals with a preliminary experiment in which lift and drag coefficients of boomerang arms in a uniform, straight air flow were measured. Boomerang arms, i.e. the wings forming part of a boomerang, in free flight operate at Reynolds numbers of the order of 10^5 or less. In this region the wing characteristics may seriously deviate from those at the higher Reynolds numbers associated with ordinary aircraft (see e.g. [Schmitz, 1957], [Muesmann, 1959], [Kraemer, 1961a]).

To investigate this matter with respect to our boomerang arms measurements were carried out with a small wind tunnel at the Twente University of Technology. Its wind speed could be varied between 0 and 30 m/s. (Degree of turbulence unknown.) The measuring cross section was square, having sides of 45.7 cm (18"). Lift and drag of wings were measured by means of a three-component spring balance mounted in one side wall of the tunnel. One end of the wing was attached to the spring balance in such a way that the wing's spanwise direction was horizontal, perpendicular to the airflow and halfway between the tunnel's bottom and ceiling. Four wings were made each of which occupied the full tunnel width, so that a two-dimensional flow (expectedly) would result. In addition six boomerang arms were cut off from actual boomerangs (which were known to fly well), and used in the experiment.

Here only part of the data shall be presented, but enough to provide a fairly representative picture of the lift and drag of boomerang arms in uniform straight flow at Re $\approx 4\times10^4$ to 10^5. It should be emphasized that the measurements were not of high precision. More extensive and accurate information (but not on hand-made boomerang arms) can be found in [Lippisch, 1951], [Schmitz, 1957, 1954], [Muesmann, 1959], [Kraemer,

1961a]. The data presented here are taken from 24 (out of 64) measuring series, and concern three of the six boomerang arms and all four "two-dimensional" wings. Their cross sections are shown in fig. 26.1.

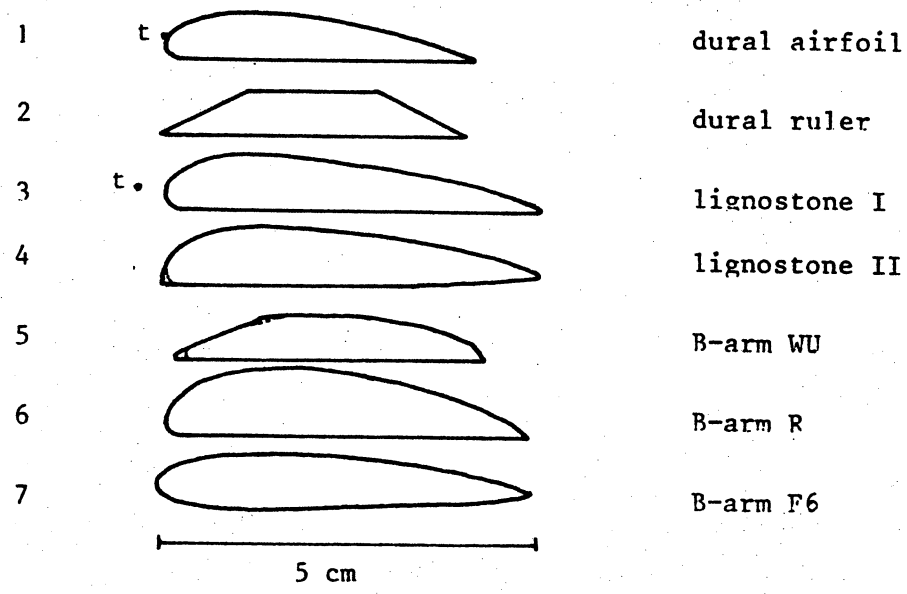

fig. 26.1. Cross sections of the wings used.
(t• = turbulence wire, ⌒ rounding off, in part of the measurements.)

wing	length l	AR	chord c	thickn. t	t/c	remarks
1 dural airfoil	45.4	∞	4.04	0.62	.154	also with turbulence wire
2 dural ruler	45.4	∞	3.97	0.57	.144	
3 lignostone I	45.4	∞	4.92	0.77	.157	also with turbulence wire
4 lignostone II	45.3	∞	4.88	0.76	.156	also rounded
5 B-arm WU	28.6	15	3.86	0.61	.158	also rounded
6 B-arm R	26.6	12	4.7	0.94	.200	
7 B-arm F6	25.6	10	4.9	0.72	.147	

table 26.1. Some dimensions (cm) of the wings used.

Table 26.1 lists some of the dimensions of the wings used. Boomerang arms R and F6 are tapered, and for these the chord and thickness in the middle are listed. The aspect ratio for the arms is defined as:

$$AR = \frac{2l^2}{s} \tag{26.1}$$

where l = spanwise length, s = wing area. The factor 2 is due to the mirror effect of the tunnel wall. For the four "two-dimensional" wings we take AR = ∞. The Reynolds number is defined as:

$$Re = \frac{Vc}{\nu} \tag{26.2}$$

where V = air velocity, ν = kinematic viscosity of air, c = chordlength as listed in table 26.1. Theoretically an elliptic spanwise lift distribution would give rise to an induced drag coefficient (see e.g. [von Mises, 1959]):

$$C_D = \frac{C_L^2}{\pi AR} \tag{26.3}$$

The corresponding parabolic curves are drawn as thin lines in fig. 26.3A, B,C. Figures 26.2A,B,C,D and 26.3A,B,C show experimental polar curves i.e. C_D, C_L graphs. The numbers in the graphs denote the angles of incidence, which, in this section, are the angles between the undisturbed airflow and the flat(test) part of the underside of the considered wing. Let us consider the experimental data wing for wing.

1. Dural airfoil: fig. 26.2A, fig. 26.3D.
This wing is milled from duraluminium. It has a smooth, airfoil-shaped profile. Similar wings were used in the experiments under water, described in §17 and §18. Comparison of the curve O Re = 77000 (V = 28.7 m/s) with the curve ⊕ Re = 44000 (V = 16.4 m/s) shows the dependence on Re of both C_L and C_D. The favourable influence of a turbulence wire at Re = 44000 (V = 16.4 m/s) is evident from a comparison between the curves ⊕ without wire and ▲ with wire. The wire consisted of a piece of 0.05 cm thick cotton string glued to the wing's nose at both ends. Its position was influenced by the airflow, especially in the middle of the wing. As the wire touched the wing's nose it should be considered as a trip wire, see [Kraemer, 1961b]. Finally the curve ◯ Re = 77000 (V = 28.6 m/s)

gives data for the reversed profile. Polar curves at Re = 81000 (not shown) are essentially the same as those at Re = 77000 (0,◯). Fig. 26.3D shows a remarkable hysteresis phenomenon. C_L and C_D are plotted as functions of Re (or V) at a constant angle of incidence of 5°. For Re > 65000: $C_L \approx 1.0$ and $C_D \approx 0.05$, whereas for Re < 53000: $C_L \approx 0.5$ and $C_D \approx 0.1$. For 53000 < Re < 65000 the lift and drag coefficients depend on whether the situation was reached from the super- or from the subcritical state (see further down in this section).

2. Dural ruler: fig. 26.2C.
This wing was milled from duraluminium. It has a trapezium-shaped cross section with sharp edges, and front-rear symmetry. The trapezium's sharp angles equal 27.4°. The lift and drag characteristics are not significantly different at Re = 79000 (V = 29.8 m/s): O and Re = 44000 (V = 16.5 m/s): ⊕. C_D increases suddenly above 7½° angle of incidence, and again above 15°.

3. Lignostone I, fig. 26.2B.
This wing was hand-made from lignostone, a kind of impregnated, compressed beech ply. It has a flat underside. Its upper side was filed into shape and sanded smooth. The measurements were done without and with turbulence wire. In the latter case the wire consisted of a 0.05 cm (= 0.01 chord) thick piece of cotton string stretched in front of the wing's leading edge, parallel to it, at a distance of 0.3 cm (= 0.06 chord). The wire was fastened to the wing by means of two screws near the wing's ends. Without wire there is a slight dependence on Re: compare curve O at Re = 97000 (V = 29.6 m/s) with curve ⊕ at Re = 55000 (V = 16.7 m/s). With wire the Re dependence is restricted to angles of incidence higher than 10°: compare curve Δ at Re = 96000 (V = 29.2 m/s) with curve ▲ at Re = 54000 (V = 16.3 m/s). The influence of the turbulence wire is very pronounced: compare Δ with O resp. ▲ with ⊕. Stall is postponed by the wire from 5° to 12½° resp. from 2½° to 10°, and the maximum C_L is increased from 1.0 to 1.3 resp. from 0.8 to 1.2. At Re = 96000 strong flutter occurred for angles of incidence near 15°. The curve ⊕ at Re = 55000 (V = 16.7 m/s) gives data for the reversed profile.

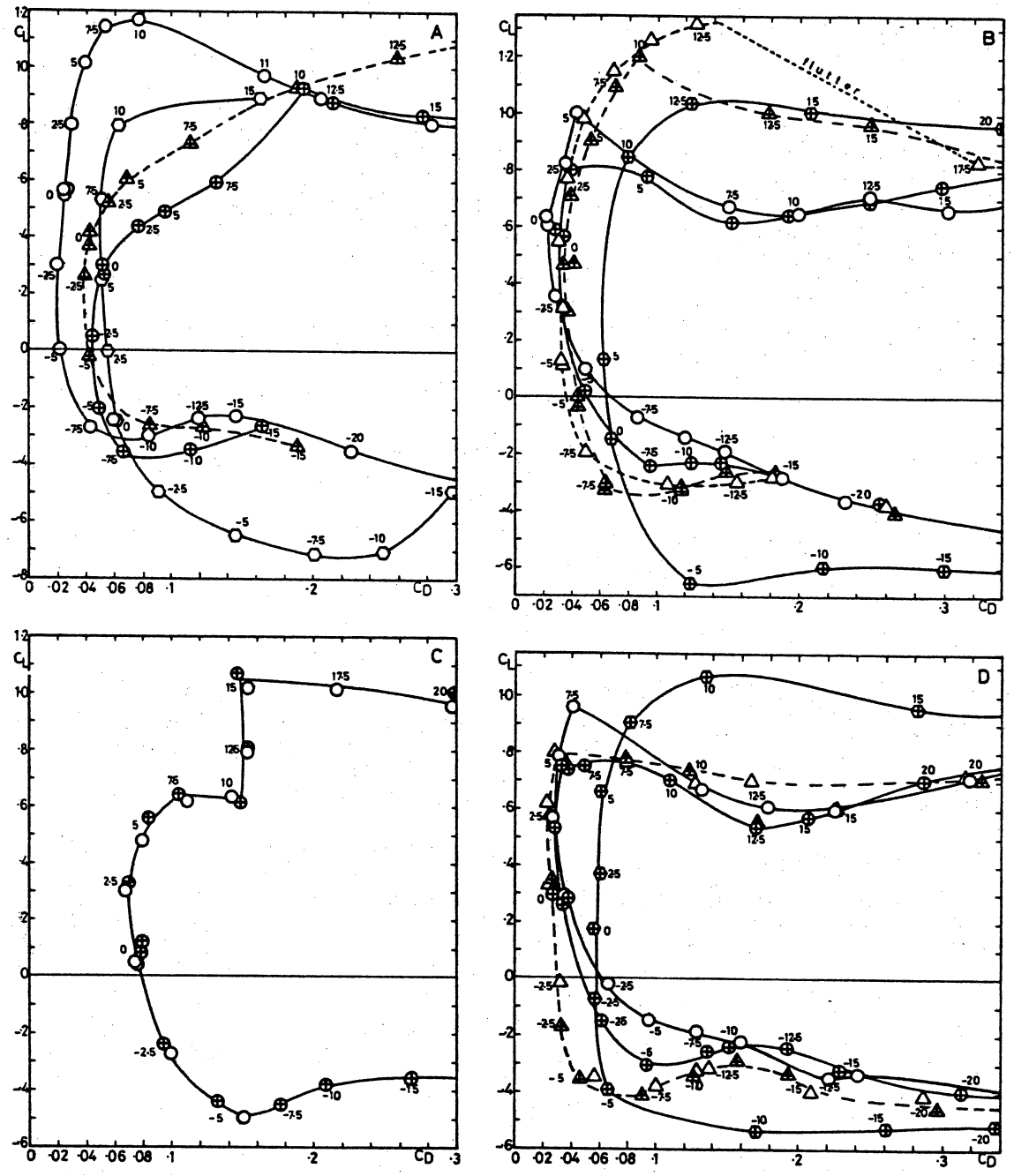

fig. 26.2. Experimental polar curves for 4 two-dimensional wings.
A. dural airfoil, O normal Re = 77000, ⊕ normal Re = 44000, ▲ with turbulence wire Re = 44000, ⬡ reversed Re = 77000.
B. lignostone I, O normal Re = 97000, ⊕ normal Re = 55000, Δ with turbulence wire Re = 96000, ▲ with turbulence wire Re = 54000, ⨁ reversed Re = 55000.
C. dural ruler, O Re = 79000, ⊕ Re = 44000.
D. lignostone II, O normal Re = 98000, ⊕ normal Re = 53000, Δ rounded Re = 96000, ▲ rounded Re = 53000, ⨁ reversed Re = 53000.
Numbers with the experimental points denote the angles of incidence.

4. Lignostone II, fig. 26.2D.
This wing was hand-made from lignostone. The main difference from lignostone I is that the underside of lignostone II is not entirely flat, but somewhat curved upward near de trailing edge. The flat part meets the nose of the profile at a right angle with a sharp edge. In addition measurements were made in which this edge was rounded off. The effects of this rounding on C_L and C_D are negligible, except at negative angles of incidence where it is favourable: compare curve O at Re = 98000 (V = 30.0 m/s) resp. ⊕ at Re = 54000 (V = 16.7 m/s) with Δ at Re = 96000 (V = 29.4 m/s) resp. ▲ at Re = 53000 (V = 16.4 m/s). The polar curves, including ⊕ at Re = 54000 (V = 16.7 m/s) for the reversed profile, resemble the corresponding curves (O,⊕,⊕ for lignostone I. The curve for the reversed profile at Re = 98000 (not shown) is not different from that at Re = 54000 (⊕).

5. B-arm WU, fig. 26.3B.
This wing was cut from a nylon boomerang, which is commercially made and available in Germany under the name "Comeback" (see fig. 28.1). Curiously, the profile has a sharp leading edge, a less sharp trailing edge and a kink in its upper side. Its underside is nearly flat. According to the designer, Mr. W. Urban (personal communication, 1970), these features were not based on aerodynamic considerations, although he had made boomerang flight trials with various wing profiles. Rounding off the leading edge and the kink has an adverse effect on C_L and C_D for angles of incidence between 2½° and 10°: compare curve O at Re = 74000 (V = 29.2 m/s) with curve Δ for the rounded wing at Re = 76000 (V = 29.4 m/s). This effect is absent at Re = 42000 (not shown). Since rounding of the kink only has no significant effect either at Re = 76000 or at Re = 42000 (not shown), the effect should be mainly due to rounding of the leading edge. The reversed wing at Re = 76000 (V = 29.4 m/s), curve ○, has roughly the same characteristics as the normal wing, except for its angle of zero lift being -2½° instead of 0°. The rounding has no substantial effect on the characteristics of the reversed profile (not shown). The polar curves of the not-rounded wing at Re = 42000 (not shown) do not differ much from those at Re = 76000 (O,○).

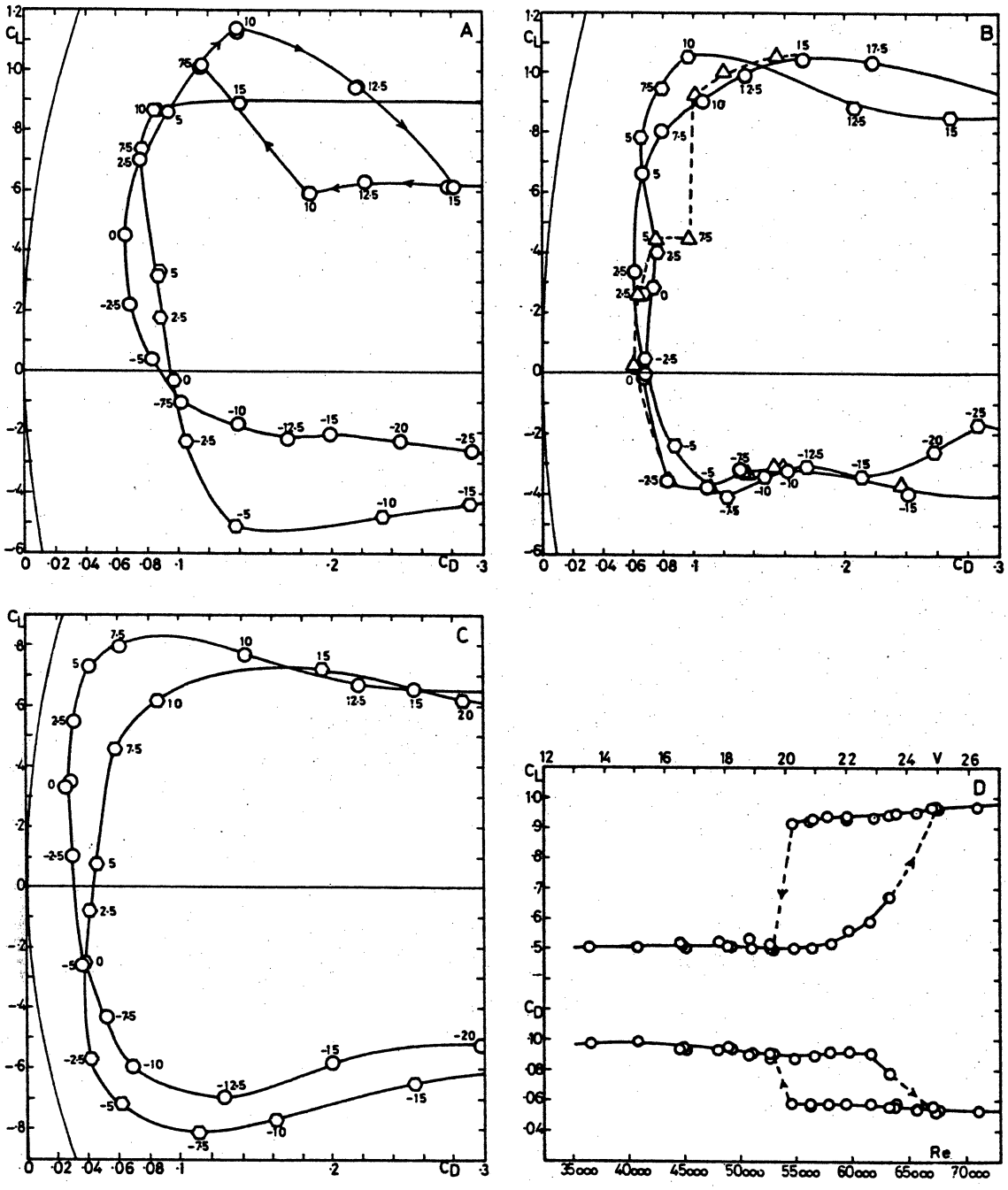

fig. 26.3. Experimental polar curves for 3 boomerang arms.
A. B-arm R, O normal Re = 92000, ⬡ reversed Re = 92000.
B. B-arm WU, O normal Re = 74000, Δ rounded Re = 76000, ⬡ reversed Re = 74000.
C. B-arm F6, O normal Re = 96000, ⬡ reversed Re = 96000.
Numbers with the experimental points denote the angles of incidence.

D. dural airfoil, C_L and C_D vs. Re at constant angle of incidence 5°.

6. B-arm R, fig. 26.3A.
This wing was cut from a hand-made, painted, birch ply boomerang. The wing has a flat underside and is rather thick. The curve O at Re = 92000 (V = 29.2 m/s) exhibits a hysteresis for angles of incidence between 7½° and 15°. The reversed profile ar Re = 92000 (V = 29.2 m/s) is not much worse: curve ⬡.

7. B-arm F6, fig. 26.3C.
This wing was cut from a hand-made, painted, mahogany ply boomerang. The wing has a biconvex profile, its underside being less convex than its upper side. The polar curves at Re = 96000 (V = 29.4 m/s), both for the normal profile: O and for the reversed profile: ⬡, show a minimum C_D which is less than that for WU or R. The maximum C_L, however, is not high: 0.8. Two other boomerang arms having approximately the same profile were found to have similar polar curves (not shown).

The data represented here show the same peculiarities that are described more completely in the literature mentioned earlier in this section. The airflow around a wing appears to have two possible main states: a supercritical state at high Re and a subcritical state, with lower C_L and higher C_D, at low Re. The transition from the sub- to the supercritical state generally occurs at a somewhat higher Reynolds number than the reverse transition (hysteresis, see e.g. fig. 26.3D). Fig. 26.4 gives a schematic picture of the flow in both states. It is taken from

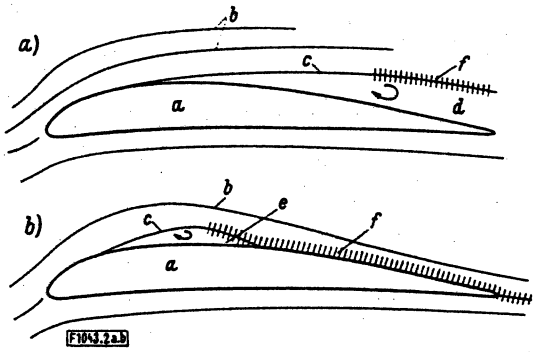

Fig. 26.4. Schematic picture of flow around airfoil (copied from [Kraemer, 1961a]). a) subcritical flow, b) supercritical flow. a = profile, b = streamlines, c = border stream line, d = dead water region, e = locally bounded dead water region ("Ablöseblase"), f = turbulent boundary layer.

[Kraemer, 1961] , together with the following clear description of the boundary layer phenomena:

Die sprunghafte Veränderung der Strömung und der aerodynamischen Beiwerte beim Durchlaufen der kritischen Reynoldszahl ist ein Grenzschichteffekt und hängt mit dem Umschlag der Grenzschicht von der laminaren in die turbulente Strömungsform zusammen. [...]
Ausgehend vom Staupunkt an der Flügelnase verläuft die Grenzschicht zunächst in jedem Fall laminar. Ist Re kleiner als die kritische Reynoldszahl, so bleibt die Grenzschicht auch hinter dem Druckminimum laminar und löst sich kurz danach von der Wand ab. Es entsteht ein Totwassergebiet, das sich bis hinter die Hinterkante erstreckt. Wird die kritische Reynoldszahl überschritten, so bildet sich im hinteren Teil der Flügel-Saugseite eine turbulente Grenzschicht; die Strömung kann nun (wenn der Anstellwinkel nicht zu gross ist) bis zur Hinterkante anliegen.
Der Grenzschichtumschlag von der laminaren in die turbulente Form vollzieht sich bei sehr grossen Reynoldszahlen in der Umgebung des Druckminimums in der anliegenden Grenzschicht. Ist jedoch die Reynoldszahl nur wenig grösser als die kritische Reynoldszahl, so schlägt die Strömung erst hinter der laminaren Ablösestelle am Rand einer "Ablöseblase" um, wie es Bild [26.4] schematisch andeutet. Die Turbulenz entsteht dabei in einigem Abstand von der Wand in der Totwassergrenze. Entscheidend für das Zustandekommen der überkritischen Strömung mit kleinem Widerstand und grossem Auftrieb ist, dass sich die turbulente Totwassergrenze wieder an die Wand anlegt. Auch im unterkritischen Fall wird die Totwassergrenze schliesslich turbulent, ohne sich jedoch wieder an die Wand anzulegen.
Die beim Überschreiten der kritischen Reynoldszahl (trotz des verhältnismässig grossen Reibungsbeiwerts der turbulenten Grenzschicht) gemessene Widerstandsabnahme rührt daher, dass der durch die Ablösung verursachte Druckwiderstand grösser als der Reibungswiderstand ist. Auch der Zusatzwiderstand von Rauhigkeiten und Störkörpern (z. B. "Turbulenzdraht") an oder vor der Nase spielt in der Regel keine Rolle, wenn dadurch bei vorgegebener kleiner Reynoldszahl noch überkritische Strömung (statt unterkritischer) erreicht werden kann. [Kraemer, 1961a, p. 34]

The data discussed in this section turn out to be interesting with regard to boomerangs in a rather unexpected way. If the measured lift and drag characteristics are used in our winglet model to compute the forces on *rotating* boomerangs, the axial (lift) force comes out too low for $\psi \gtrsim 10°$ (see §32). Similar deviations have been observed by Muesmann [1958] in the case of axial flow compressors at low Reynolds numbers.

§27 *The experimental setup.*

The following part of this chapter deals with an experiment in which forces were measured on rotating boomerangs placed in an airflow. Five different boomerangs were used (see fig. 29.1), the rotational velocity ω, the air speed V and the boomerang's angle of incidence ψ were varied, and the six force and torque components - averaged over time - acting on the boomerangs were determined. At the outset the plan was to carry out dynamic measurements, i.e. measurements of the instantaneous forces, or of the forces as functions of the boomerang's azimuthal angle. But after some consideration this plan was discarded, as enormous difficulties would have to be overcome, such as the elimination of vibrations. Although the experimentally determined time-averaged forces provide less information than the instantaneous forces, they still can be used as a basis for the calculation of boomerang flightpaths, and moreover, they can be compared to the corresponding quantities computed on basis of the theory outlined in the preceding chapters.

This section presents a description of the experimental setup shown in fig. 27.1. During the measurements a boomerang is attached to the end of the rotating shaft by means of a flat, V-shaped piece of duraluminium (see fig. 27.1b). The centre of mass of the boomerang including this V-piece is situated on the axis of the shaft, and the boomerang's principal axis of inertia coincides with the axis of rotation. The shaft consists of a hollow cylindrical aluminium tube, and is connected by means of two ball-bearings to a frame in which the motor drive is mounted. This frame is constructed from aluminium angle beams arranged in a compact tetrahedral form, so as to make it light and rigid. On the motor shaft a disk with slits is mounted which, together with a light and a photocel, serves to control the boomerang's rotational speed. Just as with the experiments in water, described in §17, this part of the apparatus is considered as one unit, B.

Unit B is connected to a second frame, C, by means of six elements, which measure the aerodynamic forces acting on unit B. (The inertial forces due to vibrations are expected to cancel after averaging with respect to time.) Frame C too has has a tetrahedral shape, it is

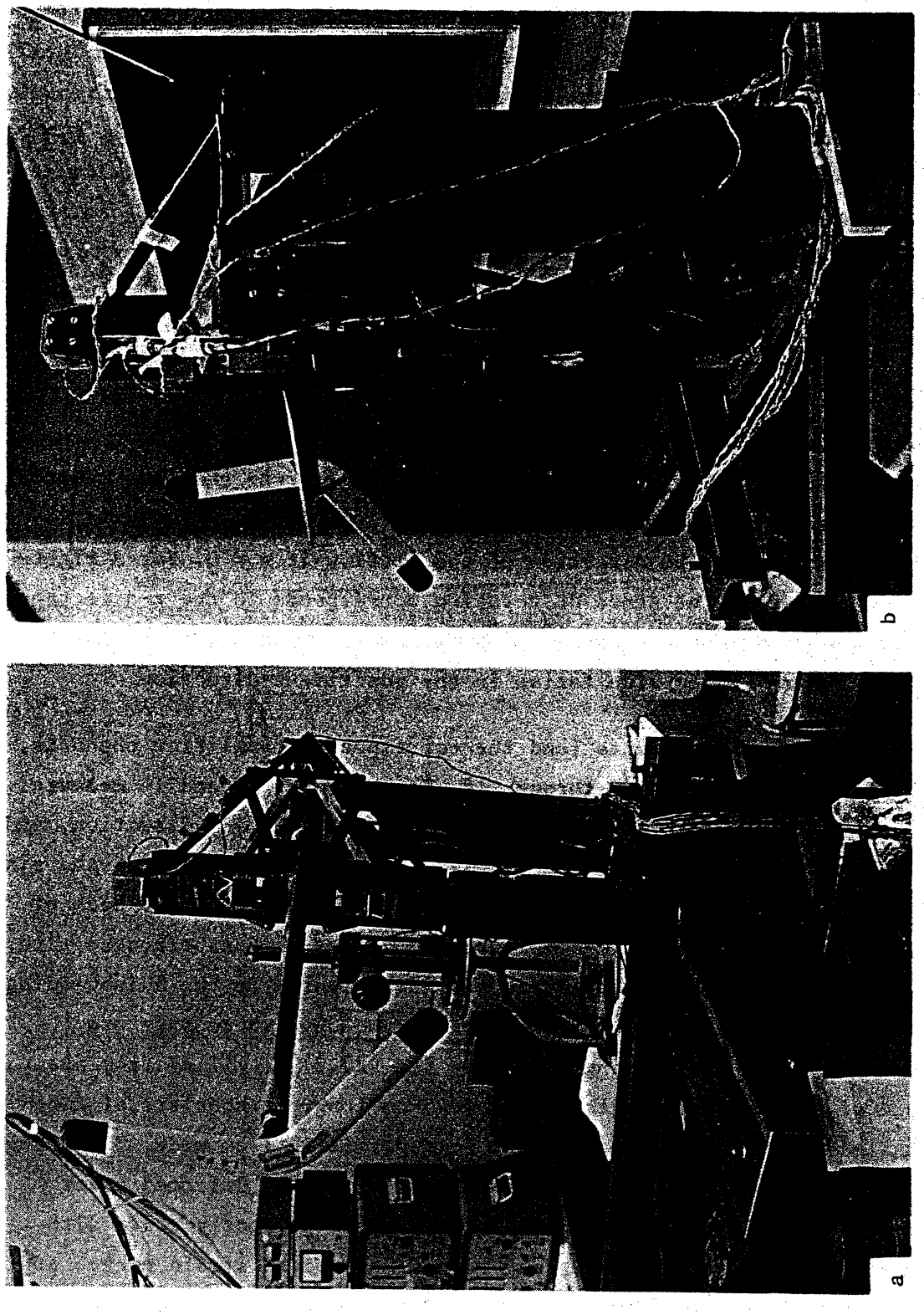

fig. 27.1. Experimental setup with boomerang L6 attached. a: front view, airflow from left to right; b: back view, outflow aperture at right.

constructed from iron angle beams. A hollow cilindrical body of symmetrical airfoil cross section surrounds the rotating shaft and thus shields it from the airflow. This shielding body is rigidly connected to frame C, its length is approximately 60 cm, its chord its chord 13.5 cm, its thickness 3.3 cm. The whole apparatus is mounted on a steel table and adjusted so that the axis of rotation is horizontal. Frame C can be rotated about a vertical axis through the boomerang, in order to obtain different positions with respect to the airflow and thus to select different values for the angle ψ.

A right-handed cartesian coordinate system (x,y,z) is defined as follows. The origin is the boomerang's centre of mass. The z-axis coincides with the axis of rotation, its positive direction is from bearings towards boomerang. The y-axis is directed vertically upwards. The x-axis is horizontal and in the direction of the airflow if $\psi = 0$. For a right-handed boomerang the sense of rotation corresponds to the z-direction as with a right-handed screw; the boomerang is mounted on the shaft with its more convex side facing in the positive z-direction.

The six measuring elements (and the corresponding amplifier channels, etc.) are numbered from 9 through 14. Elements 12, 13 and 14 measure forces in the x-direction, element 11 measures in the y-direction, and elements 9 and 10 measure in the z-direction. The positions of the six measuring elements are schematically indicated in fig. 27.3. Each of these elements consists of a measuring cube and a phosphorbronze wire. The measuring cubes were designed and manufactured in the Shipbuilding Laboratory of the Delft University of Technology, where they are routinely used. A measuring cube (see fig. 27.2) is milled from one piece of "armco" steel. Its edges are 5 cm long. It consists of two parallel square slabs connected by four parallel, 1 cm wide, 3 cm long, thin leaf springs, so that the cube can be slightly deformed under forces in one direction, while being virtually perfectly stiff with respect to the five other degrees of freedom. Eight strain gauges are glued to the four leaf springs close to their axillas at one slab of the cube. The electric resistance of the strain gauges varies linearly with their deformation and hence with the load acting on the cube (within certain limits). Each measuring cube is fastened to frame C by means of

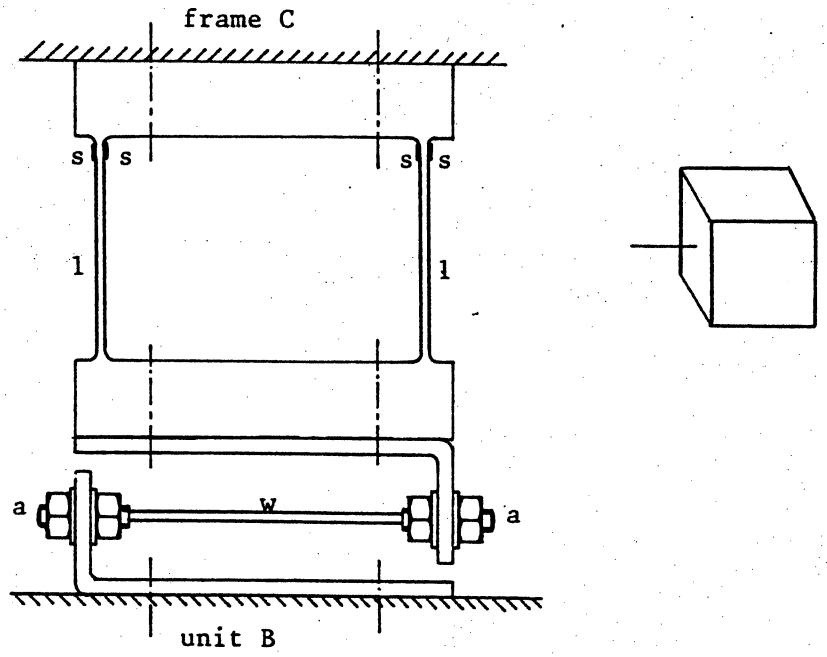

fig. 27.2. Measuring element. 1 = steel leafsprings, s = strain gauges, w = phosphorbronze wire, a = adjusting screws soldered to the wire. At right: symbolic representation of this element.

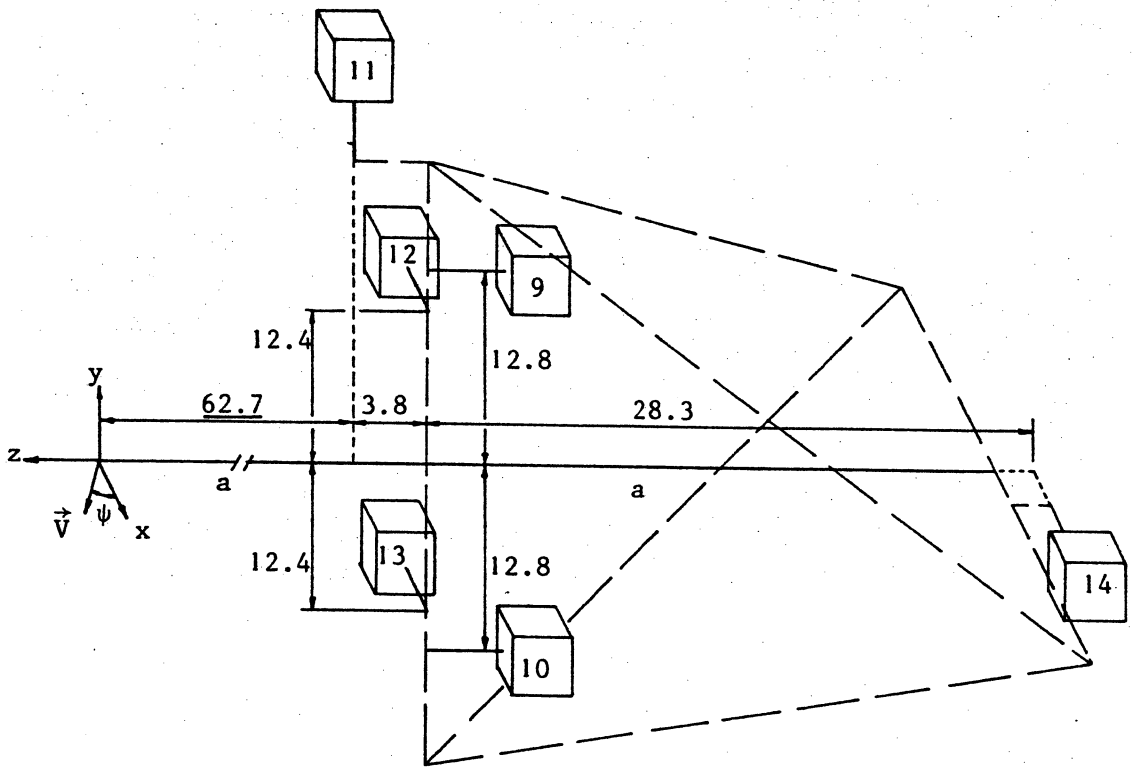

fig. 27.3. Schematic arrangement of the measuring elements 9 through 14. Broken lines: frame B, a: rotation axis, $\vec{V}$: direction of airflow, numbers with arrows: distances in cm.

four bolts through one slab, and connected to unit B by means of a 3 cm long phosphorbronze wire fastened to the other slab and directed parallel to the sensitive direction of the cube. The wire's function is to transmit forces in this direction only, with respect to the other five degrees of freedom it is comparatively very slack. The wires are heavy enough to resist buckling under compressive forces. By means of these wires each measuring cube receives precisely the forces "meant" for it. The positions and directions of the six wires determine the positions and directions in which the forces are transmitted from unit B to frame C. It should be remarked that the actual set-up deviates somewhat from this general description. The vertical wire of element 11 is about 13 cm long, but it can only buckle if the upward forces in y-direction would exceed the weight of unit B, which is not the case during the experiments. The weight of unit B (almost 5.4 kg) acts fully on element 11 and, because the centre of gravity of unit B is not situated exactly underneath the wire of element 11, also loads the elements 9 and 10. Cube 12 is attached to cube 9 rather than to frame C directly. Therefore the wires of both elements 9 and 12 are mounted between cube 12 and unit B. The same situation obtains for the elements 10 and 13.

One of the wind tunnels of the Laboratory of Aero- and Hydrodynamics of the Delft University of Technology was used with open measuring section. This wind tunnel has a very low degree of turbulence: less than 0.1%. The wind speed can be varied between 0 and 50 m/s. The horizontal airstream as it leaves the outflow aperture of the tunnel has a rectangular cross section, it is 70 cm high and 90 cm wide. The centre of the boomerang was situated 68.5 cm downstream of the outflow aperture. The boomerang's centre (the end of the rotating shaft) reached to within 8 cm of the centre line of the airflow, and was situated nearly 0.5 cm higher than this centre line. The position of the measuring apparatus with respect to the wind tunnel allowed a maximum value $\psi = 45°$. During the measurements the boomerang must be situated in the middle of the airflow, but the rest of the apparatus should disturb the flow as little as possible. In particular parts of unit B other than the boomerang itself should not be exposed to moving air. Hence the requisite length of more than 60 cm for the (shielded) shaft.

Each of the measuring channels, numbered from 9 through 14, consists of a measuring element, an amplifier, an integrator and a power supply. The channels were operated at a frequency of 1000 Hz. The signals from the strain gauges (in bridge connection) in the cubes were integrated over one measuring run of about 50 seconds and read out digitally. The six amplifiers can be used at the scale factors, 1, 2, 5 and 10. The gain is inversely proportional to these numbers. The choice of the scale factors was determined by the maximum amplitudes of the often strongly oscillating signals. For instance, if a signal would be too great for an amplifier to perform linearly at scale factor 1 or 2, scale factor 5 or 10 would be selected. Two of the measuring cubes, 9 and 10, can be used for loads up to 20 kgf., the other four (11 through 14) contain thinner leaf springs, are twice as sensitive and can be used for loads up to 10 kgf. Table 27.1 lists the approximate characteristics of

channel nr.	9, 10	11, 12, 13, 14
max. load	≈ 20 kgf	≈ 10 kgf
1 μst	≈ 8.4 gf	≈ 4.2 gf
1 μst	≈ 27 Mc	≈ 27 Mc
1 gf	≈ 3.2 Mc	≈ 6.4 Mc.

table 27.1. Approximate characteristics of the 6 channels.

the channels 9 through 14. Here μst denotes microstrain and Mc denotes an intermediate unit: the integrated digital output of a channel after 50 sec., multiplied by the scale factor used. The whole apparatus was calibrated (see §28) in order to convert the 6 Mc values to the forces F_x, F_y, F_z in gf and the torques T_x, T_y, T_z in gf . 10 cm. (The use here of 10 cm as a "unit of length" makes the numerical values for the torques have the same order of magnitude as those for the forces.)

If the phosphorbronze wires would be ideally adjusted, the frames perfectly stiff, etc., the geometry indicated in fig. 27.3 would allow one to deduce the following matrix, which would characterize the measuring apparatus:

element	9	10	11	12	13	14
F_x	0	0	0	+ 1	+ 1	+ 1
F_y	0	0	+ 1	0	0	0
F_z	+ 1	+ 1	0	0	0	0
T_x	+ 1.28	- 1.28	+ 6.27	0	0	0
T_y	0	0	0	- 6.65	- 6.65	- 9.48
T_z	0	0	0	- 1.24	+ 1.24	0

tabel 27.2. Ideal matrix to calculate F_x, F_y, F_z (gf) and T_x, T_y, T_z (gf . 10 cm) from the forces (gf) transmitted by the measuring elements 9 through 14.

The (necessary) length of the shaft (see fig. 27.3) is reflected in the 4 large entries in table 27.2. This inevitably limits the accuracy of the components T_x and T_y. Table 27.2 may be compared with table 28.2, obtained by actual calibration of the apparatus.

The driving servo-motor is of the type Axem-Servalco F9M4. Its speed is reduced by a timing belt transmission in the ratio 3:1. The motor speed is controlled and kept constant by means of a circular disk with 240 equidistant slits mounted on the motor shaft, a light and a photocel, and an electronic feedback system with a digital read out.

The air speed V is determined by means of a pitot-tube and a manometer. These provide a value for $\frac{1}{2}\mu V^2$ where μ is the air density.

During a preliminary test without wind the boomerang's rotational speed could be increased up to 20 revs/sec.; at this point strong vibrations of unit B set in. During the actual experiments such vibrations occasionally occurred at lower speeds, e.g. 7 or 10 revs/sec.

§28 *The measurements.*

Five boomerangs were used in the experiments, they are shown in fig. 28.1. Four of them are left-handed (L1,L4,L6,F18) and hand-made from birch plywood. The fifth (WU) is right-handed, commercially made from nylon, and available in Germany under the name "Comeback" (designer: Willi Urban). The boomerangs L1, L4 and L6 each contain a tiny light bulb and two batteries, and in addition the L4 and L6 contain a piece of electronics to switch the light on and off twice a second. This equipment is for use in the field experiments described in Part III, and is not relevant to the wind tunnel experiments. Table 28.1 lists some properties of each boomerang.

1.	boomerang	L1 left	L4 left	L6 left	F18 left	WU right
2.	total weight (g)	191	190	151	151	177
3.	flight mass (g)	173	172	139	135	160
4.	mom. inertia ($g\ cm^2$)	39600	33800	22100	27400	45600
5.	max. radius (cm)	30.7	30.2	25.4	26.2	30.3
6.	a (cm)	29.8	29.1	24.9	25.8	29.6
7.	thickn./chord ≈	.16-.19	.13-.19	.17-.20	.16-.19	.16

table 28.1. Some properties of the five boomerangs. See also table 32.1.

Aerodynamic profile properties of the boomerangs are unknown (except for WU, see §26). The quantities listed in rows 1, 2, 5 and 6 are directly relevant for the experiments. Here "total weight" refers to the weight of the boomerang including its aluminium V-piece, "max. radius" denotes the maximum distance from the rotation axis to any material point of the boomerang, and a denotes the theoretical radius of the boomerang according to (20.7), which is to be used in the reduction of the experimental data. Further: "flight mass" and "mom. inertia" refer to the mass and moment of inertia of the boomerang as used in field experiments without aluminium V-piece. Row 7 lists the minimum and maximum thickness/chord ratio for each boomerang. Other dimensions (e, l, c_t,c_r, see §20) of the boomerang arms can be found in table 32.1.

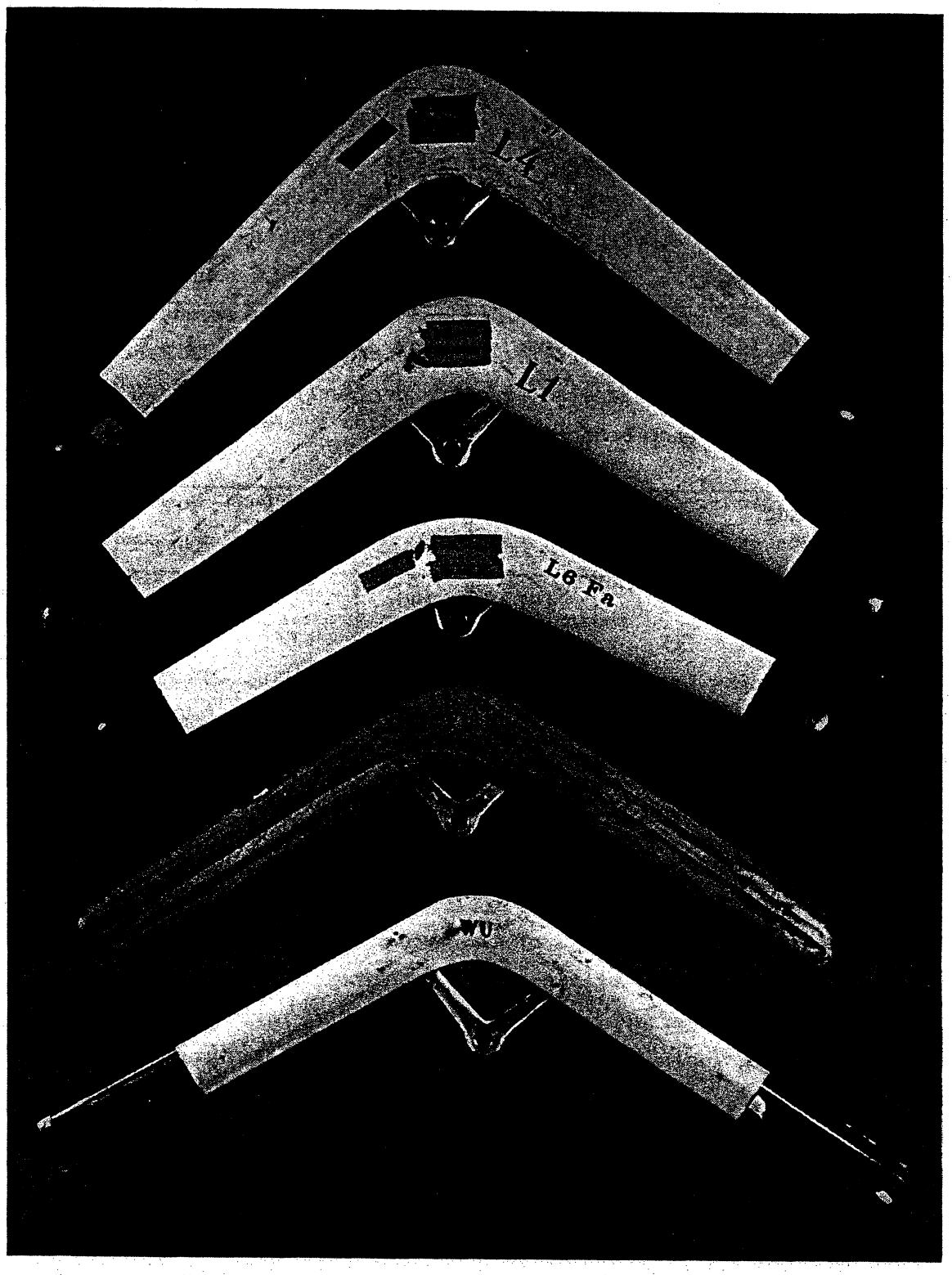

fig. 28.1. The five boomerangs used in the experiment, with V-pieces attached. From top to bottom: L4, L1, L6, F18, WU.

The measurements proceeded as follows. A boomerang was mounted on the shaft. The apparatus was put in position for one of the following 8 angles of incidence:

$$\psi = -5°,0°,5°,10°,15°,20°,30°,45° \qquad (28.1)$$

Then a series of measurements, called a run, was carried out. Each run consisted of three kinds of actions:

1) Zero-level measurements, i.e. measurements without aerodynamic forces acting on the boomerang. All amplifiers were successively set at the scale factors 1, 2, 5, 10.

2) True measurements. An air speed was chosen and three successive measurements of about 50 seconds duration were done at rotational speeds of 7, 10 and 14 revs/sec. Mostly five different air velocities were successively chosen. If strong vibrations occurred the rotational speed was slightly changed: e.g. 7.5 instead of 7.0 revs/sec. and 10.3 or 10.6 instead of 10.0 revs/sec.

3) Zero-level measurements as described under 1) except for the scale factors not used in the true measurements under 2).

One complete run thus consists of about 15 true measurements and at most 8 zero-level measurements. Consecutive runs were carried out for different values of ψ selected from (28.1).

The integral outputs of channels 9 through 14 resulting from the measurements 1), 2) and 3) were read out and written down as integer numbers. Afterwards all outputs were converted to a measuring time of exactly 50 seconds, and multiplied by the corresponding scale factors. The zero-level measurements were treated in the same manner. In general, the outputs of the measurements 1) before and 3) after the true measurements were different, due to drift. Therefore the outputs of the true measurements were corrected by means of linearly interpolated zero-level outputs. In this way 6 corrected outputs were obtained: Mc_j: $j = 9,\ldots,14$, for each true measurement. These were rounded to integral numbers.

The apparatus was calibrated by exerting known forces and torques on the end of the shaft, which in this case did not rotate. The known

forces and torques were produced by one or two weights hanging from pieces of thin string, the other ends of which were fastened either directly to the end of the shaft (force) or to excentric metal bars attached to the shaft (force and/or torque). Where necessary, smooth running pulleys were used to change the directions of the forces. For each particular arrangement of strings and pulleys the weights were varied and a run as described above, but without wind and without rotation, was carried out. The outputs of the calibration measurements too were reduced to the numbers Mc_j.

Let us denote the force and torque components as follows:

$$F_1 = F_x,\ F_2 = F_y,\ F_3 = F_z,\ F_4 = T_x,\ F_5 = T_y,\ F_6 = T_z. \qquad (28.2)$$

The relation between the six outputs Mc_j, $j = 9,\ldots,14$ and the six force components F_i, $i = 1,\ldots,6$ is described by:

$$F_i = \sum_{j=9}^{14} A_{ji} Mc_j, \qquad i = 1,\ldots,6 \qquad (28.3)$$

The coefficients A_{ji} are obtained from the calibration. Under the assumption that the measuring system is linear, six measurements would suffice to determine the matrix A from (28.3). Actually 50 calibration measurements in 12 runs were carried out, and the matrix elements A_{ji} were determined by a least squares method. They are listed in table 28.2, which indicates how F_x, F_y, F_z in gf and T_x, T_y, T_z in gf . 10 cm can be calculated if the Mc_j, $j = 9,\ldots,14$ are given.

channel		9	10	11	12	13	14
F_x	1	- .0077	- .0007	- .0031	+ .1528	+ .1529	+ .1633
F_y	2	- .0001	- .0082	+ .1677	- .0033	- .0013	- .0010
F_z	3	+ .3152	+ .3160	- .0054	+ .0026	+ .0041	+ .0059
T_x	4	+ .3937	- .4544	+1.0360	- .0163	+ .0005	+ .0071
T_y	5	+ .0455	+ .0124	+ .0155	-1.0130	-1.0071	-1.5534
T_z	6	+ .0096	- .0030	+ .0014	+ .1923	+ .1937	+ .0015

table 28.2. Calibration matrix A_{ji} of measuring apparatus, to calculate F_x, F_y, F_z (gf) and T_x, T_y, T_z (gf . 10 cm) from the corrected outputs Mc_j, $j = 9,\ldots,14$.

This calibration matrix may be compared with the ideal matrix in table 27.2, after multiplying the entries under 9 and 10 by 3.2 and the entries under 11 through 14 by 6.4, according to table 27.1. The underlined entries in table 28.2 correspond to the non-zero elements in table 27.2. As regards the estimated errors in the numbers A_{ji} see §29, particularly table 29.1.

Together 42 runs have been carried out, containing 640 usable measurements; these are listed in table 28.3. The symbols 0, X and XX are related to the zero-level measurements. XX signifies that zero-level measurements were carried out fully as described above under 1) and 3), X that they were carried out for scale factor 1 only, and 0 that the zero-levels at scale factor 1 were determined in a less precise way (see [Hess, 1972]).

	L4	L6		L1		F18	WU
	left	left		left		left	right
ψ	0	0	XX	X	XX	XX	XX
-5°	15	18*		19*		19	0
0°	15	20*		17		18	17+
5°	16	17	19*	15	16	18	13
10°	15	20	17	15		20*	16*
15°	16	18		15		15	18+
20°	14	13		14		15	10
30°	9	14		12		13	12+
45°	10	12		12		13	10
total	110	132	36	119	16	131	96

table 28.3. Listing of the numbers of measurements in 42 runs. *: including 3 measurements at V = 0, +: including 3 measurements with left-handed spin.

The maximum (averaged) axial forces F_z occurring during the measurements for the five boomerangs were: L1: ≈1.7 kgf, L4: ≈1.4 kgf, L6: ≈ 1.6 kgf, F18: ≈1.3 kgf, WU: ≈1.2 kgf.

§29 *Error analysis.*

It is rather difficult to make reliable estimates concerning the various types of errors contributing to the uncertainties in the final results. But it is worthwhile to make at least a sensible guess. The errors can be considered to result from deviations of the actual situation from an ideal situation which is supposed to be measured. In our case the ideal situation can be characterized as follows:

1) The boomerang is a rigid body. It rotates at a known, constant angular velocity about its principal axis of inertia through its centre of mass. It does not move otherwise.

2) The boomerang is placed in a uniform, unbounded airflow with a known, constant velocity. The airflow is not disturbed by objects other than the boomerang itself.

3) Six force and torque components acting on the boomerang, averaged with respect to time, are measured.

Let us now consider the various kinds of errors affecting the measurements.

a) Calibration errors.

The elements A_{ji} of the matrix characterizing the measuring apparatus, as listed in table 28.2, inevitably contain errors which cause systematic deviations in the experimentally determined force components. Sources of these errors are: uncertainties dp in the point of application of the known forces, i.e. in the fastening of the strings; uncertainties dd in the direction of the known forces, i.e. in the direction of the strings; variations da in the gain of the amplifiers. Realistic estimates for these errors are:

$$dp = 0.1 \text{ cm}, \quad dd = 0.01 \text{ radian}, \quad da = 0.5\%. \tag{29.1}$$

Errors in the magnitude of the exerted forces (weights) are negligible. By taking into account the geometry of the calibration measurements, and supposing that the errors combine in the most unfavourable way, we obtain the calibration error matrix DA_{ji} (see table 29.1) for the calibration matrix A_{ji} given in table 28.2. The calibration errors lead to errors d_1F_i in the force components F_i, see (28.2) and (28.3), according

to:

$$d_1F_i = \sum_{j=9}^{14} DA_{ji}|Mc_j|, \qquad i = 1,\ldots,6. \tag{29.2}$$

	9	10	11	12	13	14
1	.0054	.0056	.0070	.0060	.0059	.0087
2	.0055	.0056	.0062	.0077	.0076	.0095
3	.0017	.0017	.0017	.0025	.0025	.0017
4	.0076	.0079	.0123	.0123	.0121	.0157
5	.0077	.0079	.0106	.0138	.0136	.0173
6	.0046	.0048	.0122	.0138	.0136	.0173

table 29.1. Calibration error matrix DA_{ji} for calibration matrix A_{ji} given in table 28.2.

Let us now consider the errors in the measurements proper:

b) Geometrical errors.
A boomerang was normally attached to the shaft only once. Hence an uncertainty ($dp \approx 0.1$ cm) in the boomerang's position and uncertainties ($dd \approx 0.01$ rad.) in the boomerang's orientation with respect to the axis of rotation would lead to (small) systematic errors in the results. Uncertainties ($dd \approx 0{,}01$ rad.) in the angle ψ, which is set once before each measuring series, also lead to small errors.

c) Errors in V, ω and time.
Errors in the rotational velocity ω are negligible ($< 0.1\%$). Relative variations in space and time of the air velocity V are limited to about 0.5%. The finite extent of the air stream may cause small errors. Three of the five boomerangs have a diameter of about 60 cm, whereas the height of the air stream is only 70 cm. By means of a pitot-tube the whole cross section of the airflow just a little upstream from the boomerang's position (with the boomerang absent) was scanned. It turned out that the flow was homogeneous to within better than 1% for the whole region in which the wing tips of the boomerang move.

As the pitot-tube and manometer provide a value for $\frac{1}{2}\mu V^2$ rather than for V itself, uncertainties $\Delta\mu$ in the air density μ lead to errors in V and the advance ratio U:

$$\frac{\Delta U}{U} = \frac{\Delta V}{V} = \frac{1}{2}\frac{\Delta \mu}{\mu}. \tag{29.2}$$

The "old" dimensionless force components (see §23) are not affected by these, but our "new" dimensionless components are; we have:

$$\frac{\Delta F_{1x}}{F_{1x}} = \ldots\ldots = \frac{\Delta T_{1z}}{T_{1z}} = \frac{\Delta \mu}{\mu}. \tag{29.4}$$

The density of the air was not regularly measured during the experiments, but good estimates are:

$$\mu = 1.20 \text{ kg/m}^3, \quad \left|\frac{\Delta \mu}{\mu}\right| \lesssim 2\%. \tag{29.5}$$

The variations in μ have a time scale of at least hours, hence they would cause small systematic errors of varying magnitude.

Errors in the time measurements are negligible. However, the signals are not integrated over an integral number of revolutions. A measuring time of 50 seconds corresponds to 350, 500 or 700 revolutions at 7, 10 or 14 revs/sec. The oscillating signals often had amplitudes surpassing their average values, hence a part of a period of revolution might contribute out of proportion to the outputs, but this should not be more than about 1% of the total output. Such errors could have been avoided by integrating over a fixed integral number of revolutions.

d. Errors due to presence of apparatus.
The difference in the position of the boomerang's centre of mass with and without aluminium V-piece is about 0.2 cm. During the experiments, therefore, the axis of rotation does not pass exactly through the boomerang's own centre of mass. This shift should have only a very small effect on the aerodynamic forces.

As all of the forces acting on unit B are measured rather than those acting on the boomerang only, systematic errors may result. For this reason the rotating shaft was shielded. But inevitably some aerodynamic

forces act on the moving parts of unit B: axle, gearing belts and wheels, disk with slits; and because of motion of the air, also on the rest of unit B. A few measurements without boomerang showed that the influence of these forces is small. The air flow around the boomerang is influenced by the presence of the apparatus, in particular the streamlined pipe shielding the shaft and also the V-piece. This may cause inevitable, systematic errors of perhaps considerable magnitude. But it is difficult to make a reliable estimate for these.

e) Deformation of the boomerang.
During the measurements the boomerang is kept in position by an attachment at its "elbow" close to its centre of mass. Under the influence of aerodynamic and inertial forces the boomerang may deform. Indeed, occasionally during the experiments some deformation could be clearly seen: the spinning boomerang suggested to the eye the surface of a cone rather than that of a plane circle. The deviation of the boomerang's arms from the proper plane could sometimes be as high as 10°, but this was exceptional. The magnitude of the deformation increases with increasing V and ψ. It may vary during the course of one revolution. It is difficult to estimate the systematic errors due to this cause, but they could very well be serious. During most of the measurements, however, the deformation was so small as to be scarcely perceptible.

f) Errors in the corrected outputs Mc_j.
The amplification factors of the strain gauge signal amplifiers and integrators varied somewhat. Regular checking measurements showed that these variations were always smaller than ± 0.75%. We therefore assume an error

$$da = 0.5\% \qquad (29.6)$$

in each of the 6 outputs Mc_j.

The zero-levels of a channel at the beginning and at the end of a run generally were not the same. In particular channel 11 had a relatively strong drift, always positive during the measurements and negative in between, on the average ≈ 27 Mc ≈ 1 µst ≈ 4 gf during one run, but not seldom twice this value. There were indications

that this drift was not linear in time (as was supposed in order to calculate the corrected Mc_j), but erratic, depending on the load acting on element 11. As can be seen from table 28.2, this may cause serious errors in the components F_y and T_x. Rather arbitrarily we assume an error in the output of each channel equal to half the average drift during one measuring series (rounded to integral numbers), and take:

channel	9	10	11	12	13	14	
zero-level drift error	3	0	13	1	0	1	Mc units

(29.7)

Another source of errors in the Mc_j is due to rounding to the integral numbers which are read out. This happens once for the zero-level measurements and once for the true measurements (and a third time after multiplication by the scale factor). This causes an error in the Mc_j which is taken to be 1, 2, 5, 10 Mc units, depending on the scale factor used. This concerns the runs with complete zero-level measurements, denoted by XX (see §28); the errors in the X and O measurements are taken greater:

	scale factor	1	2	5	10	
measurements	XX	1	2	5	10	errors in Mc units
	X	1	4	10	20	
	O	7	9	15	25	

(29.8)

Some arguments for this rather arbitrary choice are given in [Hess, 1972].

The possible errors DMc_j, $j = 9,\ldots,14$ in the corrected outputs Mc_j are the sums of the errors in (29.6), (29.7) and (29.8). By assuming that these combine in the most unfavourable way we obtain the resulting errors d_2F_i in the force components F_i:

$$d_2F_i = \sum_{j=9}^{14} |A_{ji}| DMc_j, \qquad i = 1,\ldots,6 \tag{29.9}$$

It is probable that the errors in the integrated outputs are related to the amplitudes rather than to the measured averages. It is difficult to

estimate the real errors but it is likely that they increase with increasing amplitudes. Actually, the stronger the oscillations, the larger the scale factors used. So the assumed errors listed in (29.8) might be relatively reasonable guesses. The real errors could not be much more than twice as high as those in (29.9), since most of the double measurements repeated within these limits or better, except sometimes for channel 11. See table 30.1 for some actual values of d_2F_i.

g) Errors of notation.
During the experiments more than 12000 numbers were written down by hand (and afterwards put on punched cards). Of course some of these numbers may be wrong due to human errors. In the few cases in which such an error (of sign for instance) was obvious, it has been corrected.

Conclusion.
Errors of the kind leading to scattering of the experimental points around the "true" values are mainly those considered under f). These may vary considerably for different measurements and for different force components. They may be partly systematic. They are relatively small for F_z and relatively large for T_x and T_y. These errors may on occasion reach 100% in an individual component. The errors considered under a) through e) are of a more slowly varying and more systematic nature. Those under a), b), c) taken together lead to relative errors in $\vec{F}$ and $\vec{T}$ of the order of 5%. The errors under d) and e) may be important for part of the measurements, but are difficult to estimate.

If this experiment would be repeated, the accuracy of the results could easily be improved by: 1^{o}_{-} replacing element 11 by one having less zero-level drift, and 2^{o}_{-} choosing somewhat different rotational velocities in order to reduce vibrations.

§30 *Processing the numerical data.*

Each of the 42 runs is treated as described in §28, and for each measurement values are obtained of U, F_{lx}, F_{ly}, F_{lz}, T_{lx}, T_{ly}, T_{lz}. With the left-handed boomerangs (L1,L4,L6,F18) the experimental values of F_x, F_y, T_x, T_y (and ω too) have been reversed in sign so as to make them conform to the corresponding quantities for right-handed boomerangs. The 9 left-handed measurements with the right-handed boomerang WU (see table 28.3) are not further considered.

As examples consider the data listed in table 30.1, which contains the results of two runs (X) for boomerang L1, the first run at $\psi = 0°$, the second at $\psi = 15°$. V is listed in m/s. The numbers between the rows represent the errors in the quantities listed directly above, calculated according to §29 f. Other errors are not listed. Pairs of duplicating measurements are nrs. 367, 370 and nrs. 368, 371 at $\psi = 0°$. The large discrepancy between the values of F_{ly} and T_{lx} from measurements 368 and 371 very probably is due to drift of element 11 (see §29).

In the experiment three independent variables enter: ψ, V and ω. It is justified (and very convenient) to reduce these to two: ψ and U ($= V/\omega a$), if the dimensionless force components are independent of the absolute magnitude of V and ω or, in other words, independent of Reynolds number. Although the experimental data indicate that this is not quite the case, the uncertainties in the data are such that the dependence on Reynolds number cannot be assessed, except perhaps for the components F_{lz} and T_{lz}. We shall ignore the Re dependence and consider the six dimensionless force components as functions of ψ and U only.

To bring the numerical results into a more simple and useful form, the data can be smoothed. For each value of ψ (fixed for one run), the values of one component can be plotted versus U, and a smooth line can be drawn from which the experimental points should not deviate too much. In [Hess, 1972], where F_{ox}, etc. were plotted vs. Ω rather than F_{lx}, etc. vs. U (see §23), these smooth lines were parabolas, but now we use a more sophisticated method. In §25 the use of doubly cubic splines for interpolation was outlined. We use similar splines to obtain a smooth least-squares approximation to the experimental data.

a)

nr	V	ω/2π	U	F_{lx}	F_{ly}	F_{lz}	T_{lx}	T_{ly}	T_{lz}
355	6.25	6.99	0.477	+.0044	-.0010	+.0224	+.0059	+.0021	-.0031
				29	16	11	37	73	8
356	6.28	10.00	0.336	+.0028	-.0009	+.0208	+.0037	+.0014	-.0027
				14	8	11	20	37	4
357	6.30	14.00	0.240	+.0020	-.0009	+.0186	+.0017	+.0020	-.0025
				8	4	6	11	20	2
358	9.47	7.00	0.723	+.0075	-.0024	+.0350	+.0078	+.0026	-.0042
				30	13	11	31	76	8
359	9.47	10.00	0.506	+.0046	-.0013	+.0264	+.0069	+.0022	-.0031
				15	8	11	21	38	4
360	9.48	14.00	0.362	+.0030	-.0011	+.0231	+.0045	+.0017	-.0025
				8	4	6	11	20	2
361	12.60	7.00	0.961	+.0118	-.0019	+.0493	+.0131	+.0036	-.0048
				31	13	12	32	79	8
362	12.64	10.00	0.675	+.0065	-.0011	+.0346	+.0107	+.0038	-.0035
				16	8	11	21	40	4
363	12.61	14.00	0.481	+.0041	-.0012	+.0267	+.0072	+.0031	-.0027
				8	4	6	11	21	2
364	18.84	7.00	1.438	+.0220	-.0019	+.0947	+.0303	+.0106	-.0058
				35	16	25	43	89	9
265	18.91	10.00	1.010	+.0120	-.0007	+.0604	+.0234	+.0058	-.0041
				17	8	23	26	45	5
366	18.86	13.99	0.720	+.0071	-.0016	+.0408	+.0137	+.0044	-.0031
				9	4	7	11	24	2
367	25.03	7.00	1.910	+.0352	-.0037	+.1616	+.0522	+.0181	-.0060
				39	17	28	45	100	10
368	24.97	10.00	1.334	+.0181	-.0009	+.0959	+.0373	+.0100	-.0044
				20	8	25	27	50	5
370	25.12	7.00	1.916	+.0347	-.0059	+.1651	+.0510	+.0171	-.0057
				39	17	28	46	100	10
371	25.10	9.99	1.341	+.0181	-.0046	+.0978	+.0301	+.0091	-.0049
				19	8	25	28	50	5
372	25.05	14.01	0.955	+.0114	-.0038	+.0634	+.0205	+.0034	-.0035
				10	4	13	15	27	3

b)

nr	V	ω/2π	U	F_{lx}	F_{ly}	F_{lz}	T_{lx}	T_{ly}	T_{lz}
409	6.14	7.00	0.468	+.0009	-.0032	+.0689	+.0115	+.0042	-.0013
				28	13	13	32	71	8
410	6.14	10.00	0.328	+.0013	-.0029	+.0498	+.0060	+.0033	-.0011
				14	8	12	21	36	4
411	6.13	13.99	0.234	+.0013	-.0020	+.0378	+.0030	+.0035	-.0011
				8	4	7	11	19	2
412	9.45	7.00	0.721	+.0004	-.0041	+.1183	+.0201	+.0061	-.0015
				28	16	26	44	72	8
413	9.46	10.00	0.505	+.0003	-.0048	+.0801	+.0141	+.0061	-.0004
				14	8	24	27	36	4
414	9.43	14.00	0.360	+.0013	-.0037	+.0558	+.0090	+.0047	+.0000
				8	4	8	12	20	2
415	12.54	7.00	0.957	-.0013	-.0043	+.1819	+.0288	+.0115	-.0011
				28	16	29	45	72	8
416	12.50	10.28	0.649	-.0012	-.0062	+.1132	+.0233	+.0103	+.0010
				14	8	24	27	35	4
417	12.52	14.00	0.478	+.0006	-.0055	+.0761	+.0153	+.0069	+.0009
				8	4	9	13	20	2
418	18.84	7.00	1.438	-.0126	-.0110	+.3900	+.0578	+.0353	+.0050
				29	17	60	60	73	8
419	18.82	10.28	0.978	-.0068	-.0134	+.2127	+.0397	+.0186	+.0048
				14	9	29	30	35	4
420	18.80	14.00	0.717	-.0015	-.0102	+.1338	+.0292	+.0114	+.0036
				8	5	17	17	20	2
421	25.03	7.00	1.910	-.0382	-.0304	+.6925	+.0977	+.0660	+.0170
				32	19	75	70	81	9
422	24.99	10.56	1.263	-.0165	-.0282	+.3353	+.0468	+.0320	+.0091
				14	9	35	33	35	4
423	24.87	13.99	0.949	-.0044	-.0171	+.2088	+.0422	+.0183	+.0069
				8	5	21	20	21	2

table 30.1. Results of two runs: (X) for boomerang L1. a: $\psi = 0$, b: $\psi = 15$

A two-dimensional mesh (see §25) in (ψ,U)-space is defined by the mesh-points (ψ_i,U_j), $i = 1,\ldots,9$, $j = 1,\ldots,7$. ψ_i and U_j are chosen as follows:

i	1	2	3	4	5	6	7	8	9
ψ_i	-5°	0°	5°	10°	15°	20°	30°	45°	90°

(30.1)

j	1	2	3	4	5	6	7
U_j	0	.25	.50	.75	1.0	1.5	2.0

(30.2)

Fig. 30.1 shows the resulting mesh.

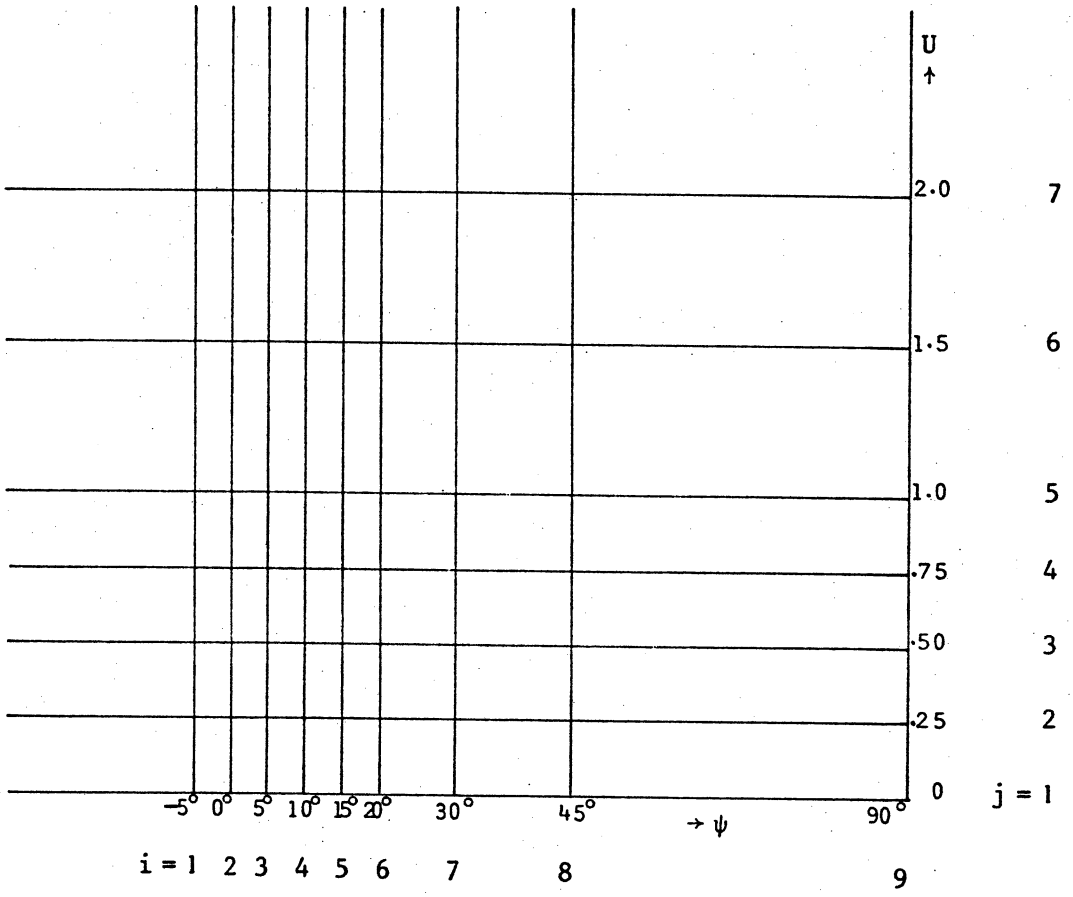

fig. 30.1. Mesh in (ψ,U)-space.

For any of the runs we have $\psi = \psi_i$, $i = 1,\ldots,8$. (The reason for the addition of $\psi_i = 90^\circ$ to (30.1) will be explained presently.) The experimental points are thus situated on the lines $\psi = \psi_i$, $i = 1,\ldots,8$ in

(ψ,U)-space, but scattered in U-direction. For each run we find a spline S_i $(i = 1,\ldots,8)$ belonging to the meshpoints U_j, $j = 1,\ldots,7$ which minimized the expression:

$$\sum_{k=1}^{n_i} [f_i^k - S_i(U^k)]^2 W_i^k \qquad (30.3)$$

Here f stands for any of the six dimensionless force components and the superscripts k $(k = 1,\ldots,n_i)$ denote the measurements in series i. The weights W_i^k are taken inversely proportional to the errors in the f_i^k calculated according to §29f. In this way we obtain the values S_{ij}, $i = 1,\ldots,8$, $j = 1,\ldots,7$ of the *doubly* cubic smoothing spline S, belonging to the considered component, at the meshpoints. This general procedure is modified if there are no experimental points in the neighbourhood of one or more meshpoints. In this case such meshpoints are omitted from the U-mesh, and afterwards the missing values S_{ij} are calculated by extrapolation (interpolation did not occur). What is meant here by "the neighbourhood" of a meshpoint in U-direction is shown in fig. 30.2. The maximum experimental values of U are ≈ 2.5 for boomerang F18 and ≈ 2 for the other boomerangs.

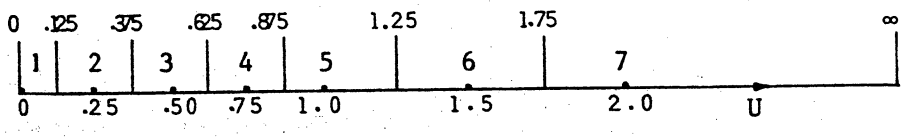

fig. 30.2. Neighbourhoods of meshpoints U_j. Meshpoints are indicated by dots, neighbourhoods are separated by vertical lines halfway the meshpoints.

In §23 we remarked that, if V cos $\psi = 0$, the components F_{1x}, F_{1y}, T_{1x} and T_{1y} must vanish because of symmetry, and the components F_{1z} and T_{1z} must be independent of ψ. In order to satisfy the relations (23.4) and (23.5) for $U = 0$ we proceed as follows. We take S_{i1}, $i = 1,\ldots,8$ equal to zero for the components F_{1x}, F_{1y}, T_{1x}, T_{1y}. For the components F_{1z} and T_{1z} we average the calculated values S_{i1}, $i = 1,\ldots,8$ (giving each run i a weight equal to the number of measurements in neighbourhood 1 plus 0.1 × the number of measurements in neighbourhood 2). The resulting value is taken as S_{i1}, $i = 1,\ldots,8$, independent of ψ. In (30.1) $\psi_9 = 90°$ is added because the experimental data will be used in the computation

of boomerang flight paths (see Part III), in which values of ψ close to 90° may occasionally occur. In agreement with (23.6) we take $S_{9,j}$, $j = 1,\ldots,7$ ($\psi = 90°$) equal to zero for components F_{1x}, F_{1y}, T_{1x}, T_{1y}. And, for lack of better, we take $S_{9,j}$ ($\psi = 90°$) equal to $S_{8,j}$ ($\psi = 45°$) for the components F_{1z} and T_{1z}. We now have a complete set of smoothed values S_{ij} for each of the six components at the meshpoints (ψ_i,U_j), $i = 1,\ldots,9$, $j = 1,\ldots,7$. Values at any other point in (ψ,U)-space are provided by the doubly cubic interpolation splines according to §25. This is just a matter of smooth interpolation, leading to the drawn curves in the figures of §31.

The theoretical results (based on the theory of the preceding chapters) with which the experimental data are to be compared in the following sections, are brought into a similar form. For a given theoretical model boomerang, values are computed of F_{1x}, F_{1y}, F_{1z}, T_{1x}, T_{1y}, T_{1z} at the meshpoints (ψ_i,U_j), $i = 1,\ldots,9$, $j = 2,\ldots,7$. It is impossible to apply our theory if $U = 0$. Here we take F_{1x}, F_{1y}, T_{1x}, T_{1y} equal to zero in accordance with (23.4), and for F_{1z} and T_{1z} we uae a spline extrapolation to find the values S_{i1}, $i = 1,\ldots,8$, which then are averaged, so that (23.5) is satisfied.

The six sets of values of the dimensionless components at the points (ψ_i,U_j), $i = 1,\ldots,9$, $j = 1,\ldots,7$ together characterize a boomerang's aerodynamic properties. To such a collection of values a "boomerang number" is attached to serve as a label. The boomerang numbers for the five experimental boomerangs are chosen as follows:

L1 : 101
L4 : 104
L6 : 106
F18: 108
WU : 109

The experimental values for these boomerangs are arranged in five tables at the end of §31. Similar tables can be computed for theoretical boomerangs. Such tables are used in Part III as a basis for flight path calculations.

§31 *The experimental results.*

This lengthy section contains 5 tables and 36 graphs showing experimental results, and 30 theoretical graphs to compare the experimental ones with. The graphs have been drawn by an automatic plotter on basis of the methods outlined in §30. The lines in the graphs have been dashed rather than drawn wherever the results are due to extrapolation rather than measurements. To these extrapolated values not much physical significance should be attached.

The graphs and tables contain data on the six dimensionless force and torque components acting on the boomerangs, as functions of the boomerang's angle of incidence ψ and the advance ratio $U = V/\omega a$. The six components, in the order of the graphs, are:

F_{1z} = axial force,
T_{1z} = axial torque,
T_{1x} = rolling torque,
F_{1y} = sideward force,
T_{1y} = pitching torque,
F_{1x} = backward force parallel to plane of rotation.

The subscript 1 indicates that the forces and torques have been made dimensionless by dividing them by $\mu\omega^2 a^4$ and $\mu\omega^2 a^5$ respectively. The dimensionless lift F_{1L} and the dimensionless drag F_{1D} are given by:

$$\left.\begin{aligned} F_{1L} &= F_{1z}\cos\psi - F_{1x}\sin\psi \\ F_{1D} &= F_{1x}\cos\psi + F_{1z}\sin\psi \end{aligned}\right\} \quad (31.1)$$

Figures 31.1 through 31.6 show graphs, for boomerang L1, of the six components as functions of U. They serve as a fairly representative example to give an impression of the scatter in the experimental data. The position of each measurement is indicated by a digit i, i = 1,...,8, denoting the angle of incidence ψ_i from (30.1). Thus 1 means $\psi = -5°$, 8 means $\psi = 45°$, etc.

The measured F_{1z} values scatter relatively little and the T_{1z} values do not scatter much either. The components that scatter most are T_{1x}

and F_{1y}. The components T_{1y} and F_{1x} are intermediate as regards scatter. Part of the scatter for the component F_{1z} must be due to the dependence on Reynolds number, since in most clusters of three experimental points the lowest point originates from a measurement at 7 revs/sec., the middle one from 10 revs/sec. and the highest one from 14 revs/sec. A quantitative investigation of this effect could be made by processing the data for each of the three rotational velocities separately, and studying the systematic differences between the resulting graphs. This, however, has not been done.

Figures 31.7 through 31.36 show graphs of the six components as functions of ψ, for all five experimental boomerangs: L1, L4, L6, F18 and WU respectively. Each figure shows experimental graphs at the left and theoretical counterparts at the right. They are made by the methods outlined in §30. The numbers in the graphs denote the U-values for each of the lines: $U = U_j$, $j = 2,\ldots,7$, see (30.2). The choice of parameters for the theoretical boomerangs is discussed in §32. An evaluation of the correspondence and differences between theory and experiment is given in §33.

Finally, tables 31.1 through 31.5 provide a condensed survey of the experimental results for each of the five boomerangs. Values of the six dimensionless components are listed for the points in (ψ,U)-space defined by (30.1) and (30.2) (see fig. 30.1). Values outside the boxes are based on extrapolation rather than measurements, and have little physical significance. Entries for $\psi = 90°$ have been omitted here, for this see §30.

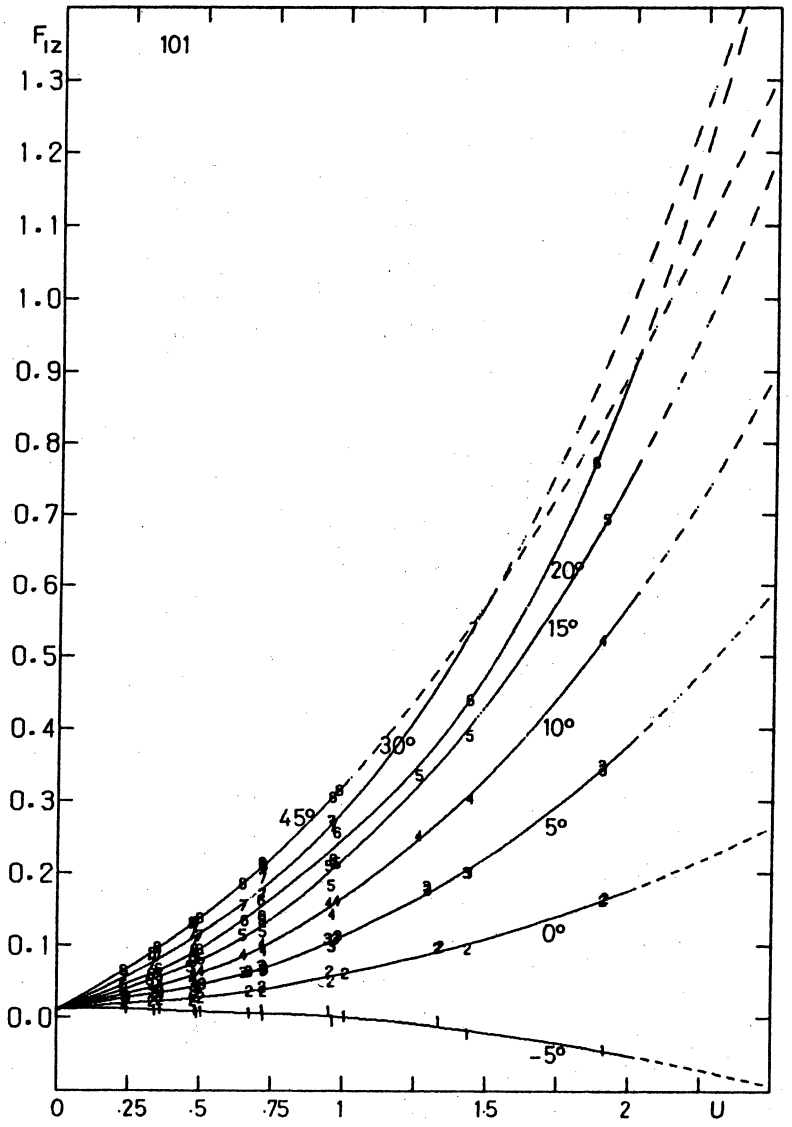

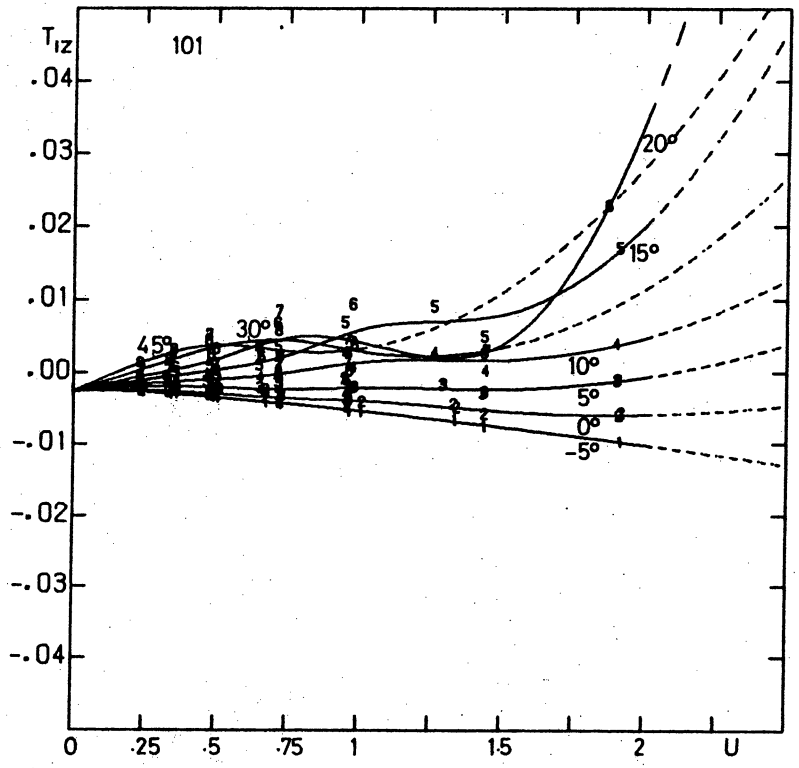

fig. 31.1 (at left). Boomerang L1, measurements component F_{1z}.

fig. 31.2. (above). Boomerang L1, measurements component T_{1z}.

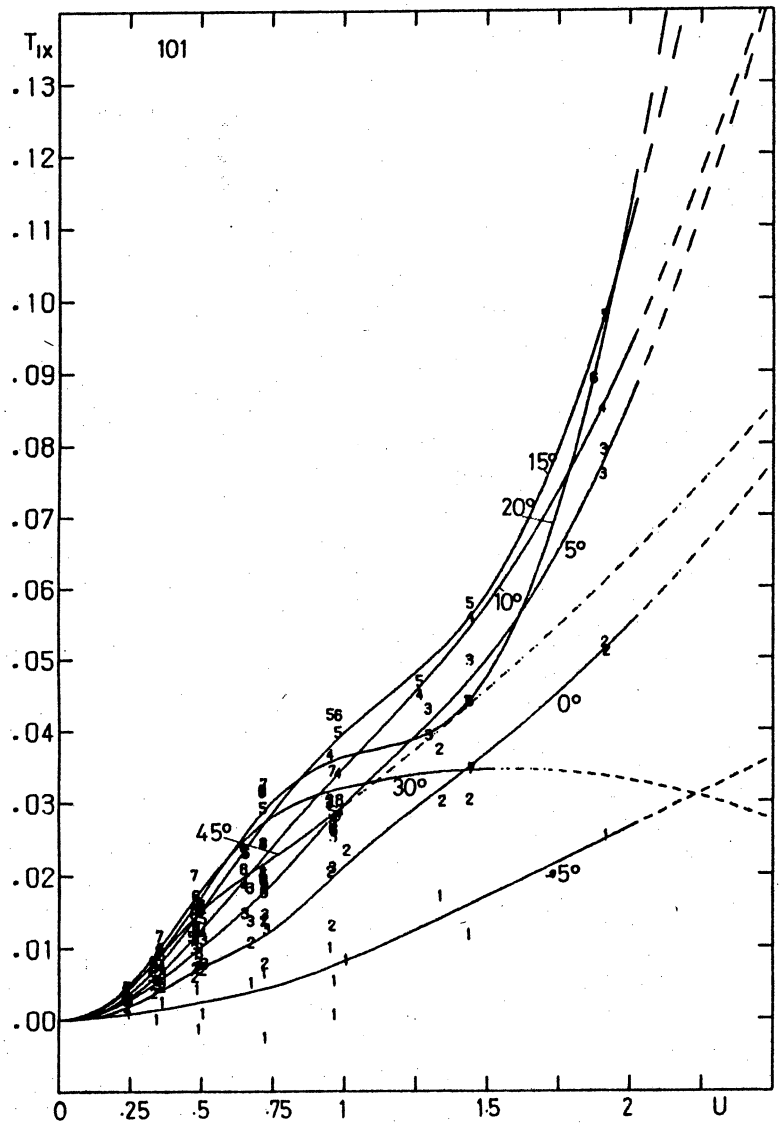

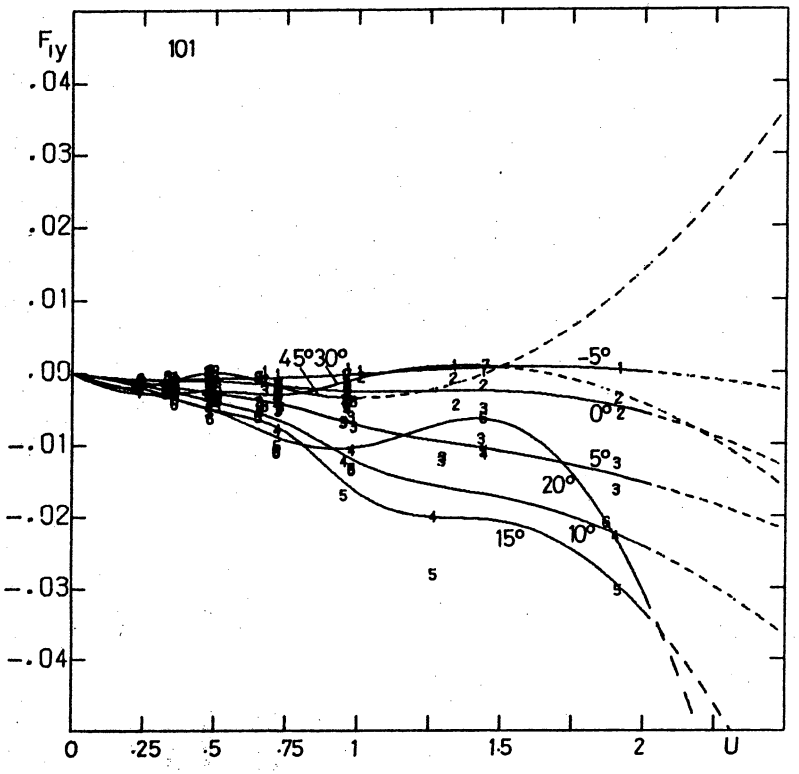

fig. 31.3. (at left). Boomerang L1, measurements component T_{lx}.

fig. 31.4. (above). Boomerang L1, measurements component F_{ly}.

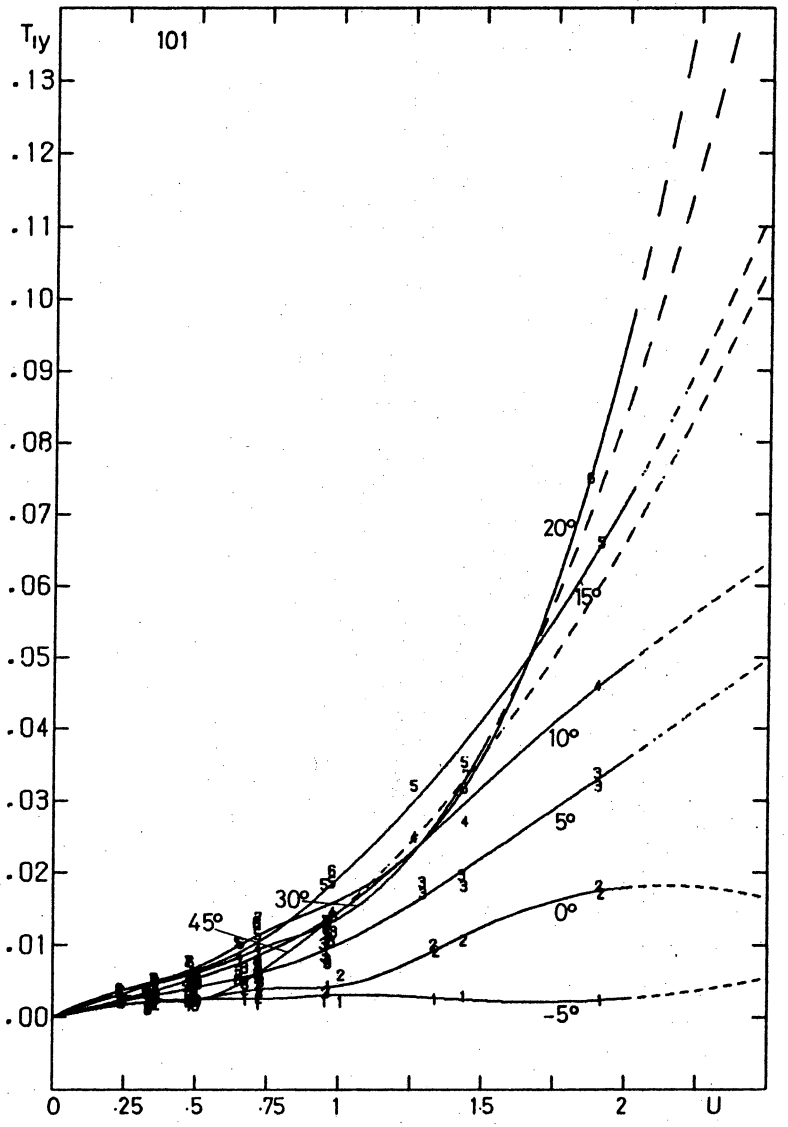

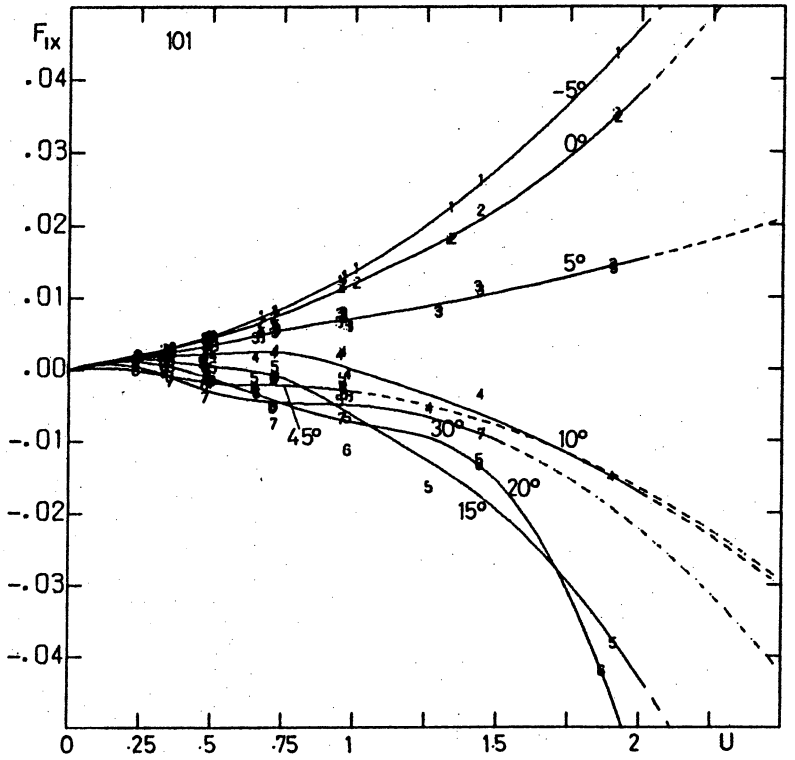

fig. 31.5. (at left). Boomerang L1, measurements component T_{ly}.

fig. 31.6. (above). Boomerang L1, measurements component F_{lx}.

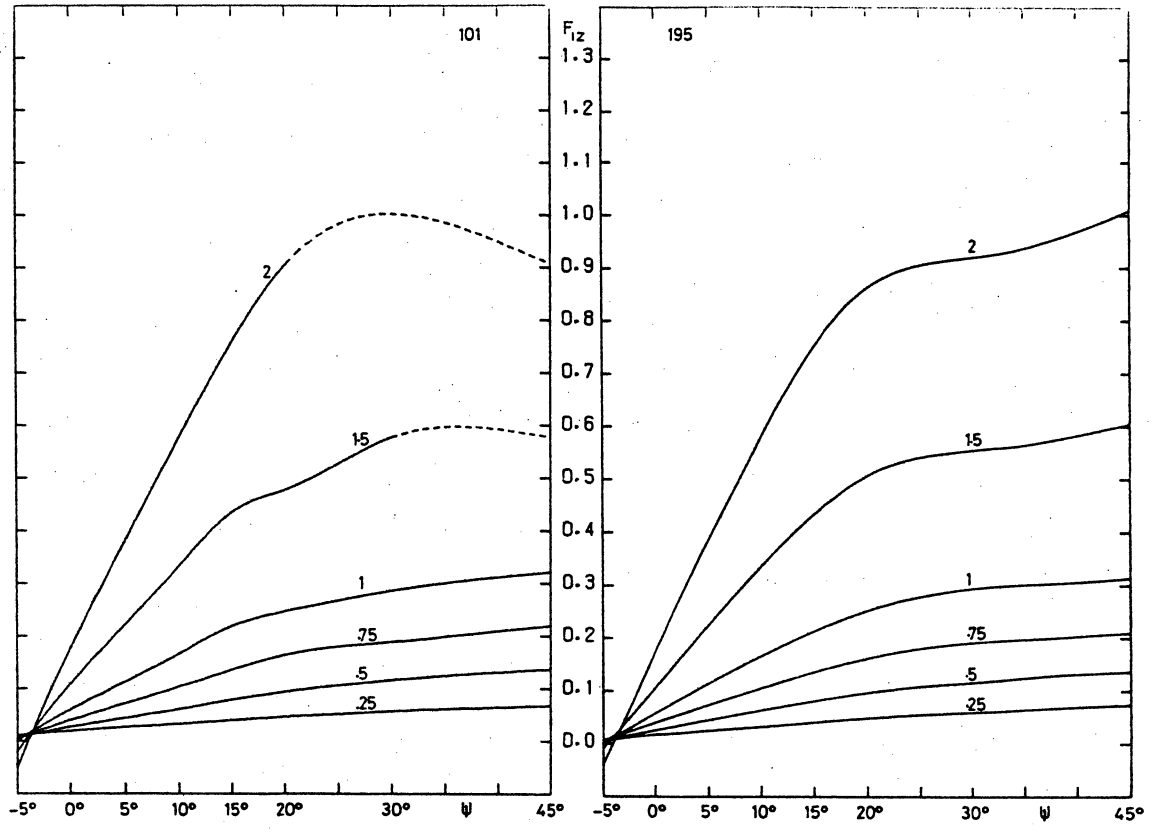

fig. 31.7. Boomerang L1, component F_{lz}. 101 = exp., 195 = theor.

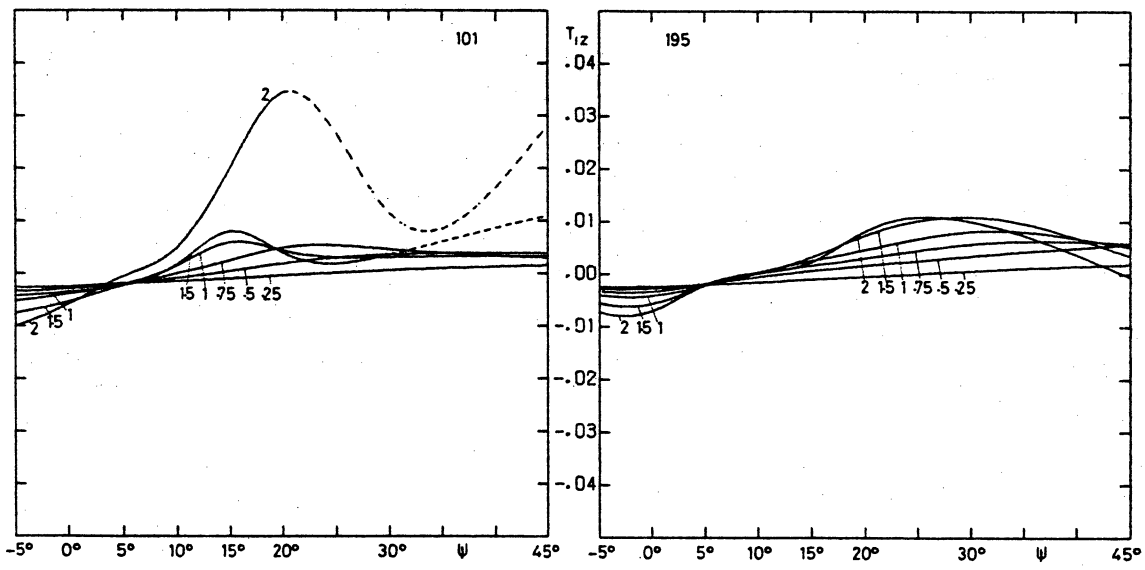

fig. 31.8. Boomerang L1, component T_{lz}. 101 = exp., 195 = theor.

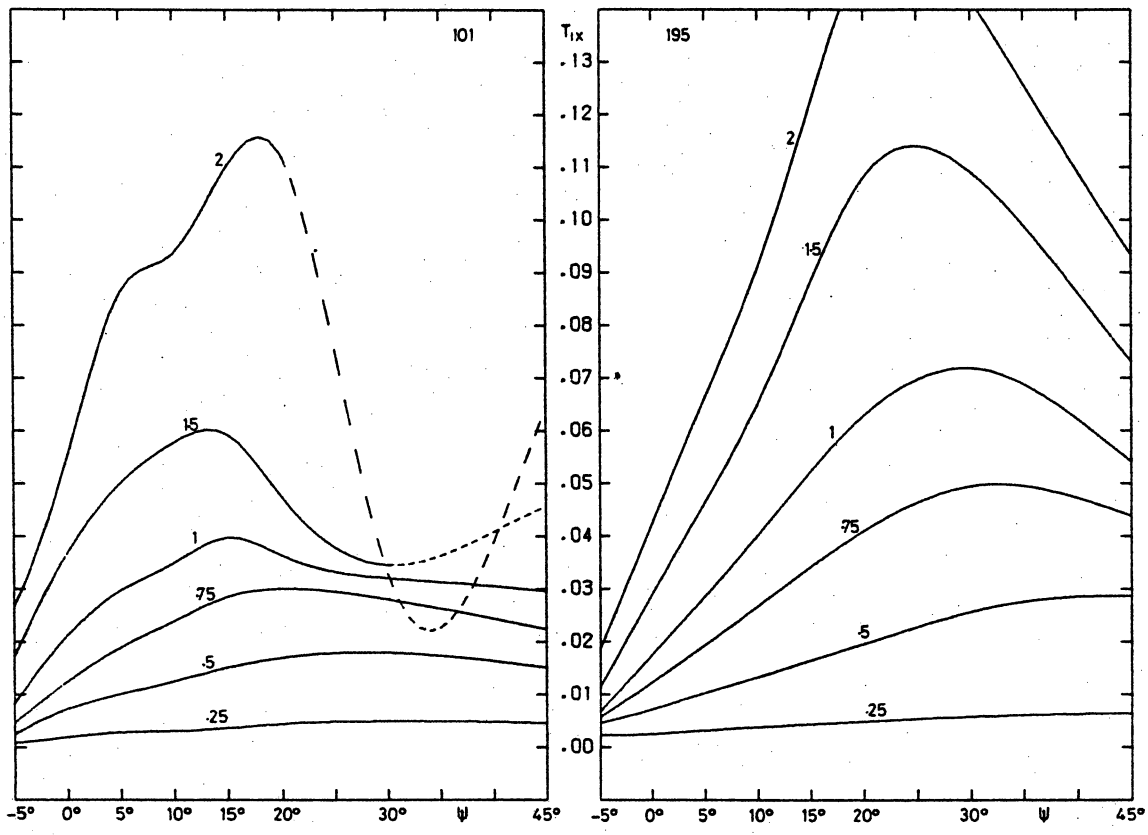

fig. 31.9. Boomerang L1, component T_{1x}. 101 = exp., 195 = theor.

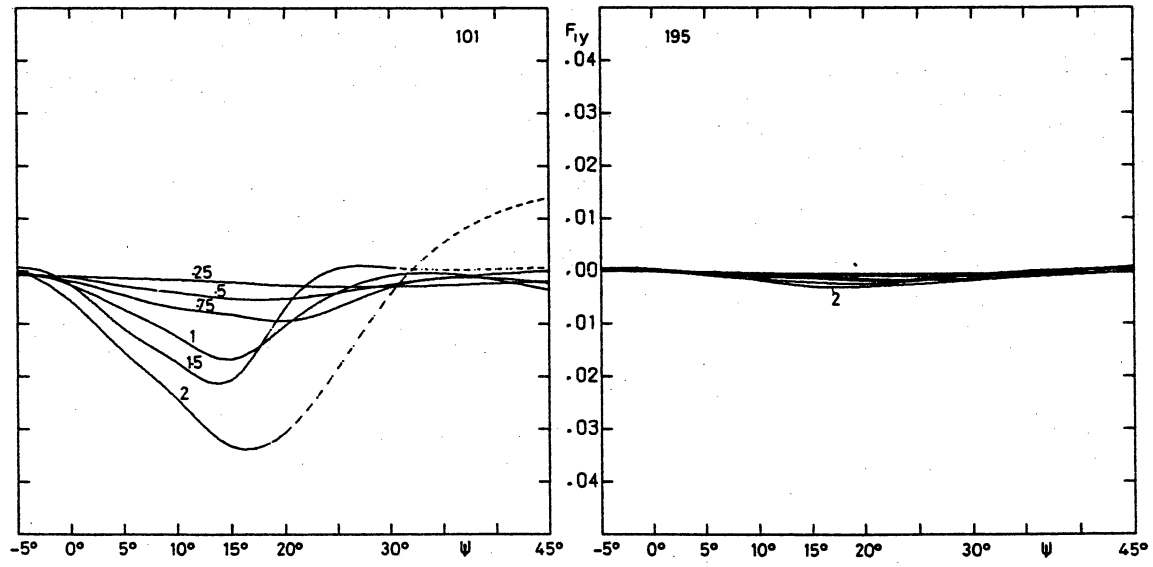

fig. 31.10. Boomerang L1, component F_{1y}. 101 = exp., 195 = theor.

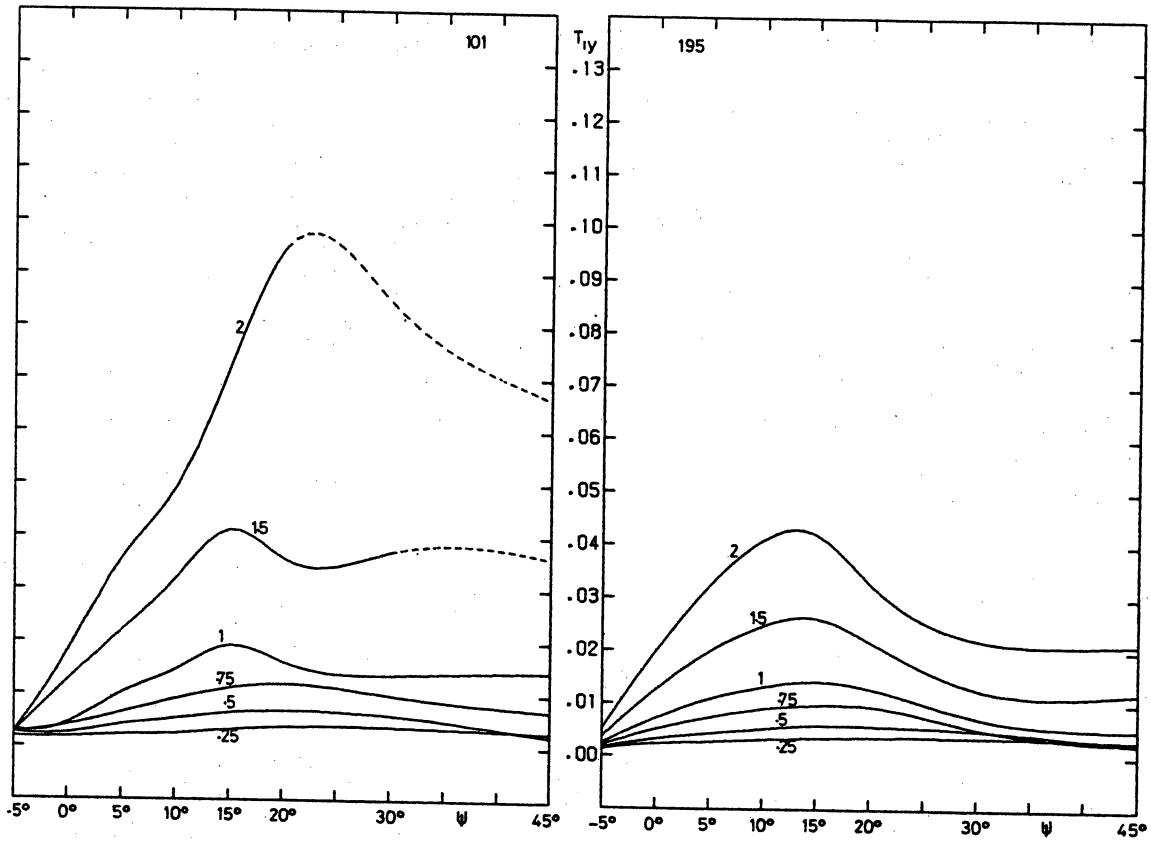

fig. 31.11. Boomerang L1, component T_{1y}. 101 = exp., 195 = theor.

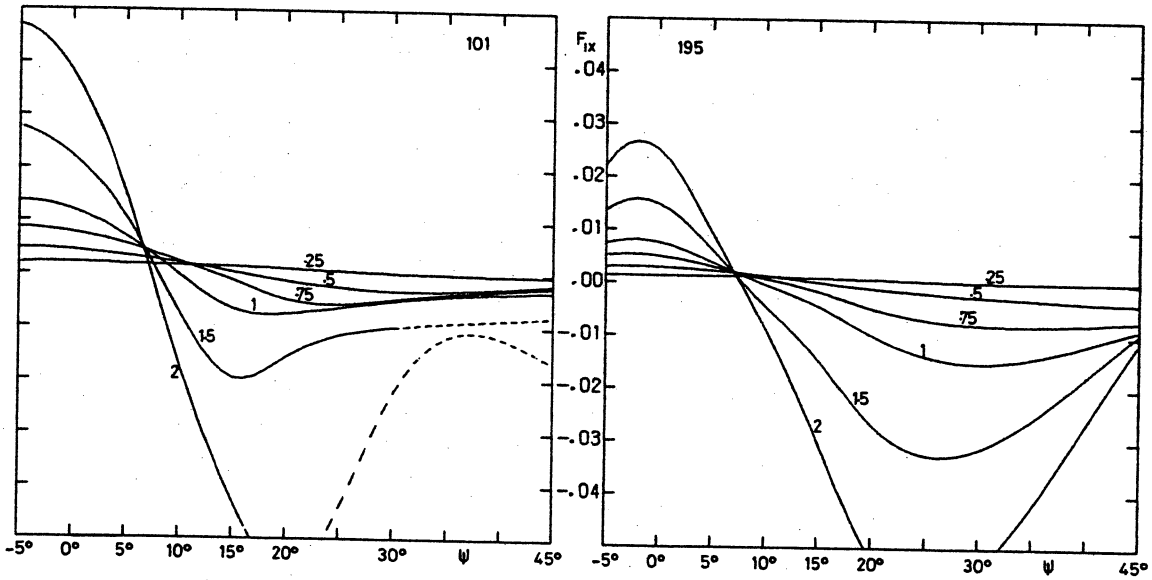

fig. 31.12. Boomerang L1, component F_{1x}. 101 = exp., 195 = theor.

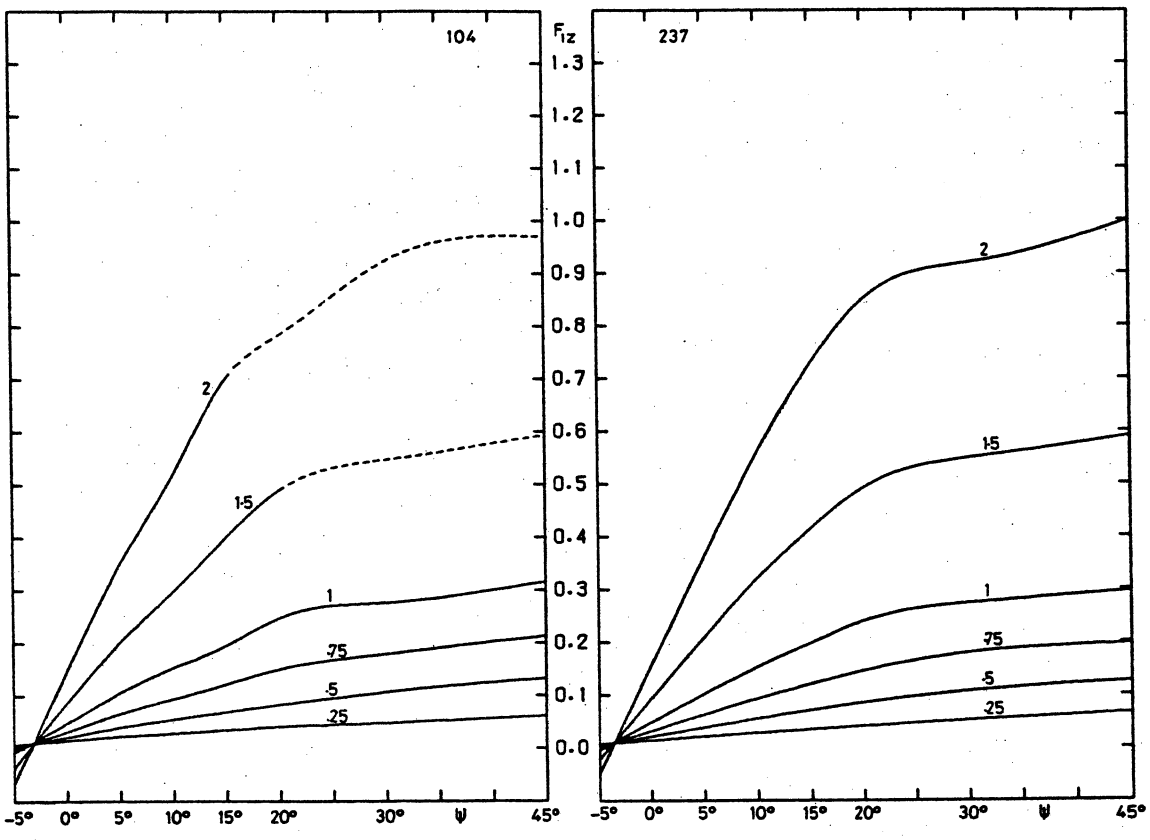

fig. 31.13. Boomerang L4, component F_{1z}. 104 = exp., 237 = theor.

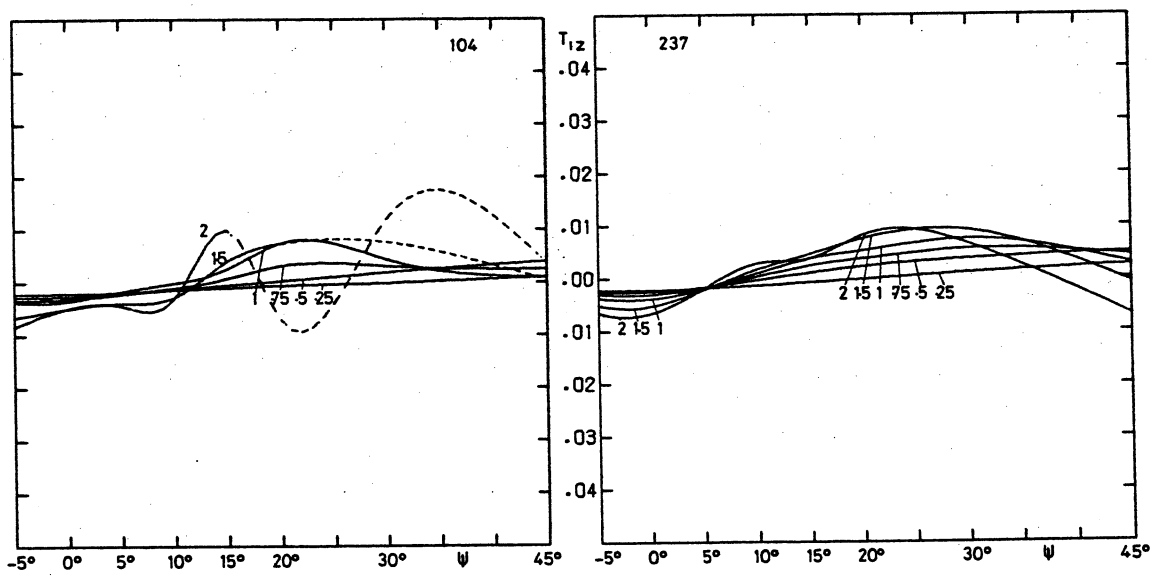

fig. 31.14. Boomerang L4, component T_{1z}. 104 = exp., 237 = theor.

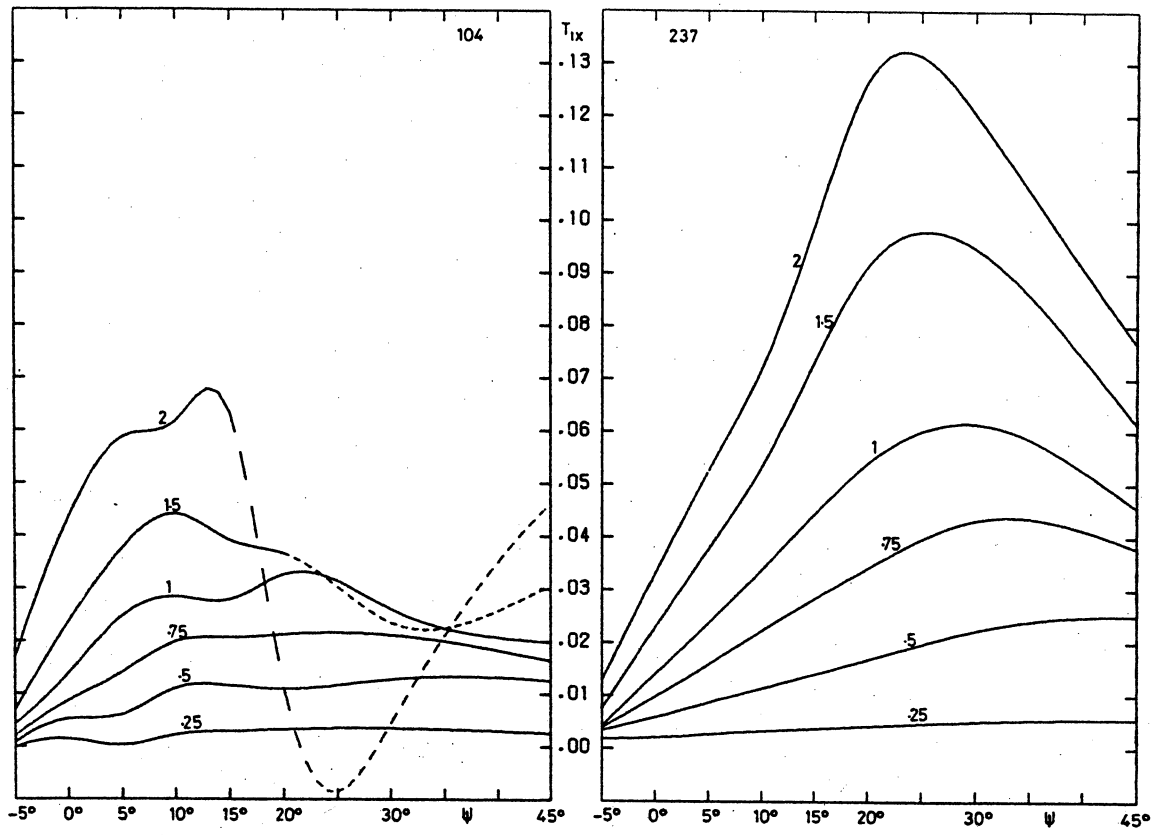

fig. 31.15. Boomerang L4, component T_{1x}. 104 = exp., 237 = theor.

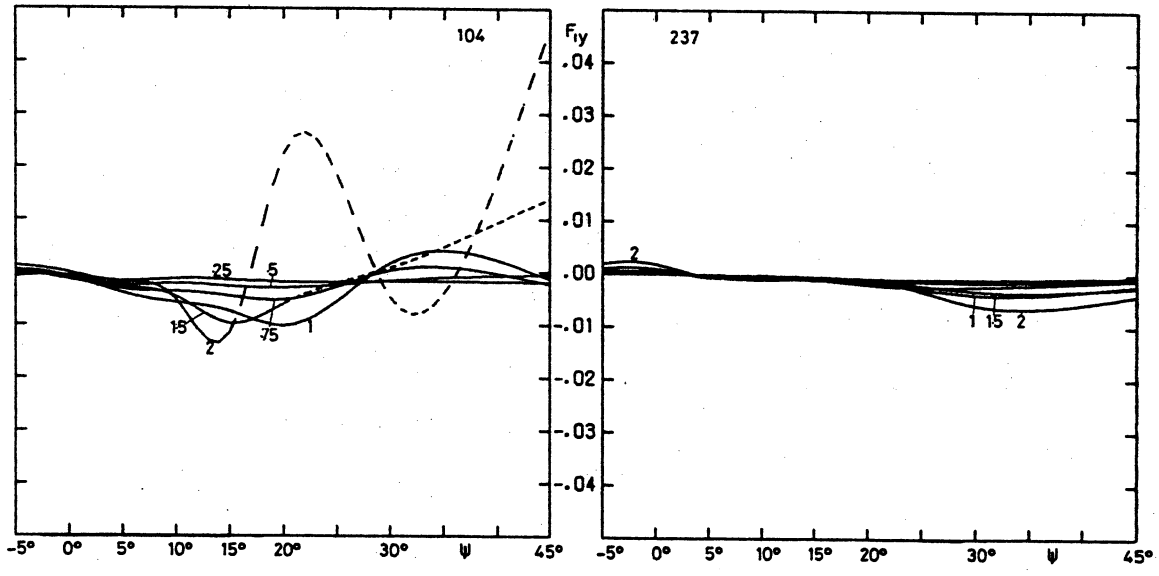

fig. 31.16. Boomerang L4, component F_{1y}. 104 = exp., 237 = theor.

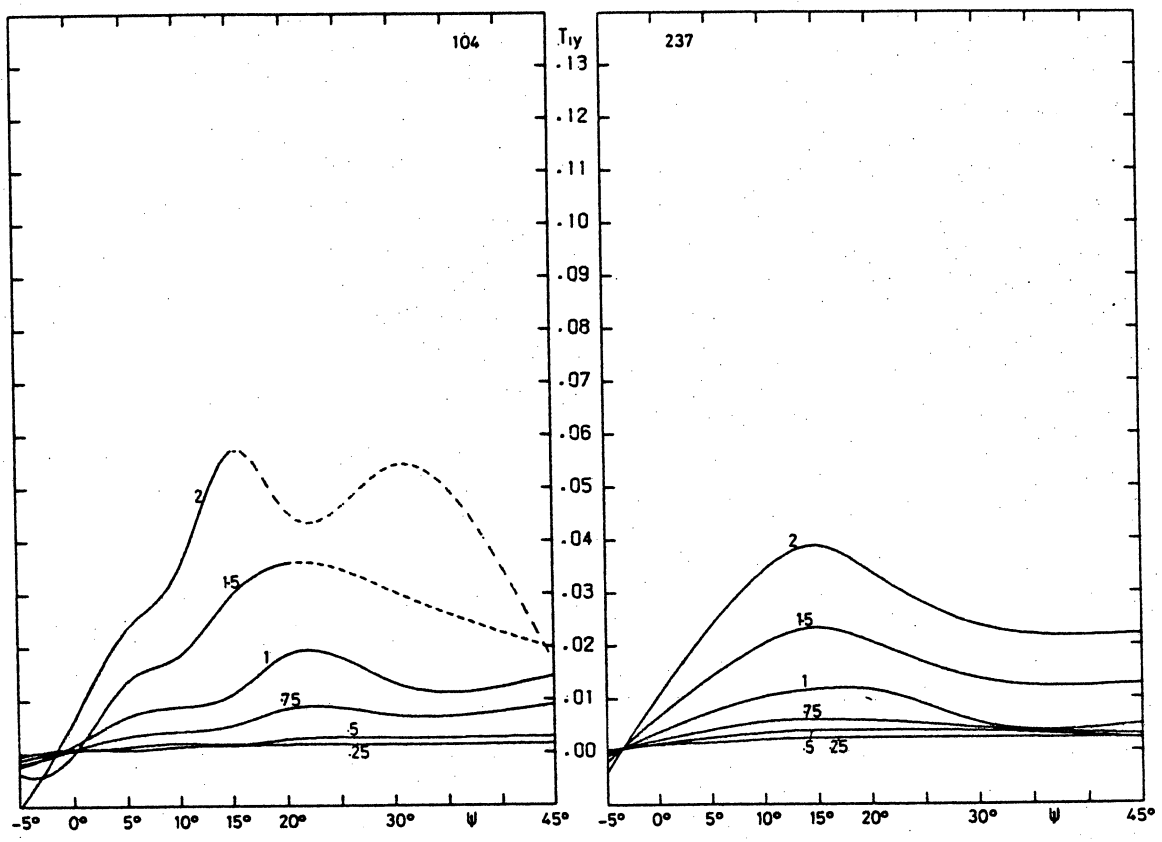

fig. 31.17. Boomerang L4, component T_{1y}. 104 = exp., 237 = theor.

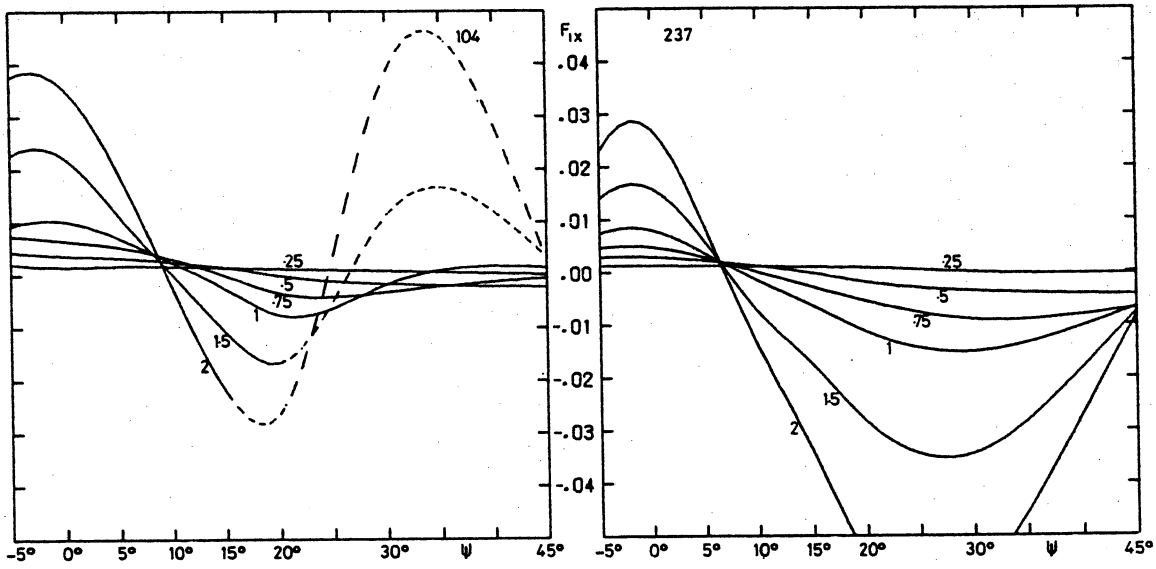

fig. 31.18. Boomerang L4, component F_{1x}. 104 = exp., 237 = theor.

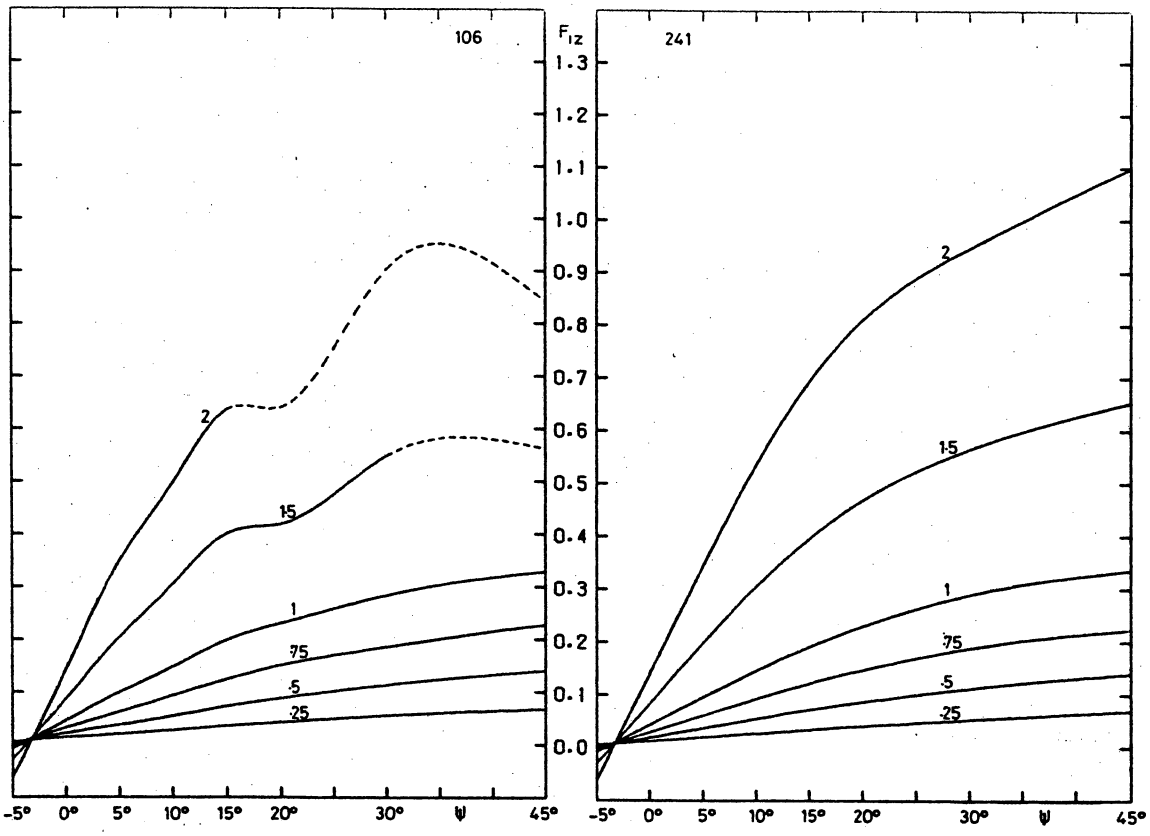

fig. 31.19. Boomerang L6, component F_{1z}. 106 = exp., 241 = theor.

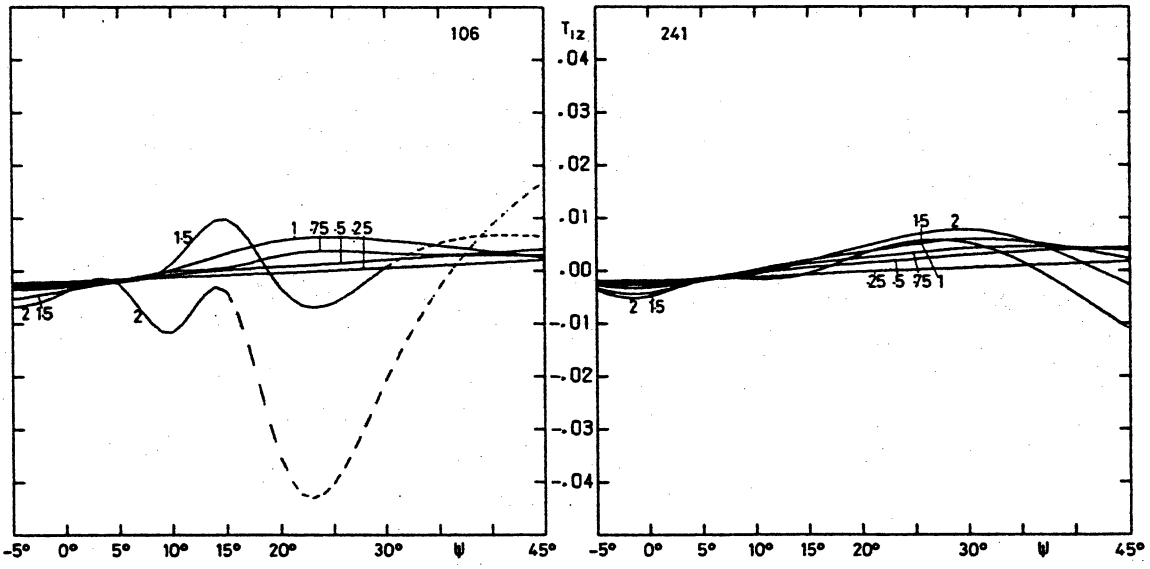

fig. 31.20. Boomerang L6, component T_{1z}. 106 = exp., 241 = theor.

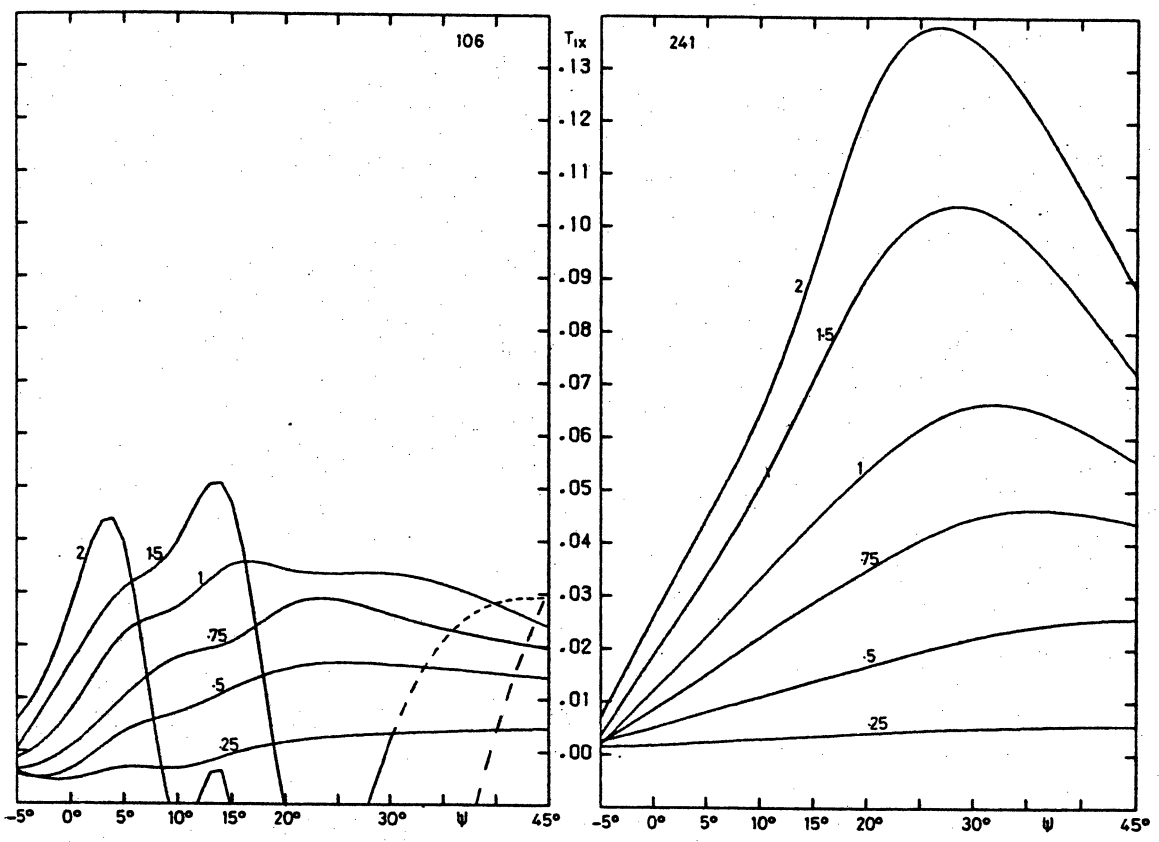

fig. 31.21. Boomerang L6, component T_{1x}. 106 = exp., 241 = theor.

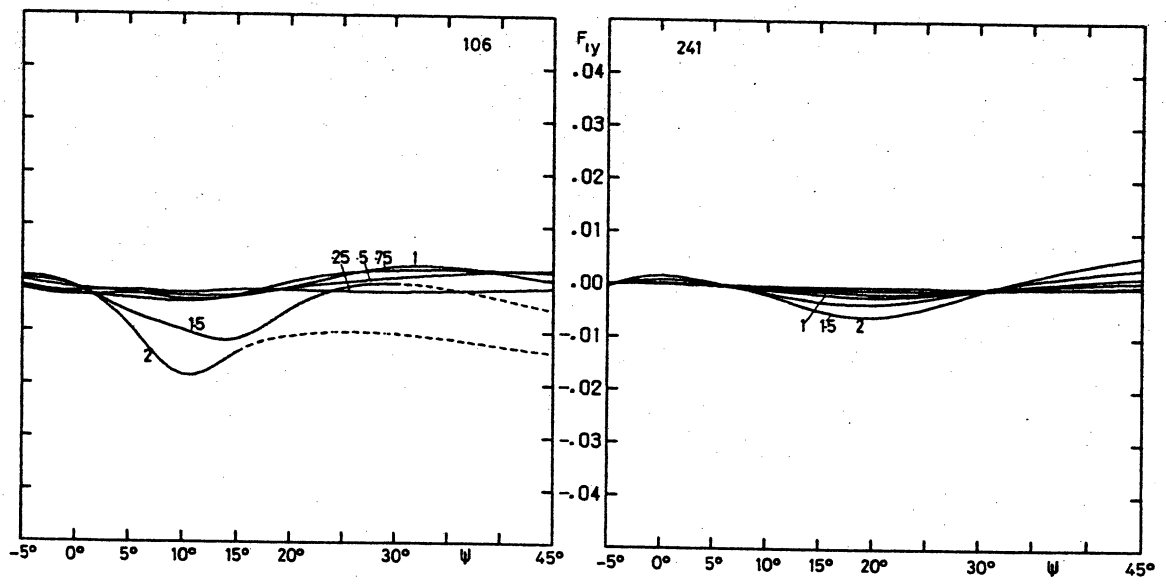

fig. 31.22. Boomerang L6, component F_{1y}. 106 = exp., 241 = theor.

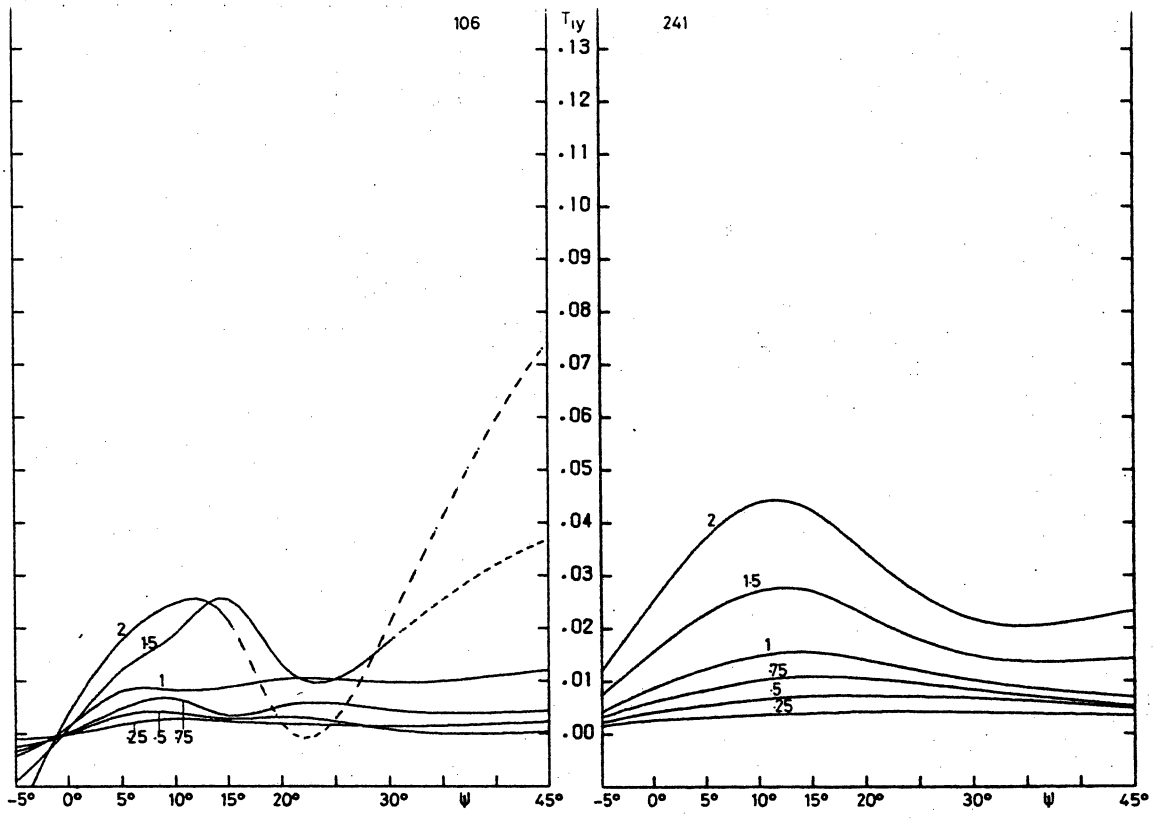

fig. 31.23. Boomerang L6, component T_{1y}. 106 = exp., 241 = theor.

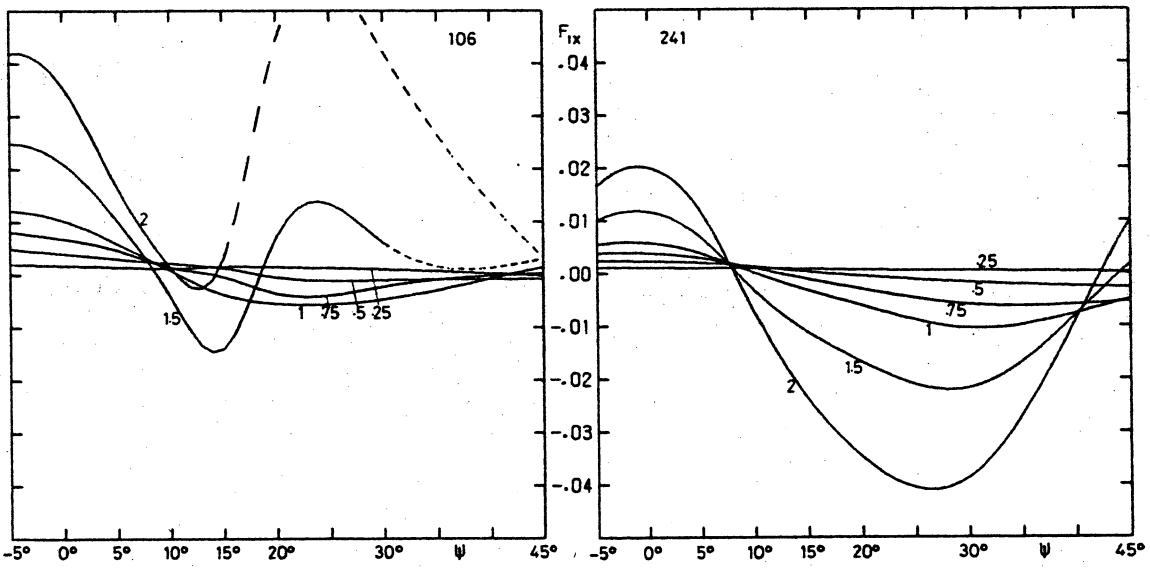

fig. 31.24. Boomerang L6, component F_{1x}. 106 = exp., 241 = theor.

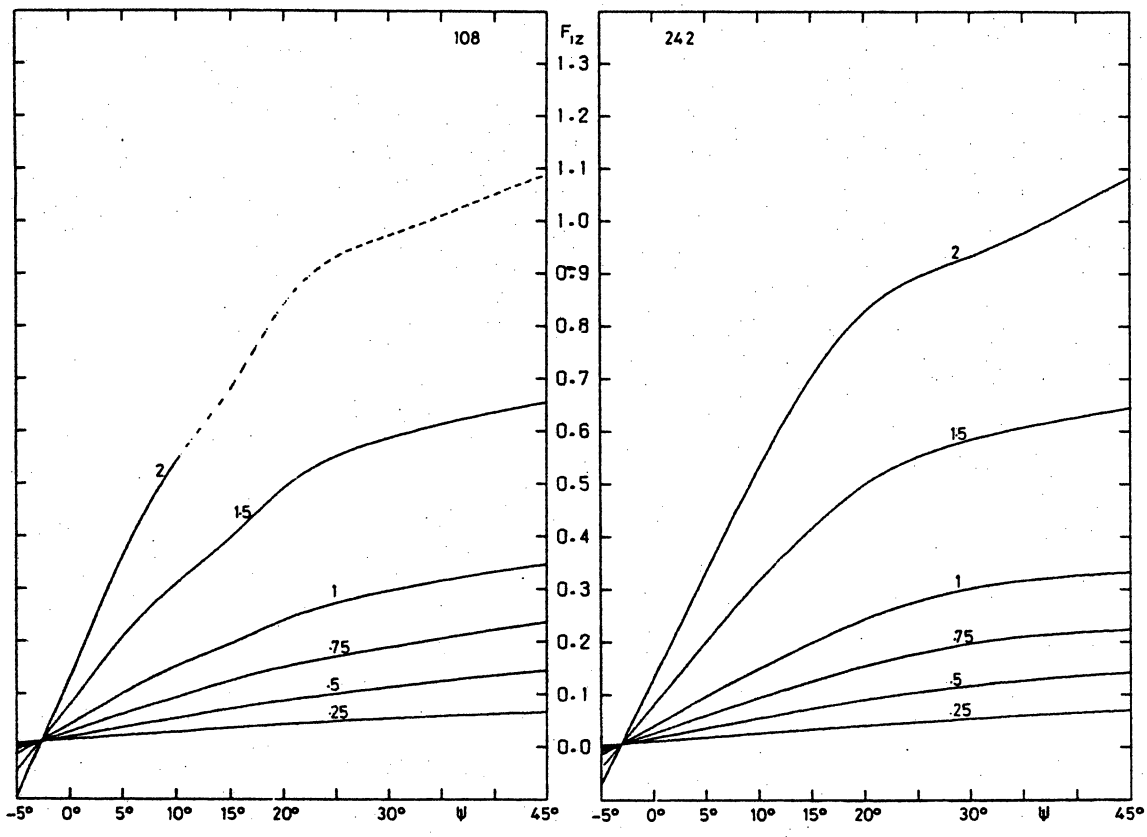

fig. 31.25. Boomerang F18, component F_{1z}. 108 = exp., 242 = theor.

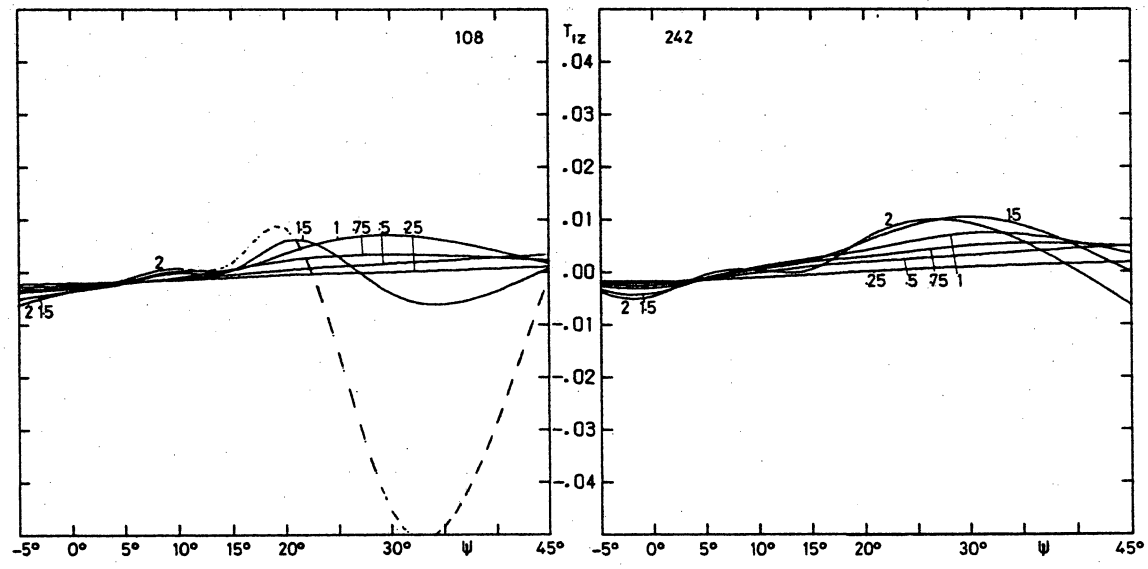

fig. 31.26. Boomerang F18, component T_{1z}. 108 = exp., 242 = theor.

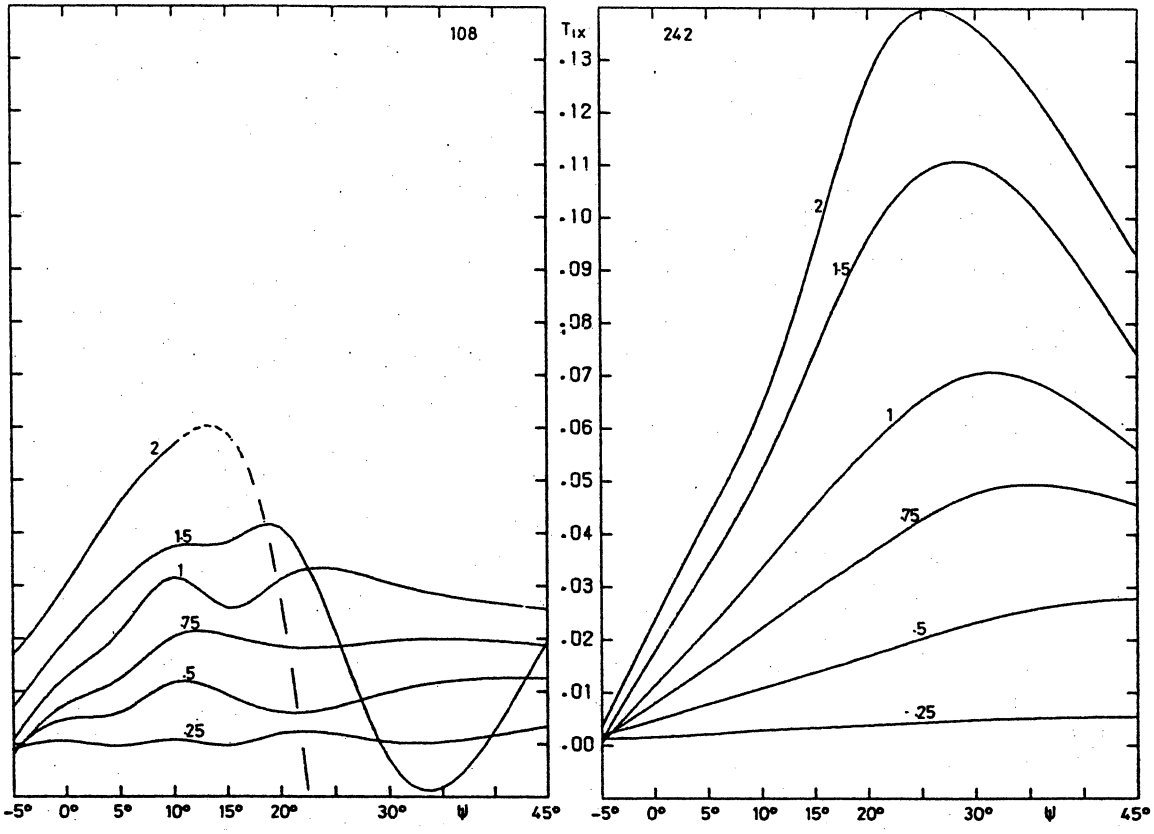

fig. 31.27. Boomerang F18, component T_{1x}. 108 = exp., 242 = theor.

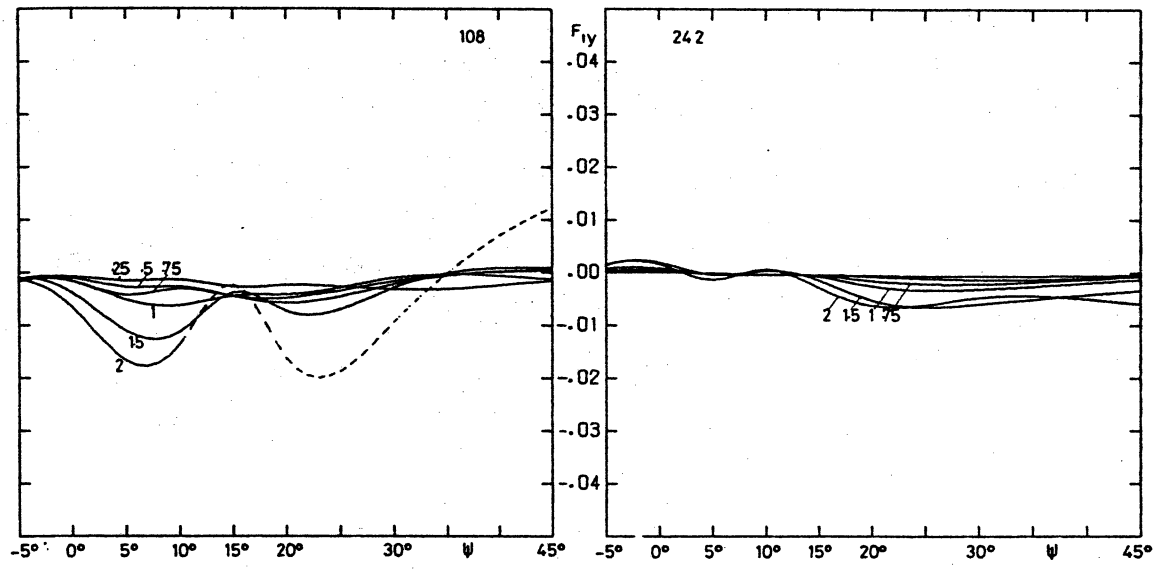

fig. 31.28. Boomerang F18, component F_{1y}. 108 = exp., 242 = theor.

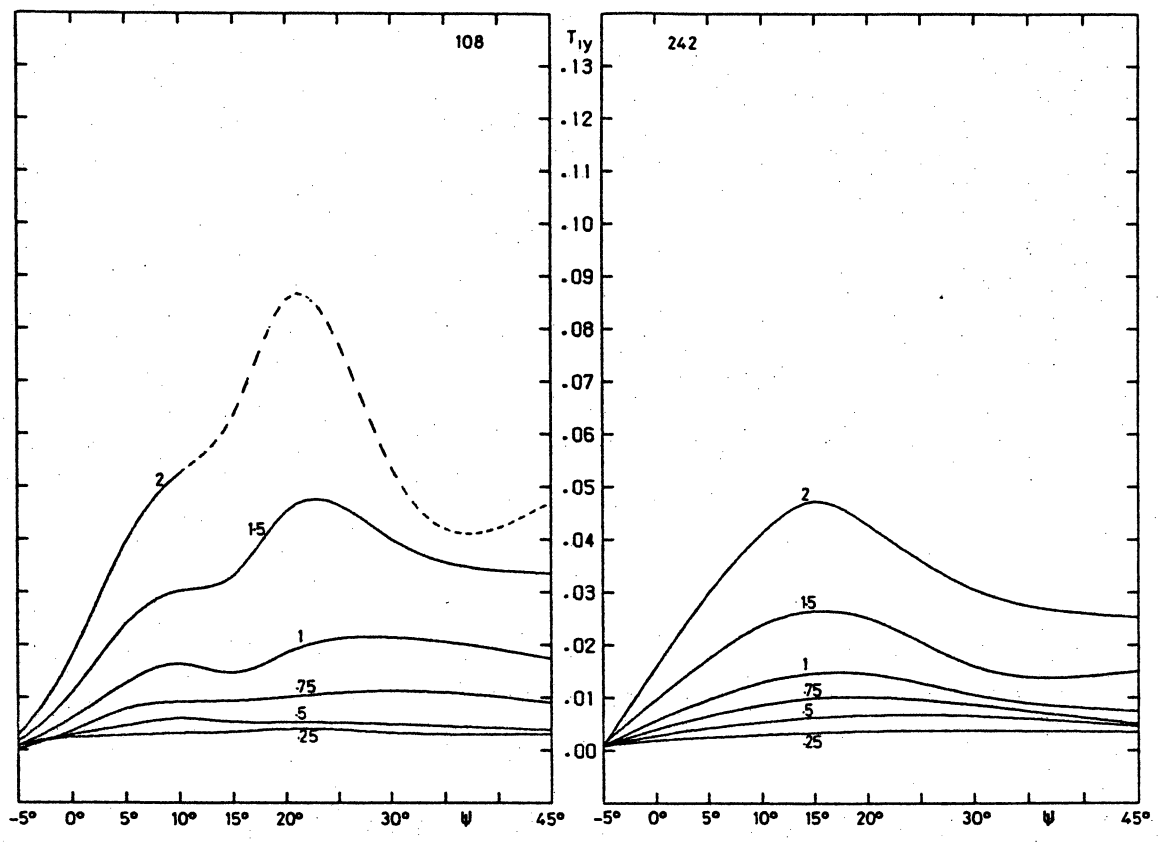

fig. 31.29. Boomerang F18, component T_{1y}. 108 = exp., 242 = theor.

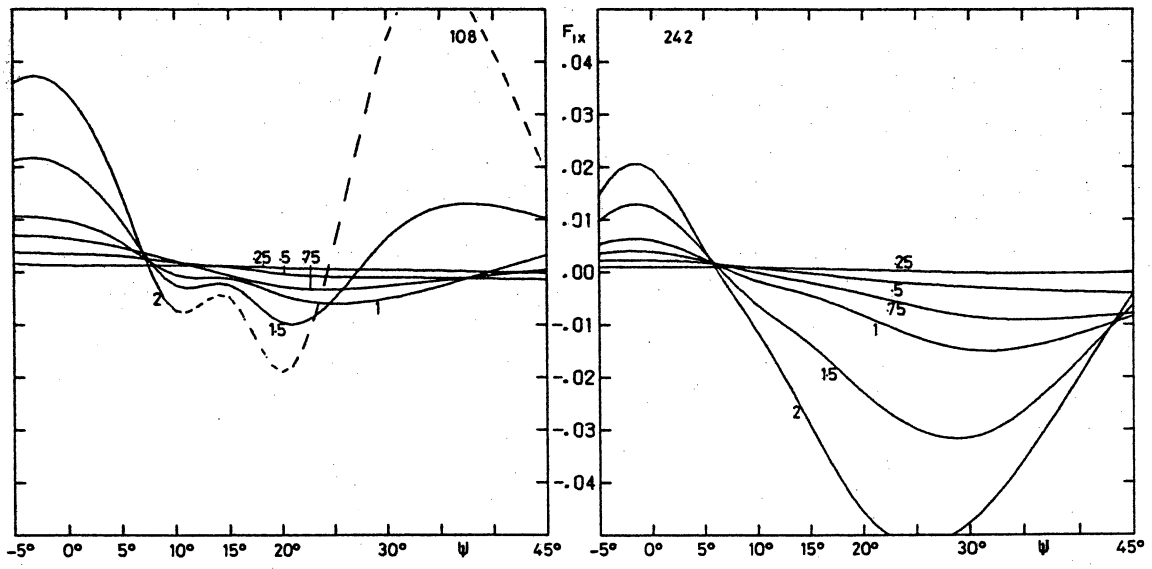

fig. 31.30. Boomerang F18, component F_{1x}. 108 = exp., 242 = theor.

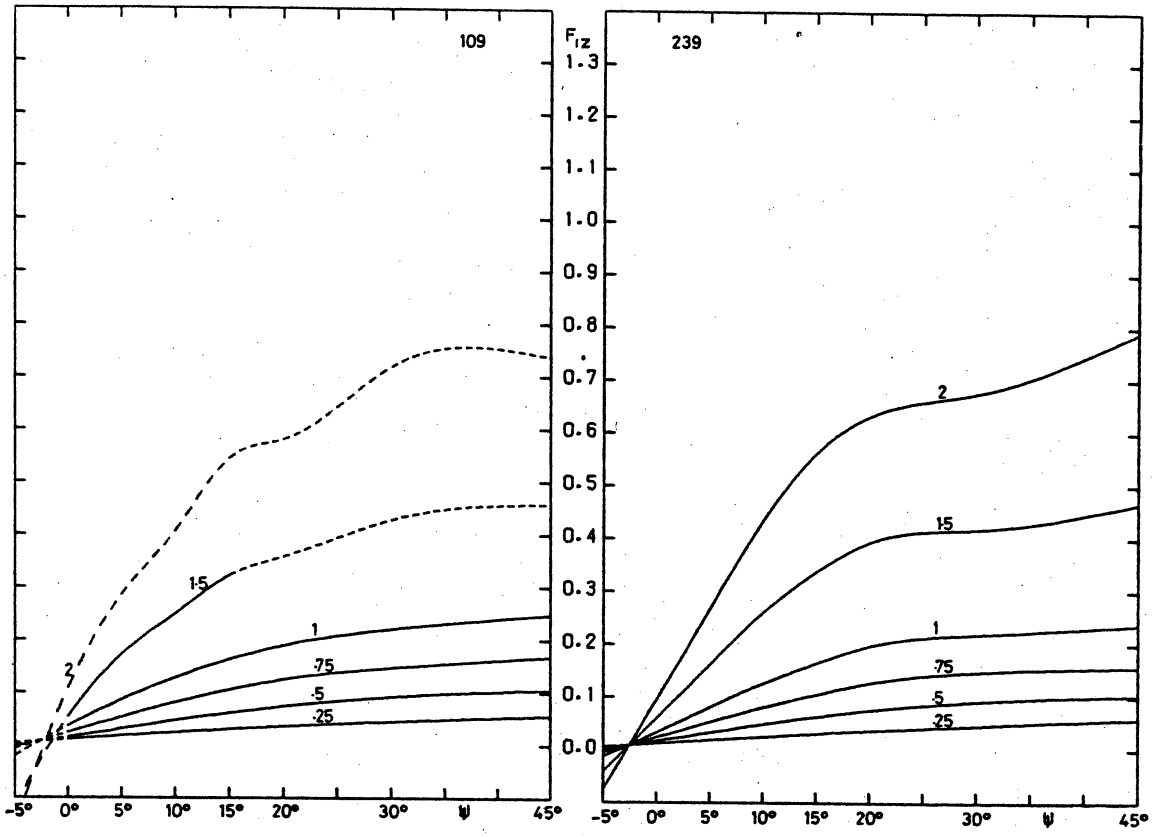

fig. 31.31. Boomerang WU, component F_{lz}. 109 = exp., 239 = theor.

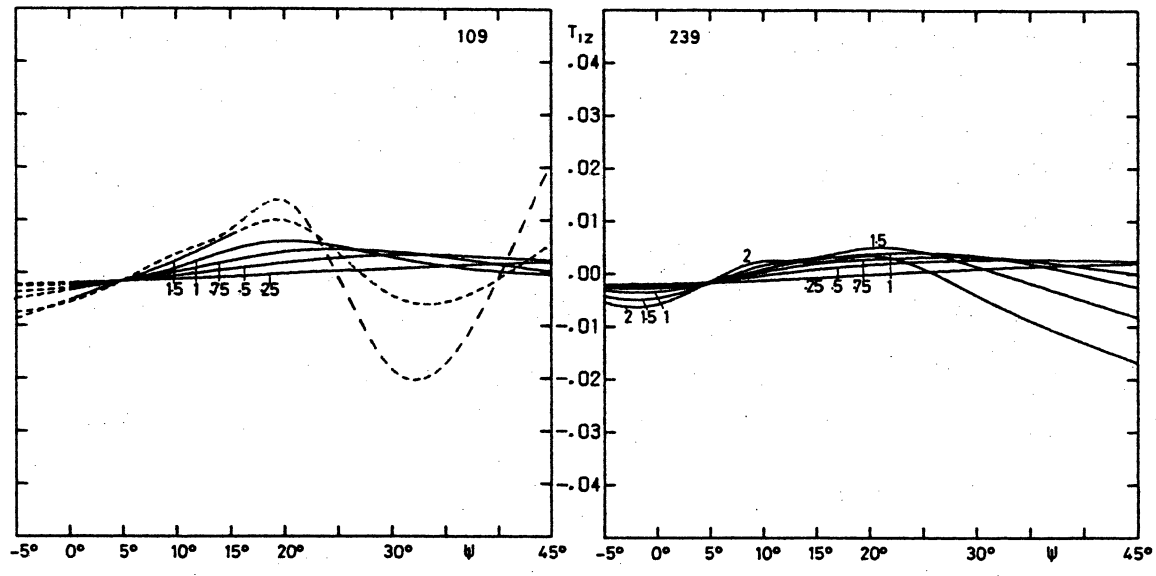

fig. 31.32. Boomerang WU, component T_{lz}. 109 = exp., 239 = theor.

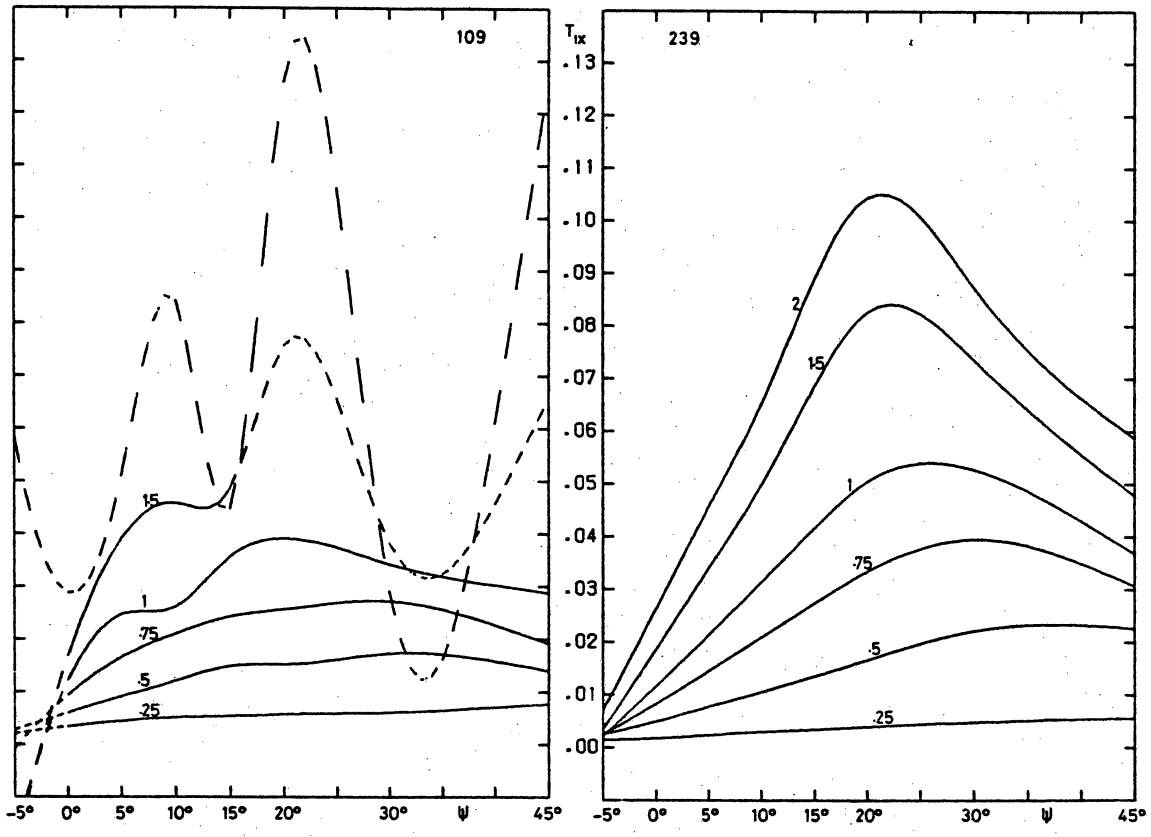

fig. 31.33. Boomerang WU, component T_{lx}. 109 = exp., 239 = theor.

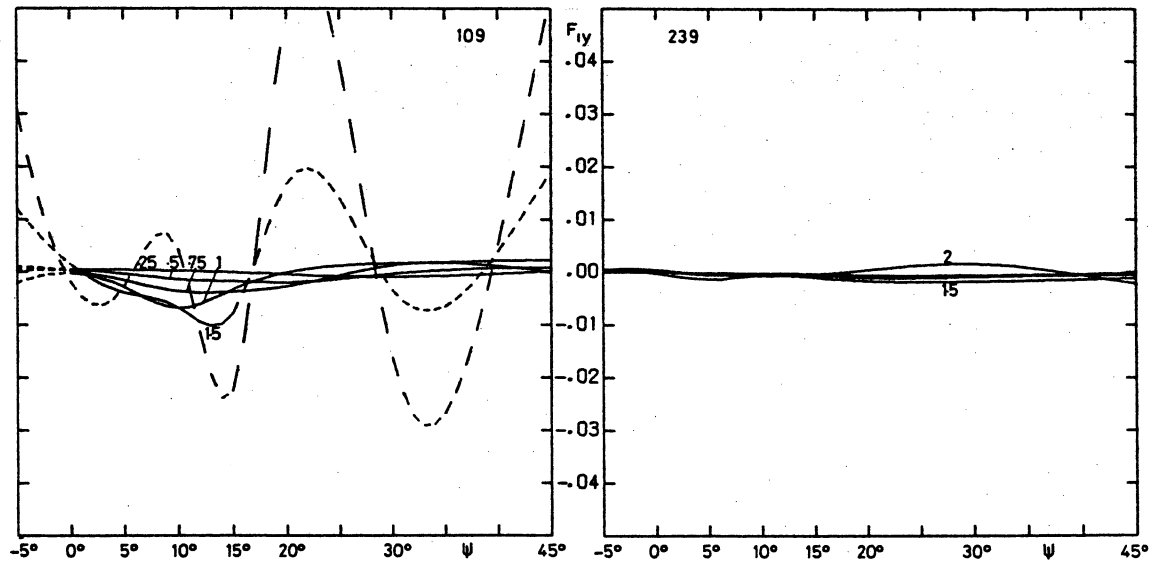

fig. 31.34. Boomerang WU, component F_{ly}. 109 = exp., 239 = theor.

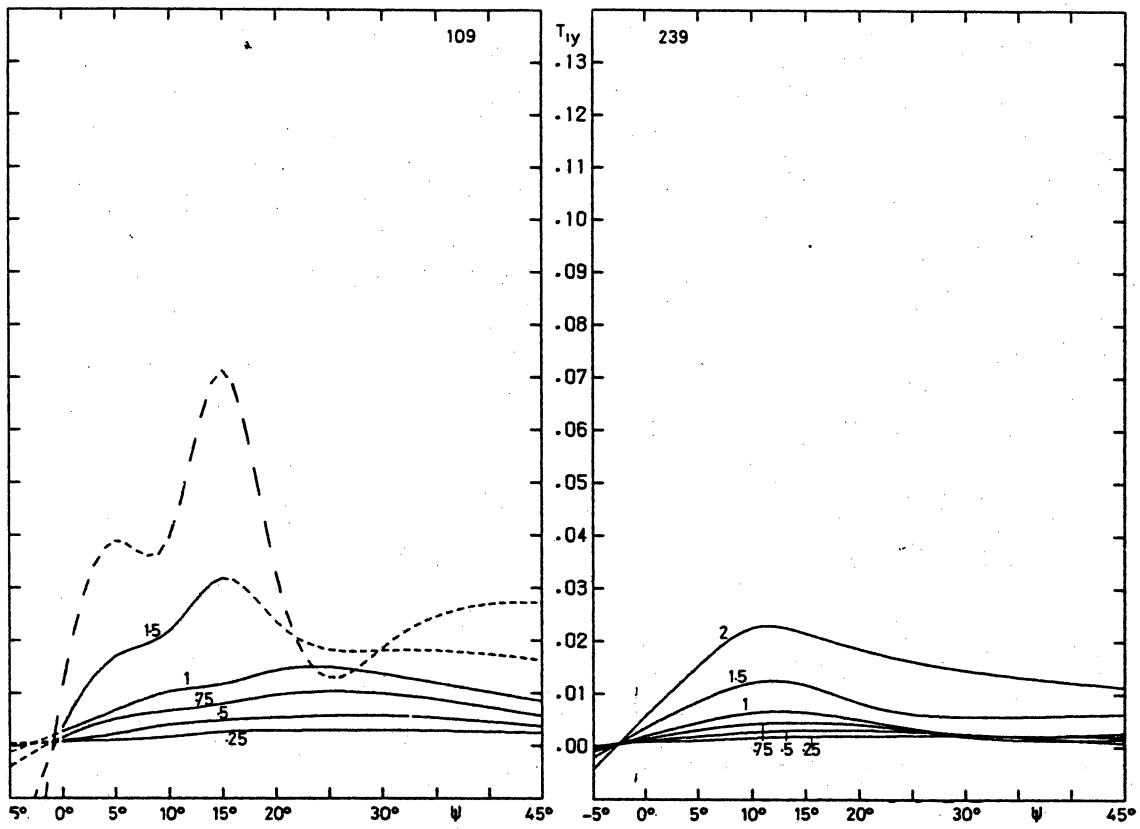

fig. 31.35. Boomerang WU, component T_{1y}. 109 = exp., 239 = theor.

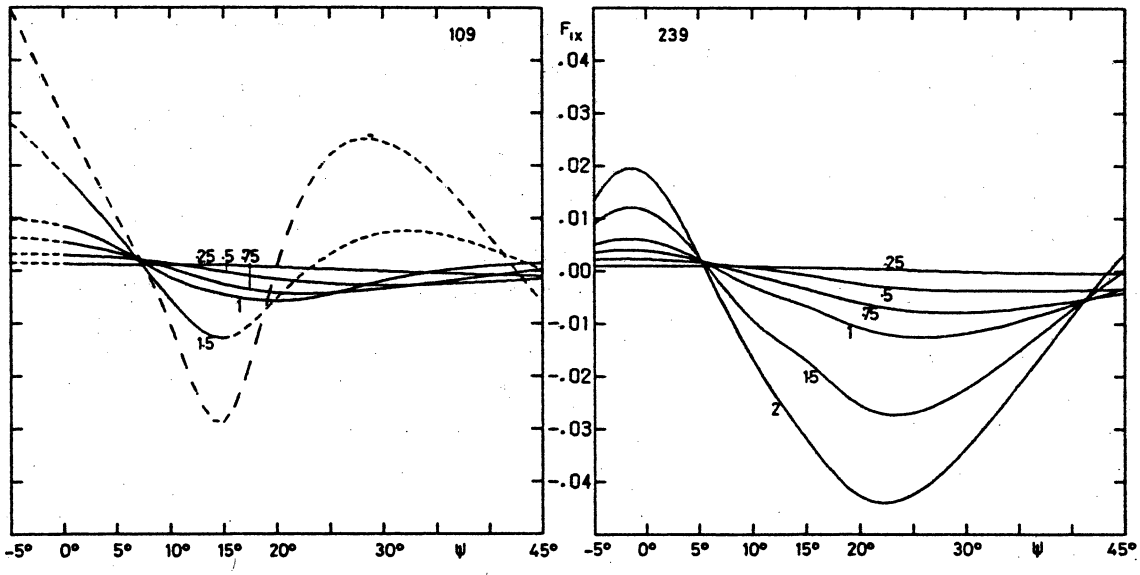

fig. 31.36. Boomerang WU, component F_{1x}. 109 = exp., 239 = theor.

F_{lz}

U↓ ψ→	−5°	+0°	+5°	+10°	+15°	+20°	+30°	+45°
2.00	−.0508	+.1763	+.3804	+.5758	+.7580	+.9041	+1.0021	+.9075
1.50	−.0198	+.1093	+.2218	+.3332	+.4354	+.4772	+ .5768	+.5782
1.00	+.0003	+.0604	+.1130	+.1659	+.2187	+.2467	+ .2855	+.3216
0.75	+.0055	+.0399	+.0718	+.1035	+.1358	+.1642	+ .1887	+.2205
0.50	+.0076	+.0265	+.0441	+.0606	+.0788	+.0942	+ .1160	+.1369
0.25	+.0114	+.0191	+.0267	+.0329	+.0397	+.0466	+ .0571	+.0679
0.00	+.0107	+.0107	+.0107	+.0107	+.0107	+.0107	+ .0107	+.0107

T_{lx}

U↓ ψ→	−5°	+0°	+5°	+10°	+15°	+20°	+30°	+45°
2.00	+.0266	+.0549	+.0861	+.0935	+.1100	+.1125	+.0330	+.0643
1.50	+.0172	+.0369	+.0500	+.0577	+.0593	+.0475	+.0346	+.0457
1.00	+.0082	+.0212	+.0297	+.0349	+.0398	+.0364	+.0321	+.0296
0.75	+.0046	+.0125	+.0189	+.0239	+.0286	+.0301	+.0281	+.0224
0.50	+.0025	+.0073	+.0101	+.0125	+.0152	+.0170	+.0180	+.0151
0.25	+.0008	+.0019	+.0028	+.0031	+.0037	+.0044	+.0050	+.0044
0.00	+.0000	+.0000	+.0000	+.0000	+.0000	+.0000	+.0000	+.0000

T_{ly}

U↓ ψ→	−5°	+0°	+5°	+10°	+15°	+20°	+30°	+45°
2.00	+.0027	+.0180	+.0357	+.0490	+.0720	+.0945	+.0847	+.0663
1.50	+.0024	+.0125	+.0221	+.0319	+.0412	+.0359	+.0371	+.0361
1.00	+.0032	+.0044	+.0102	+.0146	+.0193	+.0162	+.0137	+.0145
0.75	+.0026	+.0040	+.0065	+.0091	+.0112	+.0120	+.0099	+.0070
0.50	+.0026	+.0025	+.0042	+.0054	+.0065	+.0069	+.0061	+.0023
0.25	+.0018	+.0018	+.0023	+.0025	+.0033	+.0039	+.0039	+.0030
0.00	+.0000	+.0000	+.0000	+.0000	+.0000	+.0000	+.0000	+.0000

F_{lx}

U↓ ψ→	−5°	+0°	+5°	+10°	+15°	+20°	+30°	+45°
2.00	+.0471	+.0383	+.0153	−.0171	−.0429	−.0567	−.0223	−.0166
1.50	+.0278	+.0223	+.0107	−.0072	−.0196	−.0156	−.0099	−.0078
1.00	+.0136	+.0120	+.0071	−.0001	−.0065	−.0074	−.0050	−.0031
0.75	+.0086	+.0077	+.0056	+.0024	−.0011	−.0047	−.0046	−.0022
0.50	+.0047	+.0044	+.0034	+.0022	+.0004	−.0012	−.0031	−.0018
0.25	+.0019	+.0021	+.0018	+.0017	+.0015	+.0011	+.0003	−.0002
0.00	+.0000	+.0000	+.0000	+.0000	+.0000	+.0000	+.0000	+.0000

F_{ly}

U↓ ψ→	−5°	+0°	+5°	+10°	+15°	+20°	+30°	+45°
2.00	+.0001	−.0056	−.0153	−.0242	−.0332	−.0306	−.0044	+.0140
1.50	+.0007	−.0026	−.0109	−.0173	−.0207	−.0069	+.0007	+.0008
1.00	−.0002	−.0026	−.0073	−.0124	−.0167	−.0103	−.0008	−.0035
0.75	−.0006	−.0019	−.0045	−.0070	−.0082	−.0094	−.0030	−.0022
0.50	−.0008	−.0011	−.0028	−.0040	−.0052	−.0052	−.0025	+.0001
0.25	−.0008	−.0009	−.0013	−.0016	−.0021	−.0027	−.0029	+.0019
0.00	+.0000	+.0000	+.0000	+.0000	+.0000	+.0000	+.0000	+.0000

T_{lz}

U↓ ψ→	−5°	+0°	+5°	+10°	+15°	+20°	+30°	+45°
2.00	−.0101	−.0058	−.0006	+.0048	+.0200	+.0344	+.0115	+.0282
1.50	−.0076	−.0054	−.0023	+.0017	+.0080	+.0039	+.0035	+.0110
1.00	−.0053	−.0039	−.0021	+.0014	+.0059	+.0043	+.0030	+.0033
0.75	−.0043	−.0035	−.0023	+.0000	+.0024	+.0048	+.0046	+.0030
0.50	−.0034	−.0029	−.0020	−.0009	+.0004	+.0018	+.0036	+.0039
0.25	−.0026	−.0025	−.0019	−.0015	−.0010	−.0004	+.0006	+.0016
0.00	−.0026	−.0026	−.0026	−.0026	−.0026	−.0026	−.0026	−.0026

table 31.1. Boomerang L1, experimental results: nr. 101.

F_{lz}

U↓ ψ→	-5°	+0°	+5°	+10°	+15°	+20°	+30°	+45°
2.00	-.0666	+.1451	+.3475	+.5151	+.6981	+.7823	+.9231	+.9704
1.50	-.0376	+.0862	+.2006	+.2974	+.3988	+.4888	+.5473	+.5940
1.00	+.0073	+.0477	+.1055	+.1525	+.1948	+.2474	+.2758	+.3158
0.75	+.0006	+.0320	+.0662	+.0940	+.1220	+.1501	+.1793	+.2135
0.50	+.0035	+.0214	+.0396	+.0548	+.0693	+.0825	+.1065	+.1328
0.25	+.0075	+.0151	+.0229	+.0286	+.0349	+.0409	+.0484	+.0615
0.00	+.0119	+.0119	+.0119	+.0119	+.0119	+.0119	+.0119	+.0119

T_{lx}

U↓ ψ→	-5°	+0°	+5°	+10°	+15°	+20°	+30°	+45°
2.00	+.0169	+.0434	+.0596	+.0616	+.0634	+.0110	+.0044	+.0462
1.50	+.0069	+.0237	+.0376	+.0441	+.0391	+.0366	+.0235	+.0306
1.00	+.0042	+.0138	+.0247	+.0284	+.0278	+.0326	+.0261	+.0199
0.75	+.0020	+.0087	+.0141	+.0199	+.0207	+.0212	+.0211	+.0164
0.50	+.0007	+.0052	+.0060	+.0110	+.0115	+.0109	+.0127	+.0126
0.25	-.0002	+.0014	+.0003	+.0022	+.0029	+.0032	+.0035	+.0026
0.00	+.0000	+.0000	+.0000	+.0000	+.0000	+.0000	+.0000	+.0000

T_{ly}

U↓ ψ→	-5°	+0°	+5°	+10°	+15°	+20°	+30°	+45°
2.00	-.0105	+.0060	+.0235	+.0349	+.0572	+.0459	+.0543	+.0171
1.50	-.0039	-.0002	+.0136	+.0185	+.0300	+.0359	+.0305	+.0197
1.00	-.0020	+.0015	+.0069	+.0088	+.0111	+.0186	+.0132	+.0146
0.75	-.0025	+.0007	+.0032	+.0041	+.0052	+.0084	+.0071	+.0091
0.50	-.0013	+.0005	+.0012	+.0019	+.0017	+.0026	+.0028	+.0031
0.25	-.0006	+.0008	+.0006	+.0012	+.0014	+.0016	+.0016	+.0018
0.00	+.0000	+.0000	+.0000	+.0000	+.0000	+.0000	+.0000	+.0000

F_{lx}

U↓ ψ→	-5°	+0°	+5°	+10°	+15°	+20°	+30°	+45°
2.00	+.0375	+.0353	+.0191	-.0024	-.0219	-.0262	+.0386	+.0029
1.50	+.0227	+.0222	+.0112	+.0002	-.0107	-.0166	+.0115	+.0034
1.00	+.0093	+.0102	+.0070	+.0024	-.0026	-.0076	-.0018	+.0014
0.75	+.0074	+.0065	+.0053	+.0031	-.0001	-.0034	-.0032	-.0006
0.50	+.0045	+.0037	+.0033	+.0025	+.0015	-.0001	-.0017	-.0023
0.25	+.0021	+.0015	+.0018	+.0016	+.0014	+.0012	+.0008	+.0001
0.00	+.0000	+.0000	+.0000	+.0000	+.0000	+.0000	+.0000	+.0000

F_{ly}

U↓ ψ→	-5°	+0°	+5°	+10°	+15°	+20°	+30°	+45°
2.00	+.0012	-.0001	-.0019	-.0052	-.0115	+.0224	-.0047	+.0463
1.50	+.0003	-.0014	-.0029	-.0046	-.0098	-.0060	+.0009	+.0139
1.00	+.0004	-.0010	-.0040	-.0058	-.0074	-.0102	+.0017	-.0012
0.75	-.0005	-.0010	-.0033	-.0037	-.0046	-.0052	+.0003	-.0022
0.50	-.0009	-.0009	-.0025	-.0022	-.0027	-.0030	-.0016	-.0005
0.25	-.0009	-.0007	-.0017	-.0013	-.0015	-.0019	-.0017	-.0019
0.00	+.0000	+.0000	+.0000	+.0000	+.0000	+.0000	+.0000	+.0000

T_{lz}

U↓ ψ→	-5°	+0°	+5°	+10°	+15°	+20°	+30°	+45°
2.00	-.0084	-.0048	-.0044	-.0031	+.0100	-.0070	+.0120	+.0038
1.50	-.0066	-.0049	-.0039	-.0028	+.0041	+.0074	+.0077	+.0006
1.00	-.0036	-.0035	-.0017	-.0001	+.0026	+.0075	+.0044	+.0010
0.75	-.0033	-.0030	-.0022	-.0010	+.0008	+.0032	+.0031	+.0026
0.50	-.0027	-.0026	-.0021	-.0013	-.0005	+.0003	+.0019	+.0040
0.25	-.0021	-.0020	-.0029	-.0013	-.0010	-.0006	-.0001	+.0011
0.00	-.0021	-.0021	-.0021	-.0021	-.0021	-.0021	-.0021	-.0021

table 31.2. Boomerang L4, experimental results: nr. 104.

F_{lz}

U↓ ψ→	−5°	+0°	+5°	+10°	+15°	+20°	+30°	+45°
2.00	−.0612	+.1418	+.3475	+.4934	+.6349	+.6387	+.9007	+.8439
1.50	−.0278	+.0868	+.2034	+.3033	+.4002	+.4182	+.5476	+.5636
1.00	−.0076	+.0453	+.0987	+.1466	+.1985	+.2303	+.2833	+.3290
0.75	−.0012	+.0320	+.0623	+.0929	+.1241	+.1505	+.1856	+.2289
0.50	+.0022	+.0212	+.0366	+.0538	+.0726	+.0881	+.1133	+.1410
0.25	+.0048	+.0137	+.0198	+.0273	+.0357	+.0426	+.0558	+.0681
0.00	+.0050	+.0050	+.0050	+.0050	+.0050	+.0050	+.0050	+.0050

T_{lx}

U↓ ψ→	−5°	+0°	+5°	+10°	+15°	+20°	+30°	+45°
2.00	+.0057	+.0270	+.0396	−.0145	−.0118	−.1490	−.1016	+.0310
1.50	+.0002	+.0166	+.0308	+.0397	+.0471	+.0120	+.0021	+.0293
1.00	−.0013	+.0076	+.0222	+.0273	+.0354	+.0345	+.0338	+.0239
0.75	−.0035	+.0009	+.0103	+.0178	+.0208	+.0274	+.0261	+.0197
0.50	−.0043	−.0034	+.0037	+.0073	+.0119	+.0156	+.0165	+.0141
0.25	−.0038	−.0053	−.0030	−.0032	−.0004	+.0018	+.0035	+.0045
0.00	+.0000	+.0000	+.0000	+.0000	+.0000	+.0000	+.0000	+.0000

T_{ly}

U↓ ψ→	−5°	+0°	+5°	+10°	+15°	+20°	+30°	+45°
2.00	−.0169	+.0037	+.0177	+.0247	+.0215	+.0019	+.0206	+.0744
1.50	−.0091	+.0010	+.0121	+.0189	+.0255	+.0131	+.0175	+.0370
1.00	−.0043	+.0013	+.0081	+.0082	+.0088	+.0103	+.0097	+.0121
0.75	−.0034	+.0002	+.0048	+.0066	+.0034	+.0052	+.0045	+.0044
0.50	−.0025	−.0001	+.0034	+.0039	+.0028	+.0031	+.0008	+.0004
0.25	−.0010	−.0002	+.0017	+.0028	+.0023	+.0019	+.0014	+.0023
0.00	+.0000	+.0000	+.0000	+.0000	+.0000	+.0000	+.0000	+.0000

F_{lx}

U↓ ψ→	−5°	+0°	+5°	+10°	+15°	+20°	+30°	+45°
2.00	+.0418	+.0357	+.0167	+.0014	+.0029	+.0442	+.0423	+.0033
1.50	+.0248	+.0211	+.0103	−.0041	−.0141	+.0072	+.0060	+.0030
1.00	+.0121	+.0103	+.0059	+.0008	−.0037	−.0055	−.0047	+.0014
0.75	+.0081	+.0068	+.0047	+.0014	−.0004	−.0036	−.0023	+.0002
0.50	+.0049	+.0040	+.0030	+.0022	+.0013	−.0005	−.0011	−.0008
0.25	+.0020	+.0017	+.0014	+.0012	+.0015	+.0015	+.0010	−.0002
0.00	+.0000	+.0000	+.0000	+.0000	+.0000	+.0000	+.0000	+.0000

F_{ly}

U↓ ψ→	−5°	+0°	+5°	+10°	+15°	+20°	+30°	+45°
2.00	+.0003	−.0016	−.0088	−.0183	−.0140	−.0109	−.0103	−.0138
1.50	−.0003	−.0018	−.0064	−.0098	−.0115	−.0058	−.0008	−.0057
1.00	−.0005	−.0019	−.0027	−.0040	−.0035	−.0017	+.0024	−.0002
0.75	−.0014	−.0030	−.0038	−.0044	−.0033	−.0006	+.0017	+.0015
0.50	−.0021	−.0033	−.0030	−.0033	−.0032	−.0019	+.0002	+.0019
0.25	−.0018	−.0026	−.0023	−.0027	−.0022	−.0022	−.0024	−.0016
0.00	+.0000	+.0000	+.0000	+.0000	+.0000	+.0000	+.0000	+.0000

T_{lz}

U↓ ψ→	−5°	+0°	+5°	+10°	+15°	+20°	+30°	+45°
2.00	−.0069	−.0040	−.0025	−.0117	−.0039	−.0355	−.0207	+.0169
1.50	−.0053	−.0037	−.0021	+.0014	+.0098	−.0033	+.0007	+.0066
1.00	−.0035	−.0030	−.0017	+.0002	+.0033	+.0057	+.0058	+.0026
0.75	−.0030	−.0027	−.0017	−.0001	+.0006	+.0029	+.0034	+.0030
0.50	−.0026	−.0024	−.0016	−.0007	+.0002	+.0008	+.0021	+.0041
0.25	−.0022	−.0020	−.0016	−.0012	−.0008	−.0004	+.0006	+.0021
0.00	−.0021	−.0021	−.0021	−.0021	−.0021	−.0021	−.0021	−.0021

table 31.3. Boomerang L6, experimental results: nr. 106.

F_{lz}

U↓ ψ→	-5°	+0°	+5°	+10°	+15°	+20°	+30°	+45°
2.00	-.0958	+.1288	+.3593	+.5397	+.6783	+.8388	+.9711	+1.0891
1.50	-.0472	+.0790	+.2078	+.3092	+.3957	+.4906	+.5863	+ .6555
1.00	-.0153	+.0419	+.1006	+.1524	+.1953	+.2399	+.2962	+ .3472
0.75	-.0053	+.0280	+.0622	+.0932	+.1252	+.1514	+.1890	+ .2377
0.50	+.0006	+.0185	+.0369	+.0536	+.0721	+.0873	+.1129	+ .1462
0.25	+.0058	+.0133	+.0211	+.0280	+.0358	+.0426	+.0539	+ .0666
0.00	+.0064	+.0064	+.0064	+.0064	+.0064	+.0064	+.0064	+ .0064

T_{lx}

U↓ ψ→	-5°	+0°	+5°	+10°	+15°	+20°	+30°	+45°
2.00	+.0168	+.0301	+.0456	+.0565	+.0588	+.0274	-.1240	-.0185
1.50	+.0069	+.0197	+.0302	+.0374	+.0381	+.0409	-.0030	+.0195
1.00	+.0007	+.0127	+.0213	+.0315	+.0257	+.0311	+.0305	+.0257
0.75	-.0019	+.0076	+.0124	+.0204	+.0205	+.0184	+.0195	+.0188
0.50	-.0012	+.0047	+.0060	+.0117	+.0092	+.0060	+.0098	+.0126
0.25	-.0011	+.0006	-.0004	+.0008	-.0003	+.0020	+.0004	+.0034
0.00	+.0000	+.0000	+.0000	+.0000	+.0000	+.0000	+.0000	+.0000

T_{ly}

U↓ ψ→	-5°	+0°	+5°	+10°	+15°	+20°	+30°	+45°
2.00	+.0028	+.0179	+.0394	+.0524	+.0634	+.0855	+.0537	+.0471
1.50	+.0017	+.0110	+.0240	+.0302	+.0331	+.0453	+.0400	+.0336
1.00	+.0008	+.0061	+.0127	+.0164	+.0147	+.0185	+.0214	+.0174
0.75	+.0002	+.0037	+.0079	+.0092	+.0094	+.0101	+.0113	+.0091
0.50	+.0009	+.0029	+.0047	+.0061	+.0054	+.0053	+.0049	+.0039
0.25	+.0009	+.0024	+.0029	+.0032	+.0035	+.0040	+.0033	+.0031
0.00	+.0000	+.0000	+.0000	+.0000	+.0000	+.0000	+.0000	+.0000

F_{lx}

U↓ ψ→	-5°	+0°	+5°	+10°	+15°	+20°	+30°	+45°
2.00	+.0359	+.0339	+.0148	-.0073	-.0047	-.0190	+.0441	+.0190
1.50	+.0212	+.0198	+.0097	-.0025	-.0024	-.0096	+.0065	+.0103
1.00	+.0106	+.0097	+.0057	-.0005	-.0012	-.0044	-.0050	+.0033
0.75	+.0070	+.0064	+.0047	+.0021	-.0006	-.0028	-.0026	+.0005
0.50	+.0038	+.0035	+.0031	+.0019	+.0010	-.0003	-.0010	-.0014
0.25	+.0016	+.0013	+.0013	+.0013	+.0012	+.0008	+.0004	-.0002
0.00	+.0000	+.0000	+.0000	+.0000	+.0000	+.0000	+.0000	+.0000

F_{ly}

U↓ ψ→	-5°	+0°	+5°	+10°	+15°	+20°	+30°	+45°
2.00	-.0013	-.0066	-.0167	-.0137	-.0023	-.0162	-.0094	+.0124
1.50	-.0011	-.0039	-.0111	-.0113	-.0038	-.0073	-.0028	+.0010
1.00	-.0011	-.0016	-.0052	-.0063	-.0045	-.0042	-.0010	-.0012
0.75	-.0017	-.0017	-.0043	-.0031	-.0046	-.0049	-.0016	+.0004
0.50	-.0015	-.0010	-.0028	-.0027	-.0045	-.0058	-.0022	+.0006
0.25	-.0011	-.0008	-.0016	-.0014	-.0027	-.0024	-.0032	-.0015
0.00	+.0000	+.0000	+.0000	+.0000	+.0000	+.0000	+.0000	+.0000

T_{lz}

U↓ ψ→	-5°	+0°	+5°	+10°	+15°	+20°	+30°	+45°
2.00	-.0063	-.0037	-.0014	+.0008	+.0018	+.0085	-.0455	-.0008
1.50	-.0052	-.0036	-.0021	-.0001	+.0003	+.0060	-.0040	+.0008
1.00	-.0039	-.0031	-.0018	+.0002	+.0004	+.0036	+.0071	+.0017
0.75	-.0034	-.0029	-.0021	-.0010	+.0006	+.0022	+.0034	+.0023
0.50	-.0028	-.0025	-.0020	-.0012	-.0005	+.0004	+.0017	+.0034
0.25	-.0023	-.0020	-.0018	-.0015	-.0010	-.0005	+.0000	+.0011
0.00	-.0020	-.0020	-.0020	-.0020	-.0020	-.0020	-.0020	-.0020

table 31.4. Boomerang F18, experimental results: nr. 108.

F_{lz}

U↓ ψ→	-5°	+0°	+5°	+10°	+15°	+20°	+30°	+45°
2.00	-.1558	+.1081	+.2849	+.4054	+.5436	+.5799	+.7183	+.7377
1.50	-.1171	+.0544	+.1720	+.2490	+.3222	+.3581	+.4283	+.4580
1.00	-.0213	+.0360	+.0857	+.1279	+.1625	+.1893	+.2203	+.2475
0.75	-.0067	+.0237	+.0532	+.0811	+.1053	+.1248	+.1470	+.1682
0.50	-.0011	+.0147	+.0307	+.0467	+.0611	+.0736	+.0918	+.1055
0.25	+.0037	+.0108	+.0177	+.0243	+.0305	+.0362	+.0452	+.0563
0.00	+.0067	+.0067	+.0067	+.0067	+.0067	+.0067	+.0067	+.0067

T_{lx}

U↓ ψ→	-5°	+0°	+5°	+10°	+15°	+20°	+30°	+45°
2.00	+.0585	+.0288	+.0509	+.0843	+.0447	+.1259	+.0292	+.1261
1.50	-.0206	+.0169	+.0391	+.0458	+.0487	+.0758	+.0383	+.0657
1.00	-.0177	+.0122	+.0247	+.0261	+.0357	+.0391	+.0342	+.0288
0.75	-.0008	+.0094	+.0166	+.0210	+.0243	+.0257	+.0272	+.0192
0.50	+.0027	+.0060	+.0091	+.0121	+.0149	+.0152	+.0173	+.0140
0.25	+.0020	+.0034	+.0044	+.0051	+.0054	+.0058	+.0061	+.0077
0.00	+.0000	+.0000	+.0000	+.0000	+.0000	+.0000	+.0000	+.0000

T_{ly}

U↓ ψ→	-5°	+0°	+5°	+10°	+15°	+20°	+30°	+45°
2.00	-.0675	+.0115	+.0389	+.0394	+.0712	+.0330	+.0186	+.0273
1.50	-.0240	+.0036	+.0170	+.0218	+.0318	+.0237	+.0182	+.0164
1.00	-.0012	+.0027	+.0068	+.0103	+.0117	+.0143	+.0137	+.0086
0.75	-.0040	+.0016	+.0051	+.0067	+.0080	+.0097	+.0100	+.0058
0.50	+.0004	+.0010	+.0023	+.0040	+.0048	+.0054	+.0058	+.0038
0.25	+.0002	+.0007	+.0011	+.0017	+.0026	+.0029	+.0030	+.0025
0.00	+.0000	+.0000	+.0000	+.0000	+.0000	+.0000	+.0000	+.0000

F_{lx}

U↓ ψ→	-5°	+0°	+5°	+10°	+15°	+20°	+30°	+45°
2.00	+.0498	+.0291	+.0102	-.0103	-.0287	+.0007	+.0245	-.0059
1.50	+.0281	+.0184	+.0070	-.0054	-.0128	-.0052	+.0072	+.0003
1.00	+.0097	+.0084	+.0044	-.0013	-.0045	-.0058	-.0019	+.0015
0.75	+.0063	+.0054	+.0034	+.0005	-.0026	-.0042	-.0034	+.0003
0.50	+.0032	+.0030	+.0025	+.0014	-.0002	-.0016	-.0028	-.0015
0.25	+.0015	+.0013	+.0011	+.0011	+.0011	+.0007	-.0001	-.0010
0.00	+.0000	+.0000	+.0000	+.0000	+.0000	+.0000	+.0000	+.0000

F_{ly}

U↓ ψ→	-5°	+0°	+5°	+10°	+15°	+20°	+30°	+45°
2.00	+.0313	-.0018	-.0027	+.0044	-.0225	+.0492	-.0161	+.0526
1.50	+.0122	+.0015	-.0039	-.0067	-.0078	+.0168	-.0034	+.0191
1.00	-.0021	-.0002	-.0028	-.0068	-.0033	-.0001	+.0017	+.0023
0.75	+.0011	+.0002	-.0015	-.0036	-.0037	-.0027	+.0013	+.0001
0.50	+.0007	+.0005	-.0003	-.0013	-.0017	-.0020	-.0003	+.0009
0.25	+.0003	+.0005	+.0005	+.0003	+.0000	-.0004	-.0009	+.0002
0.00	+.0000	+.0000	+.0000	+.0000	+.0000	+.0000	+.0000	+.0000

T_{lz}

U↓ ψ→	-5°	+0°	+5°	+10°	+15°	+20°	+30°	+45°
2.00	-.0075	-.0056	-.0015	+.0036	+.0082	+.0137	-.0183	+.0209
1.50	-.0087	-.0051	-.0015	+.0023	+.0072	+.0100	-.0043	+.0055
1.00	-.0049	-.0033	-.0015	+.0009	+.0043	+.0060	+.0029	-.0003
0.75	-.0037	-.0028	-.0015	+.0002	+.0023	+.0040	+.0040	+.0003
0.50	-.0025	-.0023	-.0016	-.0006	+.0007	+.0019	+.0034	+.0024
0.25	-.0022	-.0019	-.0016	-.0012	-.0007	-.0001	+.0008	+.0021
0.00	-.0020	-.0020	-.0020	-.0020	-.0020	-.0020	-.0020	-.0020

table 31.5. Boomerang WU, experimental results: nr. 109.

§32 *The choice of parameters for the theoretical boomerangs.*

In principle a boomerang's aerodynamic properties are determined by its shape or geometry. Thus we should only need to take a boomerang's measurements and deduce the relevant aerodynamic parameters. Lack of knowledge required for this deduction makes this procedure impossible for our experimental boomerangs. A more realistic approach would be te take some measurements, especially length, excentricity and chord of the boomerang arms (see fig. 20.2), and obtain the aerodynamic quantities like C_L and C_D from experiments. Here we could make use of the results of the experiments discussed in §26.

Unfortunately this does not work. If the lift and drag characteristics of boomerang arms in straight flow (see §26) are used as input parameters in our winglet model, the resulting forces acting on the model boomerang come out wrong. A striking example, concerning boomerang L1, is provided by fig. 32.1. It contains four sets of curves, each representing the dimensionless axial force F_{1z}, three of them (a,b,c) for theoretical boomerangs differing only in the values of the parameter C_{L2}, and one (dashed) for experimental boomerang L1. C_{L2} is the maximum profile lift coefficient of the boomerang arms, see §22. Curves a are for boomerang nr. 195 with $C_{L2} = 2.0$ (2.4 for reversed profile), curves b for boomerang nr. 217 with $C_{L2} = 1.6$ (2.4 for reversed profile) and curves c for boomerang nr. 222 with $C_{L2} = 1.2$ (1.2 for reversed profile). The dashed curves are for experimental boomerang L1 (nr. 101) as far as they are different from those for nr. 195. It is evident from this example that the maximum lift coefficient of the boomerang arms cannot be much less than about 2.0. Even nr. 217 with $C_{L2} = 1.6$ has a F_{1z} which is substantially too low, let alone nr. 222 with $C_{L2} = 1.2$. Yet the maximum lift coefficients measured in straight flow was never higher than about 1.2 for boomerang arms without turbulence wire (see §26).

It seems improbable that this discrepancy is due exclusively to shortcomings in our theoretical model, and that a better model would yield the correct forces for a maximum lift coefficient of about 1.2 instead of 2.0. No doubt there are substantial differences between the airflow around a fixed boomerang arm on the one hand and an arm forming part of

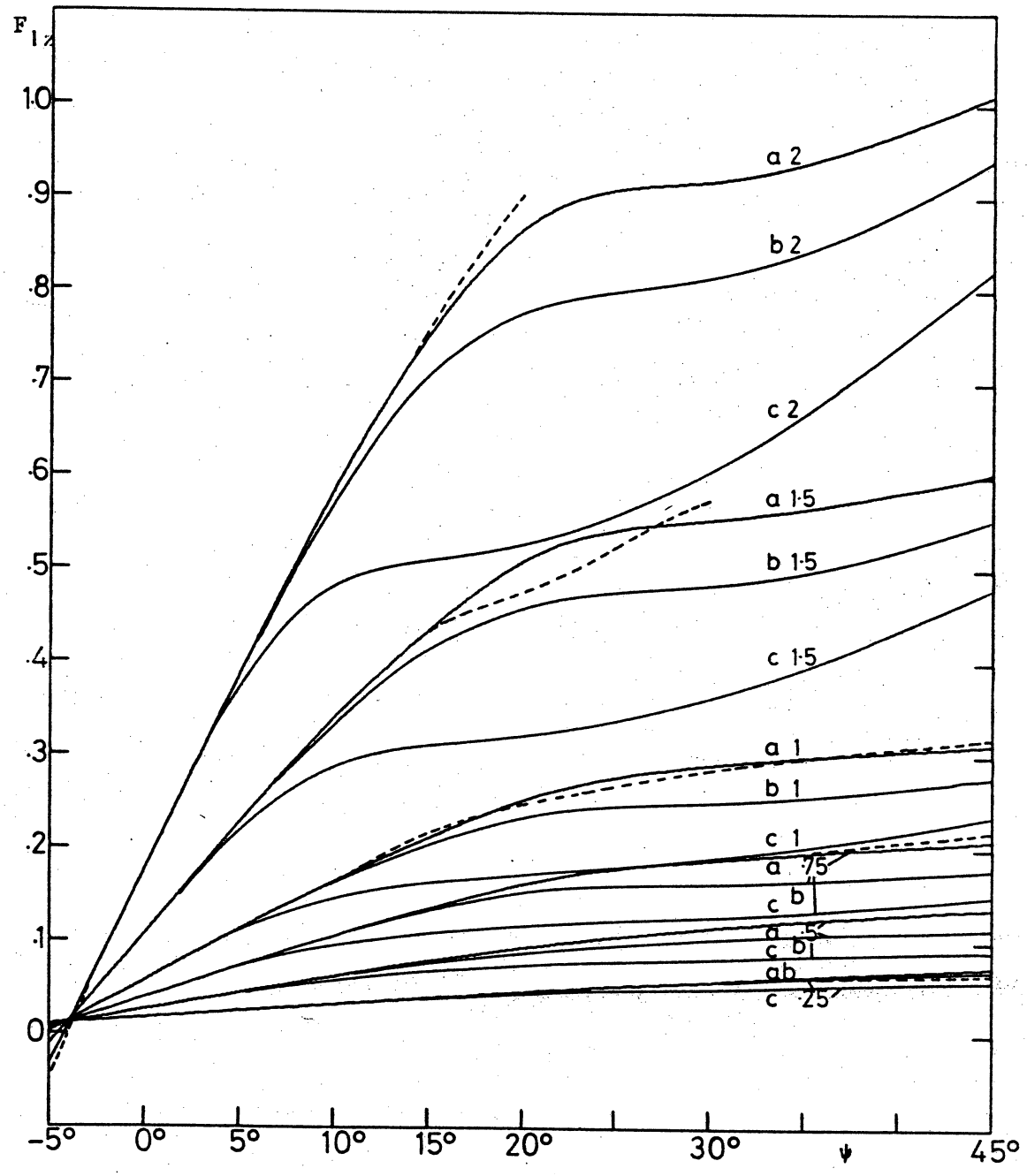

fig. 32.1. Component F_{lz} vs. ψ. Drawn curves: theory. Curves a: boomerang nr. 195, $C_{L2} = 2.0$. Curves b: boomerang nr. 217, $C_{L2} = 1.6$. Curves c: boomerang nr. 222, $C_{L2} = 1.2$. Dashed curves: experimental boomerang L1 (nr. 101) *as far as different from nr. 195*. Numbers with the curves denote U-values.

a rotating boomerang on the other hand. This will be discussed further in the next section.

Since the use of data like those of §26 for the aerodynamic parameters of the theoretical counterparts to the experimental boomerangs leads to quite wrong results, the only way to make a reasonable choice for these parameters is by trial and error. The final choice is determined by three criteria: 1^{o} the parameters should not have unrealistic values, 2^{o} the agreement of the computed six force components with the measured ones should be as good as possible, 3^{o} the flight paths calculated on basis of the computed forces should look realistic. This is admittedly a poor way of finding the parameters, as it inevitably holds some danger of working towards a spurious agreement between theory and experiment. But there seems to exist no better way at present.

In principle we can choose, for each boomerang arm, parameters characterizing the aerodynamic properties of the profiles at the tip and at the root of the arm, both for normal and for reversed flow: for a two-armed boomerang eight sets of profile parameters in all. The values of the parameters at points of the arm between tip and root are obtained by interpolation. This would lead to an enormous number of parameters, which could be varied at will. However, because our winglet model is strongly simplified with respect to reality, this would not make sense. We shall keep the parameter set described in §22. For each arm we then have, in addition to length l and excentricity e, 20 parameters. At this point see §22 for the meaning and notation of these.

For some of the parameters a fixed choice has been made for all cases. For the profiles in normal flow we take:

$$C_{L1} = -1.0,\ C_{L3} = -0.5,\ dC_D = 0.03. \tag{32.1}$$

And for the profiles in reversed flow we take:

$$\left.\begin{aligned} &dC_L = 0.10,\ C_{L1} = -1.0,\ C_{L2} = 2.4,\ C_{L3} = -0.5,\ C_{L4} = 0.8, \\ &C_{Dm} = 0.08,\ dC_D = 0.03. \end{aligned}\right\} \tag{32.2}$$

(C_{L1} and C_{L2} are respectively the minimum and the maximum lift coefficient, dC_L is the slope of C_L vs. angle of incidence (in degrees) between C_{L1} and C_{L2}. C_{L3} and C_{L4} are the lift coefficients between which C_D is constant, C_{Dm}. dC_D is the slope of C_D vs. angle of incidence if C_L is not beween C_{L3} and C_{L4}.) Except for dC_D in normal flow, the precise values of these parameters are not of much importance: C_{L1} and C_{L3} are only relevant at negative angles of incidence, and the reversed profiles are not very important except for high U-values. The chords at the tips and at the roots, c_t and c_r, are simply measured. There remain the following parameters, which can be varied:

$$\left.\begin{array}{l}\text{normal profile : } \alpha_{ot},\ \alpha_{or},\ dC_L,\ C_{L2},\ C_{L4},\ C_{Dm} \\ \text{reversed profile: } \alpha_{ot},\ \alpha_{or}\end{array}\right\} \quad (32.3)$$

which are 8 variable parameters for each boomerang arm. (α_{ot} and α_{or} respectively denote the geometric angles of incidence at the tips and at the roots of the arms.)

The trial and error method of choosing these 16 parameters for each boomerang is predominantly aimed at an agreement with experiment for the axial force F_{lz}, as this component is measured with the highest relative precision. A very good agreement can be attained, witness fig. 32.1, which fixes particularly the parameters α_{ot}, α_{or}, dC_L, C_{L2}. The component considered next is the axial torque T_{lz}. Here C_{L4} and C_{Dm} play a role; they influence T_{lz} but also F_{ly} and F_{lx}. The pitching torque T_{ly} can be "adjusted" by increasing α_{ot} and/or α_{or} for one arm and decreasing the corresponding values for the other arm. This hardly influences any of the five other components. Finally the rolling torque T_{lx} can be influenced to some extent by shifting some lift from the tips to the roots of the arms, for instance by increasing α_{or} and decreasing α_{ot}.

We paid attention to one of the more serious shortcomings of our theory, namely that it produces too high values for T_{lx} (see §33). We have tried several ways to decrease the ratio T_{lx}/F_{lz}. The one finally employed is the choice of rather high values of the angles of incidence at the roots of the arms, α_{or} (except for boomerang WU), and a high value $C_{L2} = 2.4$

of the maximum lift coefficient for the reversed profiles. But we have also experimented with a higher value of C_{L2} at the root than at the tip. A more drastic method was to introduce a "relaxation parameter" as a sort of correction for the fact that the flow around a boomerang arm is non-stationary. This might cause a delay in the circulation around the arm assumed to be proportional to the circulation's rate of change. This rather complicated procedure, which involved numerical differentiation of the lift function $f_z(x,y)$, yielded only slightly better results, not enough to justify the method any way.

The final choice of the parameters for the five model boomerangs which should simulate the experimental boomerangs L1, L4, L6, F18 and WU are listed in table 32.1.

Boomerang nr. 195 belonging to L1: a = 298

arm	e	l	c_t	c_r	α_{ot}	α_{or}	dC_L	C_{L1}	C_{L2}	C_{L3}	C_{L4}	C_{Dm}	dC_D
1	+71	286	43	57	+5.0	+8.0	.10	-1.0	+2.0	-0.5	+1.0	.06	.03
	reversed profile				-1.0	+5.0	.10	-1.0	+2.4	-0.5	+0.8	.08	.03
2	-61	296	41	57	+2.0	+8.0	.10	-1.0	+2.0	-0.5	+1.0	.06	.03
	reversed profile				+2.0	+5.0	.10	-1.0	+2.4	-0.5	+0.8	.08	.03

Boomerang nr. 237 belonging to L4: a = 291

arm	e	l	c_t	c_r	α_{ot}	α_{or}	dC_L	C_{L1}	C_{L2}	C_{L3}	C_{L4}	C_{Dm}	dC_D
1	+79	280	37	63	+2.0	+7.0	.09	-1.0	+1.8	-0.5	+1.0	.06	.03
	reversed profile				+2.0	+4.0	.10	-1.0	+2.4	-0.5	+0.8	.08	.03
2	-58	286	38	64	+4.0	+7.0	.09	-1.0	+1.8	-0.5	+1.0	.06	.03
	reversed profile				+0,0	+4.0	.10	-1.0	+2.4	-0.5	+0.8	.08	.03

Boomerang nr. 241 belonging to L6: a = 249

arm	e	l	c_t	c_r	α_{ot}	α_{or}	dC_L	C_{L1}	C_{L2}	C_{L3}	C_{L4}	C_{Dm}	dC_D
1	+59	241	43	53	+4.0	+11.0	.08	-1.0	+1.7	-0.5	+0.8	.04	.03
	reversed profile				+0.0	+2.0	.10	-1.0	+2.4	-0.5	+0.8	.08	.03
2	-35	247	43	53	-1.0	+7.0	.08	-1.0	+1.7	-0.5	+0.8	.04	.03
	reversed profile				+5.0	+6.0	.10	-1.0	+2.4	-0.5	+0.8	.08	.03

Boomerang nr. 242 belonging to F18: a = 258

arm	e	l	c_t	c_r	α_{ot}	α_{or}	dC_L	C_{L1}	C_{L2}	C_{L3}	C_{L4}	C_{Dm}	dC_D
1	+76	249	44	54	+3.0	+6.0	.09	-1.0	+1.8	-0.5	+0.8	.04	.03
	reversed profile				+1.0	+4.0	.10	-1.0	+2.4	-0.5	+0.8	.08	.03
2	-48	251	44	54	+1.0	+6.0	.09	-1.0	+1.8	-0.5	+0.8	.04	.03
	reversed profile				+3.0	+4.0	.10	-1.0	+2.4	-0.5	+0.8	.08	.03

Boomerang nr. 239 belonging to WU: a = 296

arm	e	l	c_t	c_r	α_{ot}	α_{or}	dC_L	C_{L1}	C_{L2}	C_{L3}	C_{L4}	C_{Dm}	dC_D
1	+76	281	40	40	+3.5	+4.0	.10	-1.0	+1.7	-0.5	+1.0	.06	.03
	reversed profile				+2.0	+2.0	.10	-1.0	+2.4	-0.5	+0.8	.08	.03
2	-69	293	39	39	+3.5	+4.0	.10	-1.0	+1.7	-0.5	+1.0	.06	.03
	reversed profile				+2.0	+2.0	.10	-1.0	+2.4	-0.5	+0.8	.08	.03

table 32.1. Listing of parameters for the theoretical counterparts of the five experimental boomerangs. See §22 for explanation. Lengths in mm, angles in degrees.

§33 *What is the difference between theory and experiment?*

The extent to which the theoretical results resemble the experimental ones can be judged by inspecting the graphs in §31. We shall do this first, and then discuss the possible causes for the discrepancies between theory and experiment. Let us consider the components one by one.

The axial force F_{lz}.
A surprisingly good agreement can be attained for this component. In all five cases the differences between theory and experiment are about as small as those shown in fig. 32.1. Only for $\psi = 45^\circ$, $0.5 \lesssim U \lesssim 1.5$ the theory comes out too low.

The rolling torque T_{lx}.
Here the agreement is rather poor. Experimentally this component, considered as a function of ψ for constant U, has a maximum for $\psi \approx 10^\circ$–15° Theoretically T_{lx} increases much further and attains its maximum only for $\psi \approx 30^\circ$. Our theoretical model cannot produce results significantly better than this. We remark that the experimental values of T_{lx} may contain serious errors due to malfunctioning of measuring element 11 (see §29). With boomerang L6 quite some negative values of T_{lx} have been measured, which appears unrealistic.

The pitching torque T_{ly}.
Theoretically this component, as a function of ψ for constant U, has a maximum for $\psi \approx 15^\circ$, and for higher ψ systematically drops below the experimental values.

The backward force F_{lx}.
This component is positive for $\psi \lesssim 10^\circ$ and negative for $\psi \gtrsim 10^\circ$; in this respect theory and experiment agree. But the theoretical values are too low, particularly for higher ψ the theory produces values which are too strongly negative. This cannot be improved without impairing the agreement for T_{lz}. However, one should keep in mind that the total force acting on a boomerang is a vector with magnitude $\sqrt{F_x^2 + F_y^2 + F_z^2}$, where F_z is by far the greatest component. So the differences between theory and experiment in the components F_{lx} and F_{ly} are not of much importance as

regards the total force.

The sideward force F_{1y}.
According to the theory this component is very small: $|F_{1y}| \lesssim 0.005$. Experimentally it is less small and generally negative. This is a systematic difference between theory and experiment. Probably F_{1y} (and T_{1x} too) contains some substantial errors due to malfunctioning of element 11, see further down. But anyhow, the differences in F_{1y} between theory and experiment are not very important.

The axial torque T_{1z}.
For this component the agreement between theory and experiment is rather good, but not quite so good as for F_{1z}. A systematic difference is that the curves for constant U theoretically have a minimum at $\psi \approx -2°$, but experimentally for $\psi < -5°$. Remark: for boomerang WU a better agreement is possible by choosing $dC_D = 0.027$, instead of 0.030 according to (32.1), this would increase T_{1z} for higher values of ψ.

The differences between the theoretical and the experimental results may be due to either experiment or theory or to both. The experimental errors are discussed in §29. Since their effects are difficult to assess, it is also difficult to explain the discrepancies between theory and experiment on the basis of these errors. But it seems worthwhile to investigate the possible effects of malfunctioning of measuring element 11. Errors in element 11 influence the components F_{1y} and T_{1x} in particular, according to the matrix A in table 28.2. Consider the linear combination:

$$T_{1x} - \frac{62.7 \text{ cm}}{a} F_{1y} \approx T_{1x} - 2F_{1y}.$$

This quantity would be nearly independent of element 11, see fig. 27.3. One could compare it with the corresponding theoretical quantity. Better still: compute, starting from a corresponding theoretical boomerang (e.g. nr. 195 for L1), by means of the inverse matrix A^{-1}, the *expected* output of element 11. Then recalculate the six experimental components with this "*corrected*" output of element 11. All of these components are modified now, but especially F_{1y} and T_{1x}. Naturally, the "corrected" F_{1y} resembles its theoretical counterpart much more now, but what has

become of T_{1x}? The graphs (not shown here) look better, they have less humps. The values for boomerang L6 are not negative anymore. This strongly indicates that substantial irregularities in F_{1y} and T_{1x} (see the graphs in §31) are indeed due to errors in element 11. However, the "corrected" values of T_{1x} turn out to be systematically too high. If they are used in flight path calculations, the flight paths are not nearly as realistic as those based on the original experimental components. One cannot but conclude that, although the experimental values of T_{1x} may contain serious errors, in the main this component has been measured reasonably well, at least in that part of (ψ,U)-space which is traversed in boomerang flights. Also the negative experimental values of F_{1y} probably are realistic. Finally this means that our theoretical model actually produces too high values for T_{1x} at $\psi \gtrsim 10^\circ$. The flight path comparisons in Part III, Ch. III provide additional material relevant to the aerodynamics of boomerangs.

What are the shortcomings of the theoretical model? Two categories can be distinguished: 1. the winglet model is too simple, 2. the air flow around rotating boomerang arms does not behave like an ideal fluid. Examples of the first category: the winglet model has an infinite number of winglets in a steady flow instead of two arms in an unsteady flow, the model is linearized, the main aerodynamic forces are supposed to be perpendicular to the boomerang's plane of rotation. Better models could be developed which would be more realistic in these respects, but still be based on the equations of an ideal fluid. One aspect of the differences between the winglet model and a model in which each boomerang arm is represented by a lifting line (such as Ichikawa's [1967] theory for helicopter rotors), is the distribution of the shed free vorticity over space. Figure 33.1 illustrates this point. It relates to a boomerang with two straight, thin arms joined at an angle of 180°, in other words: a rotating straight stick. Fig. 33.1 shows in which parts of the circular region S this boomerang meets free vorticity shed by it previously (i.e. comes into contact with fluid which has touched the boomerang previously). The vorticity is supposed to drift with the undisturbed flow. The boomerang's angle of incidence ψ is zero. The pictures exhibit a striking difference from the winglet model in which the winglets meet free vorticity all over S.

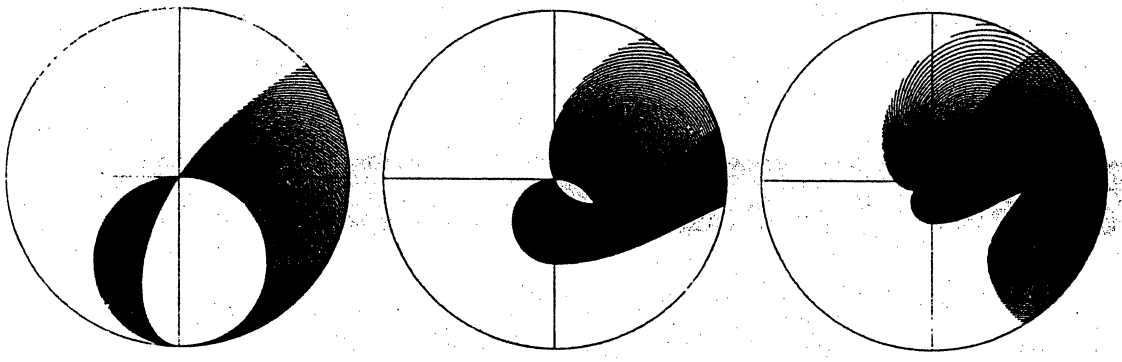

fig. 33.1. A rotating "straight stick" boomerang meets free vorticity shed by it previously in the shaded parts of circular region S. Rotation counterclockwise. Undisturbed flow from left to right. $\psi = 0°$. a: $U = 1$, b: $U = 0.5$, c: $U = 0.25$.

As to the second category: The lift and drag characteristics may depend on the momentary flow situation as well as on previous conditions (hysteresis). Also the flow around a boomerang arm may be not so smooth, the airflow may separate, the Kutta condition may be violated, etc. About these matters not much appears to be known. The knowledge would first have to come from experiments before it could be incorporated in theoretical models. That the flow around rotating airfoils may substantially differ from two-dimensional flow around the same airfoils at the same local Reynolds numbers seems certain. As was remarked in §32, the profile lift coefficients of arms forming part of rotating boomerangs can be much higher than in straight flow. This effect is so strong, that boomerangs with the experimental lift and drag characteristics of §26 would hardly be able to traverse return flight paths, in contradistinction to real boomerangs (see Part III, §31).

A similar phenomenon has been investigated by Muesmann [1958] for axial-flow compressor blades at low Reynolds numbers. It should be emphasized

that Muesmann's case differs from our own in the direction of the main flow with respect to the axis of rotation. With axial-flow compressors the blades experience a steady flow. With boomerangs the flow has a component parallel to the boomerang's main plane (except if $\psi = \pm 90°$), so that the arms experience an unsteady, periodic flow. (Helicopter rotors resemble boomerangs in this respect, but operate at much higher Reynolds numbers. As far as I am aware, the presence of the mentioned phenomenon has not been established for helicopter rotor blades.) Muesmann [1958] compared the experimental compressor performance with calculations based on the lift and drag characteristics of the blade profiles measured in two-dimensional flow. These latter measurements [Muesmann, 1959] were done at Reynolds numbers (Re) between 17000 and 400000. The local effective Reynolds numbers (Re^*) at the rotating compressor blades varied between 10000 and 400000. The geometry of Muesmann's compressor rotor is shown in fig. 33.2. The blade profiles

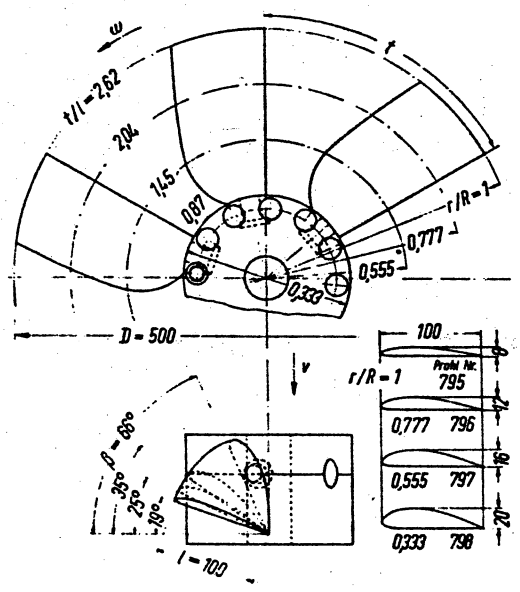

fig. 33.2. Taken from [Muesmann, 1958, p. 351]. Geometry of Muesmann's experimental axial-flow compressor rotor. Measurements in mm.

increase in thickness from 8% at the tips to 20% at the roots. Chords are constant. The under (pressure) sides are flat. According to Muesmann [1958], the main difference between the experimental performance of the compressor and what would be expected on basis of the measurements in straight flow can be interpreted as a decrease of the critical

Reynolds number (= Re at which transition from supercritical to subcritical flow occurs, see §26) for rotating blades, see table 33.1.

r/R	th/ch	Re crit	Re^* crit
1	.08	40000	30000-40000
7/9	.12	50000	30000-35000
5/9	.16	83000	25000-30000
1/3	.20	105000	20000-30000

table 33.1. From [Muesmann, 1958, p. 360]. Local critical Reynolds numbers Re^* crit of rotating compressor blade profiles (see fig. 33.2) compared to those in two-dimensional flow, Re crit.

What is the cause of this remarkable phenomenon? Muesmann [1958, p. 360] states that it must be essentially due to the boundary layer's being influenced by centrifugal and coriolis forces, which lessen the flow's tendency to separate from the airfoil. It is likely that similar effects play a role in the aerodynamics of boomerangs. It is exactly the prevention of separation which makes a good performance at low Reynolds numbers possible for boomerangs. It would be extremely interesting to investigate experimentally the relevant phenomena, in particular the effects due to unsteadiness of the flow.

To sum up: despite its obvious limitations, our winglet model produces results which do not agree too badly with experiments. In particular for the axial force F_z an almost perfect correspondence with experiment can be attained. Although the theoretical model boomerangs show some systematic differences from the measurements, they nevertheless behave like true boomerangs. This is also shown by the flight path calculations presented in Part III.

References for Part II.

Abbot, I.A. & Von Doenhoff, A.E., 1959.
Theory of wing sections. (Dover Publ., New York, 1959)

Ahlberg, J.H., Nilson, E.N. & Walsh, J.L., 1967.
The theory of splines and their applications. (Academic Pr., New York, London, 1967)

Barakat, R., 1967.
"Incompressible flow around porous two-dimensional sails and wings." Journal of Mathematical Physics, 47 (1967) p. 327-349

Hess, F., 1968.
"The aerodynamics of boomerangs." Scientific American, 219, 5 (Nov. 1968) p. 124-136

Hess, F., 1972.
Boemerangs roterend in een luchtstroom: krachtmetingen. (Rapport TW-118, Mathematisch Instituut, Rijksuniversiteit Groningen, 1972)

Hess, F., 1973.
Rotating airfoils in steady flow. (Report TW-111, Mathematisch Instituut, Rijksuniversiteit Groningen, 2nd. ed. 1973)

Hildebrand, F.B., 1956.
Introduction to numerical analysis. (McGraw-Hill, New York, 1956)

Ichikawa, T., 1967.
"Linear aerodynamic theory of rotor blades." Journal of Aircraft, 4, 3 (1967) p. 210-218

Kotschin, N.J., Kibel, I.A. & Rose, N.W., 1954.
Theoretische Hydromechanik Bd. I. (Akademie Verlag, Berlin, 1954)

Kraemer, K., 1961a.
"Flügelprofile im kritischen Reynoldszahl-Bereich." Forschung auf dem Gebiete des Ingenieurwesens, 27, 2 (1961) p. 33-46

Kraemer, K., 1961b
"Über die Wirkung von Stolperdrähten auf der Grenzschichtumschlag." Zeitschrift für Flugwissenschaften, 9, 1 (1961) p. 20-27

Labrujere, Th.E. & Zandbergen, P.J., 1973.
"On the application of a new version of lifting surface theory to non-slender and kinked wings." Journal of Engineering Mathemeatics, 7, 1 (1973) p. 85-96

Lippisch, A.M., 1951.
"Profile für Flugmodelle." Thermik-Modellflug 4, 10, 1 (1951) p. 54-59, 73,76 (translated from: Air Trails, April-May 1950)

Muesmann, G., 1958.
"Zusammenhang der Strömungseigenschaften des Laufrades eines Axialgebläses mit denen eines Einzelflügels." Zeitschrift für Flugwissenschaften, 6, 12 (1958) p. 345-362

Muesmann, G., 1959.
"Messungen und Grenzschicht Beobachtungen an affin verdickten Gebläseprofilen in Abhängigkeit von der Reynoldszahl." Zeitschrift für Flugwissenschaften, 7, 9 (1959) p. 253-264

Multhopp, H., 1950.
Methods for calculating the lift distribution on wings (subsonic lifting surface theory). (Reports and Memoranda No. 2884, Jan. 1950)

Muskhelishvili, N.I., 1953.
Singular integral equations. (Noordhoff, Groningen, 1953)

Schmitz, F.W., 1954.
"Zur Aerodynamik der kleinen Reynolds-Zahlen." Jahrbuch 1953 Wiss. Ges. Luftfahrt (Braunschweig, 1954) p. 149-166

Schmitz, F.W., 1957.
Aerodynamik des Flugmodells, Tragflügelmessungen I. (Carl Lange Verlag, Duisburg, 3rd. ed. 1957)

Van Spiegel, E., 1959.
Boundary value problems in lifting surface theory.(thesis,Delft,1959)

Zandbergen, P.J., Wouters, J.G. & Labrujere, Th.E., 1967.
A new approach to the numerical solution of the equation of subsonic lifting surface theory. (NLR-TR G.49, National Aerospace Laboratory NLR, 1967)

PART III
MOTION

Dies ist der wunderbare Bumerangwurf, der vor allen anderen Würfen den Schauenden in Staunen und Verwunderung versetzt.

[Gerlach, 1886, p. 86]

§1. *Introduction*

Part III is about the dynamics and motion of boomerangs. The investigations reported here are both theoretical and experimental. In Chapter I equations of motion for the flight of a boomerang are derived. The boomerang is considered as a fast spinning rigid body on which unspecified forces and torques act. The exact equations are simplified by "smoothing": fluctuations within one spin period of quantities such as the boomerang's velocity and orientation or the aerodynamic forces are disregarded. The final equations of motion contain the unspecified aerodynamic forces, which are functions of the - as yet unknown - motion. §5 forms a link with Part II: it deals with the forces acting on a boomerang in its flight. In the numerical flight path calculations we shall use either the theoretical or the experimental aerodynamic forces of Part II. This means: if, at a given instant during a theoretical flight, the boomerang's speed is V, its spin ω_z and its angle of incidence Ψ, the aerodynamic forces of Part II for this combination of V, ω_z and Ψ are used. However, it should be emphasized that any other aerodynamic boomerang model may also provide numerical values for the forces to be used in the equations of Part III. Some general aspects of boomerang flight paths are discussed in §7.

Chapter II deals with field experiments. Four experimental boomerangs, each equipped with an electric light, were thrown at night. Their flight paths were photographically recorded by a pair of cameras. A selection of the resulting stereo pictures is presented in Chapter III, together with stereograms of computed flight paths. On the basis of this material the reader may form his own opinion as to the agreement between theory and experiment.

Chapter IV, which is mainly theoretical, contains various examples of how a boomerang's flight path is influenced by certain changes in the manner of launching and the boomerang's shape, or by the presence of wind. §35 is about straight-flying boomerangs. In both Chapter III and Chapter IV the flight path pictures are intended to

serve as sources of information on the motion of boomerangs, rather than as mere illustrations. The text of these chapters may rightly be considered as less important than the pictures.

The reader who wants to follow the main line of Part III is suggested to read the following sections:
Chapter I: §§ 2, 3, 4, 5, 6, 7.
Chapter II: §§ 10, 12, 14.
Chapter III: any selection including § 22.
Chapter IV: any selection.

A list of references is given at the end of Part III.

CHAPTER I

THEORY OF BOOMERANG MOTION.

§2 *Smoothing and stability.*

In the next sections we shall derive equations of motion for boomerangs, in which the aerodynamic forces are left unspecified. The actual magnitudes of these forces must be derived either from a theoretical model or from measurements.

A boomerang is considered to be a rigid body behaving like a fast top. It is assumed to rotate rapidly about the principal axis through the centre of mass with the greatest moment of inertia. The forces acting on a boomerang can be expected to have fluctuations with a period equal to the period of rotation. We shall work, however, with smoothed or averaged forces. This has the advantage that the equations of motion are simplified, and that in the numerical calculation of boomerang fligh paths considerably less integration steps are required. Another reason for this simplification arises from the fact that both the aerodynamic model and the experiments described in Part II deal with the averaged aerodynamic forces only.

The justification of smoothing can be based on the assumption that the fluctuations and variations in all relevant variables during a boomerang flight are of two distinct kinds: they are either fast or slow. Fast variations have characteristic times of the order of one rotation period or less, whereas slow variations have characteristic times much greater than the rotation period. For instance, variations in a boomerang's phase angle and the aerodynamic forces during one spin period are of the fast kind, whereas substantial variations in a boomerang's linear speed, rotational velocity, angle of incidence, position and orientation of spin axis are of the slow kind. The fast fluctuations are considered as small disturbances which cancel after integration with respect to time, and the operation of smoothing can be regarded as a sort of time-averaging over a small number of rotation periods. Integration of the

exact equations of motion would undoubtedly result in all the variables having fast fluctuations. If one starts with smoothed equations of motion, the resulting variables turn out to be smooth also, but one cannot be certain that their values correspond to those obtained from smoothing the results of the exact equations.

A disadvantage of this smoothing or averaging is, of course, that information concerning fast variations of mechanical and aerodynamic quantities is lost. A far more serious drawback is that the smoothed equations of motion may in some cases lead to a motion which deviates very much from the motion based on the exact equations. This problem is closely related to the question of stability of motion. If its motion is not sufficiently stable, a boomerang may "wobble" more and more, loose its spin and descend fluttering like a wounded bird. Such unstability may be caused by bad launching (spin too slow) or by a bad shape of the boomerang. For instance, boomerangs of which the arms include a very obtuse angle ($\gtrsim 150^\circ$) have a relatively small difference between the greatest and the middle principal moments of inertia. It seems that the motion of such a boomerang can easily become unstable. In the absence of aerodynamic forces, a boomerang's spin would be unstable if this difference would vanish.
Remark: If principal axes are mentioned, it is to be understood that these are through the boomerang's centre of mass; the principal moments of inertia are with respect to these axes. If mention is made of *the* principal axis or of *the* moment of inertia, the one associated with the greatest principal moment of inertia is meant.

It would be of considerable interest to derive some definite rules as to the conditions under which a boomerang's motion would be stable or unstable. This problem, however, is rather difficult to solve, since detailed information would be needed concerning the aerodynamic forces and their variations during a rotation period, with and without wobbling. At present such information is not available. We have, however, tried to make a simplified investigation into this question of stability, by using an aerodynamic model in which the induced velocity of the air is neglected. We investigated the theoretical behaviour of boomerangs with 2, 4 and ∞ identical arms, but the results did not seem to be meaningful.

Therefore we omit a discussion of the conditions for stability of motion altogether.

It seems probable that the smoothed equations of motion, which will be used as a basis for our flight path calculations, form reasonable approximations to the exact equations as long as the exact motion would be stable. Cases in which the exact motion would not be stable cannot be distinguished by our theory and hence would be treated incorrectly. We cannot give any theoretical criterion for stability, except for these two qualitative ones: 1^{o}_{-} the boomerang's spin should be sufficiently fast, and 2^{o}_{-} the boomerang's greatest principal moment of inertia should be sufficiently greater than the middle one.

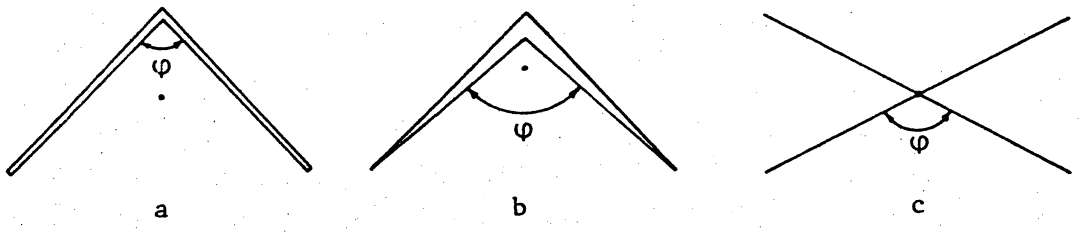

fig. 2.1. Three idealized types of boomerangs. Dots denote centres of mass.

Just for example let us consider three idealized types of boomerangs with regard to point 2^{o}_{-}. The first two consist of two equal, straight, thin arms joined at an angle φ. Type a has a constant mass per unit of length along the arms, type b has a mass per unit of length which varies linearly along the arms and is zero at the tips. Type c consists of four equal, straight, thin arms joined crosswise at angles φ and $\pi-\varphi$. See fig. 2.1. Let the principal moments of inertia in each case be I_1, I_2 and I_3 with $I_1 \leq I_2 \leq I_3$. Because the boomerangs are plane bodies: $I_1 + I_2 = I_3$. Figure 2.2 contains graphs of the quantity $(I_3 - I_2)/I_3$ vs. φ for each of the cases a, b and c. If, for instance, $(I_3 - I_2)/I_3$ should be greater than 0.1, then φ should not exceed 113° for type a, 120° for type b and 143° for type c boomerangs.

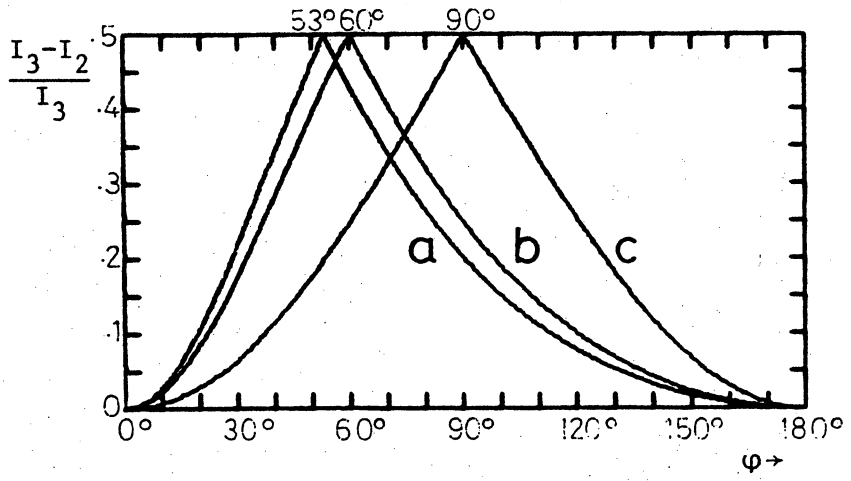

fig. 2.2. Graphs of $(I_3 - I_2)/I_3$ vs. φ for the cases a, b, c of fig. 2.1.

It is not suggested that $(I_3 - I_2)/I_3 \gtrsim 0.1$ is an actual condition for stable spin of boomerangs. By very careful launching it is possible to make a straight "boomerang" ($\varphi = 180°$), with a length of 20 cm and a width of 2½ cm, spin stably (see Part I, §9 about Celebes). For such an object: $(I_3 - I_2)/I_3 \approx 1/65$.

§3 *Equations of motion (I).*

Throughout this chapter, a boomerang is considered as a rigid body. The angular momentum vector of this body is approximately parallel to the body's principal axis with the greatest moment of inertia.

We shall use three right-handed cartesian coordinate systems:

1° (X,Y,Z), a fixed inertial system with respect to which we want to calculate the boomerang's flight path.

2° (1,2,3), a system fixed to the boomerang. Its origin is the boomerang's centre of mass, the axes are the principal axes of the boomerang, in the order of increasing principal moments of inertia.

3° (x,y,z), a system partially fixed to the boomerang. The z-axis coincides with the 3-axis. The projection of the velocity of the boomerang's centre of mass onto the (x,y)-plane points in the negative x-direction. The origin is again the boomerang's centre of mass.

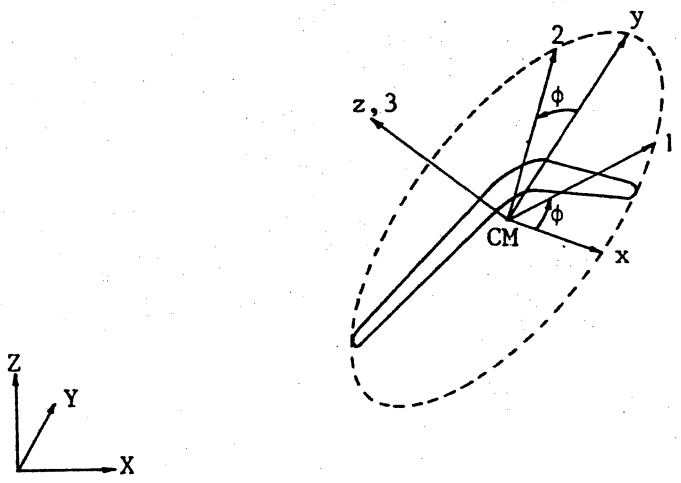

fig. 3.1. The three coordinate systems (X,Y,Z), (x,y,z), (1,2,3).

We shall first derive the boomerang's equations of motion with respect to the (x,y,z)-system, since this system is directly related to the boomerang's state of motion with respect to the air. The (x,y,z)-system rotates at an angular velocity:

$$\vec{\Omega} = (\Omega_x, \Omega_y, \Omega_z)$$

Ω_z is determined kinematically by the fact that the y-component of the velocity of the boomerang's centre of mass is zero by definition. The motion of the boomerang can be separated into two parts: the motion of its centre of mass, and the motion of the body with respect to its centre of mass.

A. *Motion of the centre of mass.*

The velocity of the boomerang's centre of mass is

$$\vec{V} = (V_x, V_y, V_z)$$

where the components are given in the x,y,z-directions respectively. By definition of the (x,y,z)-system we have

$$\left.\begin{aligned} V_x &< 0 \\ V_y &= 0. \end{aligned}\right\} \quad (3.1)$$

Let further $\vec{F}$ be the resultant force acting on the boomerang, m the boomerang's mass. Now:

$$\left.\begin{aligned} \vec{F} &= \dot{\vec{p}} \\ \vec{p} &= m\vec{v} \end{aligned}\right\} \quad (3.2)$$

A dot indicates differentiation with respect to time. As shown e.g. by Hauser [1965, Ch. 3]:

$$\vec{F} = \frac{d\vec{p}}{dt} = \left(\frac{d\vec{p}}{dt}\right)' + \vec{\Omega}\times\vec{p} \qquad (3.3)$$

where the prime indicates that the differentiation has to be performed with respect to the rotating (x,y,z)-system. Thus we have, using (3.1),

$$\left.\begin{aligned} F_x &= m(\dot{V}_x + V_z\Omega_y) \\ F_y &= m(V_x\Omega_z - V_z\Omega_x) \\ F_z &= m(\dot{V}_z - V_x\Omega_y) \end{aligned}\right\} \quad (3.4)$$

The second of these equation determines Ω_z. The exact equations (3.4) are now replaced by the approximate, smoothed ones:

$$\left.\begin{aligned} \overline{F}_x &= m(\dot{\overline{V}}_x + \overline{V}_z\overline{\Omega}_y) \\ \overline{F}_y &= m(\overline{V}_x\overline{\Omega}_z - \overline{V}_z\overline{\Omega}_x) \\ \overline{F}_z &= m(\dot{\overline{V}}_z - \overline{V}_x\overline{\Omega}_y) \end{aligned}\right\} \quad (3.5)$$

Here overbars denote smoothed quantities. $\overline{F}_x$, $\overline{F}_y$, $\overline{F}_z$ are the smoothed or time-averaged forces (which, in our case, are either taken from the winglet model or from wind tunnel measurements). The other smoothed quantities: $\overline{V}_x$, $\overline{V}_z$, $\overline{\Omega}_x$, $\overline{\Omega}_y$, $\overline{\Omega}_z$, are to be solved from the complete, smoothed equations of motion. This solution will not be exact, since equations (3.5) are not correct. One can only hope that they provide a reasonable approximation for the motion of the boomerang's centre of mass, and that it is merely the fast variations which are neglected.

B. *Motion with respect to the centre of mass.*
(A good reference on this subject is [Hauser, 1965, Ch. 4].) Let the boomerang's angular velocity be $\vec{\omega} = (\omega_x, \omega_y, \omega_z)$. Because of the definition of the (x,y,z)-system:

$$\left.\begin{aligned} \Omega_x &= \omega_x \\ \Omega_y &= \omega_y \end{aligned}\right\} \quad (3.6)$$

Let $\vec{T}$ be the resultant torque acting on the boomerang and $\vec{L}$ the angular momentum vector of the boomerang. Then

$$\vec{T} = \dot{\vec{L}} \quad (3.7)$$

and

$$\vec{T} = \frac{d\vec{L}}{dt} = \left(\frac{d\vec{L}}{dt}\right)' + \vec{\Omega}\times\vec{L} \quad (3.8)$$

where again the prime indicates differentiation with respect to the (x,y,z)- system. Thus:

$$\left.\begin{aligned} T_x &= \dot{L}_x - L_y\Omega_z + L_z\Omega_y \\ T_y &= \dot{L}_y - L_z\Omega_x + L_x\Omega_z \\ T_z &= \dot{L}_z - L_x\Omega_y + L_y\Omega_x \end{aligned}\right\} \quad (3.9)$$

These equations are only useful if we have expressions for L_x, L_y, L_z and their time derivatives. Therefore we now consider the (1,2,3)-system. Its coordinate axes coincide with the boomerang's principal axes with corresponding principal moments of inertia I_1, I_2, I_3 with $I_1 \leq I_2 \leq I_3$. As stated in the beginning of this section the 3-axis is identical with the z-axis. The angle between 1-axis and x-axis (and between 2-axis and y-axis) be ϕ, so that

$$\left.\begin{aligned} \dot{\phi} &= \omega_3 - \Omega_z \\ \omega_3 &= \omega_z \end{aligned}\right\} \quad (3.10)$$

The angular momentum components with respect to the (1,2,3)-system are related to the principal moments of inertia in a simple way:

$$\left.\begin{aligned} L_1 &= I_1\omega_1 \\ L_2 &= I_2\omega_2 \\ L_3 &= I_3\omega_3 \end{aligned}\right\} \quad (3.11)$$

The transformation of the components of a vector from the (1,2,3)-system to the (x,y,z)-system and vice versa goes according to the scheme:

	1	2	3
x	$\cos\phi$	$-\sin\phi$	0
y	$\sin\phi$	$\cos\phi$	0
z	0	0	1

(3.12)

Therefore we have:

$$\left.\begin{aligned} L_x &= L_1\cos\phi - L_2\sin\phi = I_1\omega_1\cos\phi - I_2\omega_2\sin\phi \\ L_y &= L_1\sin\phi + L_2\cos\phi = I_1\omega_1\sin\phi + I_2\omega_2\cos\phi \\ L_z &= L_3 = I_3\omega_3 \end{aligned}\right\} \quad (3.13)$$

$$\left.\begin{aligned} \omega_1 &= +\omega_x\cos\phi + \omega_y\sin\phi \\ \omega_2 &= -\omega_x\sin\phi + \omega_y\cos\phi \\ \omega_3 &= +\omega_z \end{aligned}\right\} \quad (3.14)$$

Substitute (3.14) into (3.13):

$$\left.\begin{aligned} L_x &= \tfrac{1}{2}(I_1 + I_2)\omega_x + \tfrac{1}{2}(I_1 - I_2)(\omega_x \cos 2\phi + \omega_y \sin 2\phi) \\ L_y &= \tfrac{1}{2}(I_1 + I_2)\omega_y + \tfrac{1}{2}(I_1 - I_2)(\omega_x \sin 2\phi - \omega_y \cos 2\phi) \\ L_z &= I_3\omega_z \end{aligned}\right\} (3.15)$$

Using (3.10) we obtain by differentiating (3.13):

$$\left.\begin{aligned} \dot{L}_x &= I_1\dot{\omega}_1 \cos\phi - I_2\dot{\omega}_2 \sin\phi + (\omega_3 - \Omega_z)(-I_1\omega_1 \sin\phi - I_2\omega_2 \cos\phi) \\ \dot{L}_y &= I_1\dot{\omega}_1 \sin\phi + I_2\dot{\omega}_2 \cos\phi + (\omega_3 - \Omega_z)(+I_1\omega_1 \cos\phi - I_2\omega_2 \sin\phi) \\ \dot{L}_z &= I_3\dot{\omega}_3 \end{aligned}\right\} (3.16)$$

and by differentiating (3.14):

$$\left.\begin{aligned} \dot{\omega}_1 &= +\dot{\omega}_x \cos\phi + \dot{\omega}_y \sin\phi + (\omega_z - \Omega_z)(-\omega_x \sin\phi + \omega_y \cos\phi) \\ \dot{\omega}_2 &= -\dot{\omega}_x \sin\phi + \dot{\omega}_y \cos\phi + (\omega_z - \Omega_z)(-\omega_x \cos\phi - \omega_y \sin\phi) \\ \dot{\omega}_3 &= +\dot{\omega}_z \end{aligned}\right\} (3.17)$$

Substitute (3.14) and (3.17) into (3.16):

$$\left.\begin{aligned} \dot{L}_x &= \tfrac{1}{2}(I_1 + I_2)\dot{\omega}_x + \tfrac{1}{2}(I_1 - I_2)(-\dot{\omega}_x \cos 2\phi + \dot{\omega}_y \sin 2\phi) + \\ &\quad + (I_1 - I_2)(\omega_z - \Omega_z)(-\omega_x \sin 2\phi + \omega_y \cos 2\phi) \\ \dot{L}_y &= \tfrac{1}{2}(I_1 + I_2)\dot{\omega}_y + \tfrac{1}{2}(I_1 - I_2)(+\dot{\omega}_x \sin 2\phi + \dot{\omega}_y \cos 2\phi) + \\ &\quad + (I_1 - I_2)(\omega_z - \Omega_z)(+\omega_x \cos 2\phi + \omega_y \sin 2\phi) \\ \dot{L}_z &= I_3\dot{\omega}_z \end{aligned}\right\} (3.18)$$

Substitute (3.13) and (3.18) into (3.9) and use (3.6):

$$\left.\begin{aligned} T_x &= \tfrac{1}{2}(I_1+I_2)\dot{\omega}_x - \tfrac{1}{2}(I_1+I_2)\omega_y\Omega_z + I_3\omega_z\omega_y + \tfrac{1}{2}(I_1-I_2)(-\dot{\omega}_x \cos 2\phi + \dot{\omega}_y \sin 2\phi) + \\ &\quad + \tfrac{1}{2}(I_1-I_2)(2\omega_z-\Omega_z)(-\omega_x \sin 2\phi + \omega_y \cos 2\phi) \\ T_y &= \tfrac{1}{2}(I_1+I_2)\dot{\omega}_y + \tfrac{1}{2}(I_1+I_2)\omega_x\Omega_z - I_3\omega_z\omega_x + \tfrac{1}{2}(I_1-I_2)(+\dot{\omega}_x \sin 2\phi + \dot{\omega}_y \cos 2\phi) + \\ &\quad + \tfrac{1}{2}(I_1-I_2)(2\omega_z-\Omega_z)(+\omega_x \cos 2\phi + \omega_y \sin 2\phi) \\ T_z &= I_3\dot{\omega}_z + (I_1-I_2)[(\omega_x^2 + \omega_y^2)\sin 2\phi - \omega_x\omega_y \cos 2\phi] \end{aligned}\right\} (3.19)$$

In the special case with $I_1 = I_2 = I_{12}$, (3.19) reduces to

$$\left.\begin{aligned} T_x &= I_{12}\dot{\omega}_x + (I_3\omega_z - I_{12}\Omega_z)\omega_y \\ T_y &= I_{12}\dot{\omega}_y - (I_3\omega_z - I_{12}\Omega_z)\omega_x \\ T_z &= I_3\dot{\omega}_z \end{aligned}\right\} \quad (3.20)$$

which are the equations for a symmetric top with respect to the (x,y,z)-system. Up to this point all of the equations are exact.

We simplify the equations (3.19) by smoothing them and write:

$$\left.\begin{aligned} \overline{T}_x &= \tfrac{1}{2}(I_1 + I_2)\dot{\overline{\omega}}_x - \tfrac{1}{2}(I_1 + I_2)\overline{\omega}_y\overline{\Omega}_z + I_3\overline{\omega}_z\overline{\omega}_y \\ \overline{T}_y &= \tfrac{1}{2}(I_1 + I_2)\dot{\overline{\omega}}_y + \tfrac{1}{2}(I_1 + I_2)\overline{\omega}_x\overline{\Omega}_z - I_3\overline{\omega}_z\overline{\omega}_x \\ \overline{T}_z &= I_3\dot{\overline{\omega}}_z \end{aligned}\right\} \quad (3.21)$$

The remarks made with regard to (3.5) also apply to (3.21). The terms with $\sin 2\phi$ and $\cos 2\phi$ have been omitted, as they seem to be important only with regard to the fast variations.

Using the abbreviations $I_{12} = \frac{1}{2}(I_1 + I_2)$, we can write (3.21) as

$$\left.\begin{aligned} \overline{T}_x &= I_{12}\dot{\overline{\omega}}_x + (I_3\overline{\omega}_z - I_{12}\overline{\Omega}_z)\overline{\omega}_y \\ \overline{T}_y &= I_{12}\dot{\overline{\omega}}_y - (I_3\overline{\omega}_z - I_{12}\overline{\Omega}_z)\overline{\omega}_x \\ \overline{T}_z &= I_3\dot{\overline{\omega}}_z \end{aligned}\right\} \quad (3.22)$$

This resembles the equations for a symmetric top (3.20). A second simplification can be made. Boomerangs spin rapidly, i.e. we generally have:

$$\left.\begin{aligned} &|\overline{\omega}_x|,\ |\overline{\omega}_y|,\ |\overline{\Omega}_z| \ll |\overline{\omega}_z| \\ &|\dot{\overline{\omega}}_x| \ll |\overline{\omega}_y\overline{\omega}_z|,\ |\dot{\overline{\omega}}_y| \ll |\overline{\omega}_x\overline{\omega}_z| \end{aligned}\right\} \quad (3.23)$$

The last two inequalities express that $\overline{\omega}_x$ and $\overline{\omega}_y$ vary relatively little within a small number of spin periods. Thus we obtain as an approximation of (3.22):

$$\left.\begin{aligned} \overline{T}_x &= +I_3\overline{\omega}_z\overline{\omega}_y \\ \overline{T}_y &= -I_3\overline{\omega}_z\overline{\omega}_x \\ \overline{T}_z &= I_3\dot{\overline{\omega}}_z \end{aligned}\right\} \quad (3.24)$$

These are our final equations for the motion of a boomerang with respect to its centre of mass.

A slightly different way of arriving at (3.24) from (3.19) results from interchanging the order of the smoothing and the fast spin approximation. If we first use the inequalities (3.23), which now are understood to hold between the exact variables rather than between the smoothed variables, (3.19) can be simplified to:

$$\left.\begin{aligned} T_x &= +I_3\omega_y\omega_z + (I_1 - I_2)\omega_z(-\omega_x \sin 2\phi + \omega_y \cos 2\phi) \\ T_y &= -I_3\omega_x\omega_z + (I_1 - I_2)\omega_z(+\omega_x \cos 2\phi + \omega_y \sin 2\phi) \\ T_z &= I_3\dot{\omega}_z + (I_1 - I_2)\{(\omega_x^2 + \omega_y^2)\sin 2\phi - \omega_x\omega_y \cos 2\phi\} \end{aligned}\right\} (3.22^*)$$

Smoothing (3.22^*) yields (3.24).

The equations (3.5) and (3.24) will be used as a basis for the calculation of boomerang flight paths.

§4 *Equations of motion (II).*

The equations of motion of a boomerang with respect to the (x,y,z)-system are given by (3.5) and (3.24). From now on we shall use the smoothed or averaged variables exclusively and omit the overbars.

In this section we shall derive the equations of motion with respect to a fixed inertial system (X,Y,Z), The Z-axis points verically upward, the (X,Y)-plane is horizontal. The relation between both coordinate systems is determined by the Euler angles φ, ψ, ϑ, as shown in fig. 4.1. By definition $0 \leq \vartheta \leq \pi$.

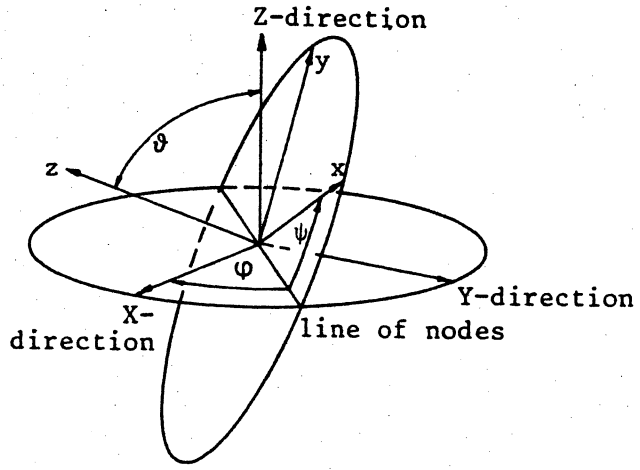

fig. 4.1. The Euler angles defining the relation between the (x,y,z)- and the (X,Y,Z)-directions.

The transformation of the components of a vector from the (x,y,z)-directions to the (X,Y,Z)-directions and vice versa is given by the following scheme (see [Hauser, 1965, Ch. 9]):

	x	y	z
X	$+\cos\psi\ \cos\varphi - \cos\vartheta\ \sin\varphi\ \sin\psi$	$-\sin\psi\ \cos\varphi - \cos\vartheta\ \sin\varphi\ \cos\psi$	$+\sin\vartheta\ \sin\varphi$
Y	$+\cos\psi\ \sin\varphi + \cos\vartheta\ \cos\varphi\ \sin\psi$	$-\sin\psi\ \sin\varphi + \cos\vartheta\ \cos\varphi\ \cos\psi$	$-\sin\vartheta\ \cos\varphi$
Z	$+\sin\vartheta\ \sin\psi$	$+\sin\vartheta\ \cos\psi$	$+\cos\vartheta$

(4.1)

For the angular velocity $\vec{\Omega}$ of the (x,y,z)-system we now have [Hauser, 1965, Ch. 9]:

$$\left.\begin{aligned}\Omega_x &= +\dot{\vartheta}\cos\psi + \dot{\varphi}\sin\vartheta\sin\psi \\ \Omega_y &= -\dot{\vartheta}\sin\psi + \dot{\varphi}\sin\vartheta\cos\psi \\ \Omega_z &= \dot{\psi} + \dot{\varphi}\cos\vartheta\end{aligned}\right\} \quad (4.2)$$

which leads to

$$\left.\begin{aligned}\dot{\vartheta} &= \Omega_x\cos\psi - \Omega_y\sin\psi \\ \dot{\varphi} &= \frac{1}{\sin\vartheta}\,(\Omega_x\sin\psi + \Omega_y\cos\psi) \\ \dot{\psi} &= \Omega_z - \frac{\cos\vartheta}{\sin\vartheta}\,(\Omega_x\sin\psi + \Omega_y\cos\psi)\end{aligned}\right\} \quad (4.3)$$

From (3.24) we obtain, using (3.6):

$$\left.\begin{aligned}\Omega_x &= \omega_x = -\frac{T_y}{I_3\omega_z} \\ \Omega_y &= \omega_y = +\frac{T_x}{I_3\omega_z} \\ \dot{\omega}_z &= \frac{T_z}{I_3}\end{aligned}\right\} \quad (4.4)$$

And from (3.5):

$$\left.\begin{aligned}\Omega_z &= \frac{F_y}{mV_x} + \frac{V_z\omega_x}{V_x} \\ \dot{V}_x &= \frac{F_x}{m} - V_z\omega_y \\ \dot{V}_z &= \frac{F_z}{m} + V_x\omega_y\end{aligned}\right\} \quad (4.5)$$

At this point we introduce the variables V and Ψ defined by:

$$\left.\begin{aligned}V_x &= -V\cos\Psi \\ V_z &= -V\sin\Psi \\ V &> 0, \quad |\Psi| < \tfrac{1}{2}\pi\end{aligned}\right\} \quad (4.6)$$

(Remember: $V_x < 0$, $V_y = 0$.) V is the boomerang's linear velocity, Ψ is the angle between the negative x-axis and the direction of the

boomerang's velocity. We call Ψ the boomerang's angle of incidence. (This same angle was denoted by ψ in Part II.) The use of Ψ and V instead of V_x and V_y is merely a matter of convenience. Now (4.5) can be written in the form:

$$\left.\begin{aligned} \Omega_z &= -\frac{F_y}{mV\cos\Psi} + \omega_x \operatorname{tg}\Psi \\ \dot{V} &= \frac{1}{m}(-F_x\cos\Psi - F_z\sin\Psi) \\ \dot{\Psi} &= \frac{1}{mV}(+F_x\sin\Psi - F_z\cos\Psi) + \omega_y \end{aligned}\right\} \quad (4.7)$$

Equations (4.3), (4.4) and (4.7) determine the motion of a boomerang. They can be taken together as:

$$\left.\begin{aligned} \dot{\omega}_z &= \frac{T_z}{I_3} \\ \dot{V} &= \frac{1}{m}(-F_x\cos\Psi - F_z\sin\Psi) \\ \dot{\Psi} &= \frac{1}{mV}(F_x\sin\Psi - F_z\cos\Psi) + \frac{T_x}{I_3\omega_z} \end{aligned}\right\} \quad (4.8)$$

$$\left.\begin{aligned} \dot{\vartheta} &= \frac{1}{I_3\omega_z}(-T_y\cos\psi - T_x\sin\psi) \\ \dot{\varphi} &= \frac{1}{I_3\omega_z}\cdot\frac{1}{\sin\vartheta}\cdot(-T_y\sin\psi + T_x\cos\psi) \\ \dot{\psi} &= -\frac{F_y}{mV\cos\Psi} - \operatorname{tg}\Psi\frac{T_y}{I_3\omega_z} - \cos\vartheta\cdot\dot{\varphi} \end{aligned}\right\} \quad (4.9)$$

For the position (X,Y,Z) of the boomerang's centre of mass we simply have:

$$\left.\begin{aligned} \dot{X} &= V\{-\cos\Psi(\cos\psi\cos\varphi - \sin\psi\sin\varphi\cos\vartheta) - \sin\Psi\sin\varphi\sin\vartheta\} \\ \dot{Y} &= V\{-\cos\Psi(\cos\psi\sin\varphi + \sin\psi\cos\varphi\cos\vartheta) + \sin\Psi\cos\varphi\sin\vartheta\} \\ \dot{Z} &= V\{-\cos\Psi\sin\psi\sin\vartheta - \sin\Psi\cos\vartheta\} \end{aligned}\right\} \quad (4.10)$$

Equations (4.8), (4.9) and (4.10) have to be integrated numerically. The forces and torques F_x, F_y, F_z, T_x, T_y, T_z must be given as known functions of the state of motion. If the initial conditions are provided,

these nine first order differential equations can be solved for the nine unknowns ω_z, V, Ψ, ϑ, φ, ψ, X, Y, Z as functions of time, t.

The equations of motion (4.8) and (4.9) contain singularities if variables in dominators vanish. Four singularities may occur, represented by:

$$\left.\begin{aligned} \sin\vartheta &\to 0 \\ \cos\Psi &\to 0 \\ V &\to 0 \\ \omega_z &\to 0 \end{aligned}\right\} \quad (4.11)$$

Let us consider these cases one by one.

Boomerang's plane horizontal.
If $\sin\vartheta \to 0$, both $|\dot{\varphi}|$ and $|\dot{\psi}|$ tend to ∞. This singularity is just a matter of coordinate systems: the line of nodes (see fig. 4.1) moves wildly around, but physically nothing happens. If $\sin\vartheta \approx 0$, $\dot{\varphi}$ and $\dot{\psi}$ have no physical significance, but the quantity $\dot{\varphi} + \dot{\psi} \approx \Omega_z$ has, and behaves properly. This singularity can be removed by choosing instead of (X,Y,Z) another coordinate system, which is to be used temporarily if $\sin\vartheta$ is smaller than some chosen value.

Boomerang's plane perpendicular to forward velocity.
If $\cos\Psi \to 0$, $|\Omega_z|$ and $|\dot{\psi}|$ tend to ∞. From a physical point of view again nothing extraordinary happens. Merely the x- and y-directions are ill-conditioned if $\Psi \approx \pm\frac{1}{2}\pi$. However, if Ω_z becomes large, the condition $|\omega_z| >> |\Omega_z|$ (3.23) can be violated, so that the equations of motion become invalid. Perhaps the theory could be improved in this respect by replacing $I_3\omega_z$ in equations (4.8) and (4.9) by $I_3\omega_z - I_{12}\Omega_z$ according to (3.22), or by $I_3(\omega_z - \frac{1}{2}\Omega_z)$. ($I_{12} = \frac{1}{2}(I_1 + I_2) \approx \frac{1}{2}I_3$ because a boomerang generally is an almost plane object.) Then Ω_z would have to be solved from

$$\Omega_z = \frac{-F_y}{mV_x} + \frac{V_z}{V_x} \cdot \frac{-T_y}{I_3(\omega_z - \frac{1}{2}\Omega_z)} \quad (4.12)$$

instead of the first equation (4.7).

Boomerang's forward velocity vanishes.
If $V \to 0$, $|\Omega_z|$, $|\dot{\psi}|$ and $|\dot{\Psi}|$ tend to ∞. As far as Ω_z and $\dot{\psi}$ are concerned,

the problem is the same as above: in both cases $V_x = V \cos\Psi \to 0$. However, if $V \approx 0$ the boomerang's angle of incidence Ψ is ill-conditioned. Again, from a physical viewpoint nothing extraordinary happens: both V_x and V_y vanish, but $\dot{V}_x$ and $\dot{V}_y$ behave properly, so that these quantities could be used instead of $\dot{V}$ and $\dot{\Psi}$.

Boomerang's rotational velocity vanishes.
If $\omega_z \to 0$, the equations of motion would be completely invalid. Our model is based on the assumption that ω_z is sufficiently large in comparison to ω_x and ω_y. As soon as $\omega_z \approx 0$ would occur in flight path calculations, the results would have no meaning at all. This is not actually a serious problem, however, as we do not intend to apply the theory to such cases. In reality ω_z is never small during a reasonable boomerang flight, or the boomerang would lose its boomerang-like qualities and flutter down.

§5 *The forces acting on a boomerang.*

We shall make the following assumptions concerning the boomerang, the medium (air) through which it moves, and gravity:

a) The boomerang is a rigid body. Its size is characterized by its "radius" a, which is the radius of the circle occupied by the boomerang when spinning about its principal axis. (For a more precise definition of a, see Part II, §20.) The boomerang's mass is m, its principal moments of inertia, in increasing order, are I_1, I_2, I_3. Its average density (= mass/volume) is ρ.

b) The medium is homogeneous, isotropic, constant in time, infinite in extent. Its density is μ, its kinematic viscosity is ν. Aerodynamic or mechanical effects due to the presence of objects such as ground and trees are not taken into account.

c) The constant acceleration due to gravity is $\vec{g}$, directed downward in negative Z-direction.

The forces acting in a boomerang are of two kinds: forces due to gravity and forces due to interaction with the air. We denote the gravitational forces by a subscript g and the aerodynamic forces by a subscript a. Thus we have:

$$\left.\begin{aligned} \vec{F} &= \vec{F}_g + \vec{F}_a \\ \vec{T} &= \vec{T}_a \end{aligned}\right\} \quad (5.1)$$

The components of $\vec{F}_g$ in the (X,Y,Z)-system are:

$$\vec{F}_g = -mg(\sin\vartheta \sin\psi,\ \sin\vartheta \cos\psi,\ \cos\vartheta) \qquad (5.2)$$

Hydrostatic forces can be taken into account by replacing g by:

$$g' = g(1 - \mu/\rho) \qquad (5.3)$$

If the boomerang is inhomogeneous the hydrostatic force may produce a torque which should be added to $\vec{T}_a$ in (5.1). We shall neglect the effects due to such a torque (although it would be quite easy to take these into account).

It is not quite so simple to obtain expressions for the aerodynamic

forces, which may depend on:

a) the properties of the air: e.g. density, viscosity, turbulence.

b) the shape of the boomerang.

c) the boomerang's state of motion: e.g. Ψ, $\vec{\omega}$, V.

d) previous history.

In accordance with the methods of dimensional analysis (see e.g. [Bridgman, 1931], [Birkhoff, 1950]) $\vec{F}_a$ (or rather its x-, y- and z-components) can be written in the form:

$$\vec{F}_a = \mu a^2 V^2 \vec{f}(\Psi, \frac{V}{\omega_z a}, \frac{\omega_x}{\omega_z}, \frac{\omega_y}{\omega_z}, \phi, \text{Re}, \textit{History}, \textit{Shape}) \qquad (5.4)$$

where all of the arguments of $\vec{f}$ are dimensionless. $\text{Re} = aV/\nu$ is a Reynolds number. *History* represents the influence of conditions occurring previously in the boomerang's flight. *Shape* denotes a set of dimensionless parameters defining the boomerang's shape (not size). The medium may be considered as incompressible, hence no Mach number M enters (for ordinary boomerangs $M \approx 0.1$). The factor V^2 in (5.4) could be replaced by $(\omega_z a)^2$, if desired. $\vec{T}_a$ can be written in a similar form with an additional factor a. It is *History* which raises most difficulties, since it may depend on the complete motion of the boomerang from its start, $t = 0$, up to the present instant, $t = t_p$

On the basis of several assumptions the unknown function $\vec{f}$ in (5.4) may be simplified. Since we shall work with *averaged* (smoothed) forces, an enormous simplification can be made by averaging over one period of ϕ, and replacing *History* by a fictitious *History* in which the quantities

$$\Psi, \frac{V}{\omega_z a}, \frac{\omega_x}{\omega_z}, \frac{\omega_y}{\omega_z}, \text{Re} \qquad (5.5)$$

are constant for all $t \leq t_p$. (The theoretical winglet model developed in Part II is of this kind. The boomerang-simulating winglet structures have an infinite number of identical arms, so that ϕ does not enter at all.) This is a quasi-steady approach. The situation at $t = t_p$, for the purpose of calculating aerodynamic forces, is supposed to have been constant for $-\infty < t \leq t_p$. The previous part of the boomerang's flight path is replaced by a straight line. This extremely simplified *History*

depends only on the present ($t = t_p$) situation, and ceases to be an independent set of variables in (5.4). We now obtain:

$$\vec{F}_a = \mu a^2 V^2 \vec{f}(\Psi, U, \frac{\omega_x}{\omega_z}, \frac{\omega_y}{\omega_z}, Re, \textit{Shape}) \tag{5.6}$$

where U, the advance ratio, is defined as:

$$U = \frac{V}{\omega_z a} \tag{5.7}$$

The dependence on Re is not quite negligible (see Part II, Ch. VI): our wind tunnel measurements indicated that there may be a slight influence. The forces computed by the winglet model are independent of Re. For the purpose of boomerang flight path calculations we shall assume that the influence of Re may be neglected. Hence we write:

$$\vec{F}_a = \mu a^2 V^2 \vec{f}(\Psi, U, \frac{\omega_x}{\omega_z}, \frac{\omega_y}{\omega_z}, \textit{Shape}) \tag{5.8}$$

If ω_x/ω_z and ω_y/ω_z are very small they will have no significant influence on $\vec{F}_a$ and $\vec{T}_a$, and these parameters may be omitted from (5.8). This assumption is not necessary, however, as is shown below. We point out that the wind tunnel measurements of Part II, Ch. VI only provide experimental data for $\omega_x = \omega_y = 0$. With this additional assumption the aerodynamic forces and torques can be written as:

$$\left.\begin{aligned} \vec{F}_a &= \mu V^2 a^2 \vec{F}_o(\Psi, 1/U) \\ \vec{T}_a &= \mu V^2 a^3 \vec{T}_o(\Psi, 1/U) \end{aligned}\right\} \tag{5.9}$$

or, alternatively, as:

$$\left.\begin{aligned} \vec{F}_a &= \mu \omega_z^2 a^4 \vec{F}_1(\Psi, U) \\ \vec{T}_a &= \mu \omega_z^2 a^5 \vec{T}_1(\Psi, U) \end{aligned}\right\} \tag{5.10}$$

where $\vec{F}_o$ and $\vec{T}_o$ or $\vec{F}_1$ and $\vec{T}_1$ also depend on the boomerang's shape. The dimensionless forces and torques $\vec{F}_o$ and $\vec{T}_o$ are used in Part II up to §23, whereas $\vec{F}_1$ and $\vec{T}_1$ are used in Part II from §23 on. During real boomerang flights the linear velocity V generally varies strongly,

whereas the relative variations in the rotational velocity ω_z generally amount to less than 20%. It seems therefore convenient to use (5.10) rather than (5.9): during a boomerang flight the dimensionless $\vec{F}_1$ and $\vec{T}_1$ behave roughly like $\vec{F}_a$ and $\vec{T}_a$ themselves.

Finally we reconsider the assumption of vanishing ω_x and ω_y. The restriction imposed by it can be removed. Instead of (5.10) we then have:

$$\left.\begin{aligned} \vec{F}_a &= \mu\omega_z^2 a^4\, \vec{F}_1(\Psi,\ U,\ \frac{\omega_x}{\omega_z},\ \frac{\omega_y}{\omega_z}) \\ \vec{T}_a &= \mu\omega_z^2 a^5\, \vec{T}_1(\Psi,\ U,\ \frac{\omega_x}{\omega_z},\ \frac{\omega_y}{\omega_z}) \end{aligned}\right\} \quad (5.11)$$

At first sight it appears that there are 4 independent dimensionless variables. However, *in boomerang flights* ω_x and ω_y are *not* independent of Ψ and U. According to (3.24):

$$\left.\begin{aligned} \frac{\omega_x}{\omega_z} &= -\frac{T_y}{I_3\omega_z^2} \\ \frac{\omega_y}{\omega_z} &= +\frac{T_x}{I_3\omega_z^2} \end{aligned}\right\} \quad (5.12)$$

which can be written as:

$$\left.\begin{aligned} \frac{\omega_x}{\omega_z} &= -k\ T_{1y} \\ \frac{\omega_y}{\omega_z} &= +k\ T_{1x} \\ k &= \frac{\mu a^5}{I_3} \end{aligned}\right\} \quad (5.13)$$

Here k is a dimensionless constant, of the order of $\frac{1}{2}$ for ordinary boomerangs in air. Thus at each point in (Ψ,U)-space ω_x/ω_z and ω_y/ω_z are given by (5.12), and, for a given boomerang, $\vec{F}_1$ and $\vec{T}_1$ are completely determined by Ψ and U only:

$$\left.\begin{aligned} \vec{F}_a &= \mu\omega_z^2 a^4\, \vec{F}_1^*(\Psi,U) \\ \vec{T}_a &= \mu\omega_z^2 a^5\, \vec{T}_1^*(\Psi,U) \end{aligned}\right\} \quad (5.14)$$

The asterisks indicate that (5.13) is taken into account. This can be easily done in the winglet model, as shown in Part II, §23.

Due to precession the torques T_x and T_y cause the parts of a boomerang to have a local velocity in z-direction: $v^* = y\omega_x - x\omega_y$. Hence:

$$\frac{v^*(x,y)}{\omega_z a} = -k \left(\frac{x}{a} T_{lx} + \frac{y}{a} T_{ly}\right) \tag{5.15}$$

Usually T_{lx} and T_{ly} are positive, so that the precession has the tendency to increase (resp. decrease) the angles of attack for the boomerang arms at positive (resp. negative) x and y. This leads to somewhat higher values of T_{lx} and somewhat lower values of T_{ly} as compared with the model including the assumption of vanishing ω_x and ω_y ($v^* = 0$).

§6 *The boomerang's angle of incidence* Ψ.

Consider the third equation of (4.8); it can be written as

$$\left.\begin{aligned} \dot{\Psi} &= -\frac{F_*}{mV} + \frac{T_x}{I_3\omega_z} \\ \text{with} \qquad F_* &= F_z \cos\Psi - F_x \sin\Psi \end{aligned}\right\} \quad (6.1)$$

T_x tends to increase Ψ by means of gyroscopic precession, whereas F_* tends to decrease Ψ by accelerating the boomerang in a direction perpendicular to its velocity. (F_* and T_x generally are positive.) The value of Ψ which results from these opposing effects is of profound influence on the shape and size of a boomerang's flight path. Since F_{az} and T_{ax} generally are increasing functions of Ψ, a greater Ψ results in a stronger curvature of the flight path. Moreover, since the drag also increases, the boomerang loses its speed more quickly. The spin, however, may increase (autorotation). During a reasonable boomerang flight Ψ does not deviate too far from zero ($0 \lesssim \Psi \lesssim 15^\circ$) for most of the trajectory, except toward the end of the flight, when a boomerang may occasionally hover. The angle of incidence Ψ is stationary ($\dot{\Psi} = 0$) if:

$$\frac{F_*}{mV} = \frac{T_x}{I_3\omega_z} \qquad (6.2)$$

The value Ψ_o of Ψ for which this equality holds (if it exists) depends on U, V, ϑ and ψ (remember that F_* contains both gravitational and aerodynamic components).

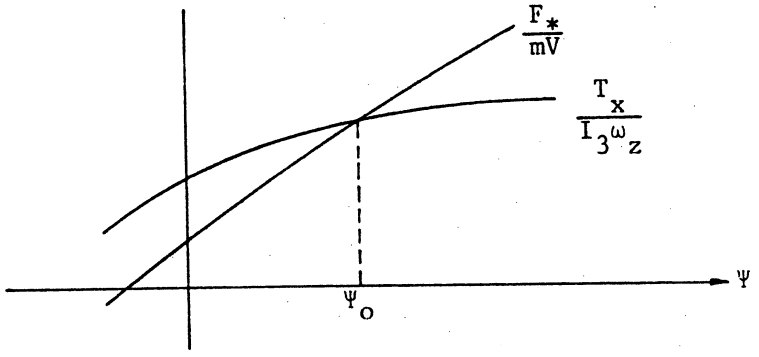

fig. 6.1. The stationary value of Ψ is Ψ_o.

If for $\Psi = \Psi_o$:

$$\frac{\partial}{\partial\Psi}\left(\frac{F_*}{mV}\right) > \frac{\partial}{\partial\Psi}\left(\frac{T_x}{I_3\omega_z}\right) \tag{6.3}$$

then Ψ_o is a stable value of Ψ. This is indicated in fig. 6.1. If the difference between the slopes of both lines is small, Ψ_o may be ill-conditioned, and slight deformations of the boomerang or slight variations in launching may give rise to substantial differences in the flight path. It is curious that models in which the induced velocity of the air is neglected may easily result in the impossibility of satisfying condition (6.3).

If Ψ is assumed to be small, (6.2) can be formulated somewhat differently. According to (5.2) and (6.1):

$$F_* = F_{az}\cos\Psi - F_{ax}\sin\Psi - mg\cos\vartheta\cos\Psi + mg\sin\vartheta\sin\psi\sin\Psi \tag{6.4}$$

For small Ψ, this can be approximated by:

$$F_* = F_{az} - mg\cos\vartheta \tag{6.5}$$

Hence we have

$$\left.\begin{aligned} F_* &= \mu\omega_z^2 a^4 F_{1z} - mg\cos\vartheta \\ T_x &= \mu\omega_z^2 a^5 T_{1x} \end{aligned}\right\} \tag{6.6}$$

We define the dimensionless λ by:

$$I_3 = \lambda m a^2 \tag{6.7}$$

Then (6.2) can be written as:

$$\frac{T_{1x}}{F_{1x} - \dfrac{mg\cos\vartheta}{\mu\omega_z^2 a^4}} = \frac{\lambda}{U} \tag{6.8}$$

For $\vartheta \approx \frac{1}{2}\pi$ (boomerang's plane vertical) this reduces to:

$$\frac{T_{1x}}{F_{1x}} = \frac{\lambda}{U} \tag{6.9}$$

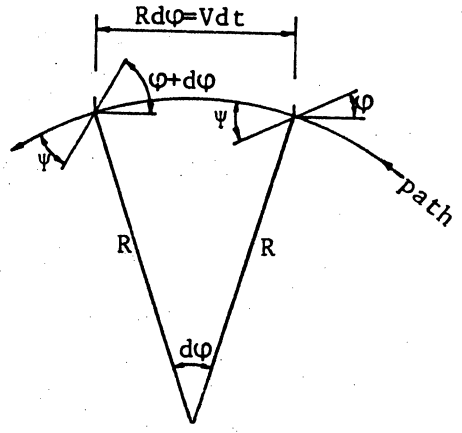

fig. 6.2. $\frac{d\varphi}{dt} = \frac{V}{R}$ for stationary ψ.

This last formula (6.9) can also be obtained in a more direct way as follows. We assume $\vartheta \approx \frac{1}{2}\pi$, $\psi \approx 0$ (boomerang's plane vertical, boomerang flies in a horizontal direction). Let the local radius of curvature of the trajectory be R. The centripetal force is provided by the "lift" $F_{aL} = F_{az} \cos\Psi - F_{ax} \sin\Psi$, hence

$$F_{aL} = \frac{mV^2}{R} \tag{6.10}$$

The precessional (angular) velocity $\dot{\varphi}$ is determined by:

$$\dot{\varphi} = \frac{T_{ax}}{I_3 \omega_z} \tag{6.11}$$

Here the boomerang is considered as a fast top. The component T_{ay} also contributes to the precession, but this results in a change of ϑ rather than φ. The angle of incidence Ψ is stationary if (see fig. 6.2):

$$\dot{\varphi} = \frac{V}{R} \tag{6.12}$$

(6.10), (6.11), (6.12) together yield:

$$\frac{T_{ax}}{F_{aL}} = \frac{I_3 \omega_z}{mV} \tag{6.13}$$

which, for $\Psi \approx 0$, is equivalent to (6.9). As to the radius of the flight path, R, we have, if $\Psi \approx 0$:

$$R = \frac{m}{\mu a^2} \cdot \frac{U^2}{F_{lz}} = \frac{\lambda m}{\mu a^2} \cdot \frac{U}{T_{lx}} \tag{6.14}$$

The very simple theoretical model for boomerang flights described by Hess [1968] can be obtained from (4.8), (4.9), (4.10) by putting:

1^{o} $\dot{\Psi} = 0$, $\Psi \approx 0$ (6.15)

and

2^{o} $T_{ax}(:)\omega_z V$, $T_{ay}(:)\omega_z V$, $T_{az} = 0$, $F_{ax}(:)\omega_z V$, $F_{ay} = 0$. (6.16)

The first assumption implies (see (6.2)):

$$\frac{F_z}{mV} = \frac{T_x}{I_3 \omega_z} \text{ at } \Psi \approx 0 \tag{6.17}$$

F_z is considered as a force of constraint, automatically satisfying (6.17). This could be justified by the assumption that F_{az} increases very much faster with Ψ than T_{ax} does. However, both the winglet model and the experiments described in Part II indicate that there is not such a fundamental difference in the behaviour of these components as functions of Ψ. A striking outcome of the simple model based on (6.15) and (6.16) is that, as far as only aerodynamic forces are considered, the size of a flight path is roughly independent of the initial values of *both* ω and V [Hess, 1968].

§7 *Similitude of boomerang flight paths.*

In this section the conditions are discussed under which boomerang flight paths are similar in shape, though possibly different in size. Dimensional analysis (see e.g. [Bridgman, 1931], [Birkhoff, 1950]) is the basis for this investigation.

We make the same assumptions here as in the beginning of §5 concerning the boomerang, the medium and gravity. It is obvious that the shape of flight paths is invariant under shifts in space (X,Y,Z) and time (t), rotations about the vertical z-axis (φ), and reflections with respect to vertical planes ($X \to -X$ or $Y \to -Y$). Remember that the presence of ground is ignored here.

We shall characterize the size of a flight path by R, which for an approximately circular path might be identified with the path radius. R is a function of (a) the initial conditions at the instant of launching ($t = t_o$):

$$t_o, X_o, Y_o, Z_o, \vartheta_o, \varphi_o, \psi_o, \phi_o, \Psi_o, V_o, \omega_{xo}, \omega_{yo}, \omega_{zo},$$

(b) the properties of the boomerang:

$$\rho, \lambda_{1,2,3}, \textit{Shape}$$

where the dimensionless $\lambda_j = I_j/ma^2$, $j = 1,2,3$ characterize the boomerang's massdistribution, (c) the properties of the air and of gravity:

$$\mu, \nu, g.$$

As mentioned above, t_o, X_o, Y_o, Z_o, φ_o do not influence R. Hence R can be expressed in the form:

$$R = a \cdot f(\Psi_o, U_o, \frac{\omega_{xo}}{\omega_{zo}}, \frac{\omega_{yo}}{\omega_{zo}}, \phi_o, \vartheta_o, \psi_o, Re_o, \frac{V_o^2}{ag}, \frac{\mu}{\rho}, \lambda_{1,2,3}, \textit{Shape}) \qquad (7.1)$$

Most of the symbols were also used in §5. V_o^2/ag can be considered as a Froude number. We shall assume that the influence of the Reynolds number Re_o may be neglected (see §5).

With the foregoing assumptions, (7.1) shows that flight paths are similar provided that:

1. $\Psi_o, U_o, \left(\frac{\omega_x}{\omega_z}\right)_o, \left(\frac{\omega_y}{\omega_z}\right)_o, \phi_o, \vartheta_o, \psi_o$ constant (7.2)

which we call the condition of similar launching;

2. $\lambda_{1,2,3}$, *Shape* constant (7.3)

which we call the condition of similar boomerangs;

3. $\frac{\mu}{\rho}, \frac{V_o^2}{ag}$ constant (7.4)

If these conditions are satisfied, then the flight path size is proportional to the boomerang size:

$$R(:)a \tag{7.5}$$

This is a fairly general result, also valid for rigid objects other than boomerangs. Perhaps the only unrealistic assumption concerns the negligible influence of Re. For constant g and μ it means that two similar boomerangs of equal density ρ, similarly launched, traverse similar flight paths with dimensions (R) propertional to the boomerangs' sizes (a), provided the initial velocities V_o are taken proportional to $\sqrt{a}$. (The Reynolds numbers, at constant ν, then are proportional to $a^{3/2}$.)

In the less general case of the model developed in §3, §4, §5, stronger results can be derived. The equations of motion (4.8), (4.9), (4.10) can be written in a dimensionless form as follows. Let us introduce the dimensionless quantities:

$$\left.\begin{aligned} G = \frac{\rho a g}{\mu V_o^2}\ ,\ \sigma = \frac{m}{\rho a^3}\ ,\ \lambda = \frac{I_3}{m a^2}\ , \\ \tau = \frac{\mu V_o t}{\rho a},\ \tilde{V} = \frac{V}{V_o}\ ,\ U = \frac{V}{\omega_z a}\ , \\ \tilde{X} = \frac{\mu X}{\rho a}\ ,\ \tilde{Y} = \frac{\mu Y}{\rho a}\ ,\ \tilde{Z} = \frac{\mu Z}{\rho a}\ . \end{aligned}\right\} \tag{7.6}$$

The first three of these are constants, the other six are variables.

V_o can be taken as the boomerang's initial velocity. The equations of motion can now be brought in the form:

$$
\begin{aligned}
\frac{d\,\frac{\tilde{V}}{U}}{d\tau} &= \frac{1}{\lambda\sigma}\,\tilde{V}\,T_{oz} \\
\frac{d\tilde{V}}{d\tau} &= \frac{1}{\sigma}\,\tilde{V}(-F_{ox}\cos\Psi - F_{oz}\sin\Psi) + G(\sin\vartheta\sin\psi\cos\Psi + \cos\vartheta\sin\Psi) \\
\frac{d\Psi}{d\tau} &= \frac{1}{\sigma}\,\tilde{V}^2(F_{ox}\sin\Psi - F_{oz}\cos\Psi) + \frac{1}{\lambda\sigma}\,U\tilde{V}\,T_{ox} + \\
&\quad + G\,\frac{1}{\tilde{V}}\,(-\sin\vartheta\sin\psi\sin\Psi + \cos\vartheta\cos\Psi) \\
\frac{d\vartheta}{d\tau} &= \frac{1}{\lambda\sigma}\,U\tilde{V}(-T_{oy}\cos\psi - T_{ox}\sin\psi) \\
\frac{d\varphi}{d\tau} &= \frac{1}{\lambda\sigma}\,U\tilde{V}\,\frac{1}{\sin\vartheta}\,(-T_{oy}\sin\psi + T_{ox}\cos\psi) \\
\frac{d\psi}{d\tau} &= -\frac{1}{\sigma}\,\frac{\tilde{V}}{\cos\psi}\,F_{oy} - \frac{1}{\lambda\sigma}\,U\tilde{V}\,\mathrm{tg}\Psi\,T_{oy} + G\,\frac{\sin\vartheta\cos\psi}{\cos\Psi} - \cos\vartheta\,\frac{d\varphi}{d\tau} \\
\frac{d\tilde{X}}{d\tau} &= \tilde{V}[-\cos\Psi(\cos\psi\cos\varphi - \sin\psi\sin\varphi\cos\vartheta) - \sin\Psi\sin\varphi\sin\vartheta] \\
\frac{d\tilde{Y}}{d\tau} &= \tilde{V}[-\cos\Psi(\cos\psi\sin\varphi + \sin\psi\cos\varphi\cos\vartheta) + \sin\Psi\cos\varphi\sin\vartheta] \\
\frac{d\tilde{Z}}{d\tau} &= \tilde{V}[-\cos\Psi\sin\psi\sin\vartheta - \sin\Psi\cos\vartheta]
\end{aligned}
\qquad (7.7)
$$

The dimensionless forces and torques F_{ox}, F_{oy}, F_{oz}, T_{ox}, T_{oy}, T_{oz} are functions of Ψ, U and *Shape* only. The equations of motion (7.7) yield instead of (7.1):

$$R = \frac{\rho a}{\mu}\cdot f(\Psi_o, U_o, \vartheta_o, \psi_o, \frac{\mu V_o^2}{\rho a g}, \lambda, \mathit{Shape}) \qquad (7.8)$$

where *Shape* includes the parameter σ. The condition μ/ρ = constant is absent here. Flight path size and boomerang size are now uncoupled. Obviously this can be realistic only if $a \ll R$, which amounts to $\mu \ll \rho$. (For wooden boomerangs in air: $\mu/\rho \approx 0.002$, $a/R \approx 0.02$.) For our boomerang model (7.8) shows that flight paths are similar provided that:

1. $$\Psi_o, U_o, \vartheta_o, \psi_o \quad \text{constant} \qquad (7.9)$$

which is the condition of similar launching;

2. λ, *Shape* constant (7.10)

which is the condition of similar boomerangs;

3. $$\frac{\mu V_o^2}{\rho a g} \quad \text{constant} \tag{7.11}$$

If these conditions are satisfied, then

$$R(:) \frac{\rho a}{\mu} \tag{7.12}$$

This means that for a change a change in flight path size R by a factor f, both $\rho a/\mu$ and V_o^2/g must be changed by the same factor f. Such a change may be effected in various ways. The conditions (7.9) and (7.10) must be satisfied in all cases, and we shall assume this throughout the rest of this section.

Let us first suppose that μ and g are kept constant. Then V_o should be changed by a factor $\sqrt{f}$ and ρa by a factor f. Table 7.1 shows several possibilities. For each of the 5 rows a certain quantity is kept constant. The columns indicate by what factors the quantities listed above should be changed in order to obtain a change of a factor f in the flight path dimensions. The symbols used are: R for flight path radius or size, T for duration of flight, V for linear velocity, ω_z for rotational velocity, a for boomerang radius or size, ρ for boomerang's density, n for total number of revolutions during a flight, m for boomerang's mass, E for kinetic (or total) energy, Re for Reynolds number.

The fifth row of table 7.1 corresponds to the similarity condition R/a = constant, and the second row corresponds to the condition Re = constant. It is impossible to satisfy both conditions simultaneously, except for identical boomerangs. Let us consider the third row as an example. Two similar boomerangs having the same size (a), but differing in density (ρ), and hence m, by a factor f can be made to traverse similar flight paths, differing in size by the same factor f, if they are launched similarly, but at velocities differing by a factor $\sqrt{f}$. (The change in Re by a factor $\sqrt{f}$ is assumed to have no influence, and the ratio R:a (changed by a factor f) is supposed to be very large in both cases.)

kept constant \ changed:	R	V T	ω_z	a	ρ, n R/a	m	E	Re
1) E	f^1	$f^{\frac{1}{2}}$	$f^{1\frac{1}{2}}$	f^{-1}	f^2	f^{-1}	1	$f^{-\frac{1}{2}}$
2) m, Re	f^1	$f^{\frac{1}{2}}$	f^1	$f^{-\frac{1}{2}}$	$f^{1\frac{1}{2}}$	1	f^1	1
3) a	f^1	$f^{\frac{1}{2}}$	$f^{\frac{1}{2}}$	1	f^1	f^1	f^2	$f^{\frac{1}{2}}$
4) ω_z	f^1	$f^{\frac{1}{2}}$	1	$f^{\frac{1}{2}}$	$f^{\frac{1}{2}}$	f^2	f^3	f^1
5) ρ, n, R/a	f^1	$f^{\frac{1}{2}}$	$f^{-\frac{1}{2}}$	f^1	1	f^3	f^4	$f^{1\frac{1}{2}}$

table 7.1. Changes in several quantities required for a change in flight path size by a factor f. Conditions (7.9) and (7.10) must be satisfied, and μ and g are constant. Five possibilities are listed.

Let us now consider some examples of the influence of changes in gravity g or air density μ. If g is lowered and μ remains unchanged, then a proportional decrease in V_o^2 allows the same flight path to be traversed, but at a slower space. If μ is lowered by a factor f (for instance by throwing boomerangs on mountain tops), the same boomerang traverses a aimilar flight path which is a factor f larger, if the initial velocity is increased by a factor $\sqrt{f}$.

The above results, represented by (7.8) through (7.12), can also be obtained in a more intuitive way. For similar flight paths the ratios between aerodynamic, gravitational and inertial forces should be constant. For similar boomerangs (7.10), similarly launched (7.9), these three kinds of forces are characterized by:

$$\left.\begin{array}{ll} \mu a^2 V_o^2 & \text{(aerodynamic)} \\ \rho a^3 g & \text{(gravitational)} \\ \dfrac{\rho a^3 V_o^2}{R} & \text{(inertial)} \end{array}\right\} \quad (7.13)$$

Hence follow the conditions:

$$\left.\begin{array}{lll} \dfrac{\mu V_o^2}{\rho a g} & \text{constant} & \text{(aero:grav)} \\ \dfrac{\mu R}{\rho a} & \text{constant} & \text{(aero:iner)} \\ \dfrac{Rg}{V_o^2} & \text{constant} & \text{(grav:iner)} \end{array}\right\} \quad (7.14)$$

(These conditions are not independent, and one of them may be omitted.) The first condition is (7.11), the other two can be written as:

$$R(:)\ \frac{\rho a}{\mu} \quad \text{and} \quad R(:)\ \frac{V_o^2}{g} \qquad (7.15)$$

We might consider $\rho a/\mu$ as a measure for "aerodynamic path size" and V_o^2/g as a measure for "gravitational path size". For the peculiar character of the behaviour of boomerangs gravity, though of importance, is not essential. If gravitational effects are left out of consideration, condition (7.11) is not relevant, and for a particular boomerang the flight path size is independent of V_o. This is a rough indication that the same boomerang cannot be made to traverse flight paths of widely different sizes by launching it faster or slower. Flight path size (in air) is to a certain extent a property of the boomerang.

Finally a remark about the *handedness* of boomerangs. Throughout the greater part of this work it is implicitly assumed that a boomerang is right-handed, i.e. that it normally flies with a right-handed spin. Its sense of rotation then corresponds to that of a right-handed screw the main axis of which proceeds in the z-direction from the less convex to the more convex side (or: from the pressure to the suction side) of the boomerang. It is obvious that if everything (including the direction of the wind, if any) is reflected with respect to a vertical plane, the result is a boomerang with a left-handed spin traversing the mirror image of the original flight path. If the original boomerang is thrown with the right hand, the left-handed boomerang which is its mirror image is preferably thrown with the left hand. Of course such a left-handed boomerang can be correctly described as a "right-handed" boomerang having arms with upside-down profiles (α_o negative), flying at negative Ψ,

or, alternatively, as a boomerang having arms with front-to-back profiles, flying at negative ω_z. But it seems more simple and less confusing to describe instead of such a boomerang its right-handed mirror image, which behaves in the normal way. The boomerangs used in the field experiments described in Chapter II are of the left-handed variety and were thrown with the left hand. The recorded flight paths (see Chapter III) are reversed (mirrored) so as to obtain "normal" right-handed pictures.

§8 *The influence of wind.*

If the influence of wind on the motion of boomerangs is to be taken into account, this can be done in a rather simple way by modifying the equations (4.8), (4.9) as follows. Suppose that the prevailing wind can be described by the vector field $\vec{W}(X,Y,Z,t)$ with given components W_X, W_Y, W_Z. The components of this velocity with respect to the $(x,y,z,)$-system, W_x, W_y, W_z, are obtained by the transformation (4.1). The velocity of the boomerang with respect to the air is now:

$$\vec{V} - \vec{W} = (V_x - W_x, -W_y, V_z - W_z) = (-V\cos\Psi - W_x, -W_y, -V\sin\Psi - W_z) \qquad (8.1)$$

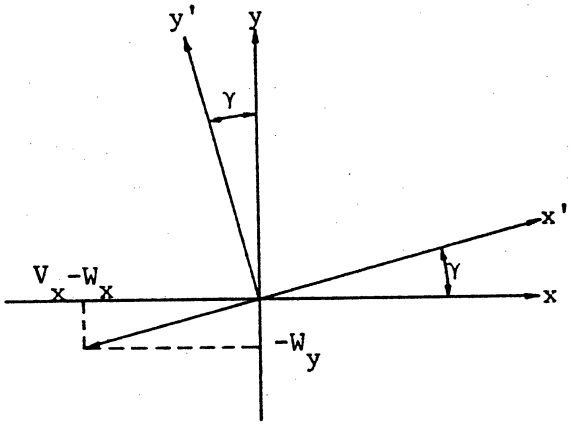

fig. 8.1. The coordinate systems (x,y,z) and (x',y',z').

Since we work with smoothed equations of motion (see §3), it is necessary to assume that $\vec{V} - \vec{W}$ varies relatively little during a spin period. Hence sudden fluctuations (time scale $\lesssim$ .1 sec.) in the wind velocity are ruled out. Moreover, since the boomerang should be surrounded by a homogeneous flow, $\vec{V} - \vec{W}$ should not vary much over distances comparable to the boomerang's size.

We introduce a new coordinate system (x',y',z'), such that the boomerang's velocity relative to the air has a vanishing component in y'-direction. The z'-axis is identified with the z-axis and we demand:

$$\left.\begin{aligned} V_{y'} - W_{y'} &= 0 \\ V_{x'} - W_{x'} &< 0 \end{aligned}\right\} \quad (8.2)$$

which corresponds to (3.1). Let the angle between the x- and x'-axes be γ, then

$$\gamma = \operatorname{arctg} \frac{W_y}{V \cos\Psi + W_x} \quad (8.3)$$

The transformation from (x,y,z)-components to (x',y',z')-components and vice versa proceeds according to the scheme:

	x	y	z
x'	$+\cos\gamma$	$+\sin\gamma$	0
y'	$-\sin\gamma$	$+\cos\gamma$	0
z'	0	0	1

(8.4)

where γ is given by (8.3). The boomerang's velocity relative to the air can be written as:

$$\vec{V} - \vec{W} = (-\sqrt{(V\cos\Psi + W_x)^2 + W_x^2}, 0, -V\sin\Psi - W_x) \quad (8.5)$$

where the components are given in the (x',y',z')-system. In the equations of motion (4.8) and (4.9), as far as the aerodynamic forces and torques are concerned, V, U, Ψ have to be replaced by the corresponding values relative to the moving air:

$$\left.\begin{aligned} V' &= \sqrt{(V\cos\Psi + W_x)^2 + W_y^2 + (V\sin\Psi + W_z)^2} = \\ &= \sqrt{V^2 + W^2 + 2V(W_z\sin\Psi + W_x\cos\Psi)} \\ U' &= \frac{V'}{\omega_z a} \\ \Psi' &= \operatorname{arctg} \frac{W_y + V\sin\Psi}{\sqrt{(V\cos\Psi + W_x)^2 + W_y^2}} \end{aligned}\right\} \quad (8.6)$$

Instead of the (x,y,z)-components of $\vec{F}_a(\Psi,U,V)$ and $\vec{T}_a(\Psi,U,V)$, the (x',y',z')- components of $\vec{F}_a(\Psi',U',V')$ and $\vec{T}_a(\Psi',U',V')$ have to be used. The components of these aerodynamic forces and torques have to be transformed back according to:

$$\left.\begin{aligned} F_{ax} &= F_{ax'}(\Psi',U',V')\cos\gamma - F_{ay'}(\Psi',U',V')\sin\gamma \\ F_{ay} &= F_{ax'}(\Psi',U',V')\sin\gamma + F_{ay'}(\Psi',U',V')\cos\gamma \\ F_{az} &= F_{az'}(\Psi',U',V') \end{aligned}\right\} \quad (8.7)$$

and corresponding equations for $\vec{T}_a$.

For simulation of realistic wind conditions it is probably sufficient to take a constant windspeed W, which is a function of height (Z) only. The direction of the wind is horizontal, deviating from the X-direction by a constant angle β. Thus one can take

$$\vec{W} = W(Z) \cdot (\cos\beta,\ \sin\beta,\ o) \quad (8.8)$$

where the components are given in the (X,Y,Z)-system. In our actual calculations we use (8.8) with

$$W(Z) = W_o + W_1 \cdot Z \quad (8.9)$$

Here W_o is the wind velocity at the level $Z = 0$, and W_1 is the wind velocity gradient.

§9 *The calculation of flight paths.*

The numerical calculation of boomerang flight paths is based on the - smoothed - equations of motion (4.8), (4.9), (4.10). If the influence of wind is to be taken into account, these equations are modified as outlined in §8.

The - smoothed - forces and torques acting on a boomerang are described by (5.1), (5.2) and (5.10) or (5.14), where the dimensionless aerodynamic components F_{lx}, F_{ly}, F_{lz}, T_{lx}, T_{ly}, T_{lz} must be provided either by the winglet model developed in Part II, or by the experimental measurements described in Part II, Chapter VI. In either case these components as functions of Ψ and U are given in the form of tables containing the values at the points (Ψ_i, U_j) in (Ψ,U)-space. We take $i = 1...9$, $j = 1...7$, and Ψ_i and U_j are chosen as follows (see also Part II, §31):

i	1	2	3	4	5	6	7	8	9
Ψ_i	-5°	0°	5°	10°	15°	20°	30°	45°	90°

j	1	2	5	4	5	6	7
U_j	0	.25	.50	.75	1.0	1.5	2.0

(9.1)

Such tables are listed at the end of Part II, §31 for five experimental boomerangs. If, in the course of the flight path computations, the six force components must be evaluated at a certain point in (Ψ,U)-space, their respective values are obtained by a smooth two-dimensional interpolation by means of doubly cubic splines (see Part II, §25).

The simultaneous numerical integration of the equations of motion is carried out by a Runge-Kutta method. For given tolerance requirements the algorithm determines the length of the integration steps, which may vary in the course of the integration process. One step involves the computation of the right-hand sides of (4.8), (4.9), (4.10) at 7 points in time. In our actual calculations the boomerang's state of motion, orientation and position are computed at 0.1 seconds intervals. If an accuracy of about 1 cm is desired in the boomerang's position throughout its flight, the minimum number of 7 evaluations per integration

interval of 0.1 sec. suffices during the greater part of most theoretical flight paths.Finer integration steps occur when V or ϑ is small or Ψ is large. This is closely connected with the singularities discussed in §4. It is clear that a very fine subdivision in integration steps may be needed if one or more of the singularities (4.11) is closely approached. This trouble will occur very seldom, except for the special case in which a boomerang is launched exactly at $\vartheta = 0$ (i.e. with its plane horizontal). If this occurs we modify (4.9) and simply put:

$$\dot{\varphi} = 0, \ \dot{\psi} = \Omega_z \text{ if } \sin\vartheta < .001 \tag{9.2}$$

This crude procedure has the disadvantage of giving rise to discontinuities in $\dot{\varphi}$ and $\dot{\psi}$ between points which differ in the sign of $\sin\vartheta - .001$. No special precautions are taken against the other singularities of (4.11). On the other hand, in the sporadic cases where $\Psi < -30^\circ$ occurs the computation is terminated, since we did not provide aerodynamic data for such low values of Ψ, and since in real flights this situation is often accompanied by instability.

The computer program operates on two sets of data:
A: The data characterizing the boomerang. The aerodynamic properties are determined by the tables mentioned above, in which the dimensionless forces are listed at the points (9.1) in (Ψ,U)-space. The boomerang's mechanical properties are determined by the radius a, the mass m and the moment of inertia I_3.
B: The data characterizing the launching, i.e. the initial conditions. Initial values are given for: $f = \omega_z/2\pi$, V, Ψ, ϑ, φ, ψ, X, Y, Z.
C: The gravitational acceleration g and the air density μ must be given. We take:

$$\left.\begin{aligned} g &= 9.80 \text{ m/s}^2 \\ \mu &= 1.20 \text{ kg/m}^3 \end{aligned}\right\} \tag{9.3}$$

If there is wind additional parameters must be provided. According to (8.8) and (8.9) we must give values for: β, the angle between wind direction and X-axis, W_o, the wind speed at level $Z = 0$, and W_1, the wind velocity gradient.

The boomerang's state of motion, orientation and position are computed at intervals of 0.1 sec. until the boomerang has descended below ground level, Z = 0. Values for the number of revolutions completed: n, and the pathlength traversed: P are computed from the additional equations:

$$\left.\begin{aligned} \dot{n} &= \omega_z/2\pi \\ \dot{P} &= V \end{aligned}\right\} \quad (9.4)$$

The computing program was written in Algol and run on a Telefunken TR4 computer and on a CDC Cyber 74-16 computer.

An example of a theoretical boomerang flight is shown in table 9.1 and figure 9.1. The boomerang considered is called 195.1. The number 195 characterizes a certain table of dimensionless aerodynamic components computed by the winglet model on the basis of the characteristics listed in table 32.1 of Part II. The influence of ω_x and ω_y is neglected according to assumption c of §5. The .1 after 195 serves to distinguish this particular boomerang from others with the same aerodynamic table but with different a, m and I_3. The 195.1 has:

$$\left.\begin{aligned} a &= .298 \text{ m.} \\ m &= .173 \text{ kg.} \\ I_3 &= .00396 \text{ kgm}^2. \end{aligned}\right\} \quad (9.5)$$

This boomerang simulates the experimental boomerang L1 (see §10). A different choice for a, m, I_3 would lead to boomerang 195.2 or 195.3 etc.

The initial conditions for the example flight are chosen as:

$$\left.\begin{aligned} f = \omega_z/2\pi &= 10 \text{ rev/sec.} \\ V &= 25 \text{ m/s.} \\ \Psi &= 0^\circ \\ \vartheta &= 90^\circ \\ \varphi &= 0^\circ \\ \psi &= -20^\circ \\ X &= 0 \text{ m.} \\ Y &= 0 \text{ m.} \\ Z &= 1.8 \text{ m.} \end{aligned}\right\} \quad (9.6)$$

There is no wind.

The 15 columns of table 9.1 list values for respectively:

$$I,t,P,n,f,V,U,\Psi,\vartheta,\varphi,\psi,X,Y,Z,D.$$

Only the first and the last of these have not been explained. I is the number of times the right-hand sides of (4.8), (4.9), (4.10) and (9.4) were evaluated in the course of the last 0.1 sec. interval. $D = \sqrt{(X-X_o)^2 + (Y-Y_o)^2}$ is the horizontal distance from the starting point in metres.

Figure 9.1 shows three orthogonal projections of the computed flight path. The boomerang is represented by a circular disk with radius a. Its position is plotted at 0.1 sec. intervals, and its orientation can be inferred from the shape and orientation of the elliptical projections. In the (X,Y)-projection (bird's-eye view) the X-direction is leftward, the Y-direction downward. The big square surrounding this projection has sides of 30 m. In the (X,Z)-projection (upper part of fig. 9.1) the X-direction is leftward, the Z-direction upward, and in the (Y,Z)-projection (at right) the Y-direction is downward, the Z-direction rightward. The outer lines at the top and at the right of the figure correspond to a height Z = 10 m.

Finally an observation of theoretical significance. At first glance, it might seem that the equations of motion could just as well be integrated backward as forward in time. One could, for instance, take the conditions at the instant of the boomerang's touching the ground as "initial conditions" and, by integrating backwards in time, reduplicate the boomerang's original flight path. However, when such a backward numerical integration is actually performed, the boomerang's motion turns out to be unstable: it diverges more and more from the original "forward" motion. In one case, in which we took the boomerang's angle of incidence Ψ as an indicator, the difference between "forward" and "backward" values of Ψ increased exponentially, doubling every 0.27 seconds. On physical grounds the "backward" instability of a boomerang's motion is plausible: in the normal "forward" motion a boomerang continually loses energy, hence in the "backward" motion its energy increases.

I	t	P	n	f	V	U	W	θ	φ	ψ	X	Y	Z	D
7	0.0	0.0	0.0	10.0	25.0	1.34	0.0	90.0	0.0	-20.0	0.00	0.00	1.80	0.00
7	0.1	2.5	1.0	9.8	24.4	1.33	1.9	89.5	7.7	-17.9	-2.33	-0.11	2.60	2.34
7	0.2	4.9	2.0	9.6	23.8	1.32	3.5	88.6	16.6	-16.0	-4.61	-0.46	3.30	4.63
14	0.3	7.2	2.9	9.5	23.2	1.30	5.0	87.3	26.4	-14.3	-6.79	-1.10	3.91	6.87
7	0.4	9.5	3.9	9.5	22.5	1.27	6.2	85.8	36.9	-12.9	-8.80	-2.04	4.43	9.04
7	0.5	11.7	4.8	9.4	21.9	1.24	7.3	84.2	47.9	-11.8	-10.59	-3.27	4.87	11.09
14	0.6	13.9	5.7	9.4	21.1	1.20	8.3	82.4	59.2	-11.0	-12.11	-4.74	5.25	13.00
7	0.7	15.0	6.7	9.4	20.4	1.16	9.2	80.6	70.9	-10.6	-13.29	-6.41	5.58	14.70
7	0.8	18.0	7.6	9.4	19.6	1.12	10.1	79.0	82.7	-10.5	-14.12	-8.21	5.86	16.33
7	0.9	19.9	8.6	9.4	18.8	1.07	11.0	77.4	94.6	-10.7	-14.58	-10.05	6.15	17.71
7	1.0	21.7	9.5	9.4	18.0	1.02	11.7	76.1	106.4	-11.1	-14.68	-11.87	6.40	18.88
7	1.1	23.5	10.4	9.5	17.2	0.97	12.2	75.0	113.0	-11.5	-14.45	-13.60	6.63	19.84
7	1.2	25.2	11.4	9.5	16.4	0.92	12.4	74.0	129.1	-11.8	-13.92	-15.17	6.86	20.59
7	1.3	25.8	12.4	9.6	15.6	0.87	12.4	73.2	139.6	-12.0	-13.16	-16.56	7.07	21.15
7	1.4	23.3	13.3	9.6	14.9	0.82	12.3	72.3	149.3	-11.8	-12.21	-17.73	7.27	21.52
7	1.5	29.7	14.3	9.7	14.2	0.79	11.4	71.5	158.2	-11.4	-11.12	-18.68	7.45	21.74
7	1.6	31.1	15.3	9.7	13.7	0.75	10.7	70.5	166.2	-10.6	-9.94	-19.41	7.61	21.81
7	1.7	32.5	16.2	9.7	13.2	0.72	9.8	69.5	173.5	-9.4	-8.72	-19.93	7.74	21.76
7	1.8	33.8	17.2	9.7	12.8	0.70	9.0	68.4	180.2	-8.0	-7.47	-20.27	7.85	21.60
7	1.9	35.0	18.2	9.7	12.4	0.68	8.3	67.2	186.2	-6.4	-6.22	-20.43	7.92	21.36
7	2.0	36.3	19.1	9.7	12.1	0.67	7.7	65.9	191.9	-4.6	-5.01	-20.44	7.96	21.04
7	2.1	37.5	20.1	9.6	11.9	0.66	7.2	64.5	197.1	-2.7	-3.81	-20.31	7.96	20.67
7	2.2	38.6	21.1	9.6	11.7	0.65	6.9	62.9	202.2	-0.7	-2.66	-20.06	7.93	20.23
7	2.3	39.8	22.0	9.5	11.5	0.65	6.8	61.3	207.0	1.2	-1.56	-19.68	7.86	19.75
7	2.4	41.0	23.0	9.5	11.4	0.64	6.7	59.6	211.8	3.0	-0.52	-19.21	7.76	19.22
7	2.5	42.1	23.9	9.4	11.3	0.64	6.8	57.8	216.6	4.6	0.45	-18.64	7.63	18.64
7	2.6	43.2	24.9	9.4	11.3	0.64	7.0	55.9	221.4	6.0	1.36	-17.98	7.46	18.03
7	2.7	44.3	25.8	9.4	11.2	0.64	7.3	53.8	226.4	7.1	2.19	-17.24	7.28	17.38
7	2.8	45.5	26.7	9.3	11.2	0.64	7.7	51.7	231.5	7.8	2.93	-16.43	7.07	16.69
7	2.9	45.6	27.7	9.3	11.2	0.64	8.2	49.5	236.8	8.2	3.59	-15.55	6.80	15.96
7	3.0	47.7	28.6	9.3	11.1	0.64	8.7	47.2	242.5	8.3	4.16	-14.62	6.63	15.20
7	3.1	48.6	29.5	9.3	11.1	0.64	9.2	45.0	248.5	7.3	4.63	-13.64	6.41	14.41
7	3.2	49.9	30.4	9.3	11.0	0.63	9.9	42.8	255.0	6.0	5.00	-12.63	6.19	13.58
7	3.3	51.0	31.4	9.3	10.9	0.63	10.3	40.7	261.9	4.0	5.27	-11.59	5.98	12.73
7	3.4	52.1	32.3	9.3	10.7	0.62	10.9	38.8	269.4	1.5	5.44	-11.53	5.80	11.86
7	3.5	53.2	33.2	9.3	10.6	0.61	11.5	37.2	277.3	-1.7	5.51	-9.48	5.63	10.97
7	3.6	54.2	34.2	9.3	10.4	0.60	12.1	35.8	285.5	-5.4	5.48	-8.44	5.50	10.07
7	3.7	55.2	35.1	9.3	10.1	0.58	12.5	34.8	294.0	-9.3	5.36	-7.43	5.40	9.17
7	3.8	55.2	36.0	9.3	9.8	0.56	12.9	34.2	302.5	-13.4	5.16	-6.46	5.32	8.27
7	3.9	57.2	36.9	9.3	9.5	0.54	13.3	33.9	311.9	-17.4	4.88	-5.53	5.26	7.38
7	4.0	58.1	37.9	9.3	9.2	0.52	13.6	33.9	316.9	-21.1	4.54	-4.67	5.27	6.51
14	4.1	59.0	38.8	9.4	8.8	0.50	13.8	34.1	326.3	-24.2	4.14	-3.86	5.28	5.66
7	4.2	59.9	39.7	9.4	8.4	0.48	14.0	34.4	333.3	-26.8	3.70	-3.12	5.31	4.84
7	4.3	60.7	40.7	9.4	8.0	0.46	14.2	34.8	339.6	-28.7	3.22	-2.46	5.36	4.05
7	4.4	61.5	41.6	9.4	7.6	0.43	14.4	35.2	345.4	-30.0	2.72	-1.88	5.41	3.29
7	4.5	62.2	42.6	9.4	7.2	0.41	14.7	35.6	350.7	-30.6	2.19	-1.34	5.47	2.57
7	4.6	62.9	43.6	9.4	6.8	0.39	15.0	35.9	355.5	-30.5	1.66	-0.89	5.53	1.88
7	4.7	63.6	44.5	9.4	6.5	0.37	15.3	36.1	359.9	-29.8	1.12	-0.50	5.58	1.23
7	4.8	64.2	45.4	9.4	6.1	0.35	15.7	36.2	363.9	-28.5	0.58	-0.18	5.62	0.61
7	4.9	64.8	46.3	9.4	5.8	0.33	16.3	36.2	367.6	-26.5	0.05	0.07	5.64	0.09
7	5.0	65.4	47.3	9.4	5.5	0.31	16.9	36.0	371.1	-23.9	-0.48	0.27	5.65	0.59
7	5.1	65.9	48.2	9.4	5.2	0.29	17.5	35.7	374.2	-20.7	-0.99	0.41	5.63	1.07
7	5.2	66.4	49.2	9.4	5.0	0.28	18.2	35.3	377.2	-16.9	-1.49	0.51	5.60	1.57
7	5.3	66.9	50.1	9.4	4.8	0.27	18.9	34.7	380.0	-12.6	-1.97	0.53	5.54	2.04
7	5.4	67.4	51.0	9.4	4.6	0.26	19.5	34.0	382.6	-7.9	-2.43	0.51	5.46	2.46
7	5.5	67.8	52.0	9.3	4.5	0.26	20.0	33.3	385.0	-2.9	-2.87	0.45	5.35	2.90
7	5.6	68.3	52.9	9.3	4.5	0.26	20.4	32.4	387.4	2.1	-3.29	0.34	5.22	3.30
7	5.7	68.7	53.8	9.3	4.5	0.26	20.6	31.4	389.6	7.1	-3.68	0.19	5.07	3.68
7	5.8	69.2	54.8	9.3	4.5	0.26	20.7	30.3	391.7	11.8	-4.05	-0.00	4.90	4.05
7	5.9	69.6	55.7	9.3	4.6	0.26	20.7	29.1	393.8	16.1	-4.39	-0.23	4.71	4.40
7	6.0	70.1	56.6	9.3	4.7	0.27	20.7	27.8	395.9	19.8	-4.71	-0.50	4.50	4.73
7	6.1	70.6	57.6	9.3	4.8	0.28	20.6	26.4	398.1	23.1	-4.99	-0.81	4.28	5.06
7	6.2	71.1	58.5	9.3	4.9	0.28	20.4	24.9	400.3	25.7	-5.26	-1.14	4.04	5.38
7	6.3	71.6	59.4	9.3	5.1	0.29	20.3	23.4	402.6	27.7	-5.49	-1.51	3.80	5.69
7	6.4	72.1	60.3	9.3	5.2	0.30	20.3	21.7	405.1	29.1	-5.69	-1.91	3.54	6.00
7	6.5	72.6	61.3	9.3	5.3	0.30	20.2	20.0	407.9	29.8	-5.87	-2.33	3.29	6.31
7	6.6	73.1	62.2	9.3	5.4	0.31	20.2	18.3	411.1	29.7	-6.02	-2.77	3.03	6.63
7	6.7	73.7	63.1	9.3	5.5	0.31	20.3	16.5	414.8	28.8	-6.14	-3.23	2.76	6.94
7	6.8	74.2	64.1	9.3	5.5	0.32	20.5	14.7	419.3	26.9	-6.24	-3.71	2.53	7.26
7	6.9	74.8	65.0	9.3	5.6	0.32	20.7	13.0	424.7	23.6	-6.31	-4.21	2.29	7.58
7	7.0	75.3	65.9	9.3	5.6	0.32	20.9	11.3	431.6	18.8	-6.36	-4.71	2.06	7.91
7	7.1	75.9	66.9	9.4	5.5	0.32	21.2	9.8	440.5	11.7	-6.38	-5.22	1.83	8.24
7	7.2	76.4	67.8	9.4	5.5	0.31	21.5	8.5	451.9	1.8	-6.39	-5.73	1.62	8.58
7	7.3	77.0	68.7	9.4	5.4	0.31	22.1	7.7	466.2	-11.0	-6.38	-6.24	1.43	8.92
7	7.4	77.5	69.7	9.4	5.3	0.30	22.6	7.3	482.4	-26.0	-6.35	-6.74	1.25	9.26
7	7.5	78.0	70.6	9.4	5.2	0.29	23.3	7.4	498.6	-41.1	-6.31	-7.24	1.08	9.60
7	7.6	78.6	71.6	9.4	5.0	0.28	24.0	8.1	512.7	-54.3	-6.26	-7.72	0.92	9.94
7	7.7	79.1	72.5	9.5	4.8	0.27	24.9	9.6	524.0	-64.9	-6.20	-8.19	0.78	10.27
7	7.8	79.5	73.5	9.5	4.6	0.26	25.8	10.1	532.7	-73.0	-6.13	-8.64	0.64	10.60
7	7.9	80.0	74.4	9.5	4.4	0.25	27.0	11.2	539.4	-79.3	-6.07	-9.07	0.52	10.91
7	8.0	80.4	75.4	9.5	4.2	0.24	28.4	12.4	544.6	-84.3	-6.00	-9.48	0.40	11.22
7	8.1	80.8	76.3	9.5	4.0	0.22	29.9	13.4	548.7	-88.4	-5.93	-9.87	0.28	11.51
7	8.2	81.2	77.3	9.5	3.7	0.21	31.8	14.4	552.1	-92.0	-5.86	-10.23	0.17	11.79
7	8.3	81.6	78.2	9.5	3.5	0.19	34.0	15.3	554.8	-95.4	-5.80	-10.56	0.06	12.05
7	8.4	81.9	79.2	9.6	3.2	0.18	36.7	16.1	557.2	-98.7	-5.75	-10.87	-0.05	12.30

Table 9.1. Example of a computed flight path.

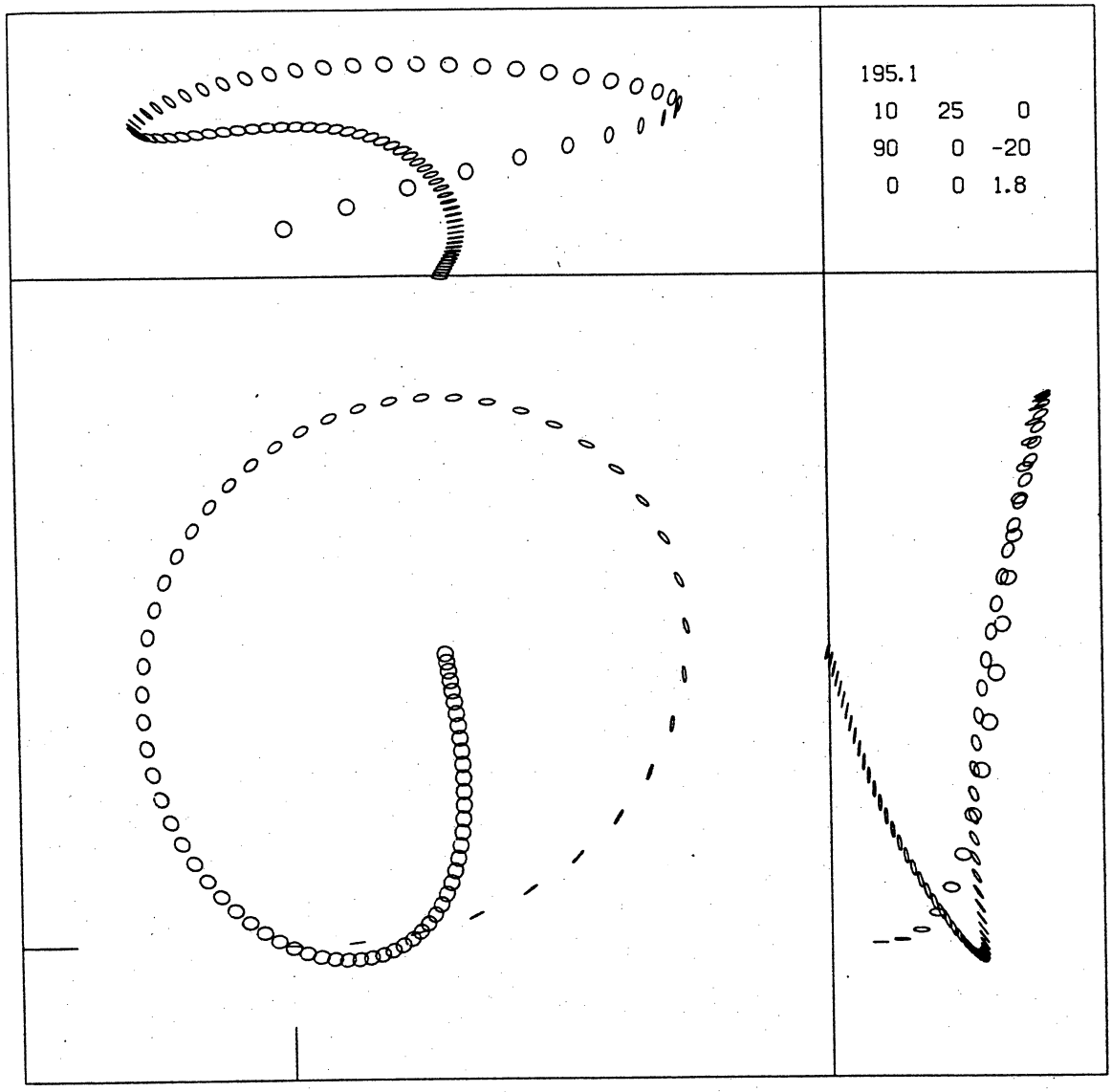

fig. 9.1. Example of a computed flight path. Three orthogonal projections are plotted. The boomerang's position is shown at intervals of 0.1 sec.

CHAPTER II

FIELD EXPERIMENTS.

§10 *The boomerangs.*

Six boomerangs played a part in the experiments; they are named respectively: L1, L4, L5, L6, F18, WU. With the exception of boomerang L5, these were also used in the wind tunnel experiments described in Part II, Chapter VI (see Part II, fig. 28.1). With four of these boomerangs: L1, L4, L5, L6 (see fig. 10.1) flight paths have been photographically recorded.

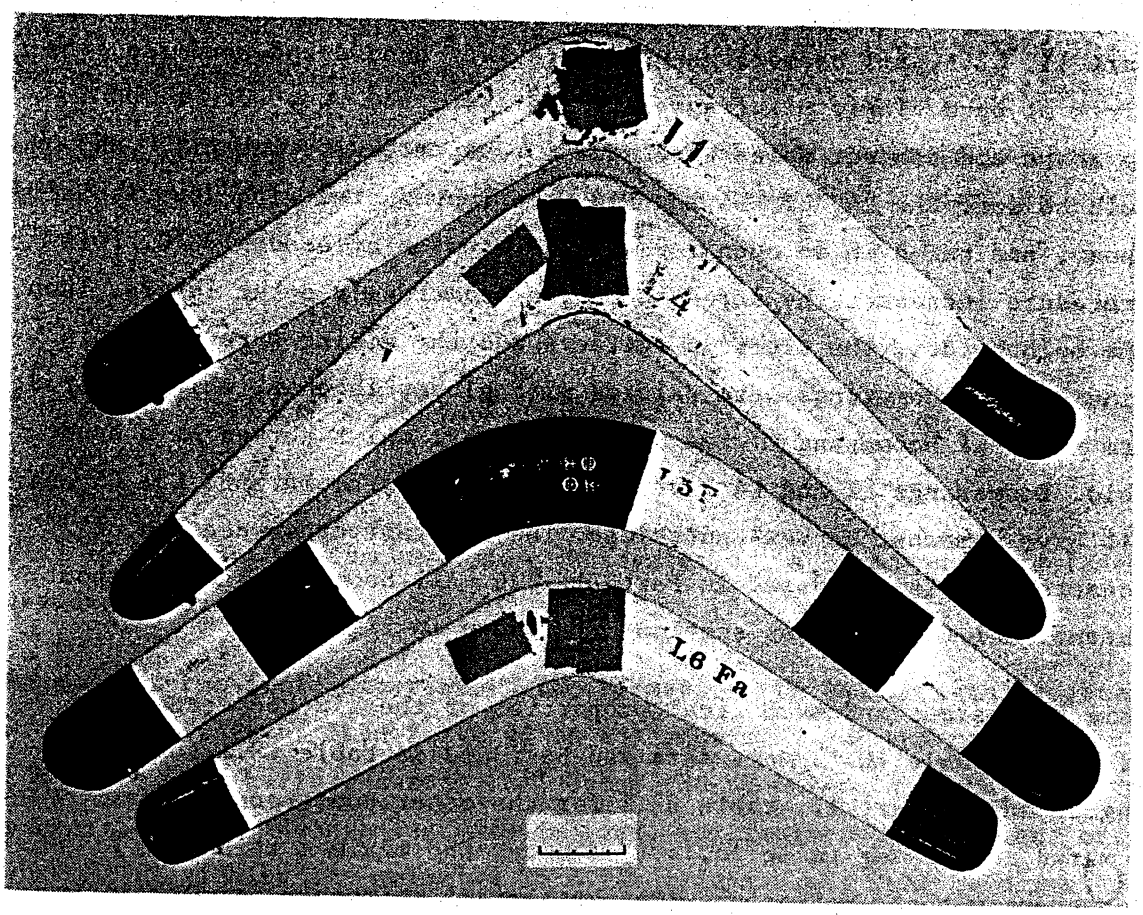

fig. 10.1. The left-handed boomerangs L1, L4, L5, L6. Each carries batteries, light bulb and, except for L1, the "time pill". During the experiments, batteries and "time pill" are covered by adhesive tape, which in the photograph is removed from boomerang L5.

These four boomerangs were equipped with batteries and light bulb. In addition the boomerangs L4, L5 and L6 carried an electronic device, called "time pill" (see §11), which switches the light on and off twice a second and thus provides a time scale in the flight path photographs. The batteries and the "time pill" were mounted in the thickest parts of the boomerangs, in suitably shaped holes where they are firmly held by elastic electric contacts. During the experiments they were covered by water-tight adhesive tape. The light bulb was inserted in a holder at the trailing edge near the tip of boomerang arm nr. 1. (Arm nr. 1 "precedes" the centre of mass, arm nr. 2 "follows" it. See Part II, §20.) Bulb holder, contacts and wiring were attached to the boomerang by means of epoxy.

Except for the right-handed, commercially produced boomerang WU (see Part II, §26), all boomerangs used were left-handed and handmade from birch plywood. Their planforms were jig-sawed and they were filed into shape and sanded. Holes were made for batteries, "time pill" and bulb holder. The L4, L5, L6 and F18 were impregnated with low-viscosity epoxy, and baked in an oven for some 20 minutes at about 130°C. This procedure increases the strength of the boomerang's outer layers. Then the bulb holder, the electric contacts and the wiring were mounted. Finally the boomerangs were painted with glossy lacquer, white and red. Arm nr. 2 of boomerang L1 has a narrower part which serves as a handhold. Boomerangs L1 and L4 have flat undersides, boomerangs L5, L6 and F18 have somewhat convex undersides. The constant cross section of boomerang WU is discussed in Part II, §26. All boomerangs are without intentional twist. Cross sections are shown in fig. 10.2.

Some dimensions and mechanical properties of the six boomerangs are listed in table 10.1. More data can be found in table 18.1 for boomerang L5 and in Part II, table 32.1 for the other boomerangs. A few remarks concerning table 10.1: t_m denotes the maximum thickness of a boomerang without batteries. (The batteries' thickness is .0113 m.) In the column under t/c the minimum and maximum thickness over chord (= wing width) ratios are listed. Each boomerang's centre of mass was determined by balancing, and its radius of gyration (r_g) and moment of inertia (I_3) by pendulum experiments. It should be noted that the

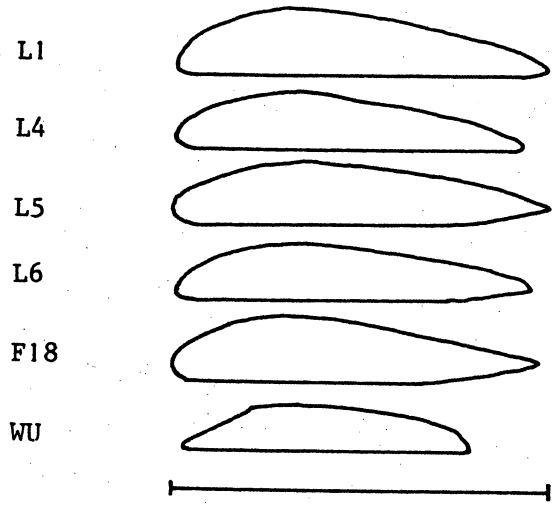

fig. 10.2. Cross sections of arms nr. 1 (arms nr. 2 are similar) at 10 cm distance from wing tips.

batteries (13 grams together) and the "time pill" (3 grams) contribute substantially to each boomerang's mass m, but only slightly to its moment of inertia I_3. The light bulb weighs less than 1 gram.

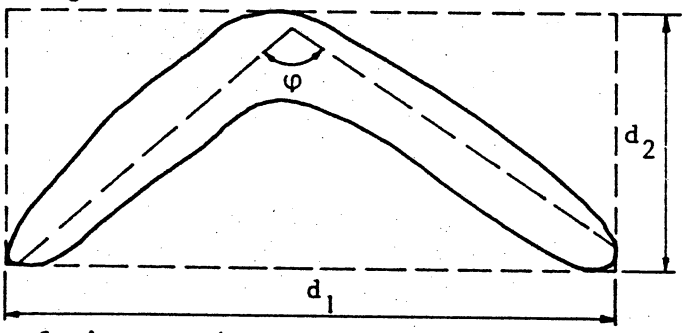

fig. 10.3. Sides of circumscribed rectangle: d_1, d_2, and angle included between arms: φ.

In some of the field experiments the boomerangs L1 and L6 were weighted with thin slices of lead fastened to the undersides of the arms near the tips. Such ballast hardly influences the boomerang's aerodynamic properties, but changes its mass (m) and, particularly, its moment of inertia (I_3). With the weighted L6 a few flight paths were recorded in which the batteries were replaced by shortened ones weighing 5 grams less. The small shift in the position of the centre of mass due to the

attaching of ballast has been neglected in all computations. Boomerang L4 has also been used while equipped with pieces of cotton-thread in front of its leading edges (trip wire, see Part II, §26). Boomerang L1 has been used in earlier experiments [Hess, 1968].

boomerang		d_1	d_2	φ	t_m	t/c	m	I_3	r_g	a	λ	k	r_1
L1 plain	0	.562	.228	110°	.0105	.16-.19	.173	.00396	.151	.298	.258	.718	.262
weighted	0	"	"	"	"	"	.188	.00455	.156	"	.272	.625	"
L4 plain	*	.532	.255	97°	.008	.13-.19	.172	.00338	.140	.291	.232	.746	.253
with wire	*	"	"	"	"	"	"	"	"	"	"	"	"
L5 plain	*	.599	.215	110°	.0115	.175-.19	.216	.00583	.164	.307	.270	.565	.271
L6 plain	*	.487	.160	121°	.011	.17-.20	.139	.00221	.126	.249	.256	.518	.215
weighted 1	*	"	"	"	"	"	.146	.00247	.130	"	.273	.463	"
weighted 2	*	"	"	"	"	"	.141	.00246	.132	"	.281	.461	"
F18 plain		.500	.193	113°	.010	.16-.19	.135	.00274	.142	.258	.305	.500	-
WU plain		.577	.203	116°	.006	.16	.160	.00456	.168	.296	.325	.599	-

table 10.1. Some properties of the experimental boomerangs.

Lengths in metres, masses in kg. a = boomerang's radius, r_g = radius of gyration, defined by $I_3 = mr_g^2$. $\lambda = I_3/ma^2$ (6.7). $k = \mu a^5/I_3$ (5.13). r_1 = distance between light bulb and centre of mass. For d_1, d_2, φ see fig. 10.3. Boomerangs used with light and "time pill": *, with light only: 0. All these data may contain errors of about 1 unit in the last decimal.

§11 *The "time pill".*

In this section an electronic device called the "time pill" is described. It can be mounted in experimental boomerangs together with batteries and a miniature light bulb. Its function is to switch the light on and off at a known, constant frequency. In this way a built-in clock is obtained, which allows one to deduce the boomerang's position as a function of time from flight path photographs.

The "time pill" operates on two 1.5V batteries (Berec D23 or Pertrix 245) connected in series. Through it the lamp (without any indication of manufacturer) is fed at a voltage of about 2.0V and a current of 195mA. The "time pill" was designed for a period of 0.50 sec. (0.4 sec. on and 0.1 sec. off).

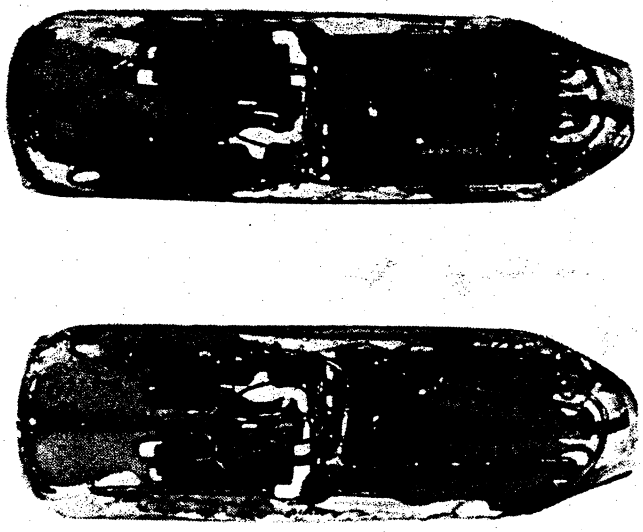

fig. 11.1. Two views of the "time pill".

The "time pill" consists of 16 discrete components soldered together and cast in transparent epoxy (hardened at 70°C), which makes it shock-proof. It is shown in fig. 11.1. Three contacts emerge from the epoxy and serve to electrically connect the device to batteries and light bulb (see fig. 11.3). The "time pill" measures 3.15 cm × 0.98 cm × 0.60 cm and weighs less than 3 grams.

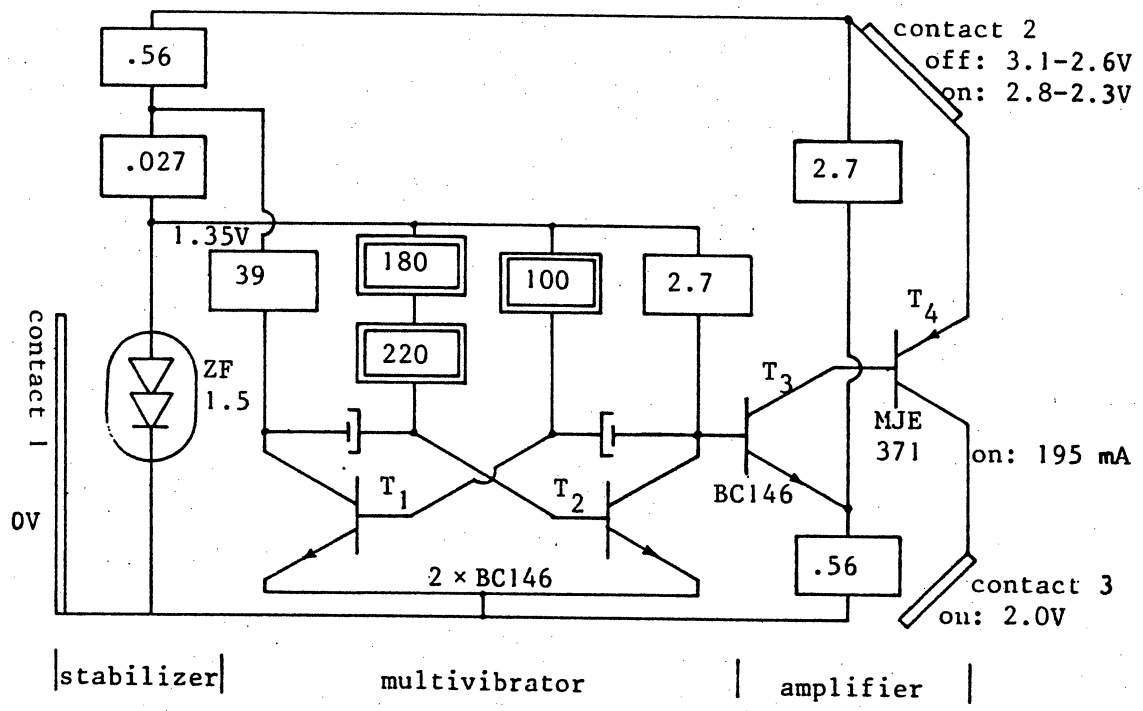

fig. 11.2. Circuit diagram. ⊣⊢ = tantalum capacitor, 1μF roughly. ▭ = carbon resistor, ▭ = metal film resistor, numbers roughly indicate resistance in kΩ. $T_{1,2,3,4}$: transistors.

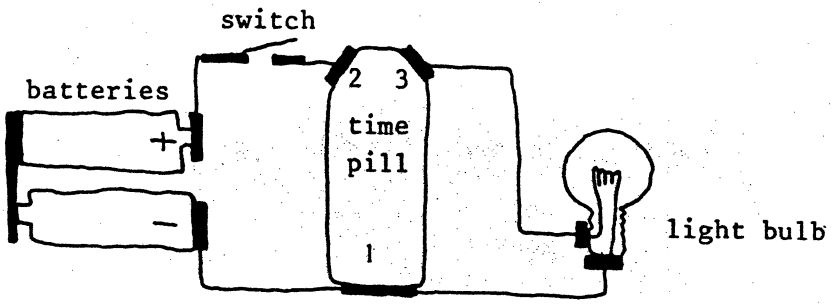

fig. 11.3. Connections between time pill, batteries and light bulb as mounted in boomerangs. ▬ = contact.

Three main parts can be distinguished in the "time pill": stabilizer, multivibrator and amplifier (see fig. 11.2). The stabilizer supplies a voltage of about 1.35V to the multivibrator. The 2.7 kΩ in the amplifier circuit serves to make the current through the light bulb less dependent on the batteries' voltage. The capacitors and some of the resistors were individually selected with great care, so that the

desired period of 0.5 seconds was obtained with high precision. The different temperature coefficients of metal film and carbon resistors have been exploited to bring the temperature coefficient of the period down to about -120 ppm per °C. A disadvantage of stabilizing lamp current rather than lamp voltage is that as the filament gradually grows thinner due to evaporation, this process is accelerated rather than slowed down. Another weakness of the present design is that the period turns out to be rather sensitive to changes in the internal resistance of the batteries, which varies from about 1.4 Ω for two fresh batteries in series to about 2.2 Ω for older, used ones. The period's internal resistance coefficient is about 1% per Ω. The period's dependence on the batteries' EMF has a coefficient of about ½% per V.

A duration test was done in which some 50 consecutive "flights" were simulated. The system was alternately switched on for 15 seconds and off for 45 seconds. During this test a pair of fresh batteries (EMF ≈ 3.1V) was used up (EMF ≈ 2.5 - 2.6V). The ambient air temperature was 11.8°C. The period was equal to .499 sec. within 0.1% throughout this test. During the field experiments the period of the "time pill" must have been $.499^{+.002}_{-.001}$ sec. Actually, its accuracy is far higher than required for our purpose.

More detailed information about the "time pill" and improved versions of it may be obtained from H.D. Coster [1973].

§12. *Photography and field geometry.*

The flight paths of an experimental boomerang were recorded by means of photographic time exposures of the light traces made by the bulb carried in the boomerang at night. As the light was carried excentrically from the boomerang's centre of mass such a trace consists of consecutive arcs of nearly cycloidal shape. The trace is continuous in the case of boomerang L1, and interrupted twice a second by the "time pill" in the cases of boomerangs L4, L5 and L6.

To obtain a three-dimensional record we used two equal cameras. These were set up at a distance, called baseline, of about 1.4 m apart, viewing parallel in a direction perpendicular to the baseline. In this way pairs of photographs can be used as stereo pictures of boomerang flight paths. The cameras were fixed to a stand consisting of a hollow aluminium beam clamped horizontally on a collapsible, Λ-shaped, aluminium ladder. The height of the cameras above ground level was about 1.4 m, and the viewing direction was tilted about 5° upward from horizontal.

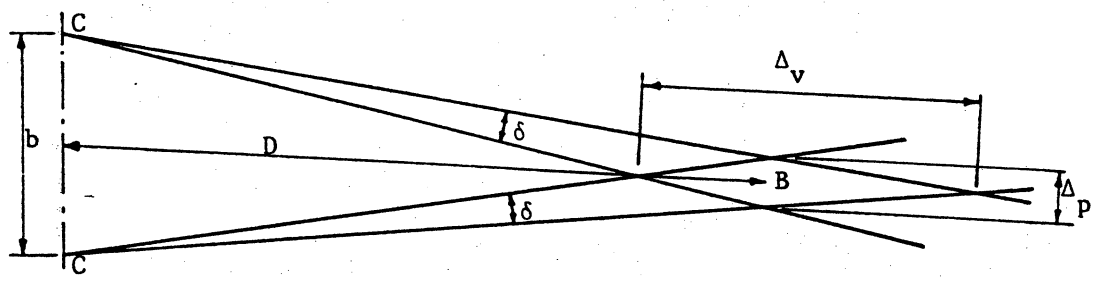

fig. 12.1. Uncertainty of boomerang's position in direction of viewing: Δ_v, and perpendicular to direction of viewing: Δ_p. C = camera, b = baseline, B = boomerang, D = distance boomerang from cameras, δ = angular uncertainty in photographs.

A disadvantage of this stereo setup is the poor resolution in the viewing direction, as is indicated in fig. 12.1. The boomerang's distance from the cameras D is much greater than the baseline b. Call the angular uncertainty in each photograph δ, the uncertainty of the boomerang's position in the viewing direction Δ_v, and perpendicular to the viewing direction Δ_p. Then we have:

$$\Delta_p \approx \delta \cdot D \qquad \Delta_v \approx \delta \cdot \frac{D^2}{\frac{1}{2}b} \qquad \frac{\Delta_v}{\Delta_p} \approx \frac{D}{\frac{1}{2}b} \tag{12.1}$$

Hence, for $b = 1.4$ m and $D = 70$ m, we have $\Delta_v/\Delta_p \approx 100$. For our flight path photographs $\delta = 0.001$ seems to be a reasonable estimate. This corresponds to $\Delta_p \approx 0.05$ m, $\Delta_v \approx 3.6$ m at $D = 50$ m, and to $\Delta_p \approx 0.07$ m, $\Delta_v \approx 7.0$ m at $D = 70$ m.

An alternative arrangement would be to set up two cameras far apart in such a way that they view the flight path in perpendicular directions. The uncertainty in all directions would then be about equal (Δ_p). However, a main advantage of our arrangement is that the stereo pictures provide an immediate three-dimensional impression, which can be compared by eye with the impression from computed theoretical flight path stereograms. Of course, both arrangements could have been combined by adding a third camera to our setup, which would view in a perpendicular direction. This would have required additional equipment and the assistance of one more person. A greater baseline of, say, 6 m could have been easily realised, however.

cameras	lens	aperture used	distance setting	baseline
2 × Werra 1	T f = 50 mm 1 : 2.8	1 : 2.8	6 m	1.409 m
2 × Canon FTb	TD f = 50 mm 1 : 1.8	1 : 2.8	∞	1.385 m
		1 : 1.8	20 m	

table 12.1. The cameras.

In the course of the field experiments two different pairs of cameras were used, see table 12.1. The chosen distance settings result in optimally sharp images from light sources at infinity. It turns out that, at maximum aperture, these distance settings tend to be somewhat smaller than the camera's distance scale indicates. The optimum settings were determined experimentally. (Several small light bulbs were put at known distances from the cameras. Pictures were taken with various distance settings. The developed negatives were viewed under a microscope. The images showed as black, mostly elliptical, spots. The respective

distance settings for which these spots had minimum dimensions were considered to be the optimum settings for the respective known distances. From these followed the settings for light sources at infinity. The boomerangs mostly moved between 40 m and 80 m distance.) The amount of image distortion was not investigated.

The film used in the field experiments was the very sensitive (over 1000 ASA) Kodak 2475 recording film, which afterwards was developed in a high-contrast developer. The light sources carried by boomerangs L4, L5, L6 with "time pill" radiated roughly 3 lumen. The continuous source carried by boomerang L1 varied from roughly 10 lumen to roughly 3 lumen, as the batteries were gradually exhausted. A light source of about 2 lumen would probably be quite sufficient in experiments like these. The fixed light bulbs used as position markers at ground level were very much

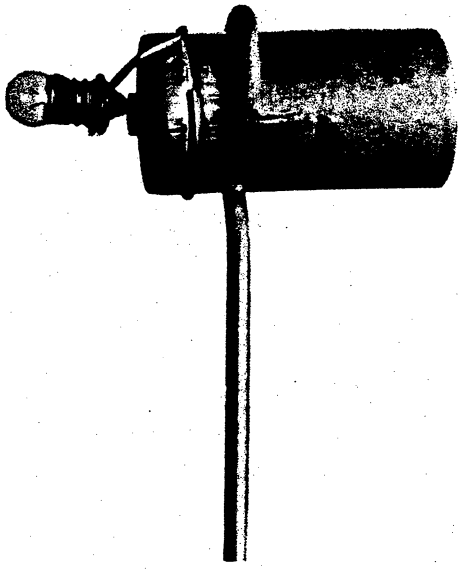

fig. 12.2. A field light.

weaker. At the exposure time of about 10 seconds, their photographic images are strong enough as long as they are clearly visible to the naked eye from the camera position. Actually, in most of our photographs these lights are overexposed. Each field light consisted of a light bulb of 2.5V, 0.1 (or 0.2)A, clamped on a 1.5V battery (R20), as shown in fig. 12.2. By means of a piece of stiff iron wire this device could be stood upright in the ground.

The experiments were carried out on a piece of grass land 4 km north of the town of Steenwijk (52°49'34"N, 6°6'10"E). The rectangular field measures 55 m × 110 m and is surrounded on all four sides by trees of

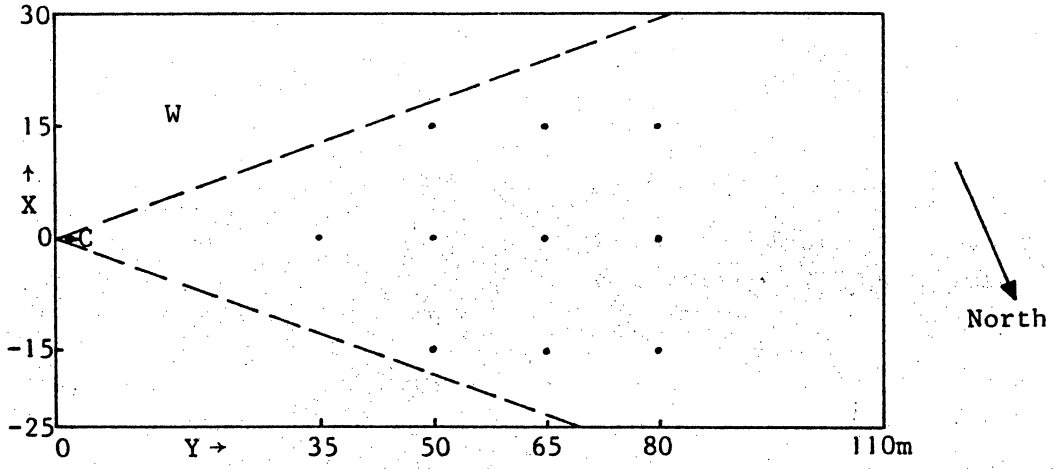

fig. 12.3. Field geometry. C = cameras, ---- = limits of field of vision, W = wind meters, . = field light.

about 8 m high. The long sides are in ESE-WNW direction. The cameras were set up at the ESE short side, the viewing direction was WNW. From the cameras' position the visible horizon was formed partly by the 8 m high trees at 110 m distance and partly by 16 m high trees at 240 m distance. The ground level seemed to be nearly horizontal, except for the far western corner, which was slightly elevated. The field lights were put in the positions indicated in fig. 12.3. We choose the cartesian coordinate system (X,Y,Z) in such a way that the origin is at ground level, halfway between the cameras, the Y-axis in the viewing direction, the Z-axis vertically upwards, and the X-axis towards SSW. In the photographs, which are reversed (reflected with respect to the Y,Z-plane), this system is right-handed. The cameras have the coordinates, in metres: (± 0.7, 0, 1.4). The (X,Y)-coordinates of the 10 field lights are respectively: (0, 35), (-15, 50), (0, 50), (15, 50), (-15, 65), (0, 65), (15, 65), (-15, 80), (0, 80), (15, 80). An unlighted marker was put at (0,0). These field markers were positioned by means of a 50 m steel measuring tape and the light rays themselves. On one occasion, when the marks put in the ground previously could not be found in the dark, except for those at the positions (0, 0) and (0, 50), the other nine positions were reproduced to within better than 5 cm, as evidenced by the old marks rediscovered in the morning. The height of

the field lights was about 20 cm above ground level, their deviations from a horizontal plane may have amounted to some 10 cm.

fig. 12.4. Example of an experimental left-handed flight path stereogram (14L28A/14R28A). A flight of boomerang L4. Bright star in upper right corner is Wega.

An example of a recorded flight path is shown in fig. 12.4. The photographs are not yet reversed, so that the flight path is left-handed. Here, boomerang L4 is launched at the approximate position (0, 50, 1.8). The thick, knotty part of the light trace was made while the boomerang was still held by the thrower's hand. Twice a second the succession of cycloidal arcs is interrupted by the "time pill". The 10 field lights, slightly above ground level are clearly visible. In the background a skyline originates from trees at two distinct distances, farther back some clouds show and, at infinity, a multitude of stars. The brightest of these, in the upper right corner, is α-Lyrae or Wega. This exposure was made in the night of 30-8-1973 with the Canon cameras, f : 1.8.

§13 *The wind meters.*

> "How is the wind? If you can feel a breeze
> on your face go home and bring out your kite.
> Every day is not a boomerang day." [Hanson, 1974, p. 37]

The condition of the air during the experiments should be known, in particular its density and its state of motion. As to the density: we assume a value of 1.20 kg/m^3. We did not determine it experimentally. The deviations from the assumed value may be about ±3%, which is not very important. The incompleteness of our knowledge of the air's state of motion is more serious. Only the interior of a very large hall could have provided a windless environment.

We took care to select almost windless nights (which are very rare in the Netherlands) for carrying out the field experiments. After some pilot experiments, the actual experiments were done during five summer nights in 1973. Naturally, there was always some wind, varying in space and time. As it is impossible to completely determine the wind met by a boomerang in the course of its flight, we must do with some rough estimates. In fact, wind measurements were made at a single point by two simple instruments: an anemometer and a vane, each positioned on top of a fiber-glass fishing rod at a height of 4.75 m. In the course of the experiments the local wind speed and direction were recorded as indicated by these instruments. In fig. 12.3 their position is indicated by W.

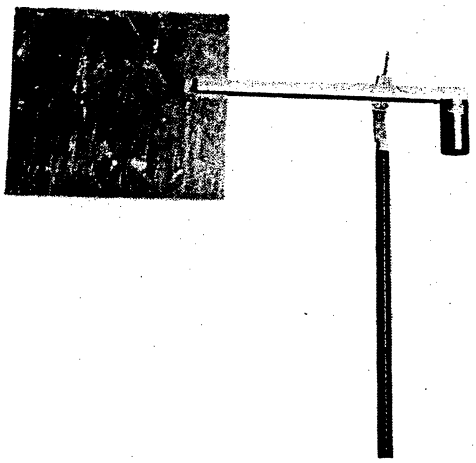

fig. 13.1. Vane

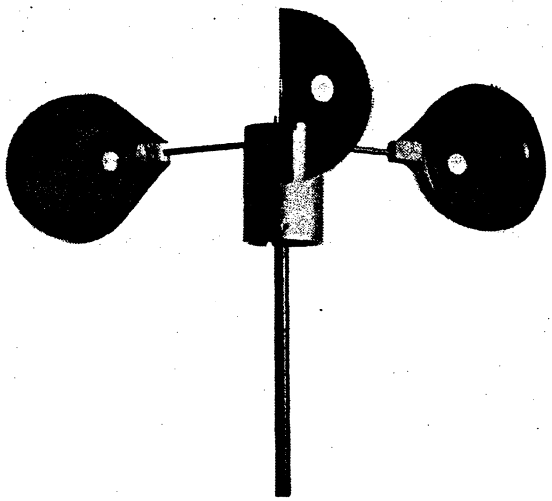

fig. 13.2. Anemometer.

The anemometer (fig. 13.2) is of a well known type: its main parts are three hemispheral cups with a diameter of 7.9 cm. These were cut from decorative plastic sheet (thickness 0.02 cm), in which an array of cups was pressed, (at the time commercially available). They are attached by thin brass rods to a hollow, aluminium, central cilinder. The distance between the cups' centres and the cilinder's central line is 11.5 cm. The lid which covers the cilinder has a hole through its centre over which a piece of rubber is glued. Through the rubber and the hole a steel sewing-needle points downward. The sharp point of the needle is supported by a glass cup the size of half a bicycle bulb. The needle point and the centres of the three cups are all in the same plane, and the anemometer's centre of mass is underneath this plane. The needle-point-on-glass-bearing has very little friction. This cup anemometer proved to be highly sensitive: it has been seen to spin slowly but steadily in an air stream of 2 cm/s, made visible by cigarette smoke. The anemometer was roughly calibrated by moving it at various velocities through a long corridor. The passing of one cup (1/3 revolution) corresponds to a wind path of about 3/4 m, with an estimated accuracy of ±20%. The instrument appears to be linear. During the field experiments the passing of 10 cups was watched by eye at irregular intervals and the corresponding times determined by a stopwatch.

The vane (fig. 13.1) is very simple. It consists of a rectangular aluminium sheet of 0.03 cm × 11 cm × 10 cm, a balsa-wood stick and a brass counterweight. The balsa stick is pierced by a needle, which rests in a glass cup, just like with the anemometer. This device is extremely sensitive: the vane has been seen moving even when the anemometer stood still. Both instruments can be used in wind speeds up to 3 m/s. At higher speeds they are blown off the fishing rods.

The wind measurements made during the field experiments are summarized in table 13.1. For each of the five nights the following quantities are listed: W, the average horizontal wind speed at Z = 4.75 m; β, the angle between average wind vector and X-axis (as explained in fig. 13.3); and ΔW, the maximum magnitude of the variations in the wind speed. The values for W may contain a systematic error of ± 20%.

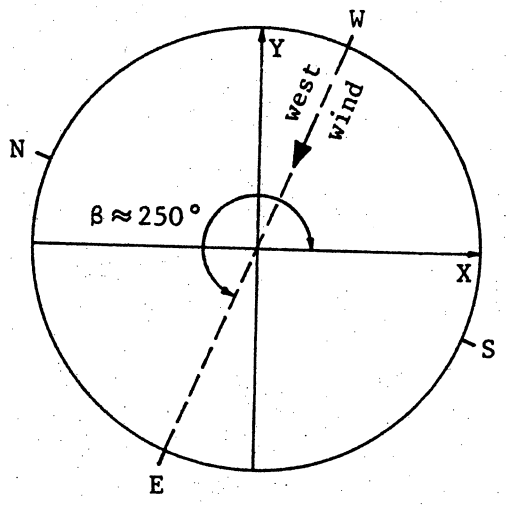

fig. 13.3. Wind direction with respect to (X,Y,Z)-coordinate system (after reflection). E.g.: for west wind, $\beta \approx 250°$ according to (8.8).

night	W (m/s)	β	ΔW (m/s)
13-7-73	0.0	200°	0.1
16-7-73	0.1	140°	0.3
17-8-73	1.6	310°	0.5
19-8-73	0.1	220°	0.3
30-8-73	0.7	250°	0.4

table 13.1. Average wind velocity and maximum variations measured at Z=4.75 m.

§14 *The launching of the boomerangs.*

In our field experiments the boomerangs were thrown by hand. Although this is the easiest way to launch boomerangs, it does not allow accurate control of the initial conditions. Here a boomerang-throwing machine would be indispensable (as was already remarked in [Hess, 1968]). Ideally, such a machine should be capable of launching boomerangs at all sorts of combinations of V_o, ω_{zo}, Ψ_o, ϑ_o, ψ_o (subscripts o refer to the instant of launching, t = o). The instrument must either be able to reproduce the selected initial conditions accurately, in which case it should be calibrated once, or it must accurately measure and record the initial conditions each time it launches a boomerang. No such accurate instruments have been built as yet. The design of a good boomerang-throwing machine is no simple matter. The instrument must accelerate boomerangs to high speeds (for example, launching boomerang L5 at f_o = 10 revs/s, V_o = 25 m/s requires an energy of 74J) and at the same time be very delicate. After spending considerable attention to the problems arising here, H.D. Coster and I came to the conclusion that developing a boomerang-throwing machine would take at least half a year's time, and we decided to abandon the attempt to build one. In the meantime a more simple boomerang launcher has been built by P. Musgrove and his students at Reading (U.K.) [Jeffery, Grantham & Hersey, 1973], [Musgrove, 1974]. Small launchers for indoor use have been made earlier by Pfaundler [1905], [1906] and Buchner [1916], [1918].

If boomerangs are thrown by hand, the initial conditions must be determined by photographic means. Let us first have a look at the launching method itself. Figures 14.1 a,b and c show the launching of boomerang L1 by my left hand. The boomerang is gripped at the end of arm nr. 2 ("following arm"). The pictures have been taken from 16mm film fragments, exposed at a speed of 64 frames per second, and mirrored to produce a right-handed image. It appears that the boomerang, while it is being accelerated to full speed in about 1/10 second, does not move precisely in its own plane. This indicates an imperfect throwing technique, which might lead to wobbling of the boomerang during the first part of its flight. Indeed, it seems that some wobbling, after the boomerang has left the hand, can be noticed in the pictures. The

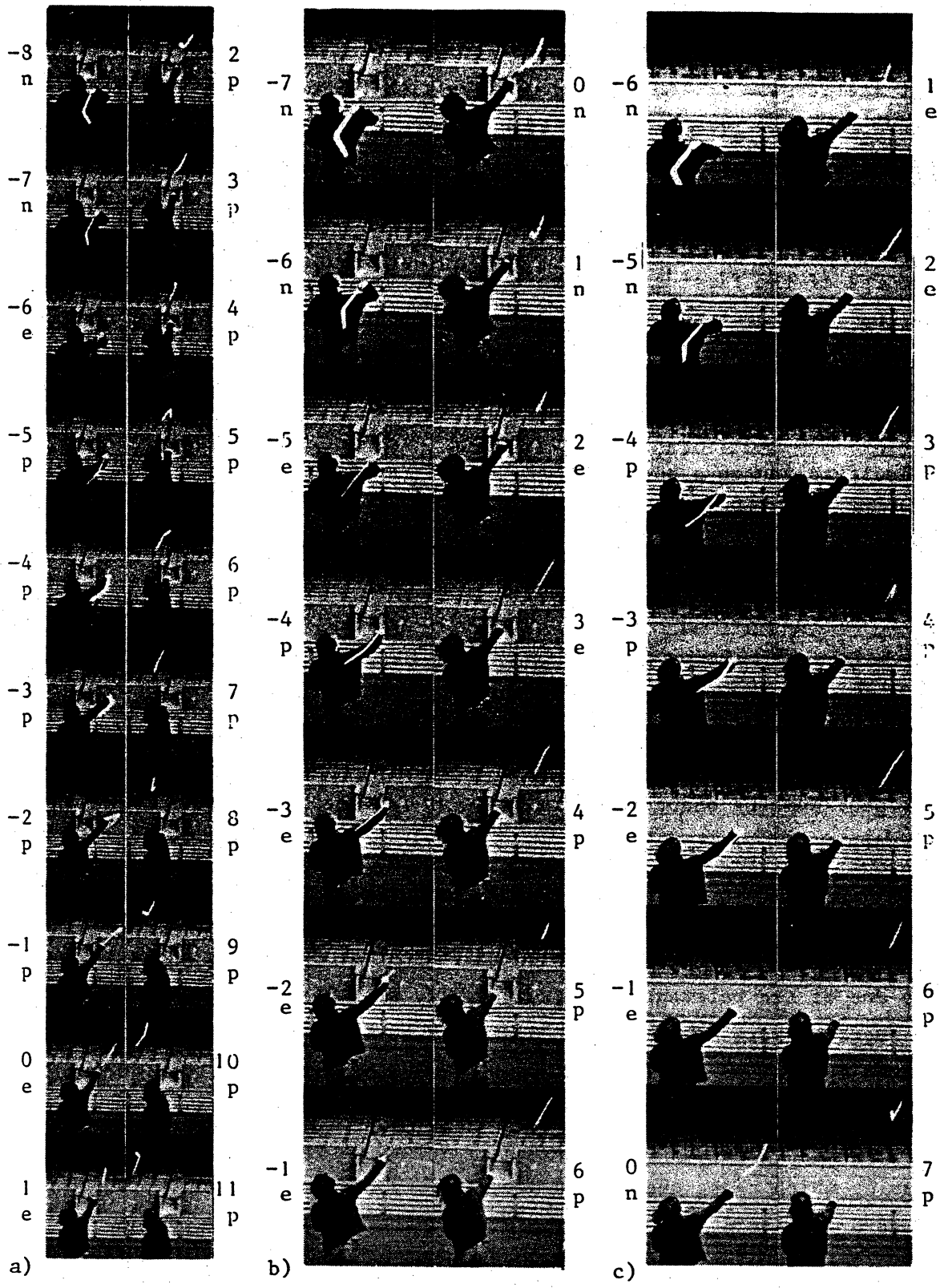

fig. 14.1. a,b,c. Three launchings of boomerang L1. Pictures taken from 16 mm film exposed at 64 frames per second. Reversed to obtain right-handed throws. Numbers denote time from instant of release in units of 1/64 sec. p, n and e denote resp. upperside, underside, edge of boomerang visible. Note the change in the orientation of the boomerang's plane between the instants -1 and +2.

flight path photographs in Chapter III, however, give no indication of wobbling. It is true, in some of the photographs the first arc (or part of it) is seen to lie in a plane significantly deviating from that of the following arcs (e.g. fig. 19.6a), but this deviation is caused by the launching motion shown in fig. 14.1, and occurs before the instant of release. An analysis of 16mm film fragments, such as the one shown in Part I, fig. 14.2, indicates that the boomerang is released in the course of the first arc. At this moment the light carried by the boomerang is about halfway this arc, see fig. 14.2. At the instant of release the boomerang's centre of mass is about 1.8 m above ground level. From the flight path photographs it appears that, generally, the boomerangs are launched at angles of incidence $\Psi_o \approx 0$. It seems to be difficult to launch a boomerang at, say, $\Psi_o = 10°$.

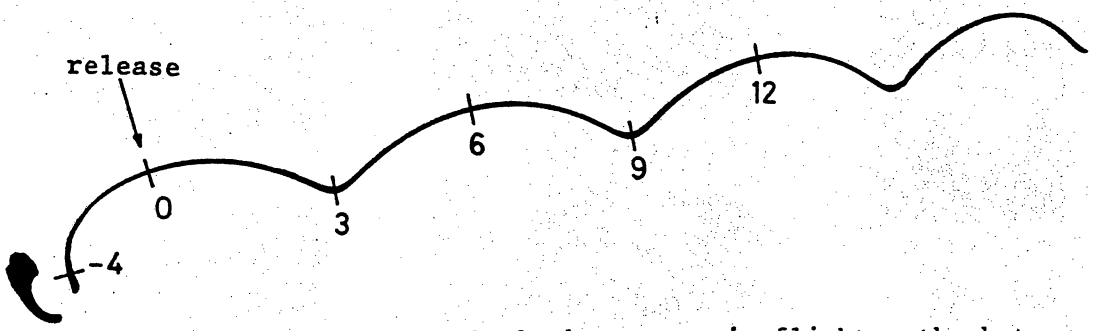

fig. 14.2. Instant of release of the boomerang in flight path photographs. Numbers denote time in units of 1/64 sec. from instant of release.

With what precision can the initial conditions be determined from our flight paths photographs? The angular uncertainty in the photographs is one of the relevant factors, see §12. With very few exceptions, the boomerangs were always launched at $Y_o = 50$ m, $Z_o = 1.8$ m, with estimated errors: $\Delta Y_o = 0.5$ m, $\Delta Z_o = {}^{+0.1}_{-0.2}$ m. X_o was not recorded during the experiments. Each of the quantities f_o, V_o, Ψ_o, ϑ_o, φ_o, ψ_o must be determined either by inspection of a number of consecutive spin periods during which these quantities may vary, or from one arc only, which does not allow a high precision either. The field lights at known positions provide length scales in the X- and Y-directions, and the "time pill" provides a time scale (except for boomerang L1). Two special cases can be distinguished. In the first case the boomerang is

launched in a direction approximately perpendicular to the viewing direction. Here f_o, V_o, ψ_o, X_o can be determined from the photographs. In the second case the boomerang is launched in a direction almost exactly parallel to the viewing direction. Here Ψ_o, ϑ_o, φ_o, X_o can be determined. Table 14.1 lists the roughly estimated errors in the determinable initial conditions for both special cases. The errors listed

1. perpendicular	2. parallel
$\Delta f_o = 0.3$ revs/s	$\Delta\Psi_o = 5°$
$\Delta V_o = 1.5$ m/s	$\Delta\vartheta_o = 5°$
$\Delta\psi_o = 2°$	$\Delta\varphi_o = 5°$
$\Delta X_o = 0.5$ m	$\Delta X_o = 0.1$ m.

table 14.1. Estimated errors in the initial conditions determined from photographs, in two special cases. Assumed: $Y_o = 50 \pm 0.5$ m.

for the second case should be much larger if the boomerang would be launched in a direction somewhat deviating from the viewing direction. For boomerang L1, which does not carry the "time pill", f_o and V_o cannot be determined. U_o $(= V_o/\omega_{zo}a)$ might still be estimated from the shape of the cycloidal arcs, but this is not a precise method.

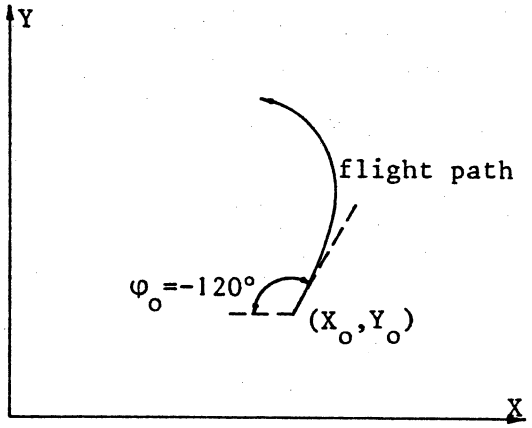

fig. 14.3. Example to explain the angle φ_o. Bird's-eye view, boomerang launched at (X_o,Y_o) with $\Psi_o = 0°$, $\vartheta_o = 90°$, $\varphi_o = -120°$.

Finally, it may be convenient for the reader to be reminded of the meaning of the angles ϑ, φ, ψ. For this see fig. 4.1. ϑ is the angle between the boomerang's plane of rotation and the horizon. As to φ (angle between horizontal line in the boomerang's plane and X-direction), it is useful to note that, if $\Psi = 0$, $\vartheta = \frac{1}{2}\pi$, $\psi = 0$, the boomerang moves in negative X-direction for $\varphi = 0$, in positive Y-direction for $\varphi = -90^\circ$ and in positive X-direction for $\varphi = \pm 180^\circ$. See fig. 14.3. If $\sin\psi < 0$ the boomerang rises, if $\sin\psi > 0$ the boomerang descends.

Generally the initial conditions were such that:

$$10 \text{ revs/s} \lesssim f_o \lesssim 12 \text{ revs/s}$$

$$20 \text{ m/s} \lesssim V_o \lesssim 30 \text{ m/s}$$

$$\Psi_o \approx 0^\circ$$

$$40^\circ \lesssim \vartheta_o \lesssim 90^\circ$$

$$-30^\circ \lesssim \psi_o \lesssim 0^\circ$$

$$-180^\circ \lesssim \varphi_o \lesssim -90^\circ$$

$$-14\text{m} \lesssim X_o \lesssim 14\text{m}$$

$$Y_o \approx 50\text{m}$$

$$Z_o \approx 1.8\text{m}.$$

The highest parts of the flight paths usually were at a greater distance from the cameras than the starting points. This helped to contain the flight paths within the cameras' field of vision.

Knowledge of the initial conditions of the photographed boomerang flights may serve to purposes. First, the influence of a particular parameter (such as ϑ_o) on a boomerang's flight can be experimentally determined. Secondly, the experimental flights can be compared with computed theoretical flights having corresponding initial conditions. For both objectives, the accuracy of the initial conditions in our field experiments is only barely sufficient.

CHAPTER III

EXPERIMENTAL AND THEORETICAL FLIGHT PATHS

§15 *Methods used.*

Stereograms of boomerang flight paths make up the bulk of this chapter. With regard to the recorded flight paths three distict levels of theorization can be distinguished:

Level 1. Actual flight paths traversed by real boomerangs. These paths are photographically recorded.

Level 2. Computed flight paths based on measured aerodynamic forces. These paths are automatically plotted.

Level 3. Computed flight paths based on theoretical aerodynamic forces. These paths are automatically plotted.

In the calculations of level 2 flights, the aerodynamic forces and torques ($F_{lx}, F_{ly}, F_{lz}, T_{lx}, T_{ly}, T_{lz}$) are taken from the results of the wind tunnel experiments described in Part II, Ch. VI. The aerodynamic forces and torques for the level 3 flights were computed by means of the winglet model developed in Part II. In some cases these latter forces contain a correction for the boomerang's precession ($\omega_x \neq 0$, $\omega_y \neq 0$, see §5); the resulting flight paths are said to be of *level 3'*.

boomerang	level 1	level 2	level 3	level 3'
L1	plain 0 weighted 0	101.1 101.2	195.1 195.2	250.1 251.2
L4	plain * with wire *	104.1 ———	237.1 ———	252.1 ———
L5	plain *	———	245.1	255.1
L6	plain * weighted 1 * weighted 2 *	106.1 106.2 106.3	241.1 241.2 241.3	253.1 254.2 254.3
F18	———	108.1	242.1	256.1
WU	———	109.1	239.1	257.1

Table 15.1. Listing of boomerangs and identification numbers of model boomerangs. (0 = with light, * = with light and "time pill").

The level (1,2,3,3') designation is also applied to the (model) boomerangs themselves. In all cases the flight path calculations proceed as outlined in §9.

The experimentel boomerangs and the identification numbers of the corresponding model boomerangs are listed in table 15.1. (More data can be found in table 10.1.) The model boomerangs are labeled by four-digit numbers. The first three digits of each number (e.g. 101 or 195) serve as a label for a table of aerodynamic force components. For five level 2 boomerangs such tables are listed in Part II, §31 (experimental forces). For level 3 boomerangs no tables are presented, but graphs (for both level 2 and level 3) are shown in Part II, fig. 31.7 through 31.36. The input parameters for the winglet model are listed in Part II, tabel 32.1, and, for boomerang 245, in Part III, table 18.1. The input parameters for level 3' boomerangs are the same as for the corresponding level 3 boomerangs, with the addition of the parameter k (see table 10.1). The fourth digit of each identification number serves to distinguish level 2 or level 3 boomerangs having the same aerodynamic table but differing in mass distribution.

Note that there are no level 2 flight paths for boomerang L5, which was not used in the wind tunnel experiments. For boomerangs F18 and WU, in which no light was mounted, level 1 flight paths could not be recorded.

The level 1 flight paths were produced and recorded as outlined in Ch. II, particularly §12. The photographs have been mirrored to obtain right-handed flights. The pictures are in negative, containing black lines on a white background, because they can be processed easier this way.

The level 2 and level 3 flights were computed as outlined in §9. Of each flight path a pair of plots was made, simulating the view of the pair of cameras used in the field experiments. The direction of viewing of the simulated cameras is in the positive Y-direction. Their positions are given by: $X = \pm 0.7m$, $Y = 0m$, $Z = 1.4m$. Their field of vision at $Y = 50m$ is given by: $-18 \pm 0.7m \leq X \leq +18 \pm 0.7m$, $-2m \leq Z \leq 22m$. The boomerang is represented by a circle with radius a, shown in perspective. Its

position and orientation are shown at intervals of 0.1 sec., until it reaches the ground (Z=0). The field lights are represented by small circles with a radius of 10 cm, at the positions: (0,35,.2), (-15,50,.2), (0,50,.2), (15,50,.2), (-15,65,.2), (0,65,.2), (15,65,.2), (-15,80,.2), (0,80,.2), (15,80,.2), in metres. A sawtooth skyline at Y = 110 m, with 7.5 m $\leq$ Z $\leq$ 8.5 m, is added in the stereograms. It simulates the treetops visible in some of the level 1 flight path photographs. Its main function, however, is to aid the perception of depth in the computed stereograms.

For some of the calculated flight paths plots were made of stereograms showing bird's-eye views. Here the simulated cameras have the positions: X = $\pm$ 3 m, Y = 50 m, Z = 80 m, and their direction of viewing is vertically downwards, in the negative Z-direction. The rather long baseline (6 m) allows an excellent perception of depth. With a few exceptions, the field of vision at ground level (Z=0) is given by -25 m $\leq$ X $\leq$ 25 m, 40 m $\leq$ Y $\leq$ 90 m for boomerangs L1 and L4, and by: -35 m $\leq$ X $\leq$ 35 m, 30 m $\leq$ Y $\leq$ 100 m for boomerangs L5 and L6. These bird's-eye stereograms should not be confused with cilindrical projections. Vertical projections of the boomerang flight paths on the plane Z=0 would look smaller and have slightly different shapes.

In most of the computed flights the wind speed is zero. In the few cases with wind, the wind speed was chosen as indicated in table 15.2. These choices agree with the measured wind speeds as listed in table 13.1. The chosen values for the wind gradient (W_1) are rather arbitrary, though not unreasonable. Anyway, the uncertainties in the actually prevailing wind velocities are such that it is hardly possible to make a better guess.

night	β	W_0	W_1
17-8-'73	310°	1.3 m/s	0.6 m/s/10 m
30-8-'73	250°	0.5 m/s	0.2 m/s/10 m
other	——	0	0

Table 15.2. Wind velocities assumed in the flight path computations.

Some 400 usable level 1 flight paths were recorded in the field experiments. A provisional catalogue of about 4000 level 2 and level 3 flight path stereograms was built up. Although this number may seem excessive, it certainly is not: Table 15.1 lists 26 model boomerangs (level 2,3,3'). The initial conditions for each flight are characterized by 6 parameters (f_o, V_o, Ψ_o, ϑ_o, φ_o, ψ_o), not counting the initial position and the wind conditions. Typically, for one model boomerang flight paths were computed with 3 values of φ_o, 7 values of ϑ_o, 7 values of ψ_o, 2 combinations of f_o and V_o, and 1 value of Ψ_o; this adds up to about 300 stereograms. For some boomerangs the computations were repeated with wind. On the other hand, for several of the listed model boomerangs hardly any flight paths were computed.

Which are the criteria for the selection of the flight paths presented in this chapter? If the initial conditions of the level 1 flights were known with high enough precision, one would only have to compute the level 2 and level 3 flight paths with these initial conditions, and afterwards make a representative selection. However, although the initial conditions can be partly inferred from the flight path photographs (see §14), the precision is not sufficient for this method. The alternative method adopted is to proceed by trial and error. In this respect our method is essentially the same as the one previously used in [Hess, 1968]. The selection process went as follows. For each level 1 stereogram the catalogue was scanned, and if a similarly looking level 2 or level 3 flight path was found, the level 1 path was provisionally selected. The next step was to compute more flight paths by varying the initial conditions. The best looking level 2 path was then selected. As to level 3, either the best looking flight path was chosen, or the one with the same initial conditions as the selected level 2 path. Finally, some 50, fairly diverse, level 1 flight paths were chosen for this chapter, together with their theoretical counterparts.

Such a method, of course, contains the risk of working towards a spurious agreement between experiment and theory. This risk can hardly be avoided, due to a lack of sufficiently accurate knowledge of the initial conditions of the level 1 flights. Indeed, in most of the presented cases the agreement between theory and experiment may be

flattered. This means that the presented evidence is primarily qualitative. On the one hand, it shows that there are certain differences between the outcomes of our theory and our experiments. On the other hand, the computed flight paths often so strikingly resemble the photographed flight paths, that the existence of an actual agreement can hardly be denied. A discussion of the results is given in §22.

The following six sections present flight path pictures for respectively the boomerangs L1, L4, L5, L6, F18 and WU. Numbers between braces, {1}, {2}, {3}, {3'} indicate the level of the flight paths. Numbers given with the level 1 pictures are the labels of the original 35 mm negatives. Numbers given with the level 2 and level 3 pictures denote respectively: boomerang identification number, f_o (rev/s), V_o (m/s), Ψ_o (degr.), ϑ_o (degr.), φ_o (degr.), ψ_o (degr.), X_o (m), Y_o (m), Z_o (m). And, if there is wind, β (degr.), W_o (m/s), W_1 (m/s/10m). In all computed flights: $\Psi_o = 0°$, $Y_o = 50$ m, $Z_o = 1.8$ m.

For convenient viewing of the stereograms, use the stereo-viewer inserted at the back cover.

§16 *Boomerang L1.*

Level 1: boomerang pictures in fig. 10.1, physical properties in table 10.1. Without "time pill". Plain and weighted. This boomerang was used earlier (October 1967) in field experiments published in [Hess, 1968].
Level 2: boomerang nr. 101.1 (plain) and 101.2 (weighted), see Part II, tabel 31.1.
Level 3: boomerang nr. 195.1 (plain) and 195.2 (weighted), see Part II, table 32.1.
Level 3': boomerang nr. 250.1 (plain) and (251.2 (weighted).
Level 2 and level 3 graphs of aerodynamic force components: Part II, fig. 31.7 through 31.12.

List of flight path pictures for boomerang L1 plain:

fig.	level	negatives or boomerang nr.	f_o	V_o	Ψ_o	ϑ_o	φ_o	ψ_o	X_o	Y_o	Z_o	β_o	W_o	W_l
16.1a	1	7R6/L6A												
b,e	2	101.1	10	25	0	85	-175	-15	0	50	1.8	0	0	0
c,f	3	195.1	10	25	0	90	-175	-15	0	50	1.8	0	0	0
d,g	3'	250.1	10	25	0	90	-175	-15	0	50	1.8	0	0	0
16.2a	1	11R30A/L30												
b,e	2	101.1	11	28	0	90	-100	-15	7	50	1.8	0	0	0
c,f	3	195.1	11	28	0	90	-100	-15	7	50	1.8	0	0	0
d,g	3'	250.1	11	28	0	90	-100	-15	7	50	1.8	0	0	0
16.3a	1	7R31/L31A												
b,e	2	101.1	11	27	0	70	-100	-20	6	50	1.8	0	0	0
c,f	3	195.1	11	27	0	75	-100	-20	6	50	1.8	0	0	0
d,g	3'	250.1	11	27	0	75	-100	-20	6	50	1.8	0	0	0
16.4a	1	7R28/L28A												
b,d	2	101.1	10	24	0	65	-180	-10	-3	50	1.8	0	0	0
c	3	195.1	10	24	0	70	-180	-10	-3	50	1.8	0	0	0
16.5a	1	7R26/L26A												
b,d	2	101.1	10	22	0	45	-185	-25	-3	50	1.8	0	0	0
c	3	195.1	10	22	0	55	-185	-25	-3	50	1.8	0	0	0
16.6a	1	4R8/L7A												
b,d	2	101.1	11	27	0	70	-150	-10	-2	50	1.8	0	0	0
c	3	195.1	11	27	0	75	-150	-10	-2	50	1.8	0	0	0
16.7a	1	4R9/L8A												
b,d	2	101.1	11	28	0	80	-160	-15	-2	50	1.8	0	0	0
c	3	195.1	11	28	0	85	-160	-15	-2	50	1.8	0	0	0
16.8a	1	11R33A/L33												
b,d	2	101.1	12	30	0	85	-160	-10	-5	50	1.8	0	0	0
e	3	195.1	12	30	0	90	-160	-10	-4	50	1.8	0	0	0
16.9a	1	7R18/L18A												
b,d	2	101.1	10	25	0	90	-100	-15	6	50	1.8	0	0	0
c	3	195.1	11	27	0	95	-100	-15	6	50	1.8	0	0	0

fig.	level	negatives or boomerang nr.	f_o	V_o	Ψ_o	ϑ_o	φ_o	ψ_o	X_o	Y_o	Z_o	β_o	W_o	W_l
16.10a	1	7R19/L19A												
b,d	2	101.1	11	27	0	80	-100	-15	6	50	1.8	0	0	0
c	3	195.1	11	27	0	85	-100	-15	6	50	1.8	0	0	0

List of flight path pictures for boomerang L1 weighted:

fig.	level	negatives or boomerang nr.	f_o	V_o	Ψ_o	ϑ_o	φ_o	ψ_o	X_o	Y_o	Z_o	β	W_o	W_l
16.11a	1	11R21A/L21												
b,e	2	101.2	11	27	0	85	-170	-15	0	50	1.8	0	0	0
c,f	3	195.2	11	27	0	85	-170	-15	0	50	1.8	0	0	0
d,g	3'	251.2	11	27	0	85	-170	-15	0	50	1.8	0	0	0
16.12a	1	11R7A/L7												
b,d	2	101.2	11	27	0	80	-160	-15	2	50	1.8	0	0	0
c	3	195.2	11	27	0	85	-160	-15	2	50	1.8	0	0	0
16.13a	1	11R8A/L8												
b,d	2	101.2	11	27	0	80	-165	-20	2	50	1.8	0	0	0
c	3	195.2	11	27	0	90	-165	-20	2	50	1.8	0	0	0
16.14a	1	11R24A/L24												
b,d	2	101.2	11	27	0	85	-160	-10	0	50	1.8	0	0	0
c	3	195.2	11	27	0	90	-160	-10	0	50	1.8	0	0	0
16.15a	1	11R22A/L22												
b,d	2	101.2	11	27	0	65	-155	-10	2	50	1.8	0	0	0
c	3	195.2	11	27	0	70	-155	-10	2	50	1.8	0	0	0
16.16a	1	11R25A/L25												
b,d	2	101.2	10	25	0	75	- 90	-10	9	50	1.8	0	0	0
c	3	195.2	10	25	0	80	- 90	-10	9	50	1.8	0	0	0
16.17a	1	11R27A/L27												
b,d	2	101.2	11	27	0	70	-100	-15	11	50	1.8	0	0	0
c	3	195.2	11	27	0	75	-100	-15	11	50	1.8	0	0	0
16.18a	1	11R11A/L11												
b,d	2	101.2	11	27	0	80	-100	-20	12	50	1.8	0	0	0
c	3	195.2	11	27	0	85	-100	-20	12	50	1.8	0	0	0

Comment.

The flight paths of boomerang L1 (plain) typically have a diameter of about 22 m. The weighted boomerang traverses flight paths with a larger diameter than similarly shaped paths of the plain boomerang have. Compare, for instance, fig. 16.1 with fig. 16.14, and, at level 2, fig. 16.10 with fig. 16.12. In the latter case the largest horizontal distance from the launching point is 22.7 m for boomerang 101.1 (plain), and 26.7 m for boomerang 101.2 (weighted). The difference is about 17%.

In the cases presented in this section the agreement between the experimental (level 1) paths and the computed flight paths of boomerangs 101.1 and 101.2 (level 2) is rather good. The agreement between the experimental paths and those of boomerangs 195.1 (level 3) is not quite so good, but still fair. Generally the initial conditions for boomerangs 195.1 and 195.2 were taken the same as for boomerangs 101.1 and 101.2, except for ϑ_o, which mostly was taken 5° greater. As can be seen in figures 16.1, 16.2 and 16.3, the flight paths of boomerang 195.1 are more strongly curved than those of boomerang 101.1. This point is discussed extensively in §22.

The few flight paths presented for boomerangs 250.1 and 251.2 (level 3') were computed with the same initial conditions as those for the corresponding level 3 flights. The agreement with experiment is not so good. Other initial conditions did not lead to significantly better results.

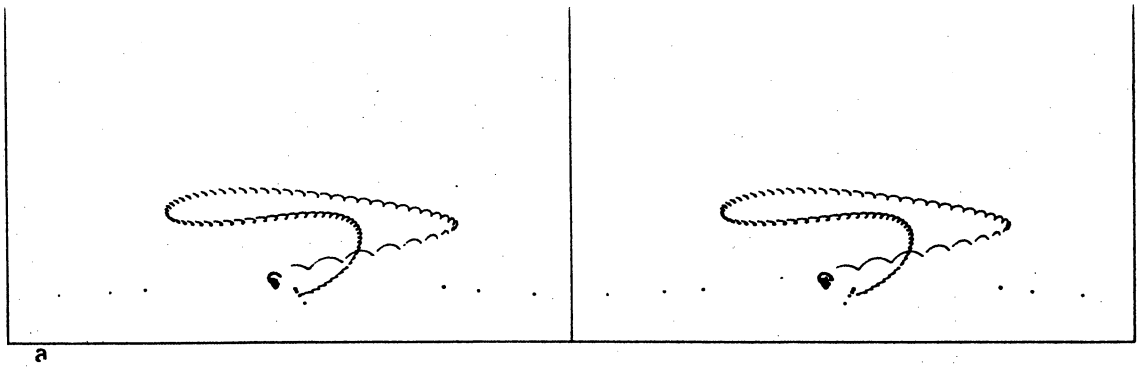

a

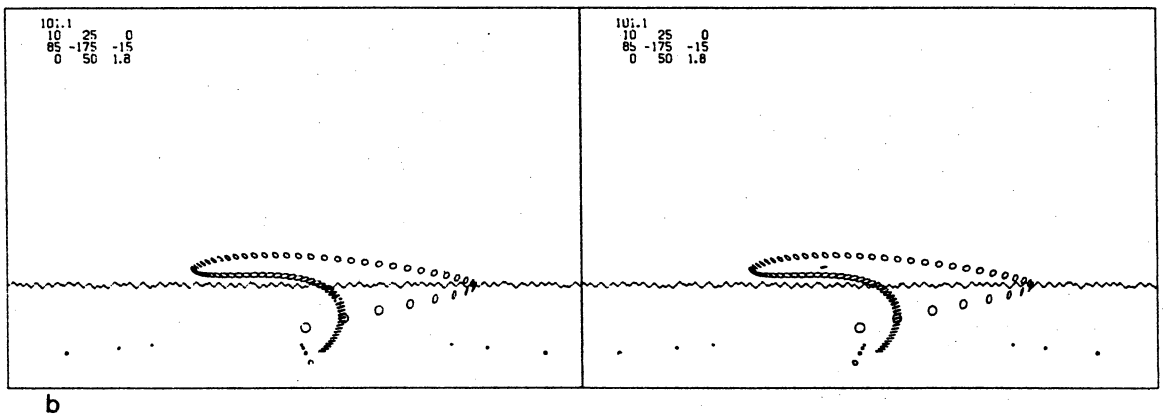

b

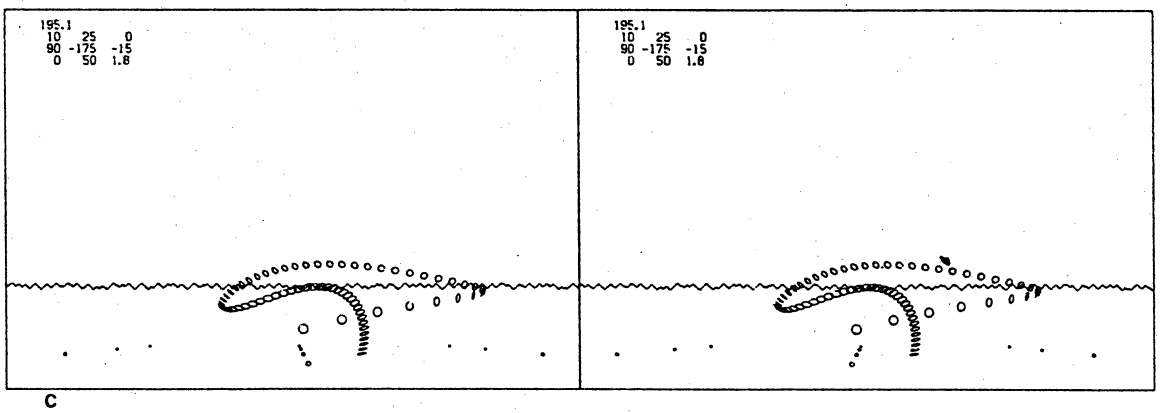

c

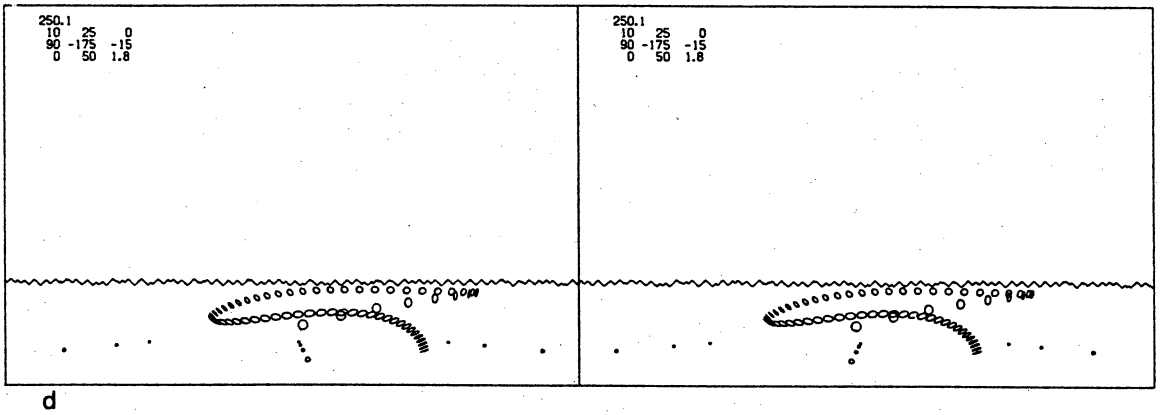

d

fig. 16.1. L1 plain. a: {1}, 7R6/L6A. b,e: {2}. c,f: {3}. d,g: {3'}.

continued on next page.

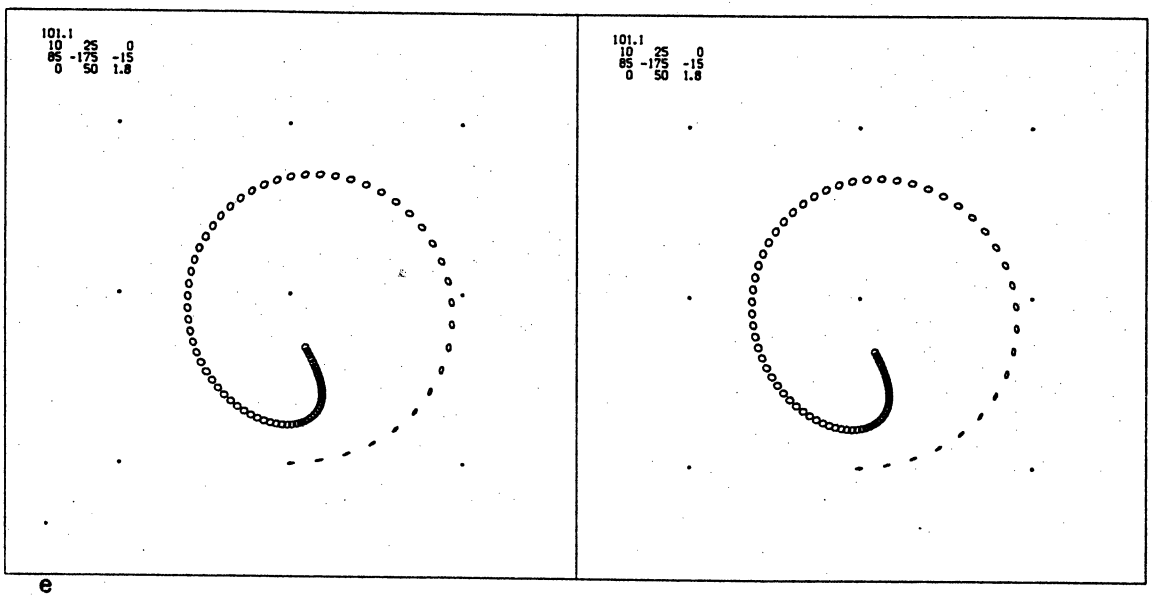

e

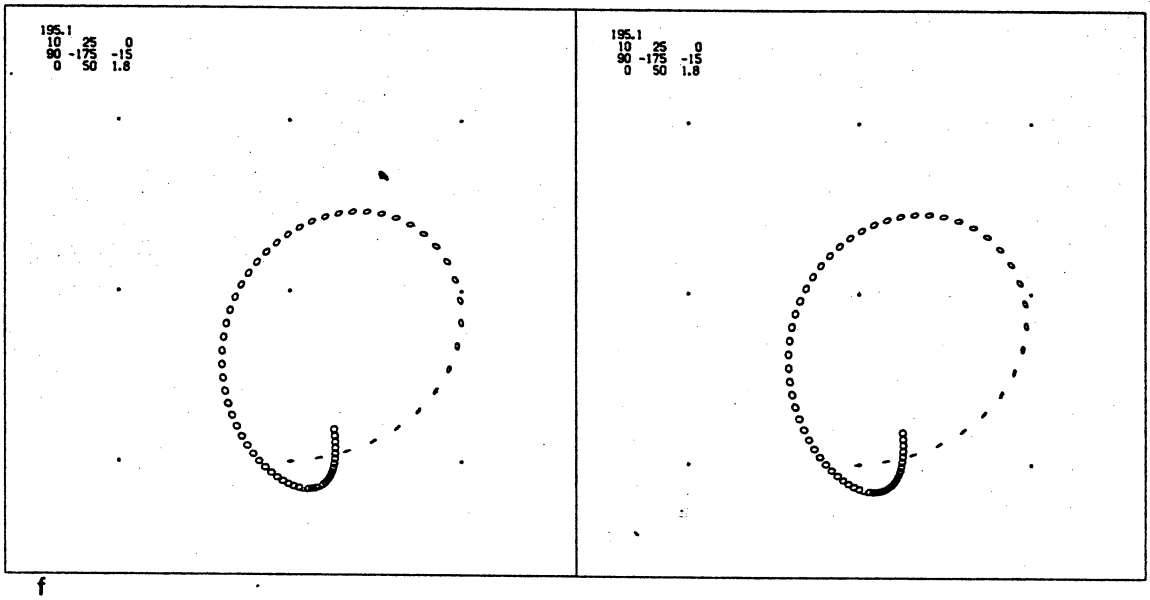

f

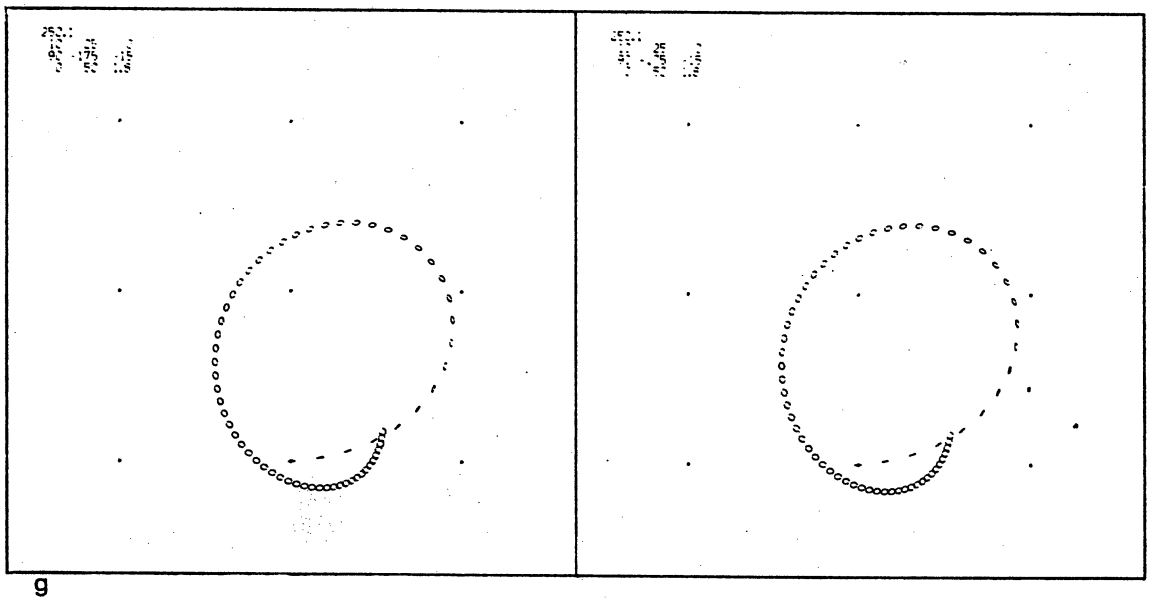

g

fig. 16.1 continued.

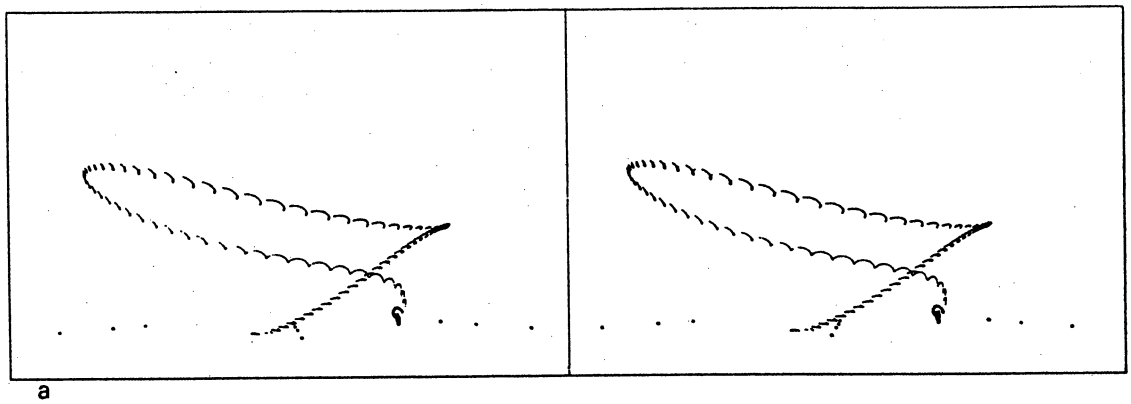

a

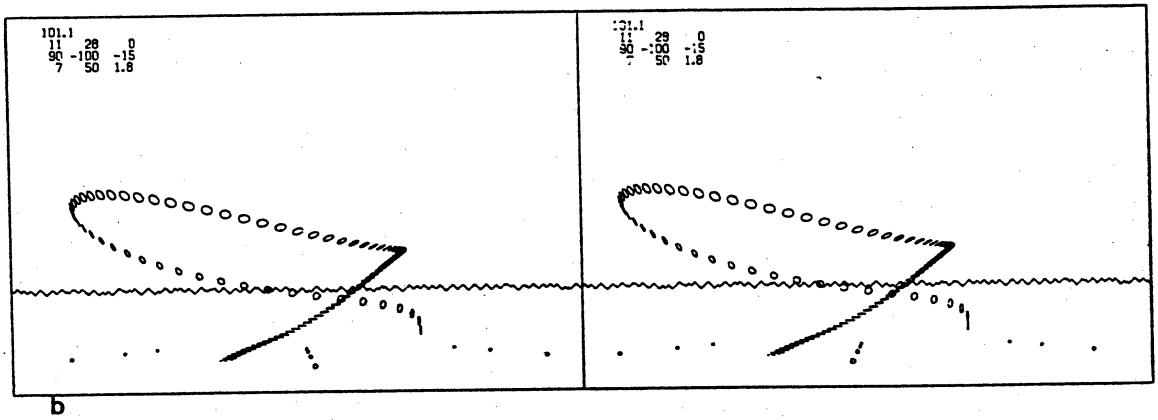

b

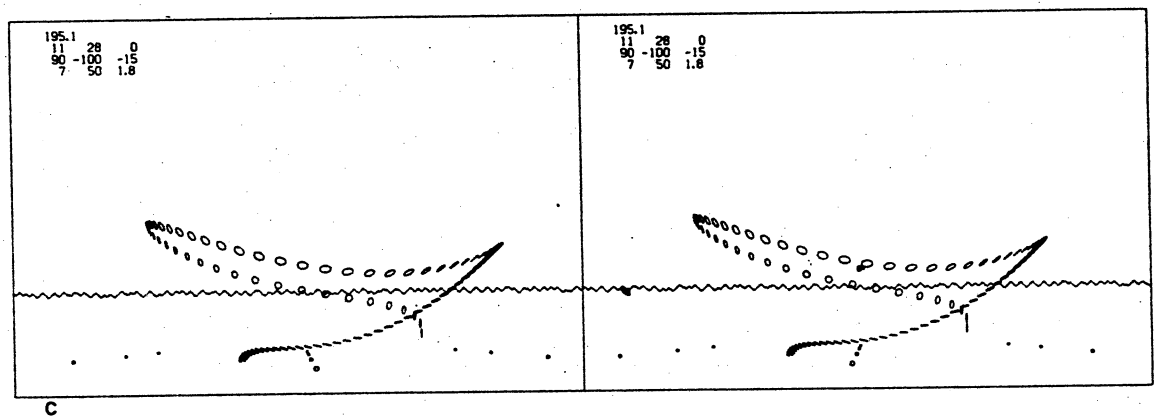

c

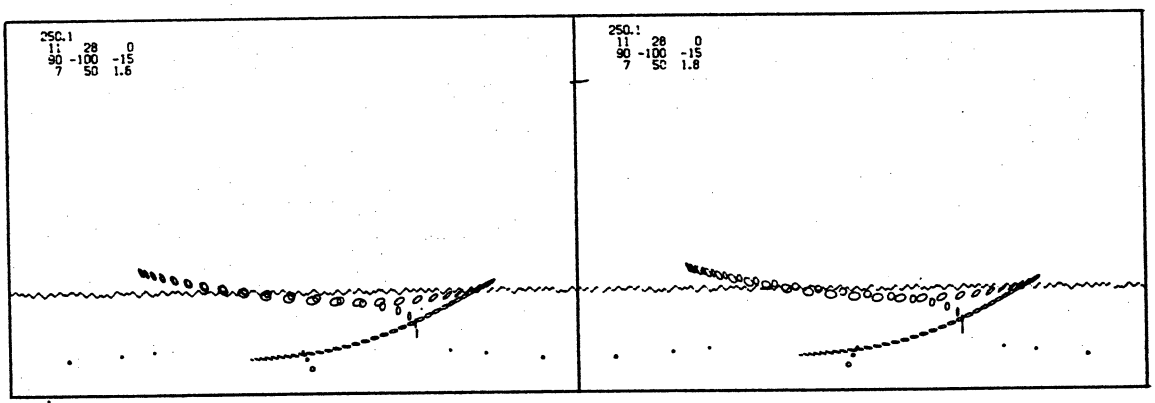

d

fig. 16.2. L1 plain. a: {1}, 11R30A/L30. b,e: {2}. c,f: {3}. d,g: {3'}.
continued on next page.

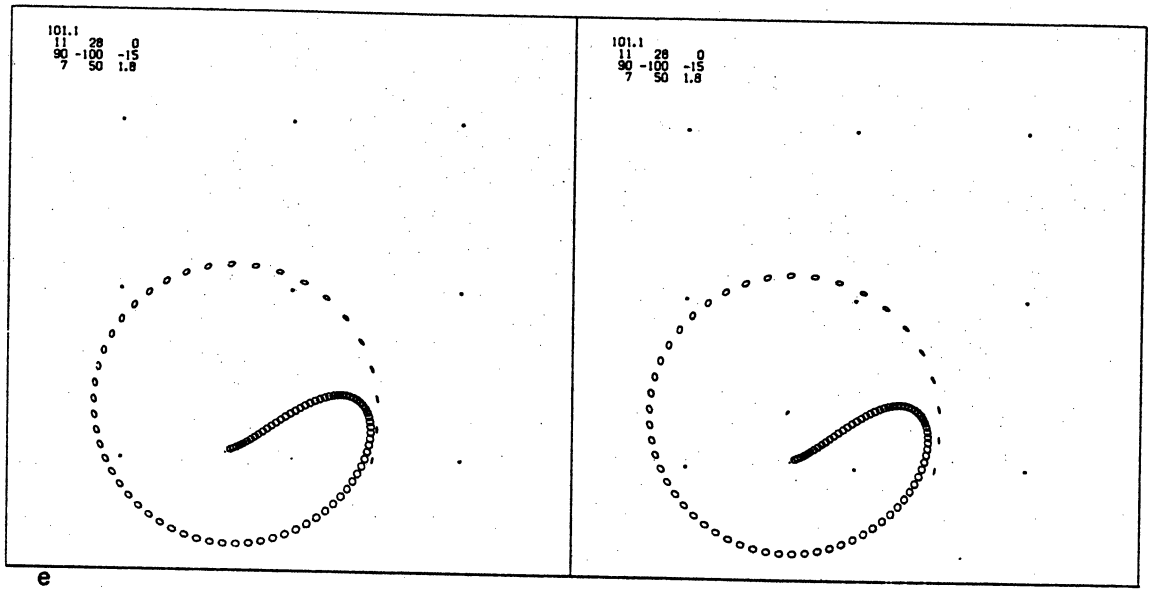

e

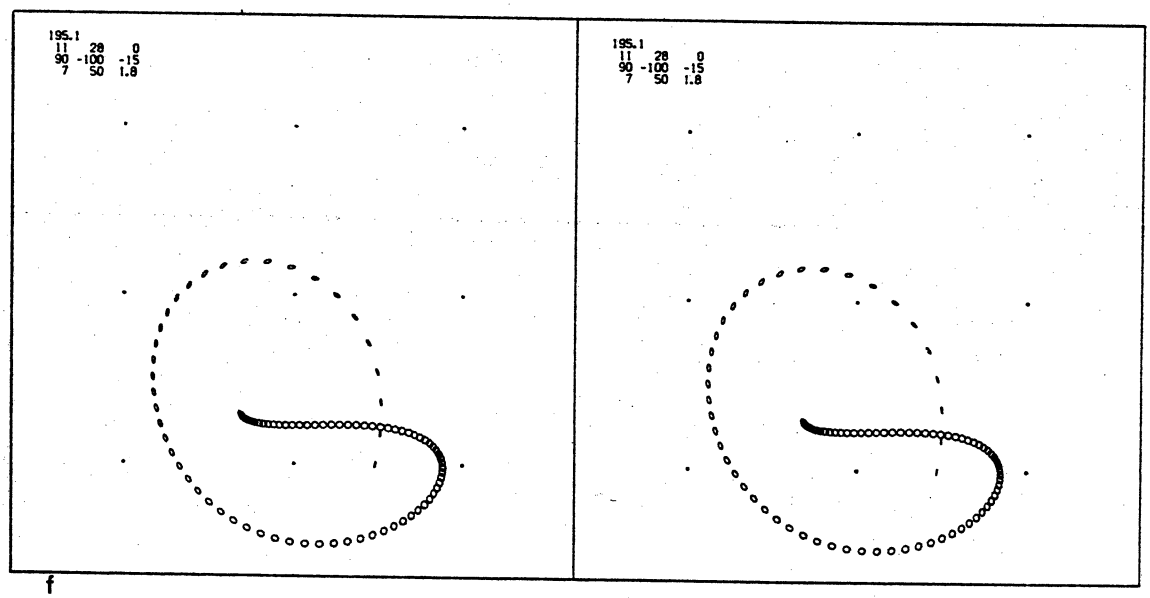

f

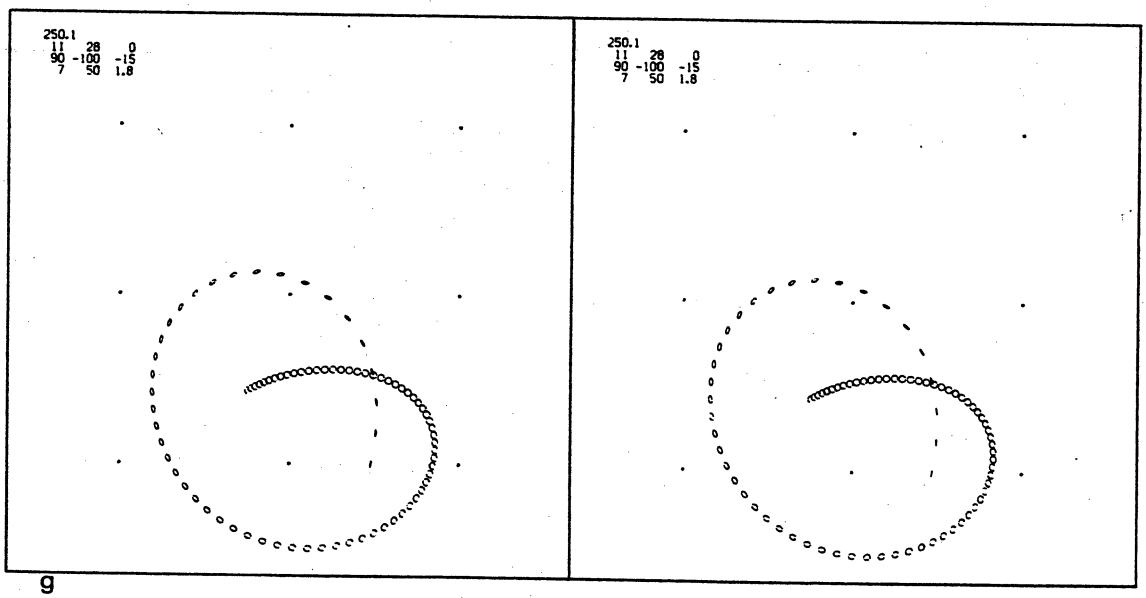

g

fig. 16.2 continued.

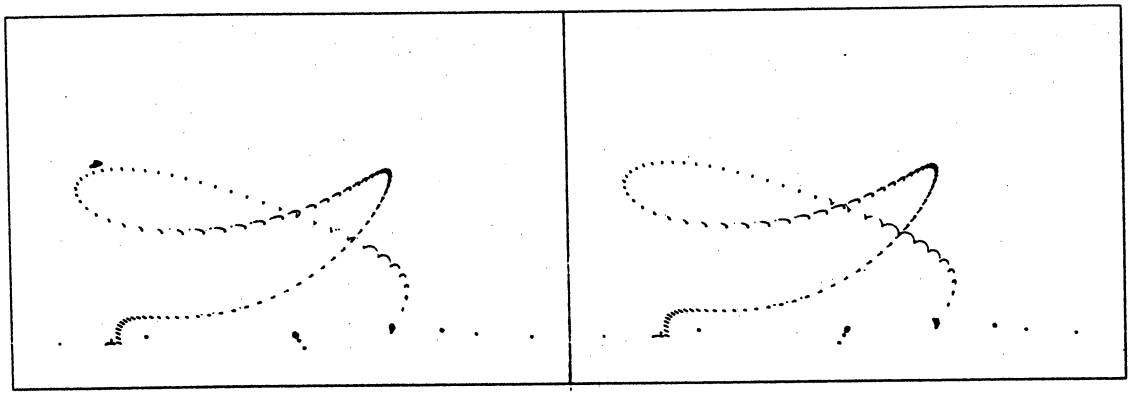

a

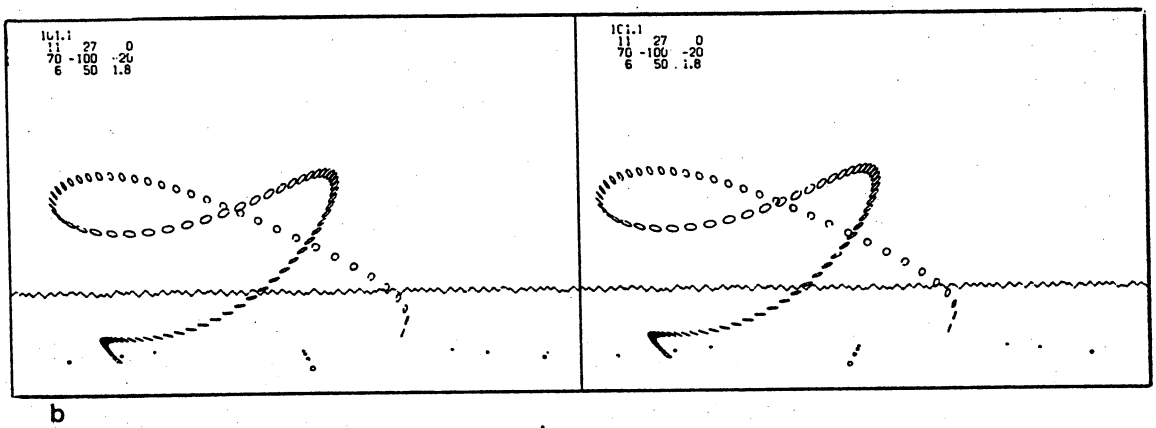

b

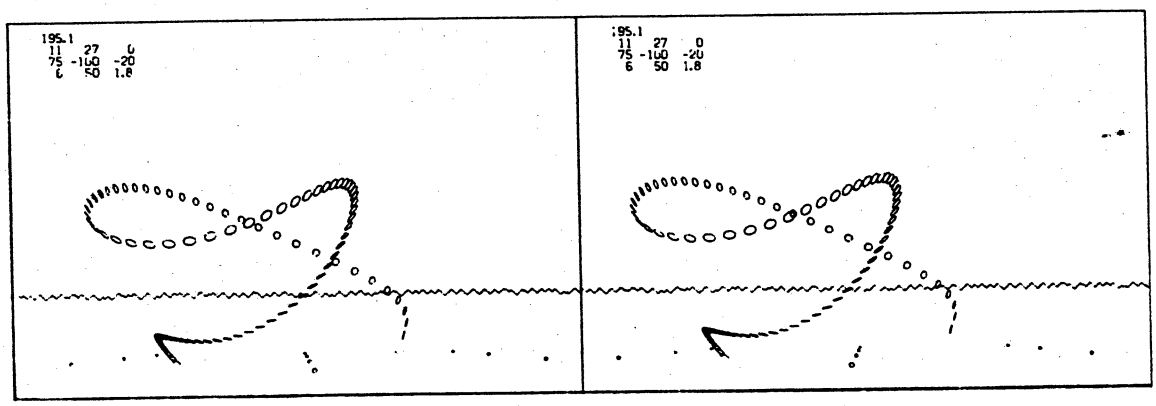

c

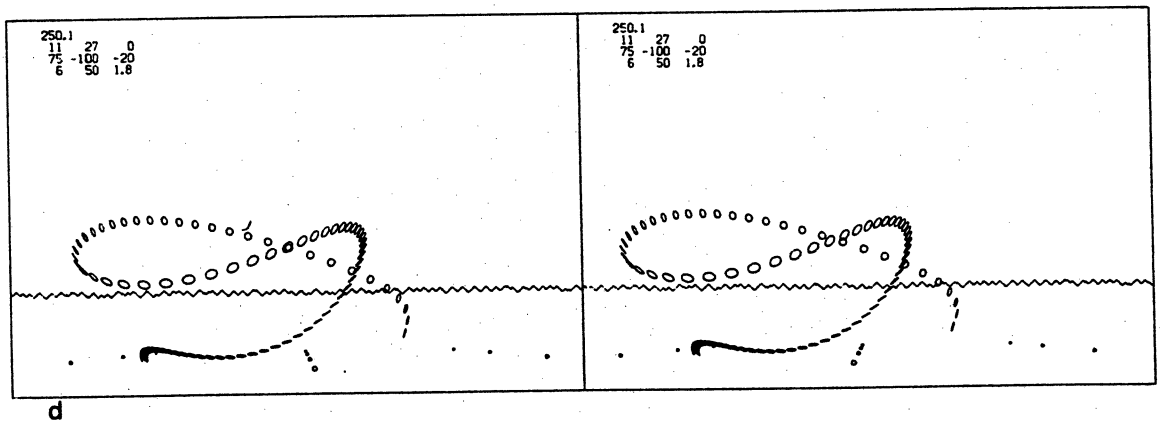

d

fig. 16.3. L1 plain. a: {1}, 7R31/L31A. b,e: {2}. c,f: {3}. d,g: {3'}.

continued on next page.

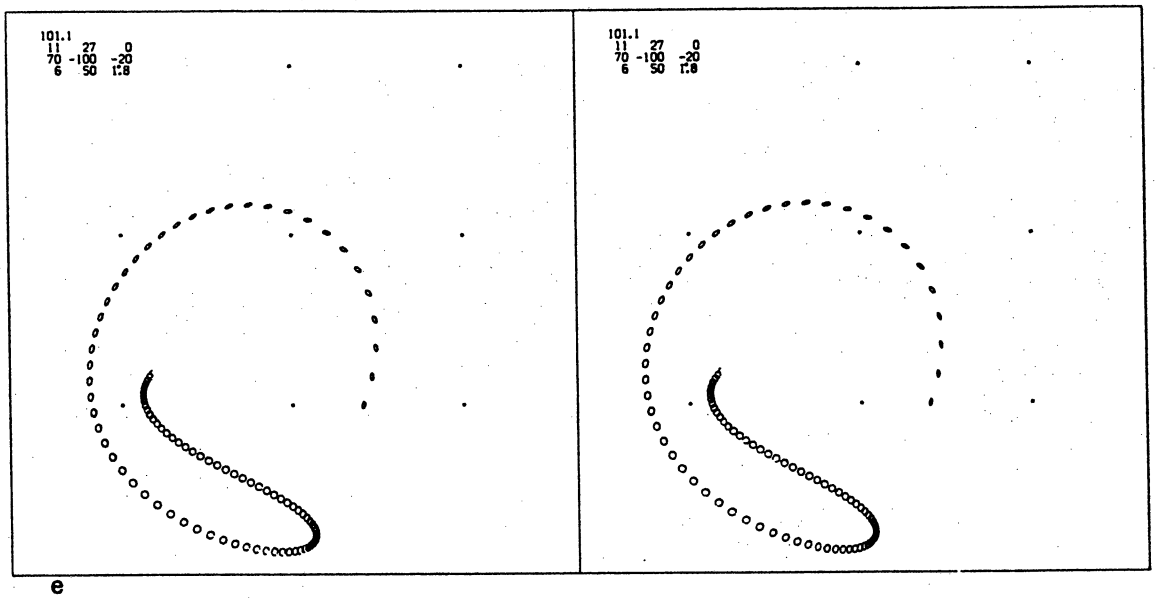

e

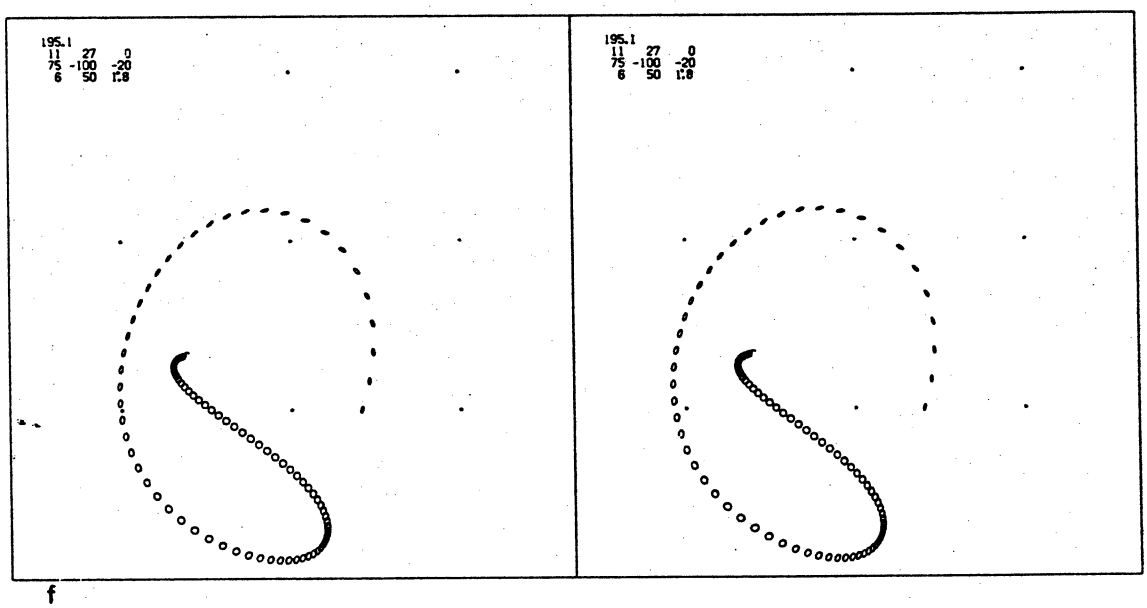

f

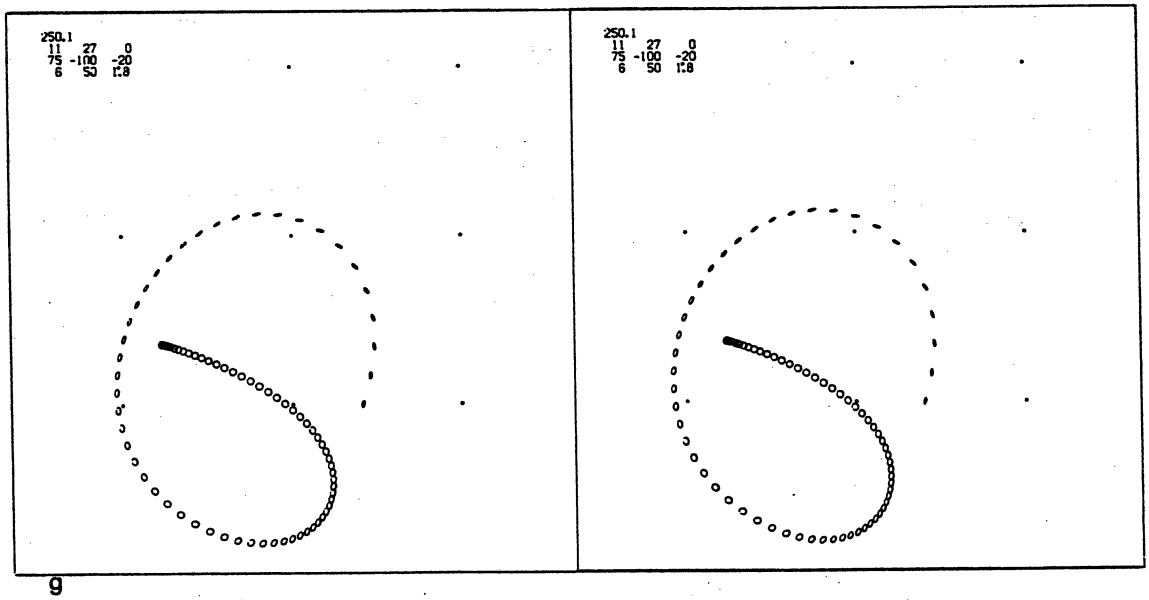

g

fig. 16.3 continued.

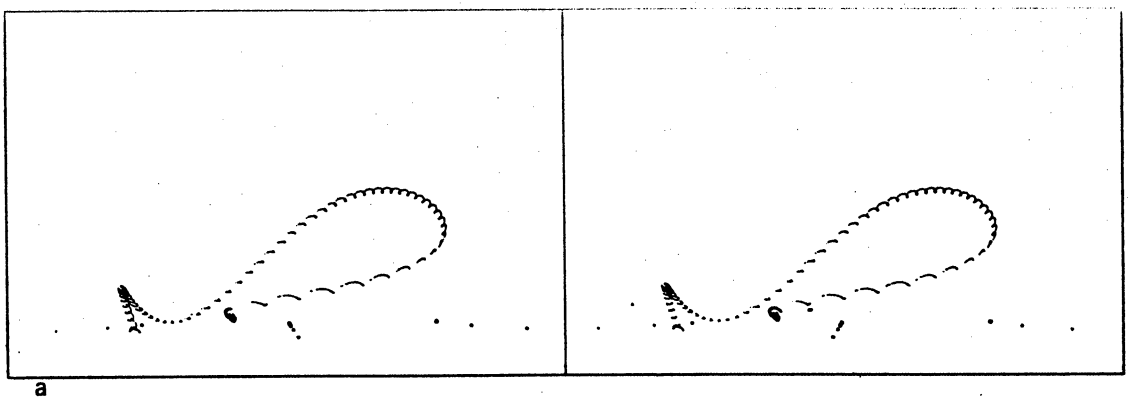

a

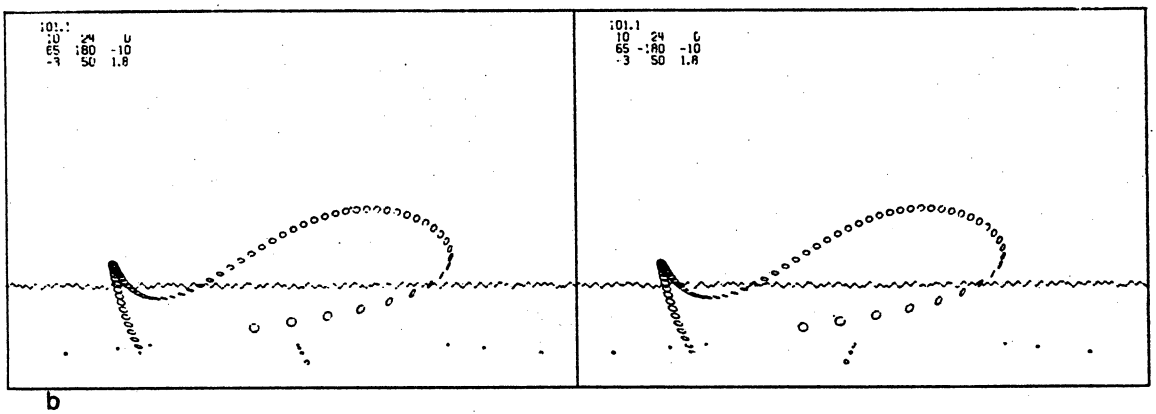

b

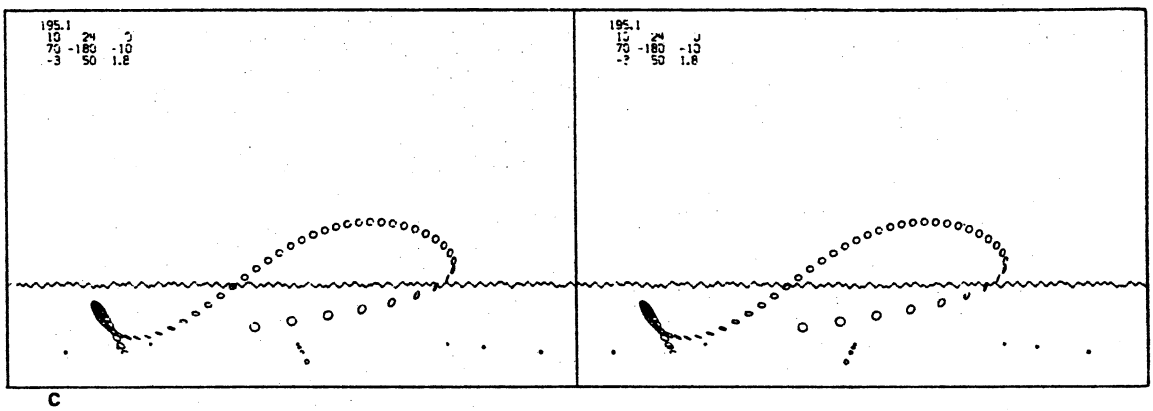

c

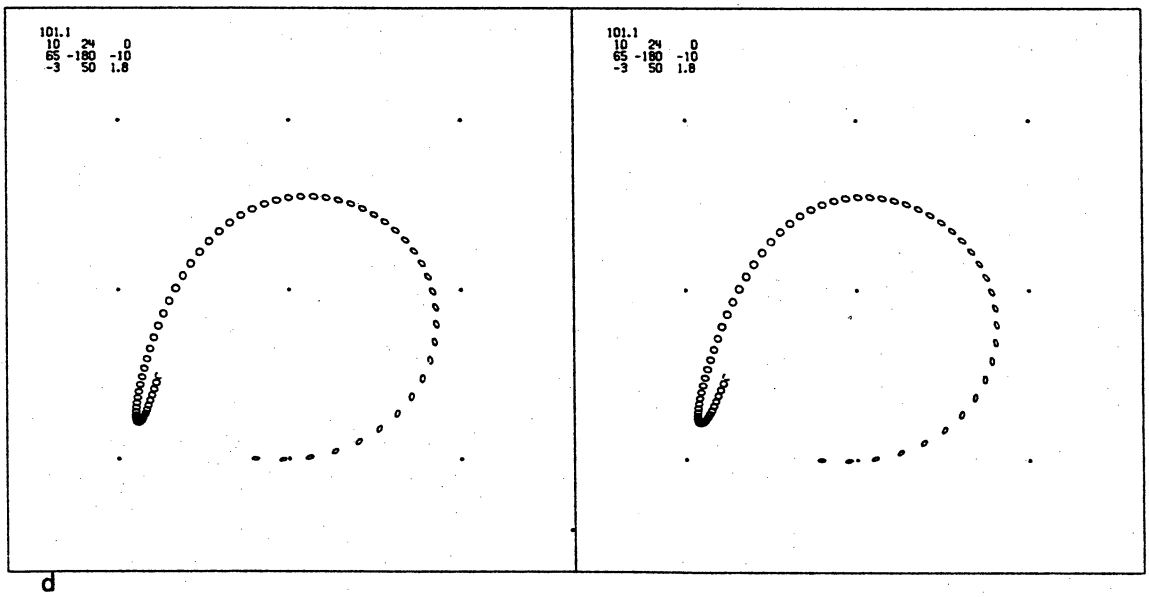

d

fig. 16.4. L1 plain. a: {1}, 7R28/L28A. b,d: {2}. c: {3}.

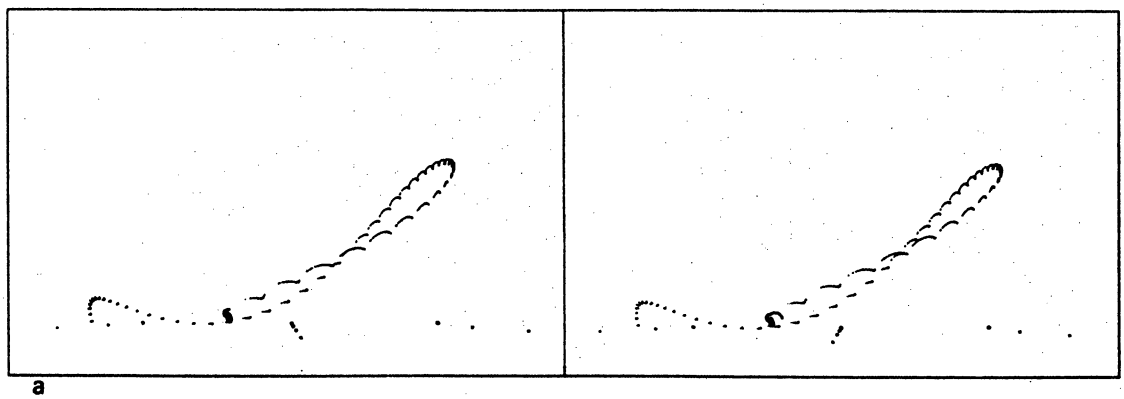

a

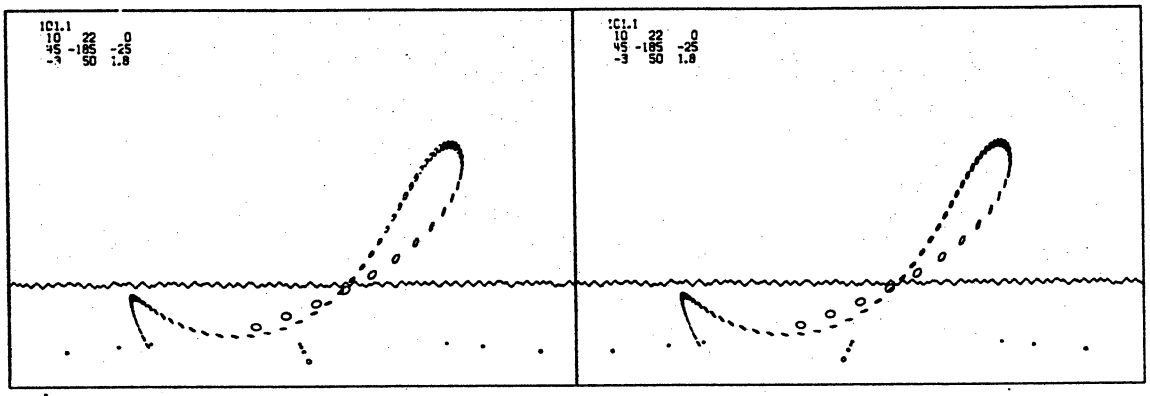

b

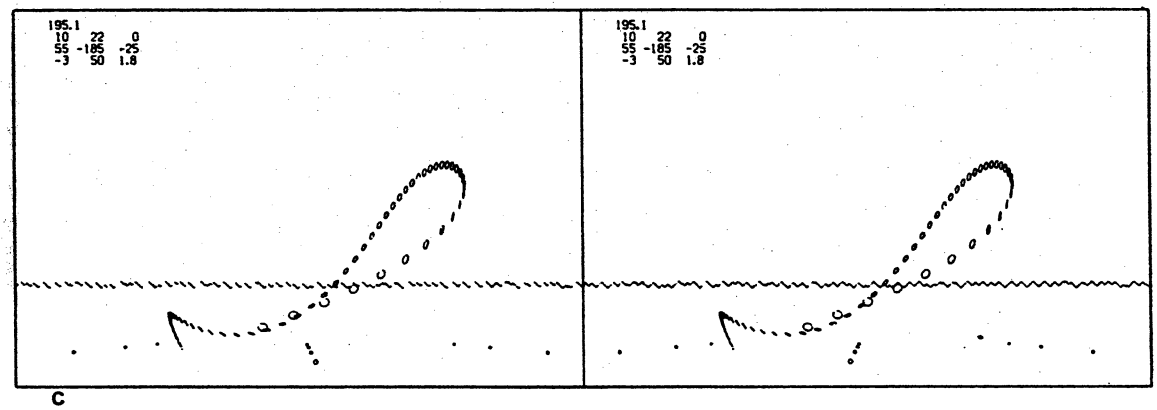

c

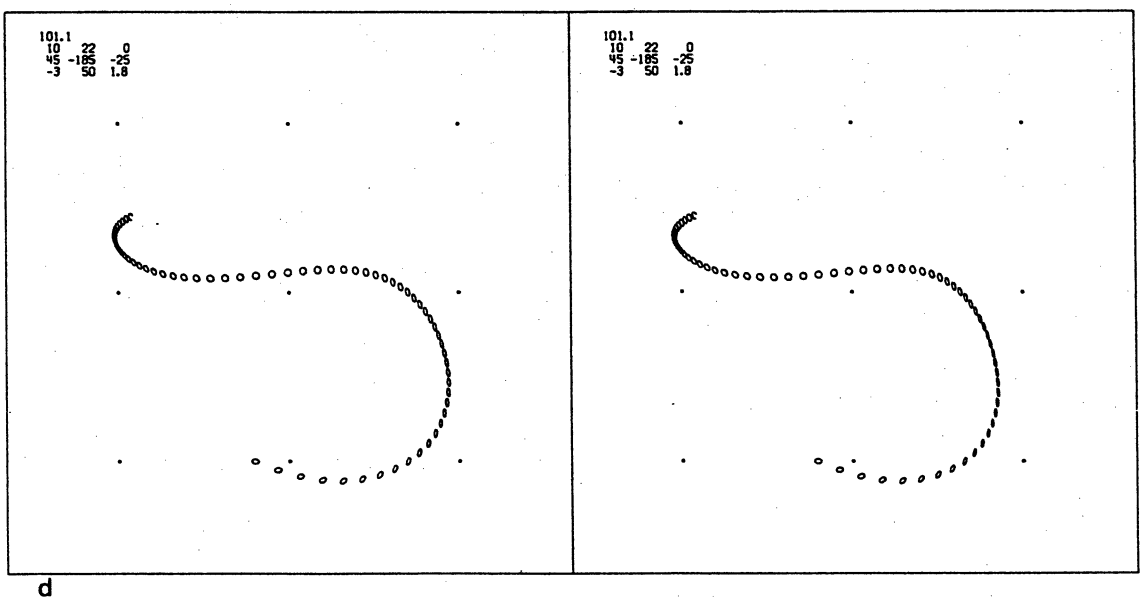

d

fig. 16.5. L1 plain. a: {1}, 7R26/L26A. b,d: {2}. c: {3}.

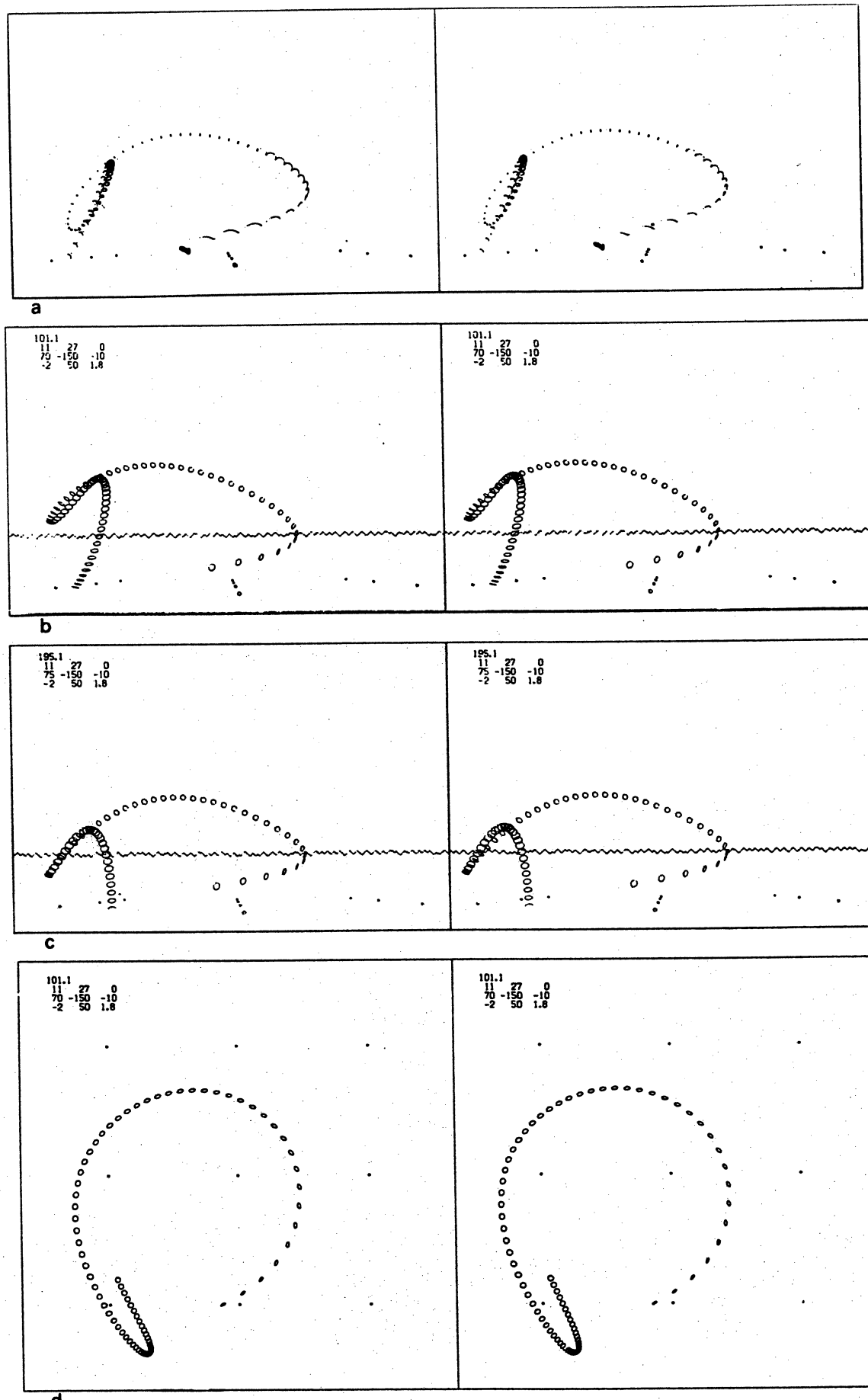

fig. 16.6. L1 plain. a: {1}, 4R8/L7A. b,d: {2}. c: {3}.

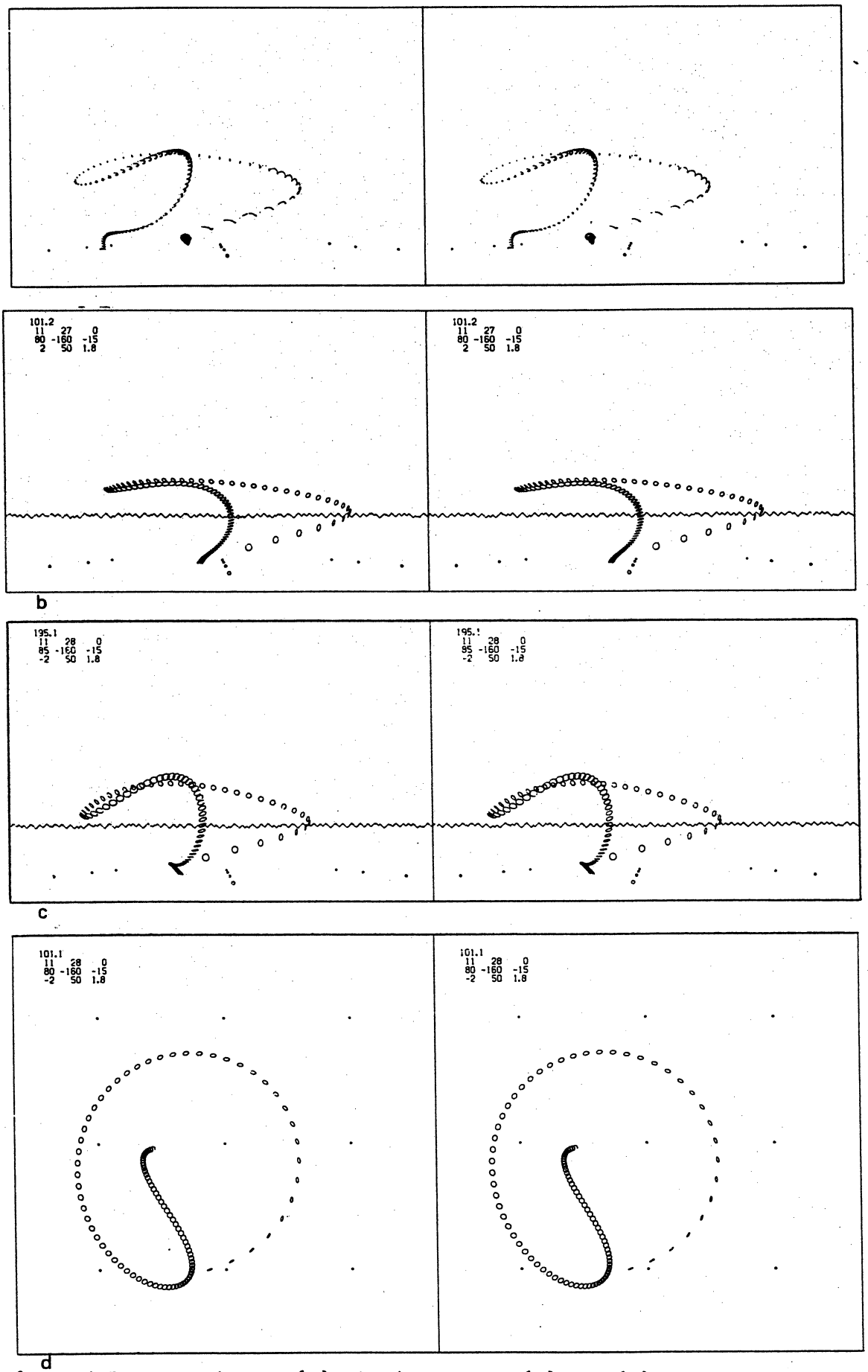

fig. 16.7. L1 plain. a: {1}, 4R9/L8A. b,d: {2}. c: {3}.

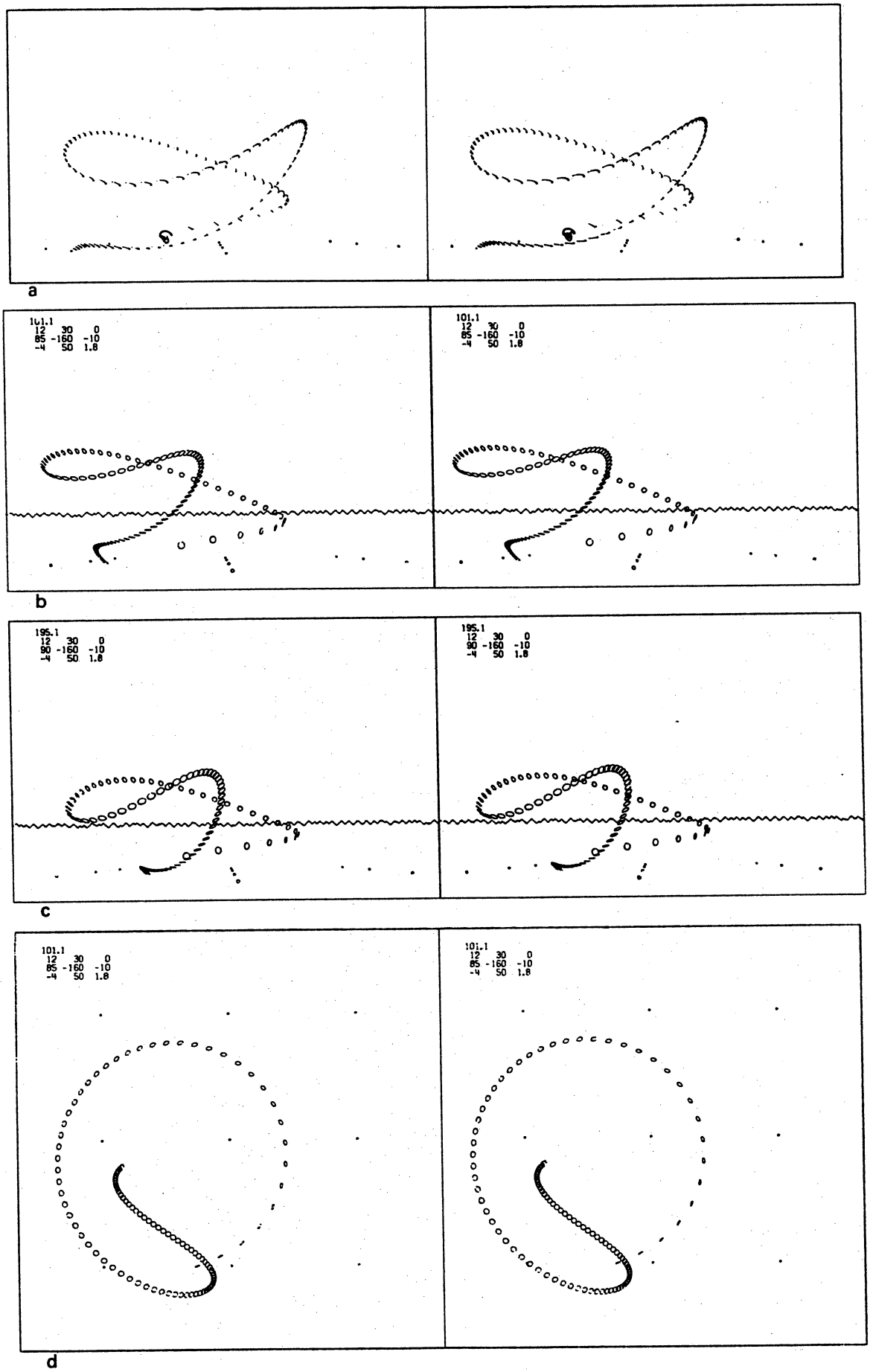

fig. 16.8. L1 plain. a: {1}, 11R33A/L33. b,d: {2}. c: {3}.

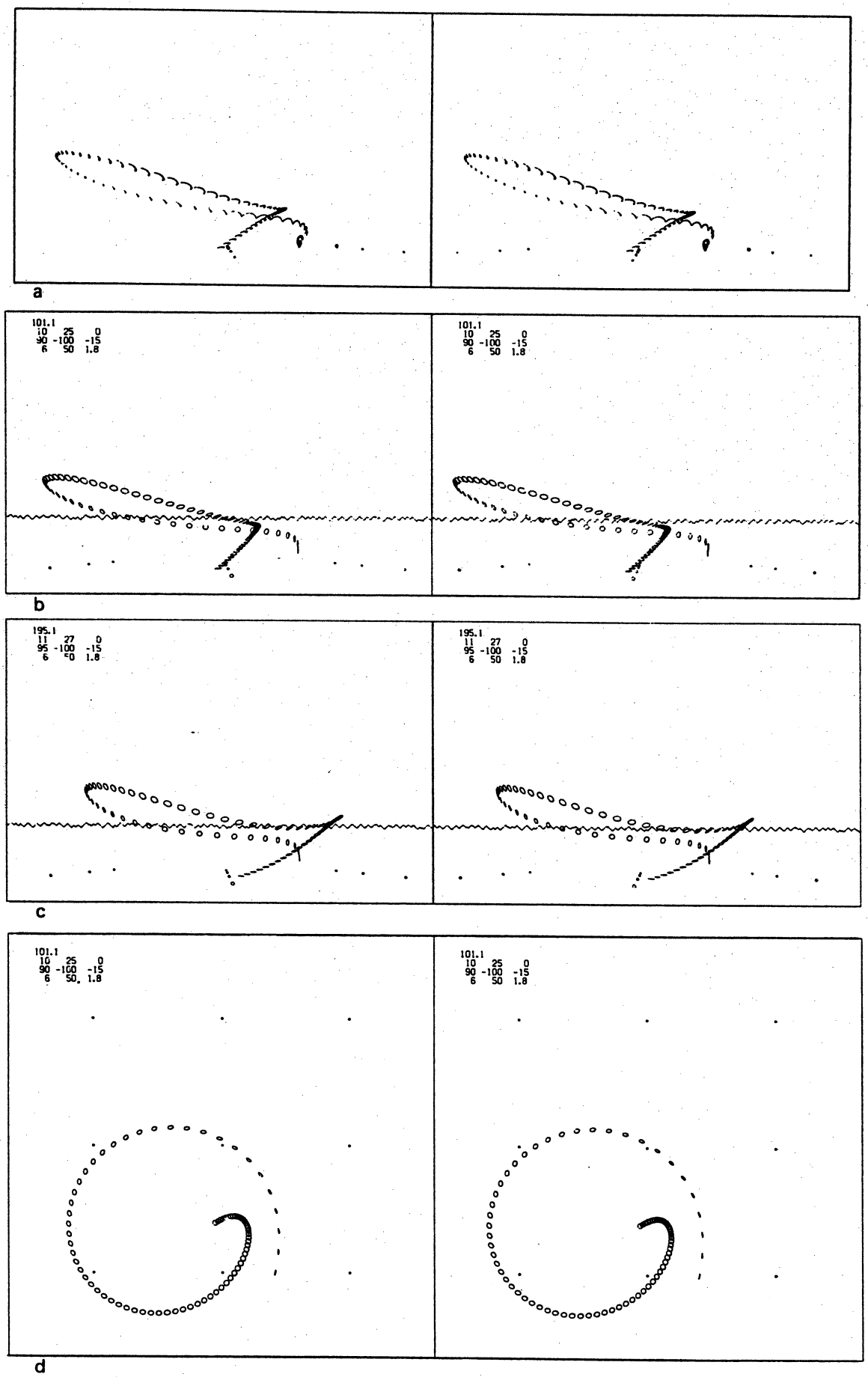

fig. 16.9. L1 plain. a: {1}, 7R18/L18A. b,d: {2}. c: {3}.

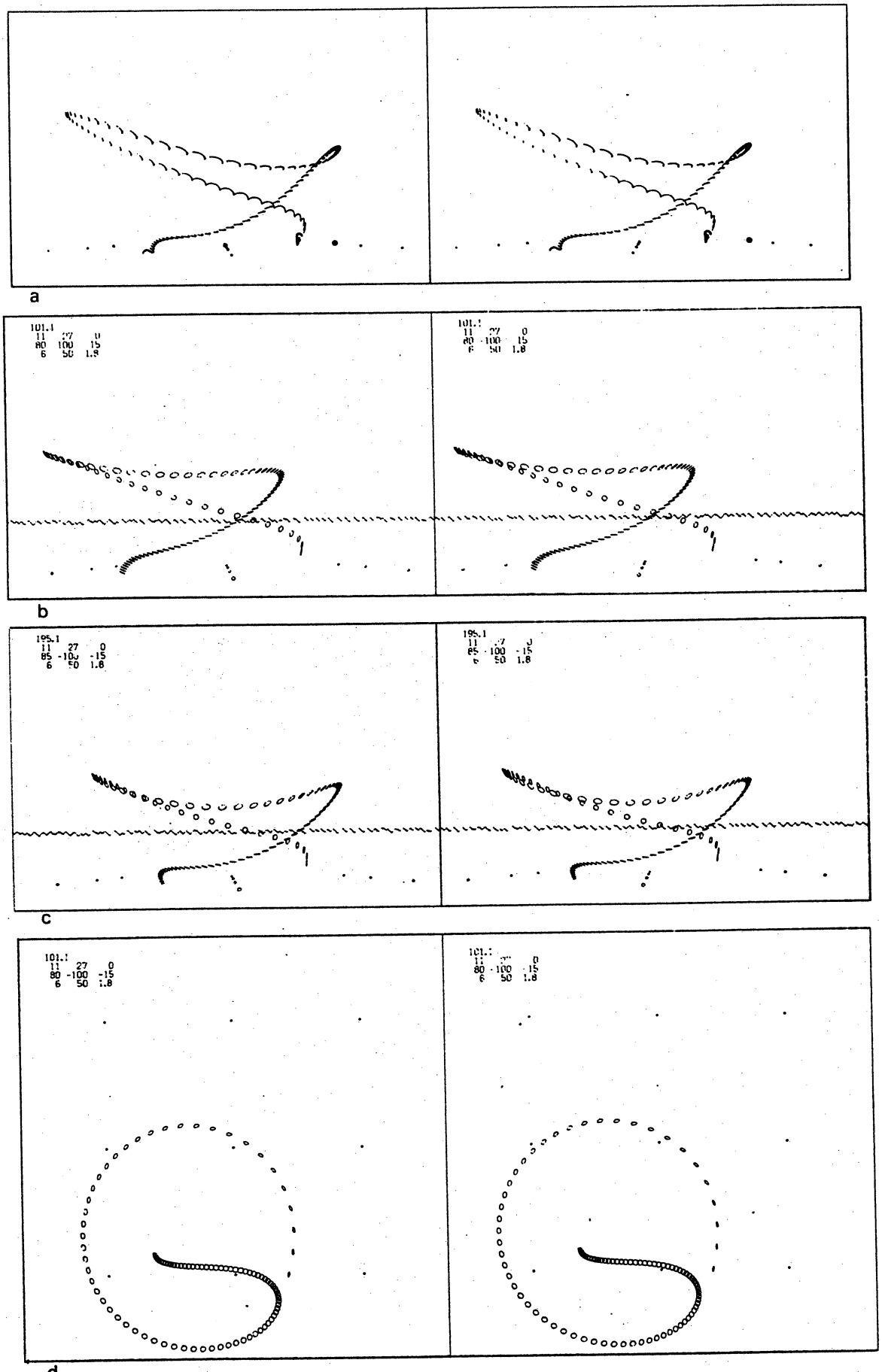

fig. 16.10. L1 plain. a: {1}, 7R19/L19A. b,d: {2}. c: {3}.

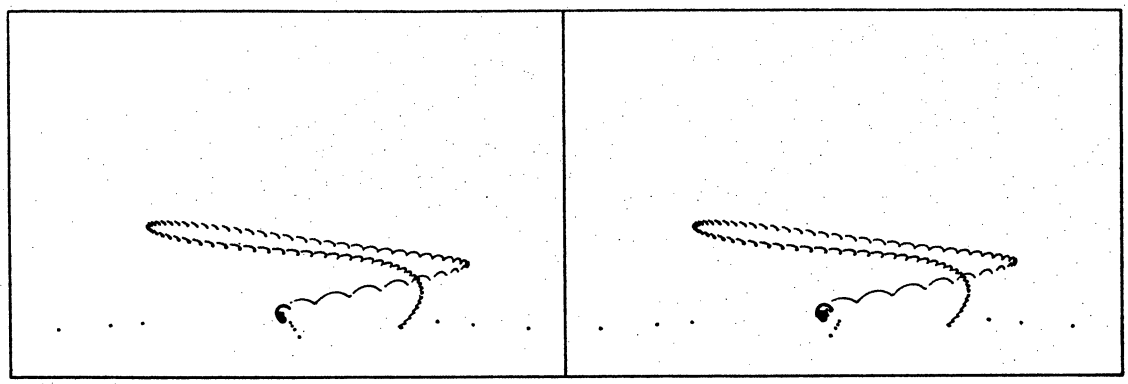

a

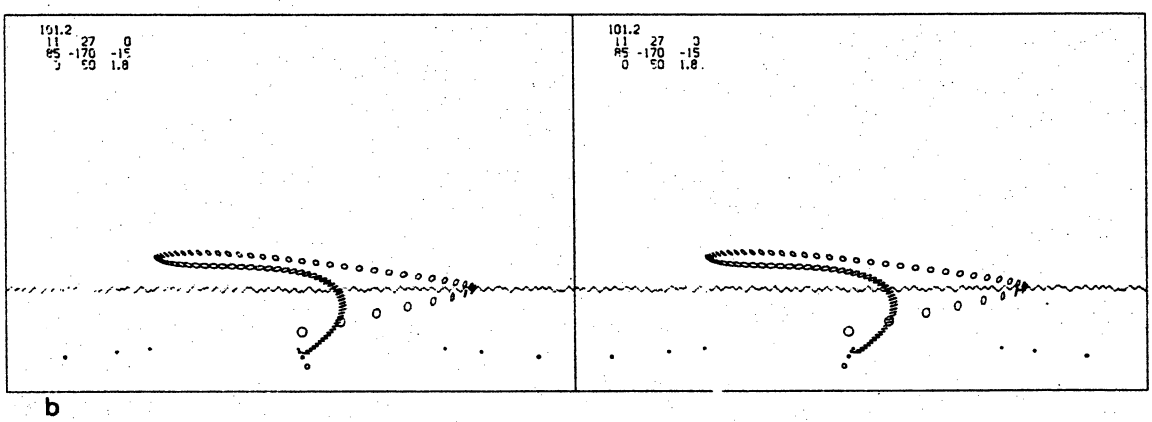

b

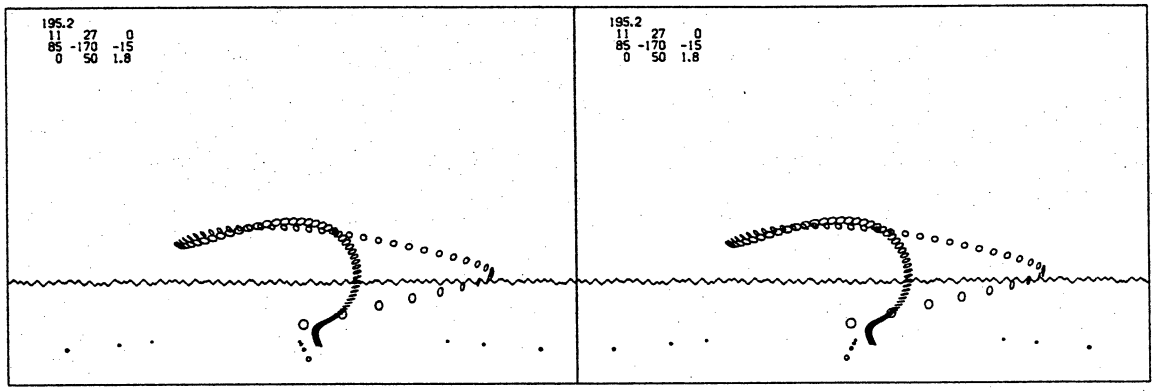

c

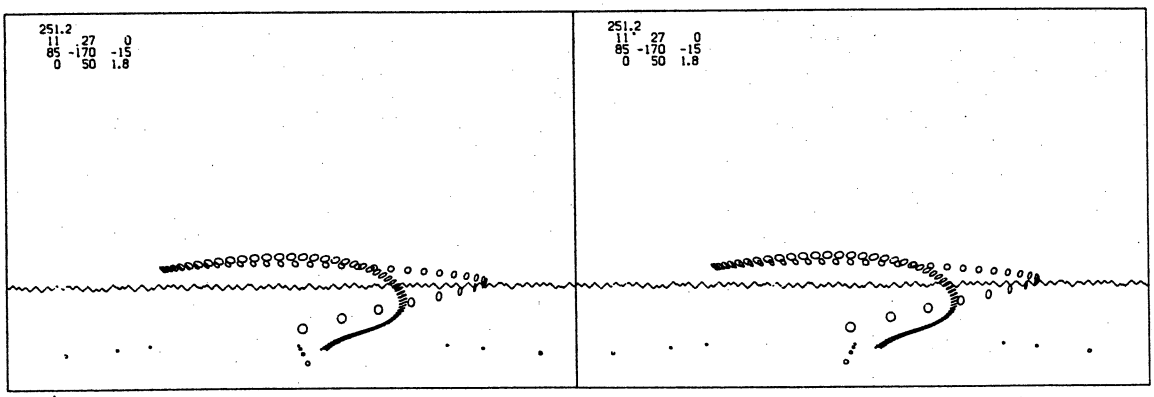

d

fig. 16.11. L1 weighted. a: {1}, 11R21A/L21. b,e: {2}. c,f: {3}. d,g: {3'}. continued on next page.

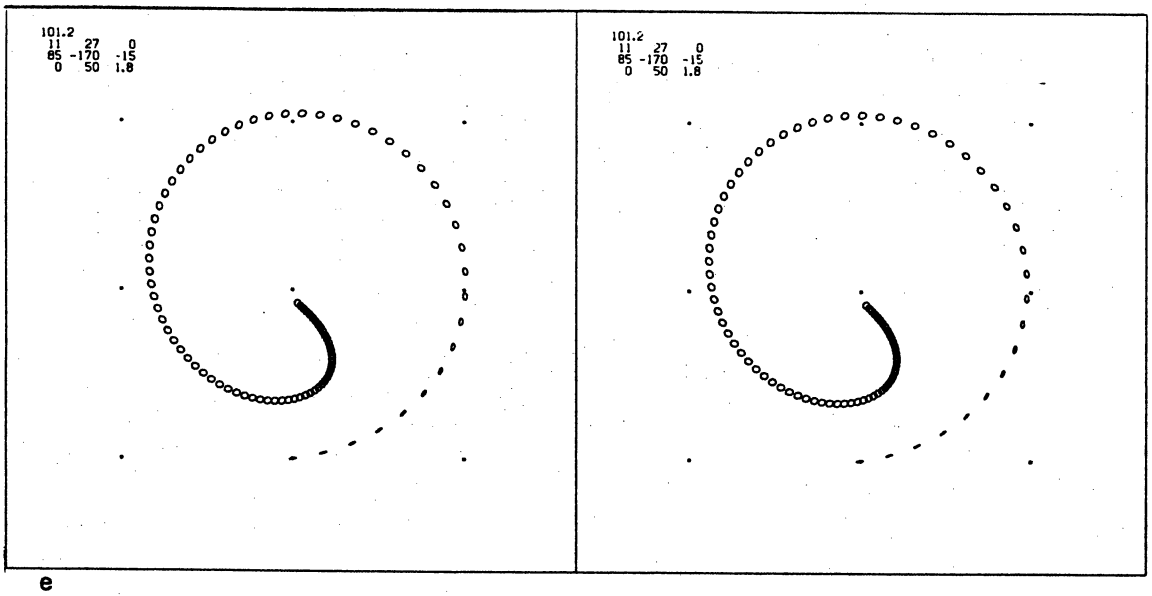

e

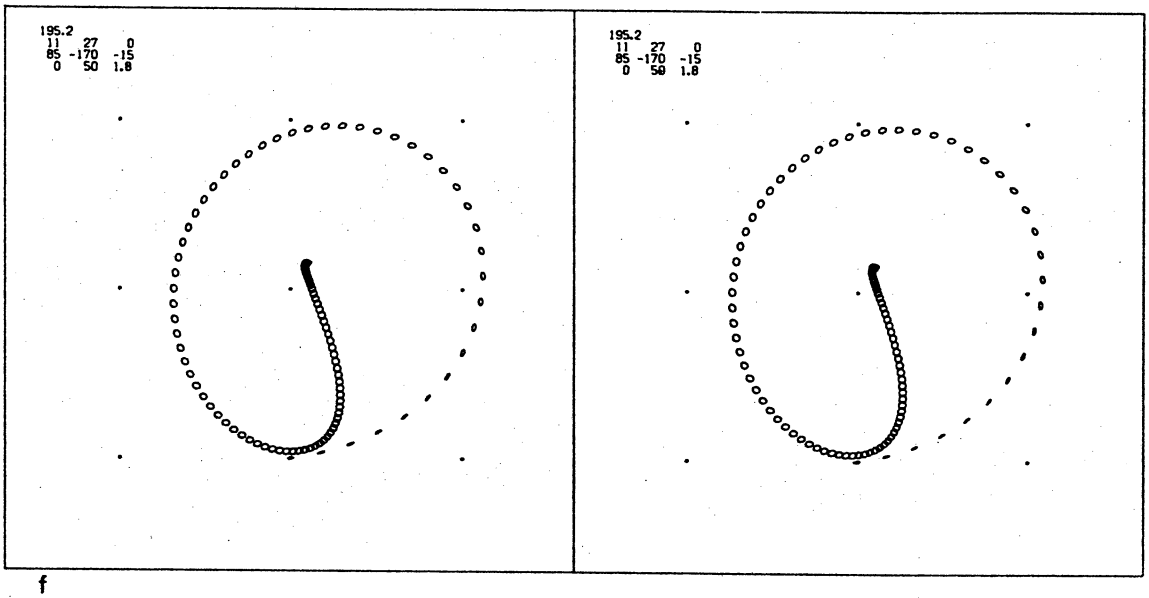

f

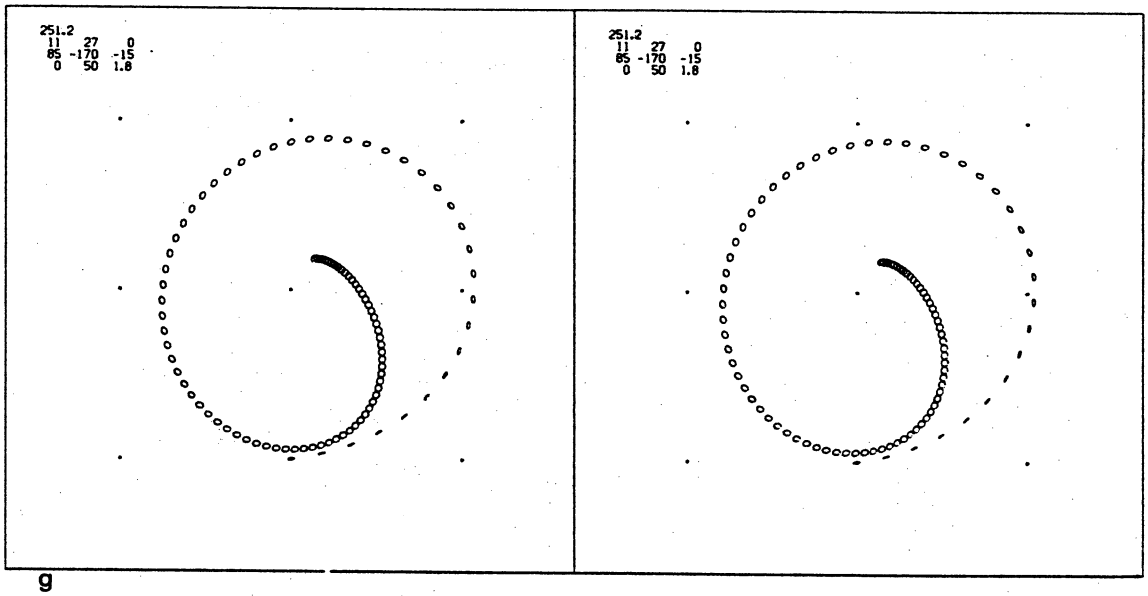

g

fig. 16.11 continued.

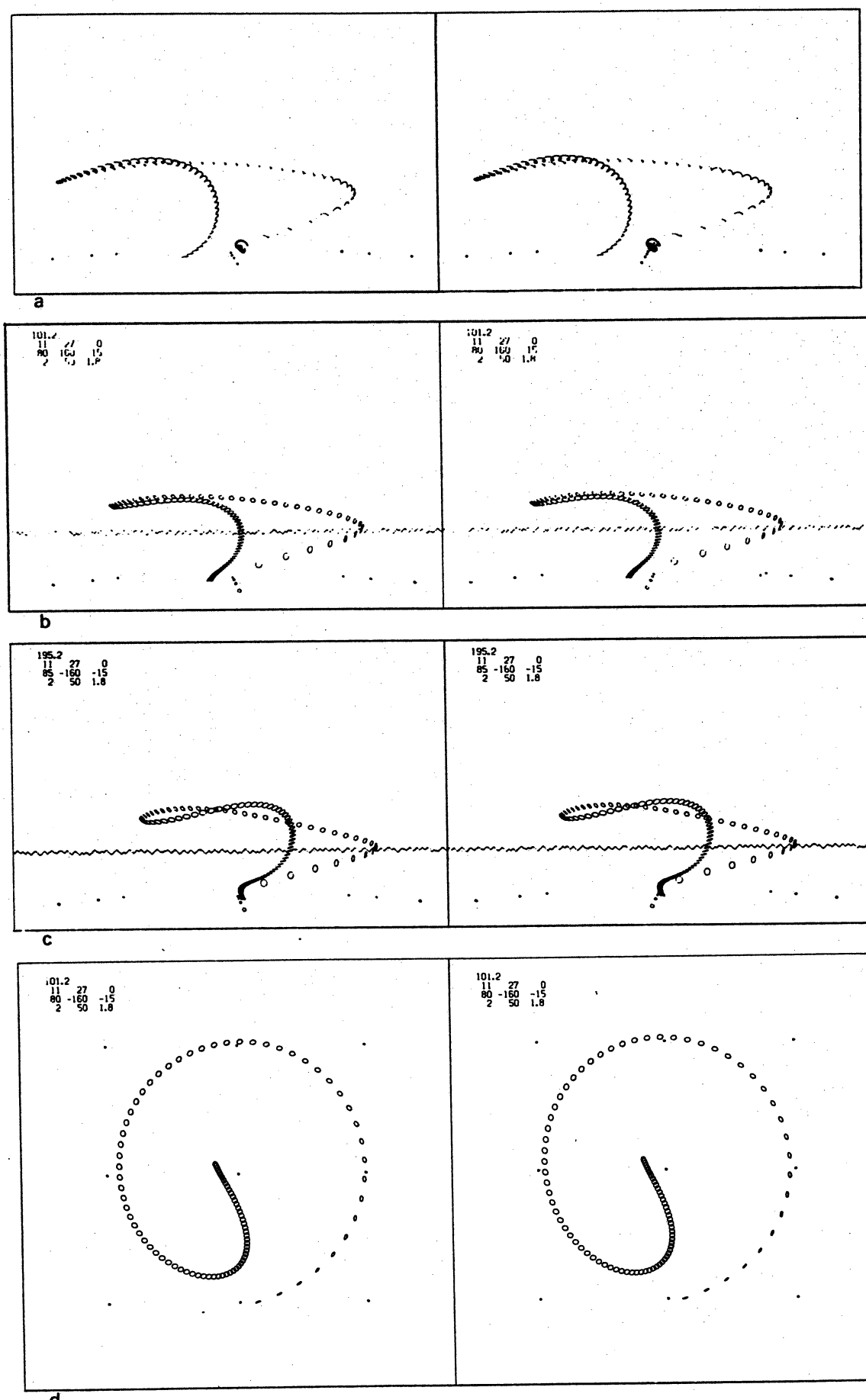

fig. 16.12. L1 weighted. a: {1}, 11R7A/L7. b,d: {2}. c: {3}.

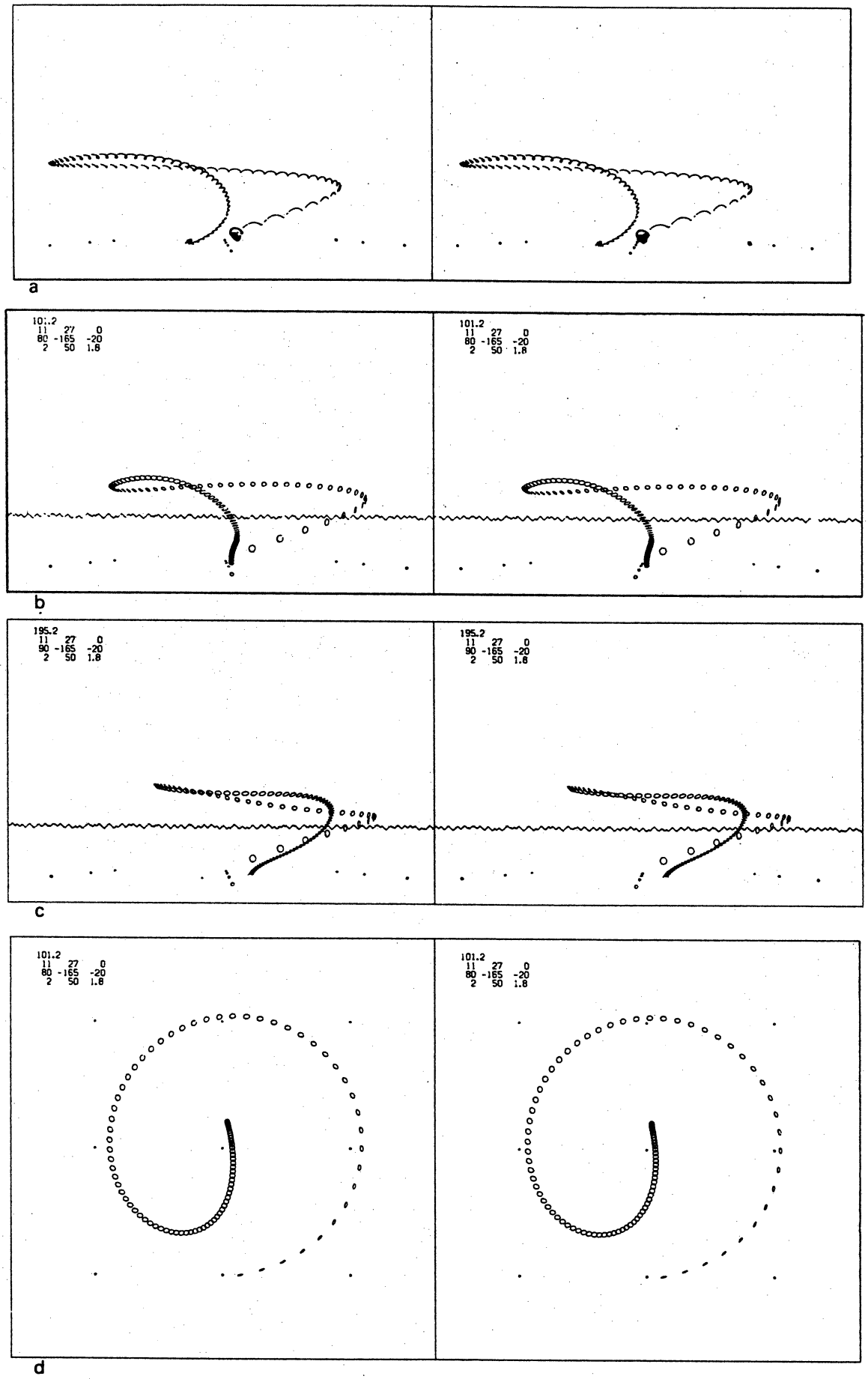

fig. 16.13. L1 weighted. a: {1}, 11R8A/L8. b,d: {2}. c: {3}.

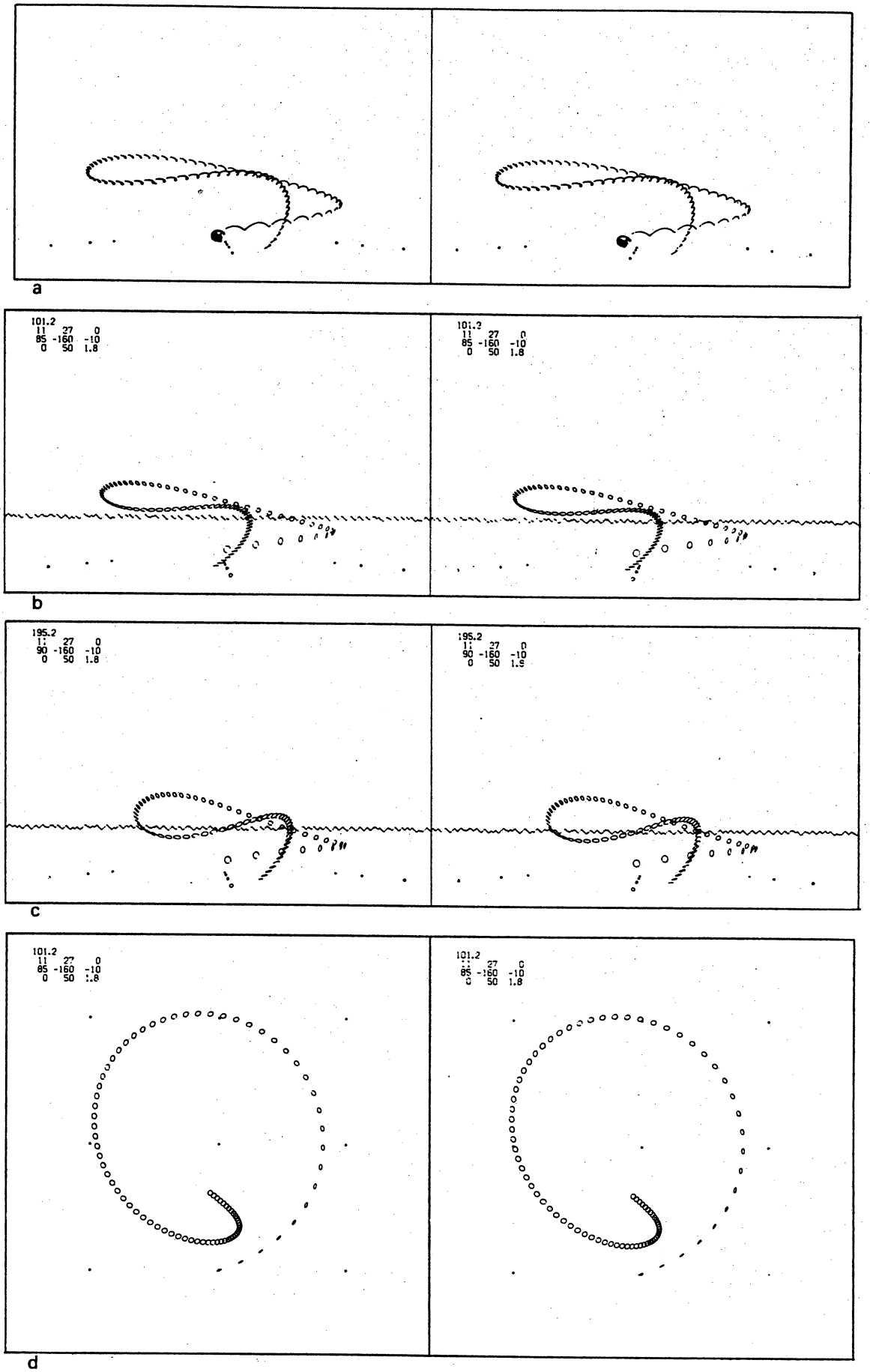

fig. 16.14. L1 weighted. a: {1}, 11R24A/L24. b,d: {2}. c: {3}.

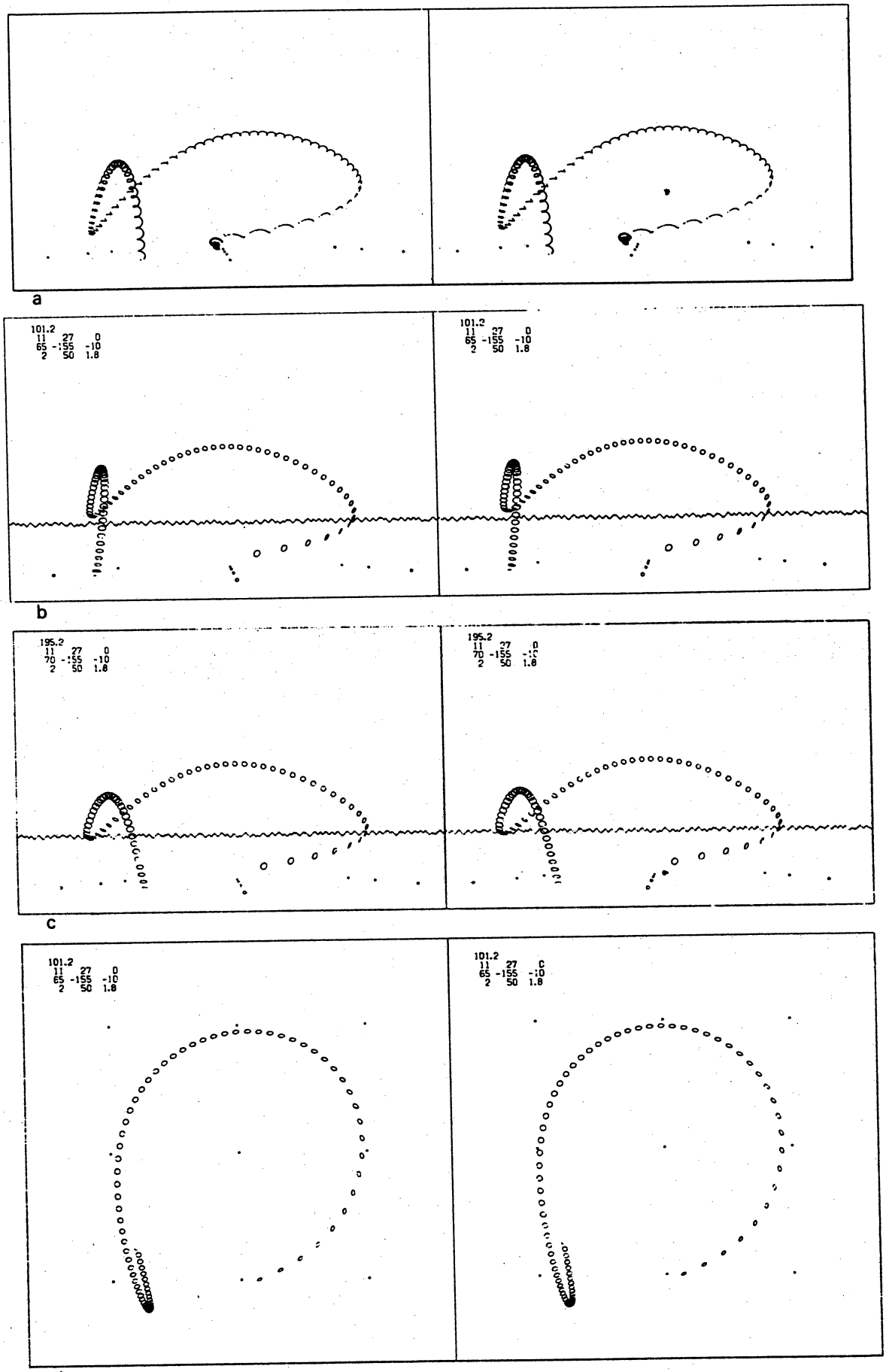

fig. 16.15. L1 weighted. a: {1}, 11R22A/L22. b,d: {2}. c: {3}.

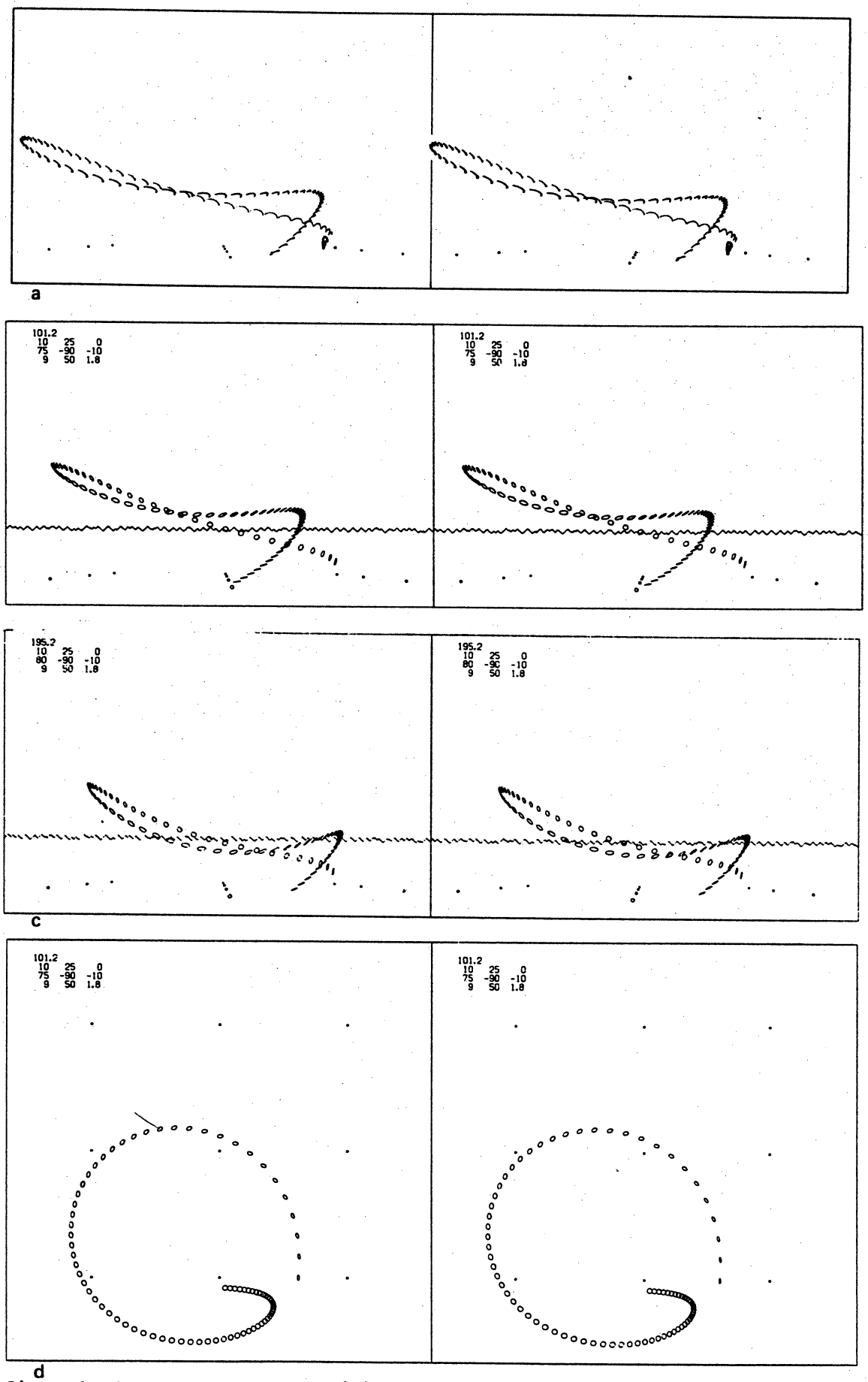

fig. 16.16. L1 weighted. a: {1}, 11R25A/L25. b,d: {2}. c: {3}.

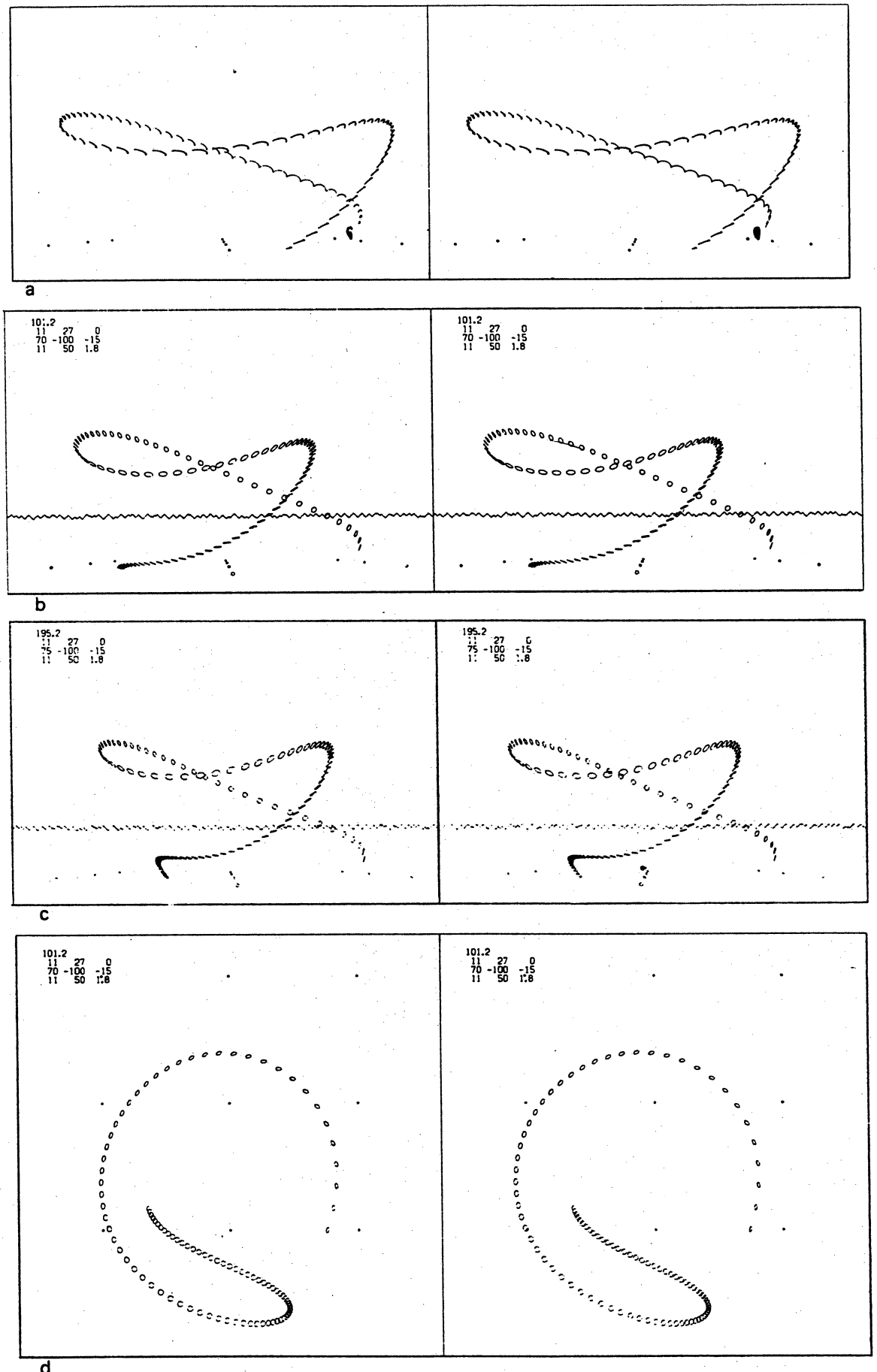

fig. 16.17. L1 weighted. a: {1}, 11R27A/L27. b,d: {2}. c: {3}.

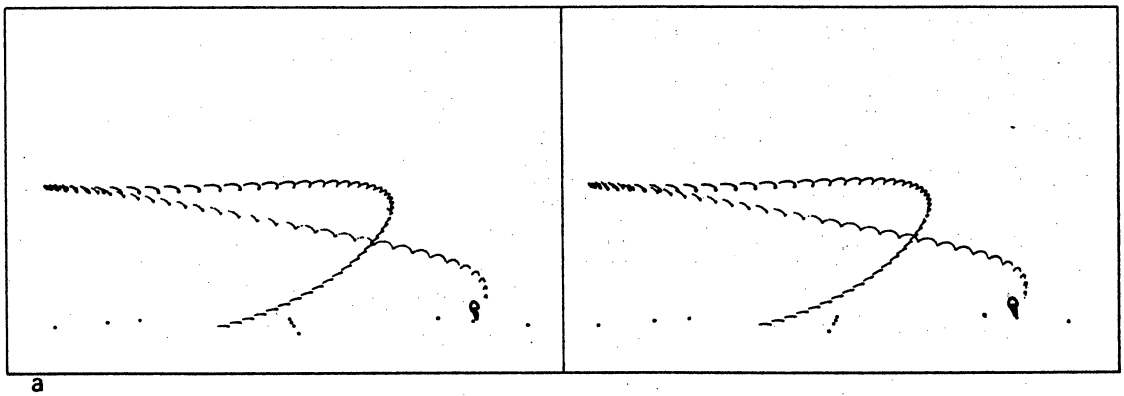

a

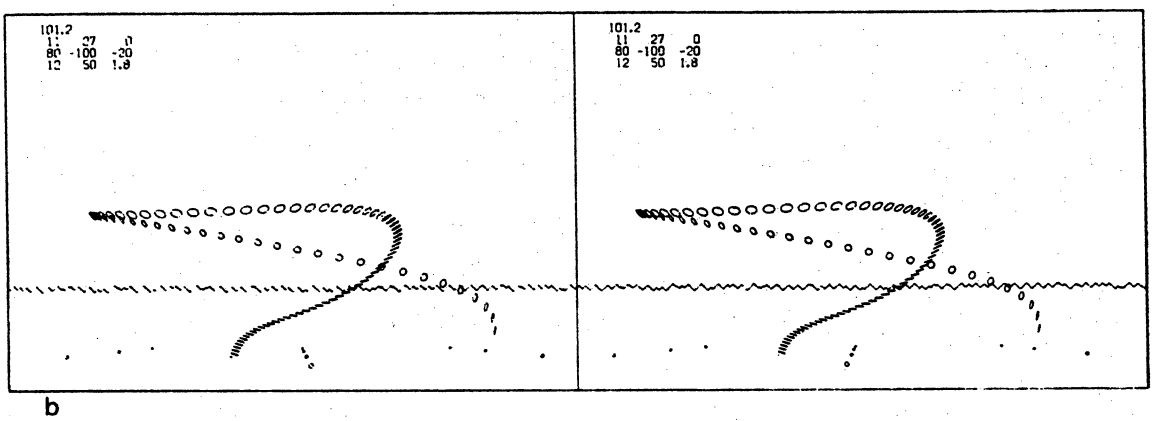

b

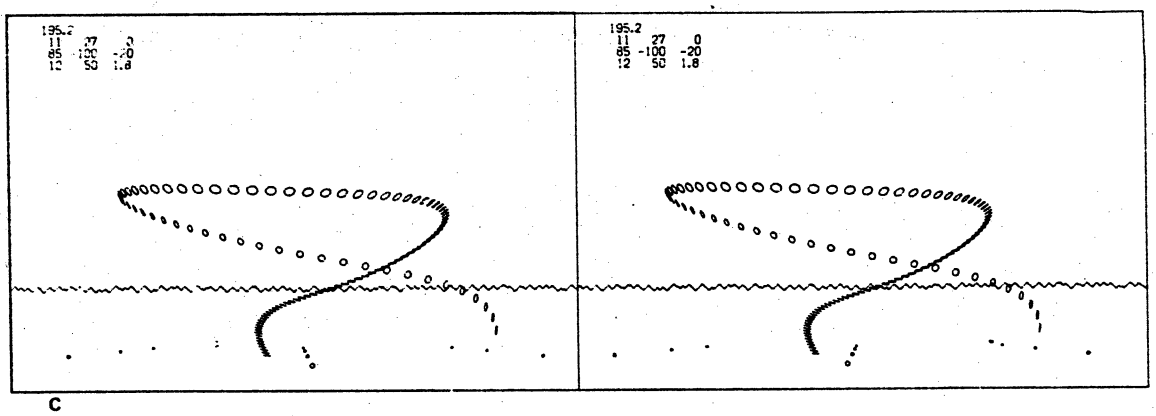

c

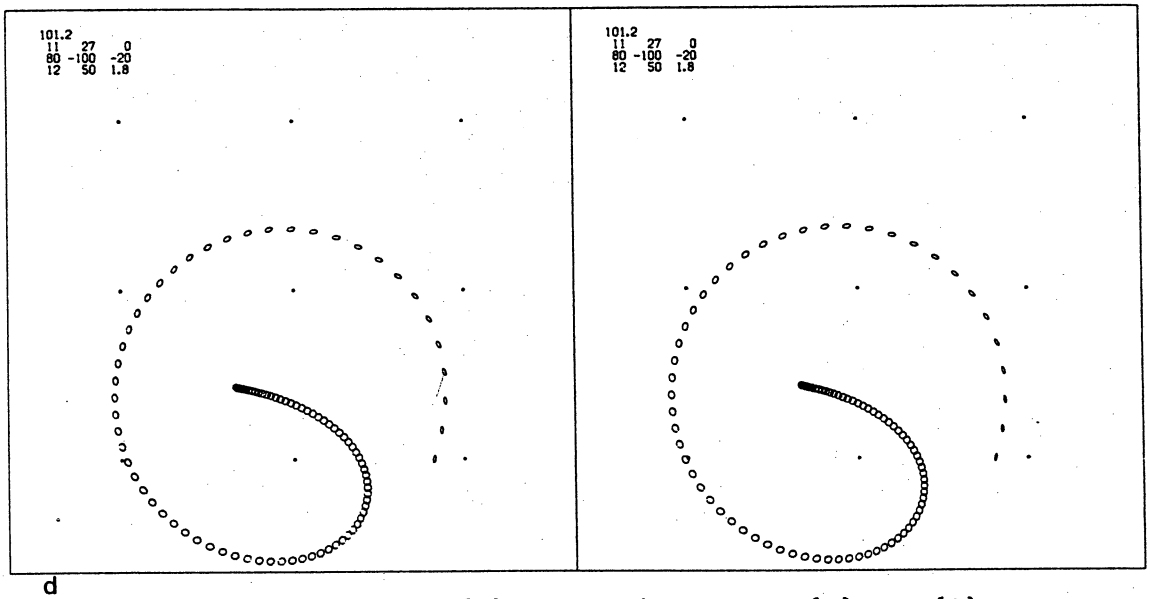

d

fig. 16.18. L1 weighted. a: {1}, 11R11A/L11. b,d: {2}. c: {3}.

§17 *Boomerang L4.*

Level 1: boomerang picture in fig. 10.1, physical properties in table 10.1. Plain and with "trip wire" in front of leading edges. Flight paths with wire are not presented here, but in §36.
Level 2: boomerang nr. 104.1 (plain), see Part II, table 31.2.
Level 3: boomerang nr. 237.1 (plain), see Part II, table 32.1.
Level 3': boomerang nr. 252.1 (plain), no flight paths presented.
Level 2 and level 3 graphs of aerodynamic force components: Part II, fig. 31.13 through 31.18.

List of flight path pictures for boomerang L4 plain.

fig.	level	negatives or boomerang nr.	f_o	V_o	Ψ_o	ϑ_o	φ_o	ψ_o	X_o	Y_o	Z_o	β_o	W_o	W_1
17.1a	1	3R10/L11												
b,e	2	104.1	10	25	0	75	-110	-15	4	50	1.8	0	0	0
c,f	3	237.1	10	25	0	80	-110	-15	4	50	1.8	0	0	0
d,g	3	237.1	11	27	0	80	-110	-15	4	50	1.8	0	0	0
17.2a	1	14R28A/L28A												
b,d	2	104.1	11	27	0	80	-165	-15	0	50	1.8	250	.5	.2
c	3	237.1	10	25	0	85	-165	-20	0	50	1.8	250	.5	.2
17.3a	1	14R24A/L24A												
b,d	2	104.1	10	25	0	70	-170	-10	-1	50	1.8	250	.5	.2
c	3	237.1	10	25	0	80	-170	-15	-1	50	1.8	250	.5	.2
17.4a	1	8R13A/L13												
b,d	2	104.1	10	25	0	70	-180	-15	-2	50	1.8	0	0	0
c	3	237.1	10	25	0	75	-180	-15	-2	50	.18	0	0	0
17.5a	1	14R32A/L32A												
b,d	2	104.1	10	25	0	85	-170	-10	1	50	1.8	250	.5	.2
c	3	237.1	10	25	0	85	-170	-10	1	50	1.8	250	.5	.2
17.6a	1	3R11/L12												
b	2	104.1	9	24	0	85	-115	-20	5	50	1.8	0	0	0
c,d	3	237.1	10	24	0	90	-115	-20	5	50	1.8	0	0	0
17.7a	1	14R34A/L34A												
b,d	2	104.1	10	25	0	80	-100	-20	10	50	1.8	250	.5	.2
c	3	237.1	10	25	0	85	-100	-20	10	50	1.8	250	.5	.2
17.8a	1	8R21A/L21												
b,d	2	104.1	10	25	0	65	-105	-15	6	50	1.8	0	0	0
c	3	237.1	10	25	0	70	-105	-20	6	50	1.8	0	0	0
17.9a	1	8R24A/L24												
b	2	104.1	10	25	0	55	-100	-25	7	50	1.8	0	0	0
c	3	237.1	10	25	0	60	-100	-25	7	50	1.8	0	0	0
d	3	237.1	10	25	0	65	-100	-25	7	50	1.8	0	0	0

Comment.

Boomerang L4 has a typical flight path diameter of about 25 m. This boomerang does not perform as beautiful as boomerang L1 does. On occasion it was hardly possible for me to make it return completely. The ease with which a good return flight could be accomplished varied from night to night. This might be due either to subtile differences in my throwing technique (fatigue), or to slight deformations of the boomerang (warp), or to both. When a "trip wire" was attached along the leading edges of the boomerang arms, the performance of boomerang L4 was much improved; its flights then often resembled those of boomerang L1. Flight path photographs showing this effect are presented in §36. We did not succeed in finding an acceptable level 3 boomerang corresponding to boomerang L4 with wire. (Here acceptability includes the assumption that only one or two of the input parameters may differ from those of model boomerang 237.1.)

The agreement between the photographed flight paths and the computed ones, both at level 2 and at level 3, is fair. Occasionally, however, the initial speed and spin in the computed flights were chosen greater than the level 1 photographs would indicate. The effect of this can be seen in fig. 17.1 for level 3. In fig. 17.2a, for instance, one can easily determine that $f \approx 10.0$ rev/s in the first second of the flight. However, flight path calculations generally indicate a significant decrease of the initial spin (and forward speed as well) immediately after the start. Hence, at the instant of launching the spin may have been $f_o \approx 10.5$ rev/s in this case.

Figure 17.8c,d (level 3) shows that a slight difference in the initial conditions (here ϑ_o) may result in a substantial shift of the point of touch-down.

As to level 3' (no flight path presented), the differences from the corresponding level 3 flights are more or less the same as in the case of boomerang L1 plain.

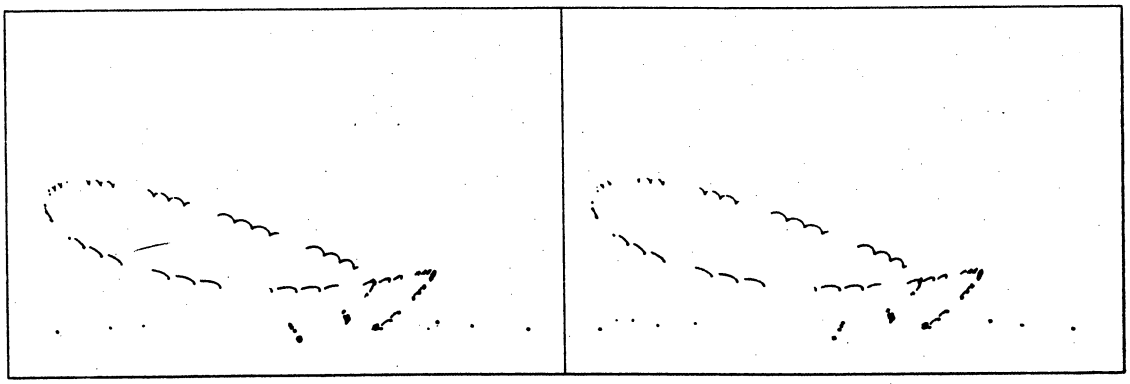

a

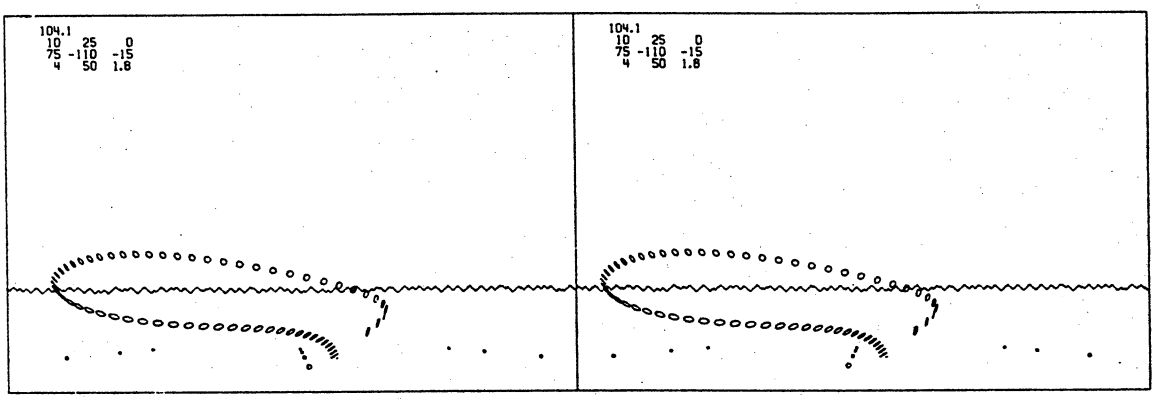

b

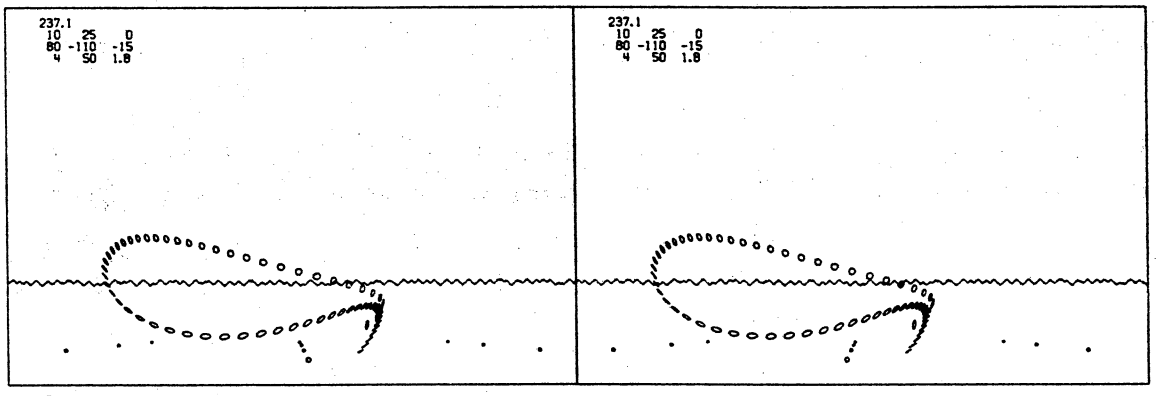

c

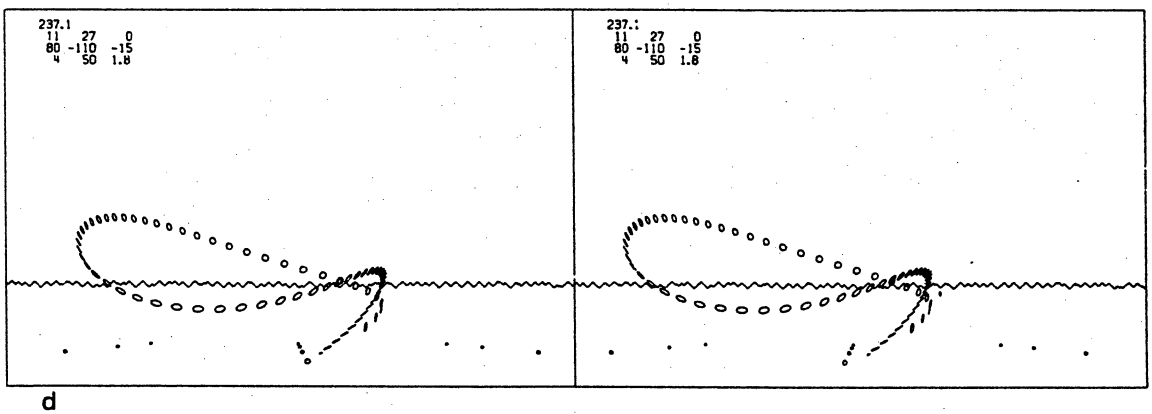

d

fig. 17.1. L4 plain. a: {1}, 3R10/L11. b,e: {2}. c,f: {3}. d,g: {3}.

continued on next page.

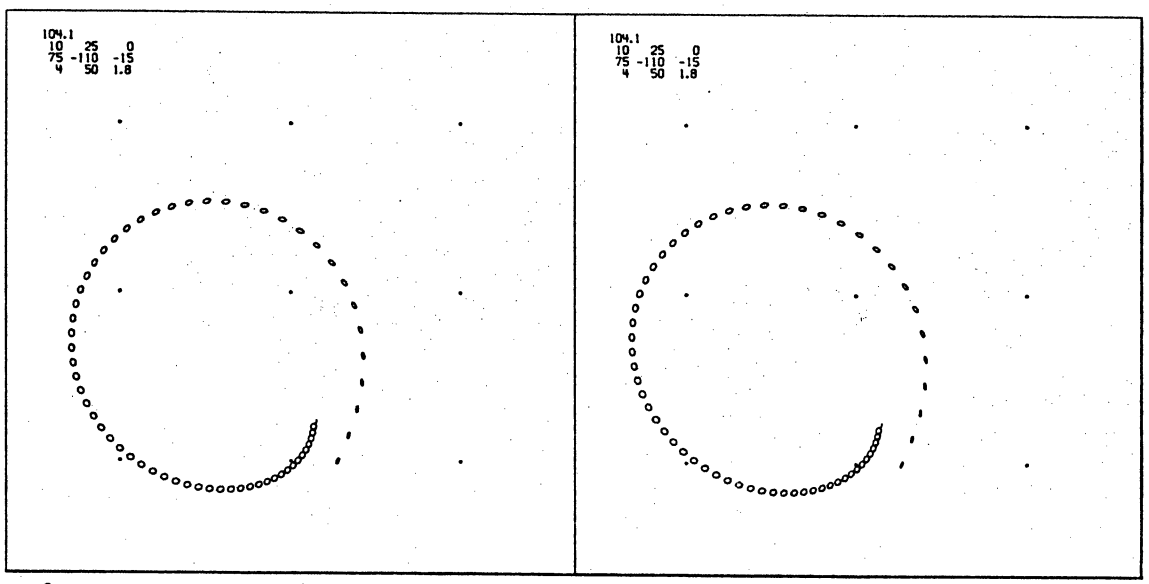

e

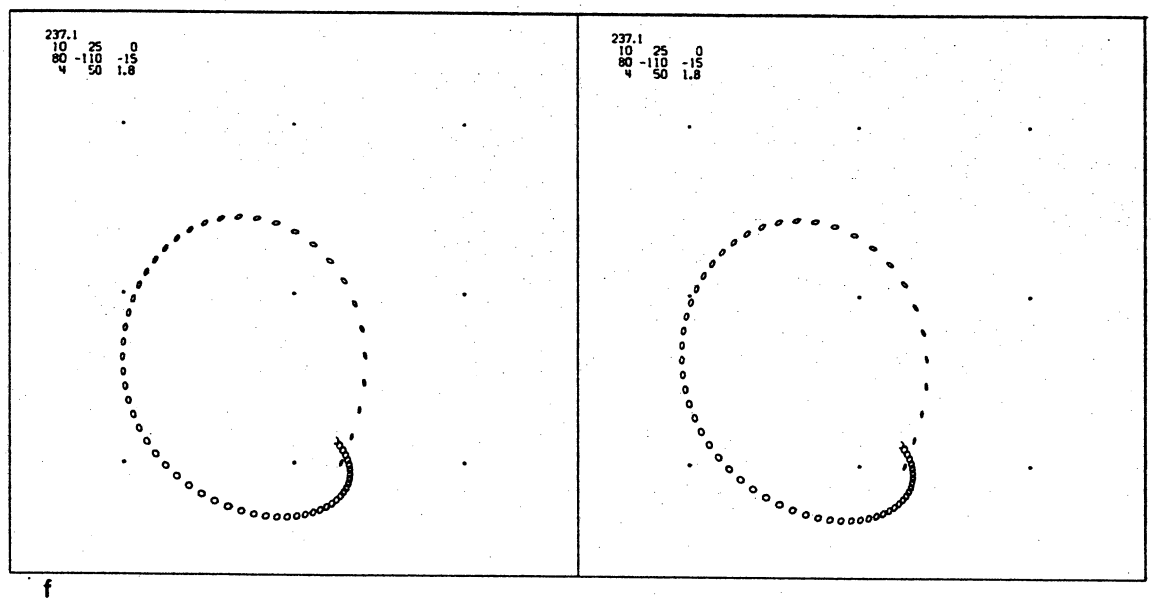

f

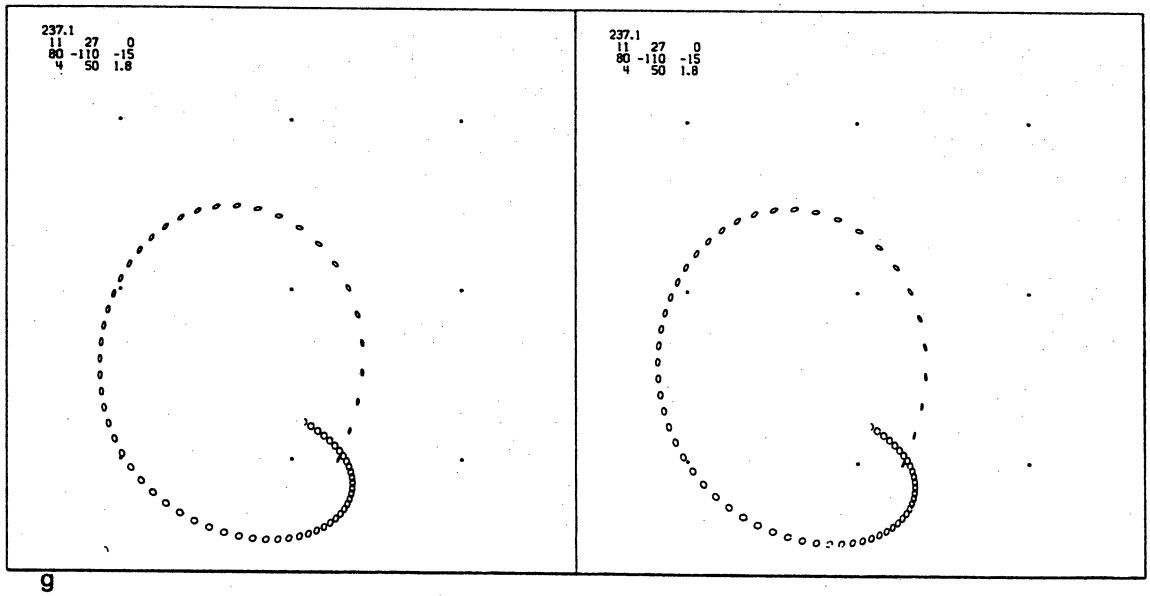

g

fig. 17.1 continued.

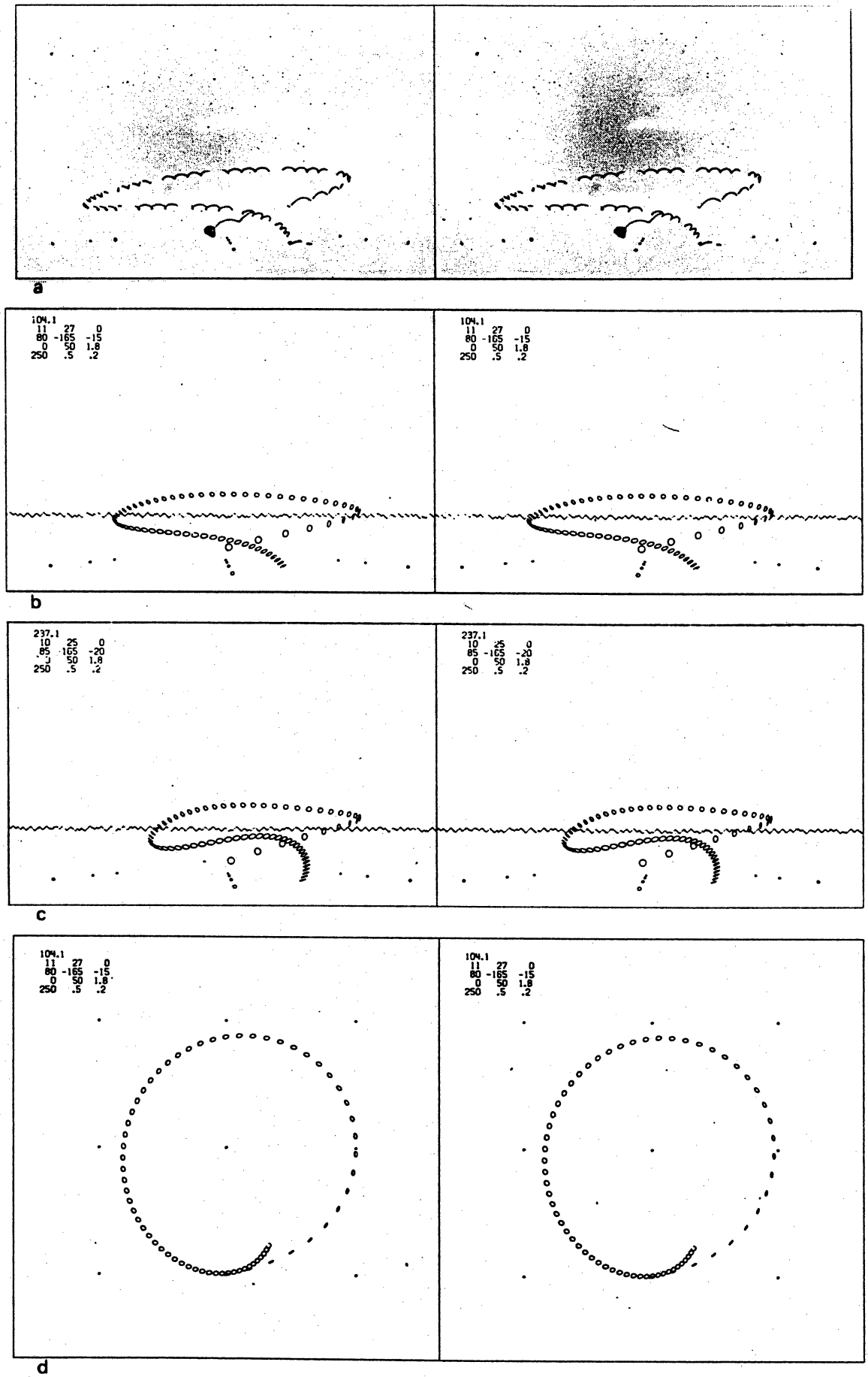

fig. 17.2. L4 plain. a: {1}, 14R28A/L28A. b,d: {2}. c: {3}.

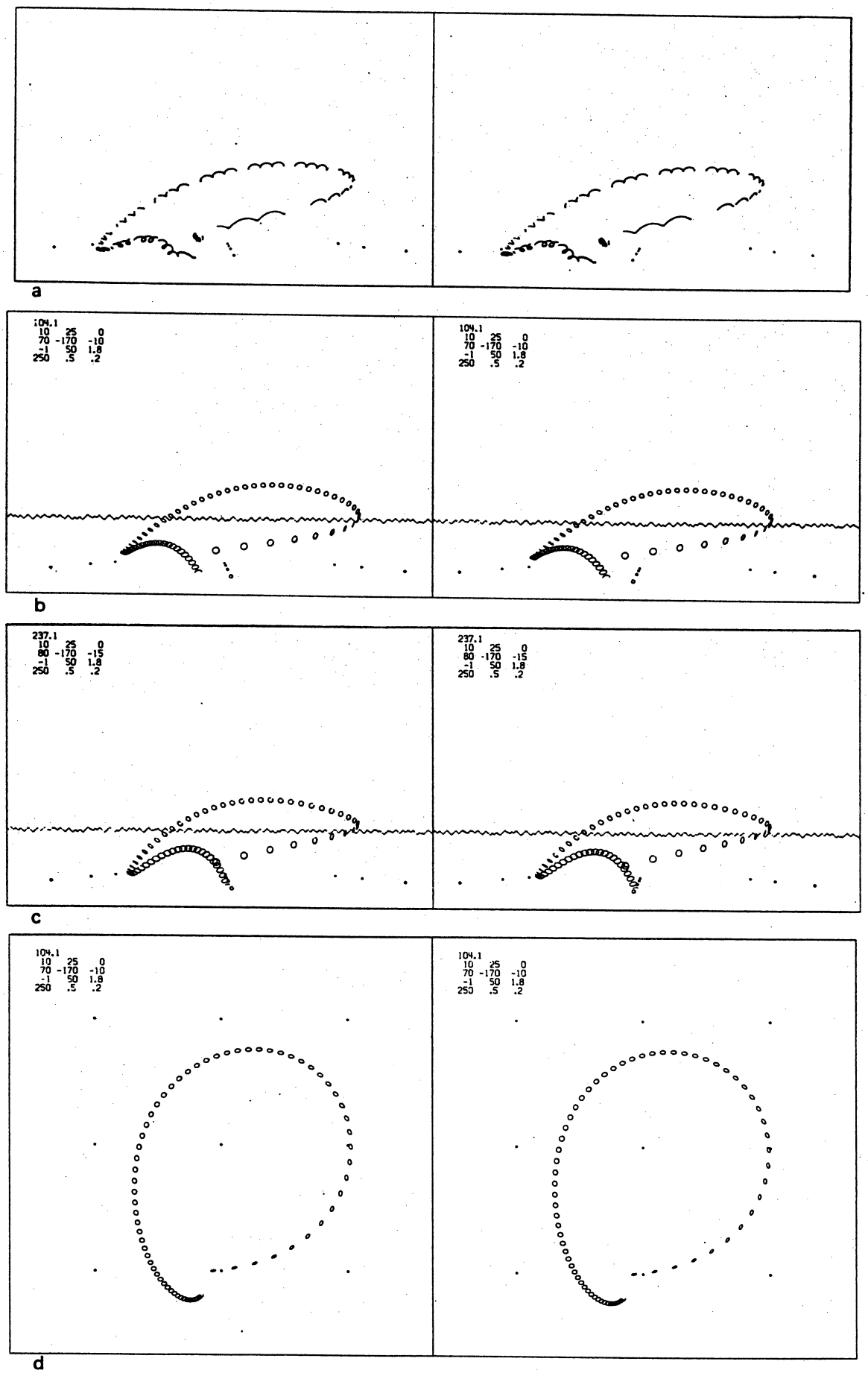

fig. 17.3. L4 plain. a: {1}, 14R24A/L24A. b,d: {2}. c: {3}.

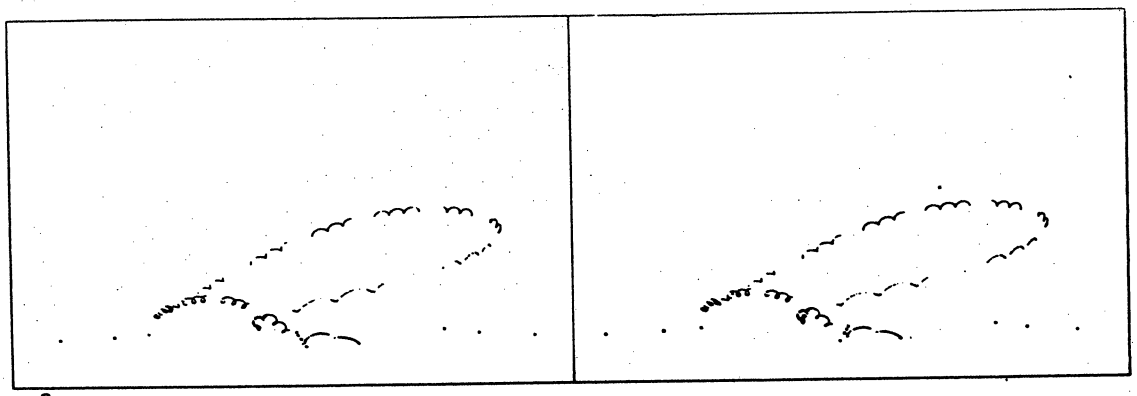

a

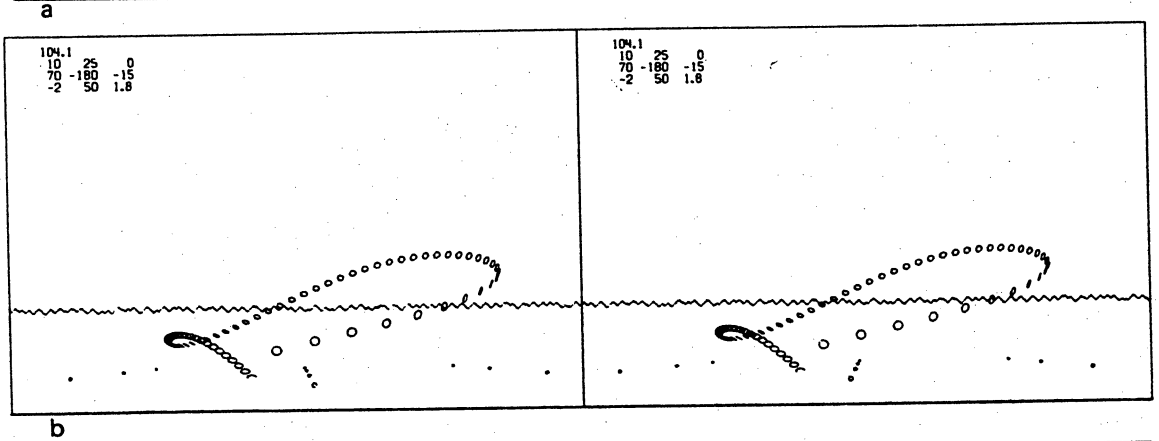

b

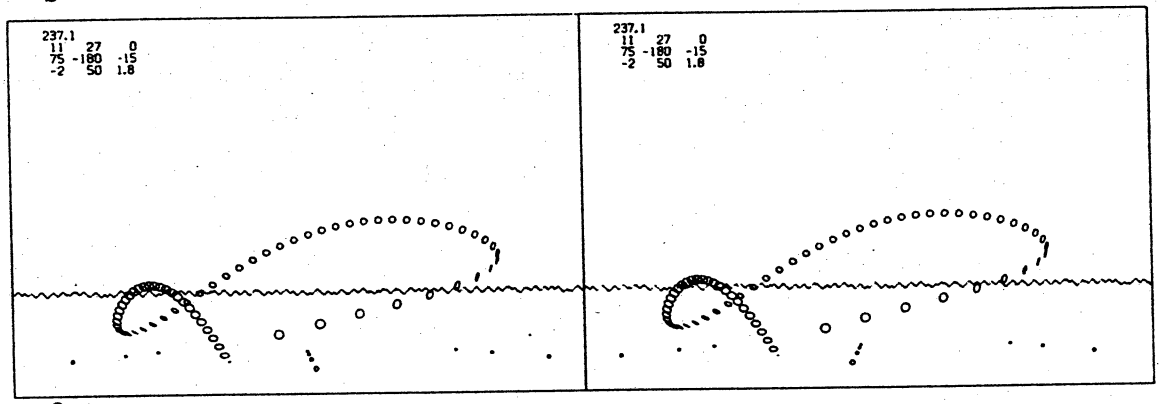

c

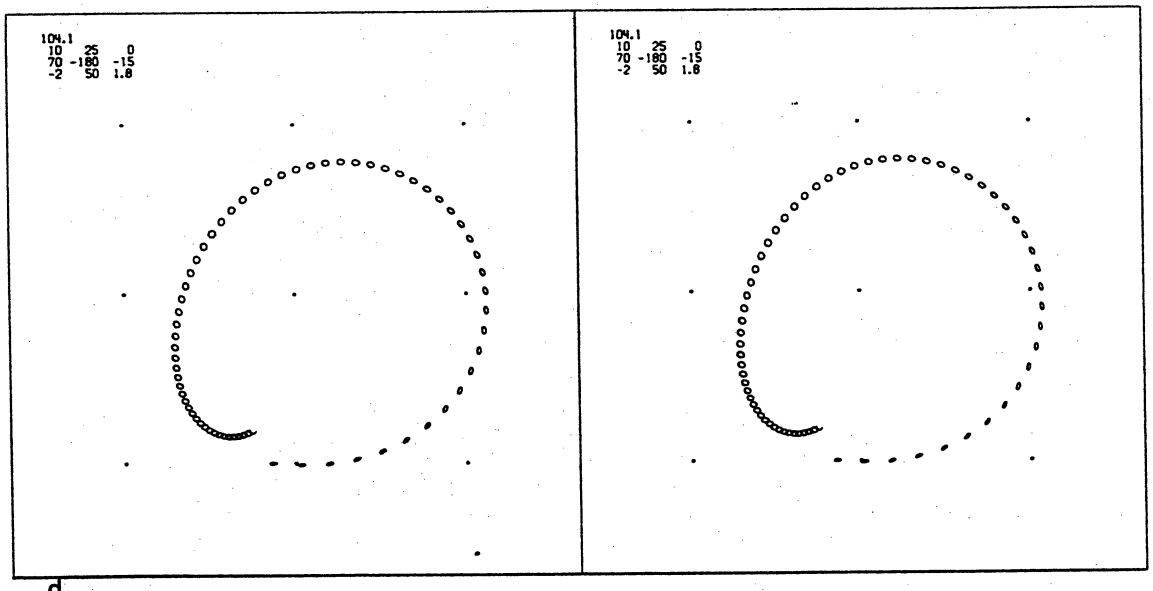

d

fig. 17.4. L4 plain. a: {1}, 8R13A/L13. b,d: {2}. c: {3}.

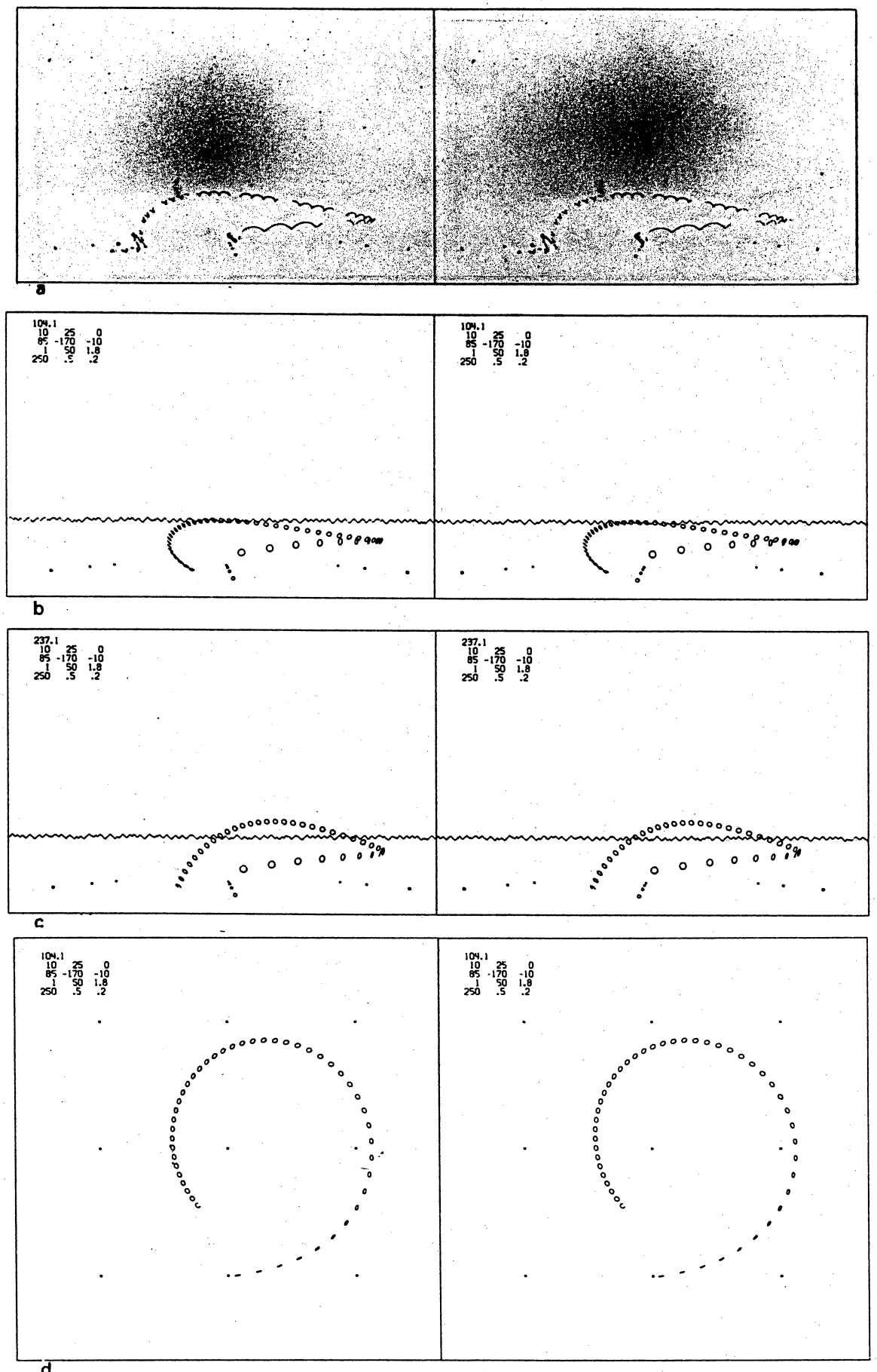

fig. 17.5. L4 plain. a: {1}, 14R32A/L32A. b,d: {2}. c: {3}.

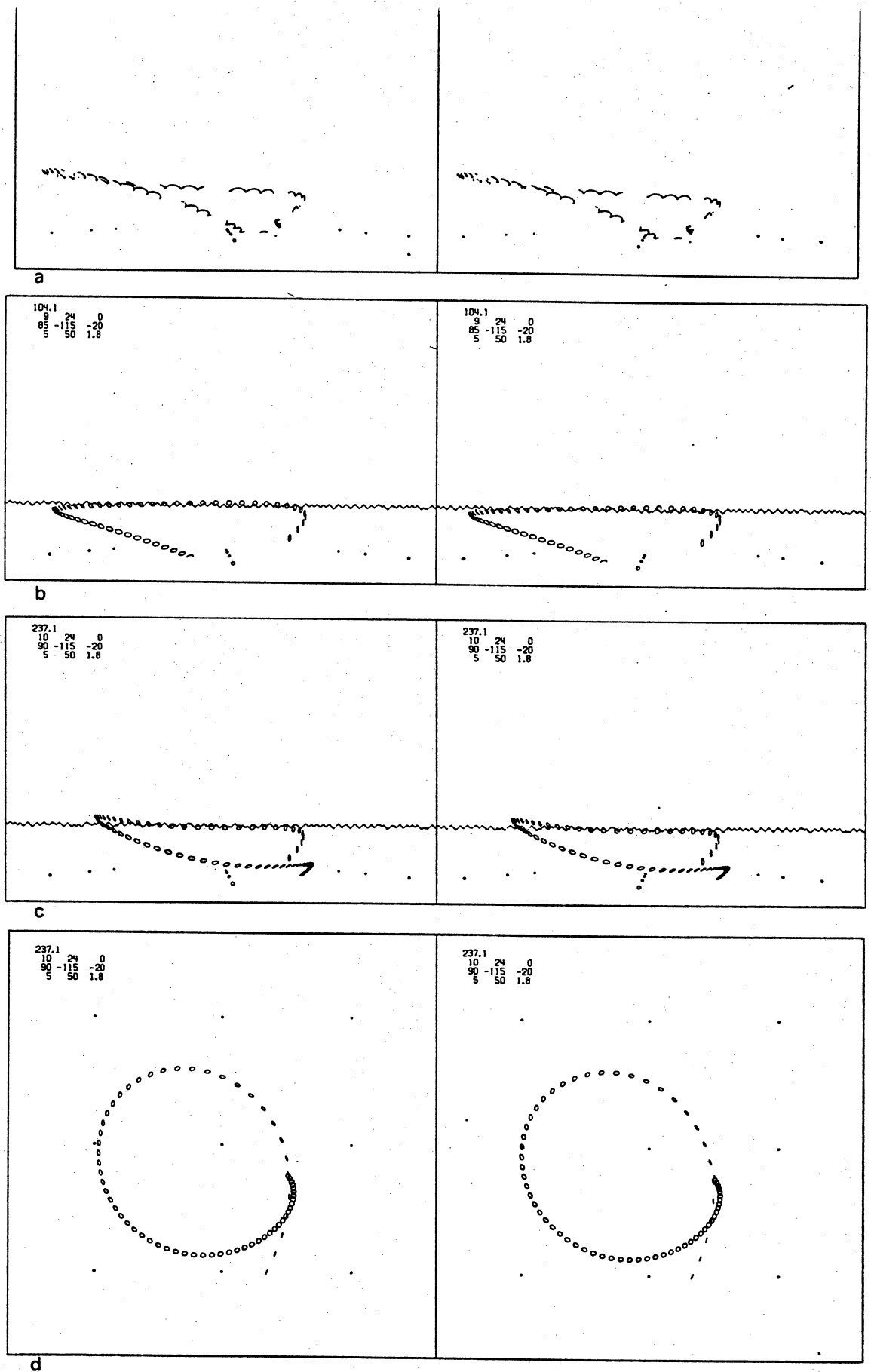

fig. 17.6. L4 plain. a: {1}, 3R11/L12. b: {2}. c,d: {3}.

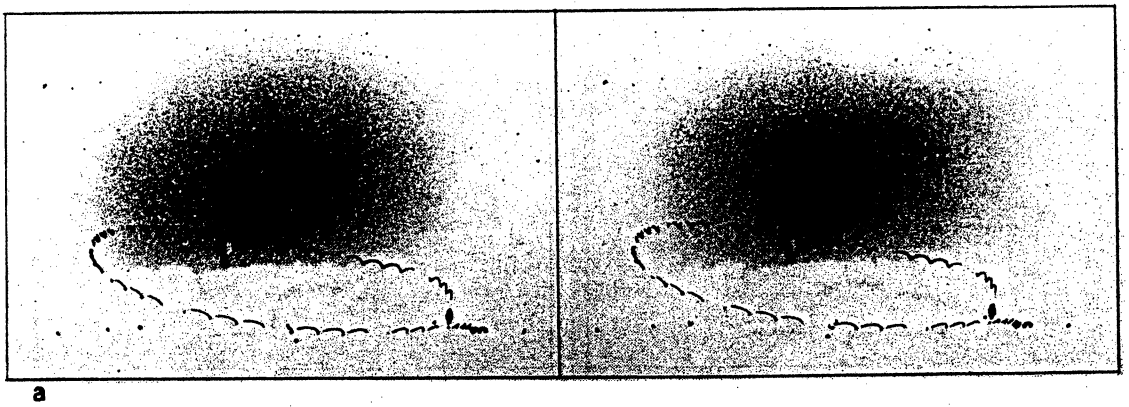

a

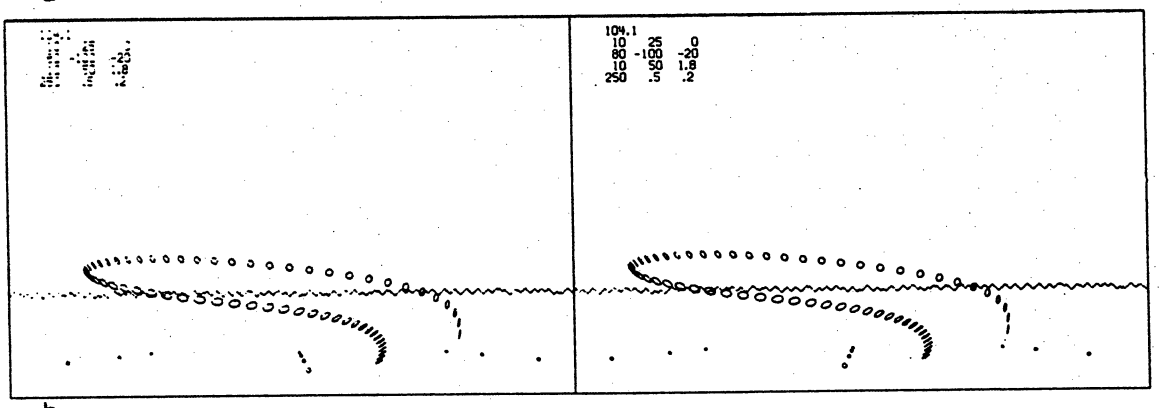

b

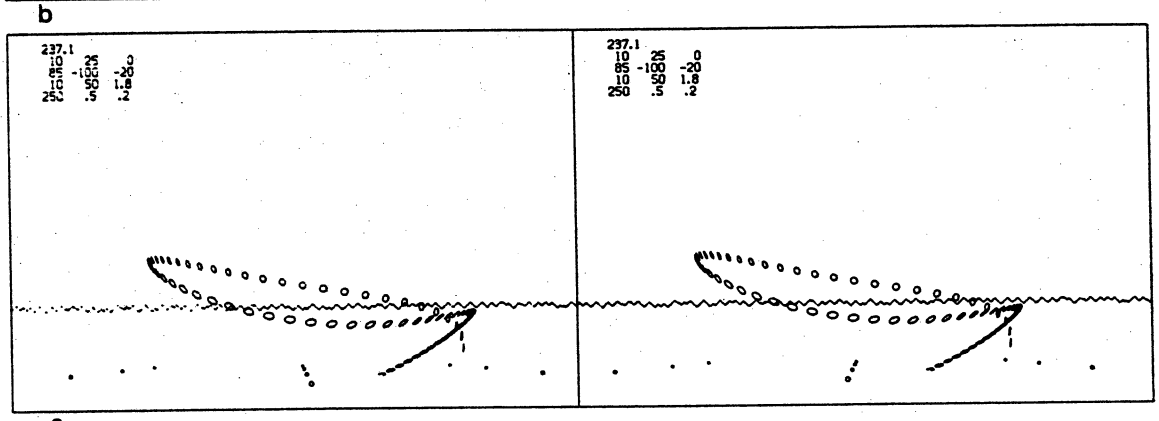

c

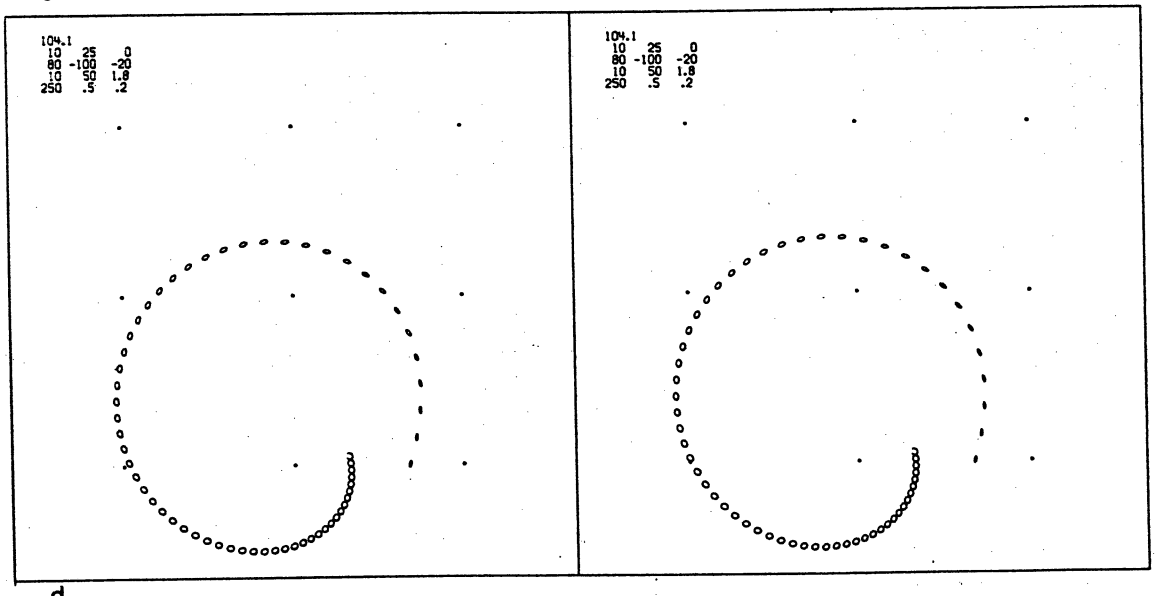

d

fig. 17.7. L4 plain. a: {1}, 14R34A/L34A. b,d: {2}. c: {3}.

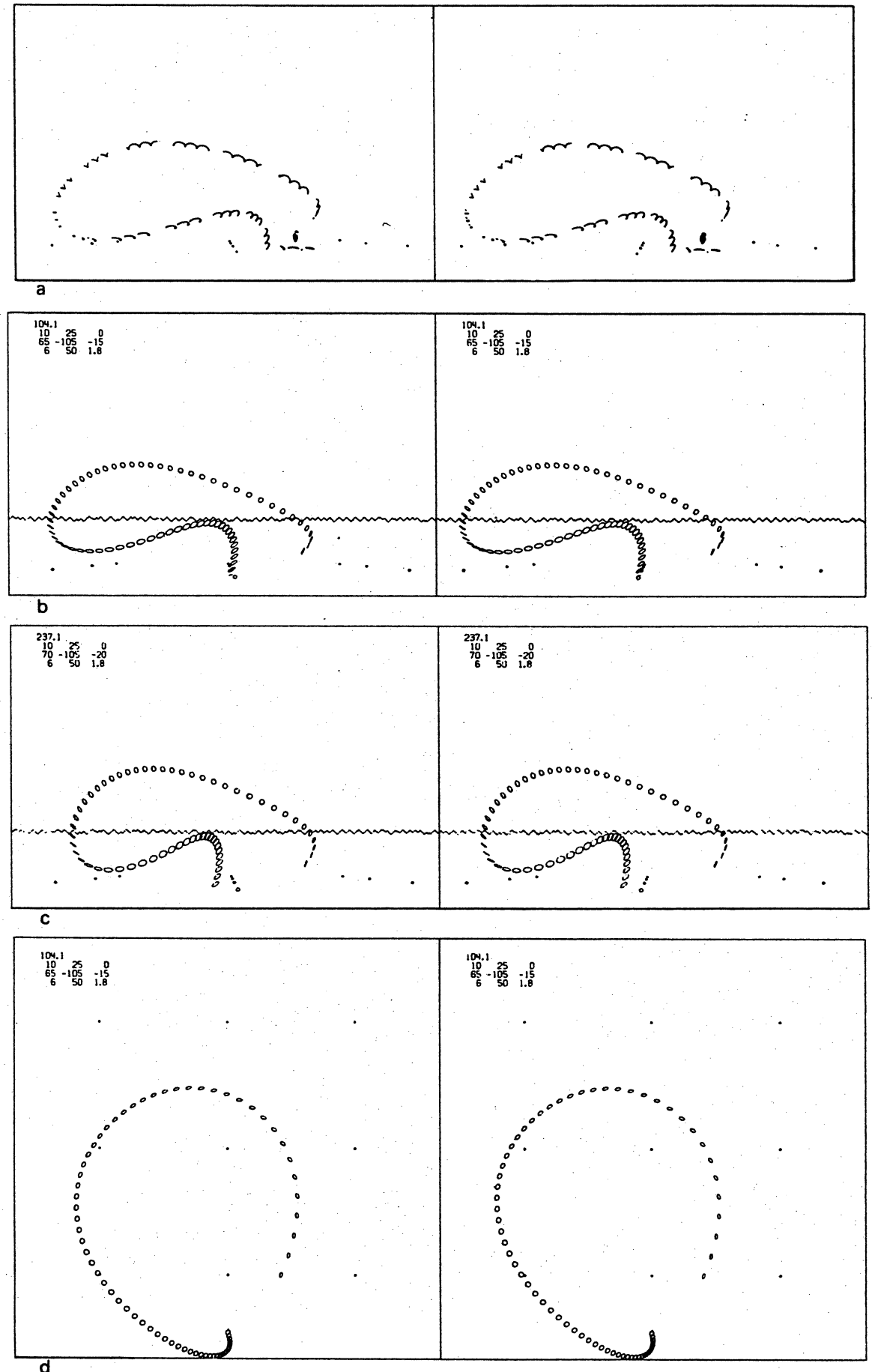

fig. 17.8. L4 plain. a: {1}, 8R21A/L21. b,d: {2}. c: {3}.

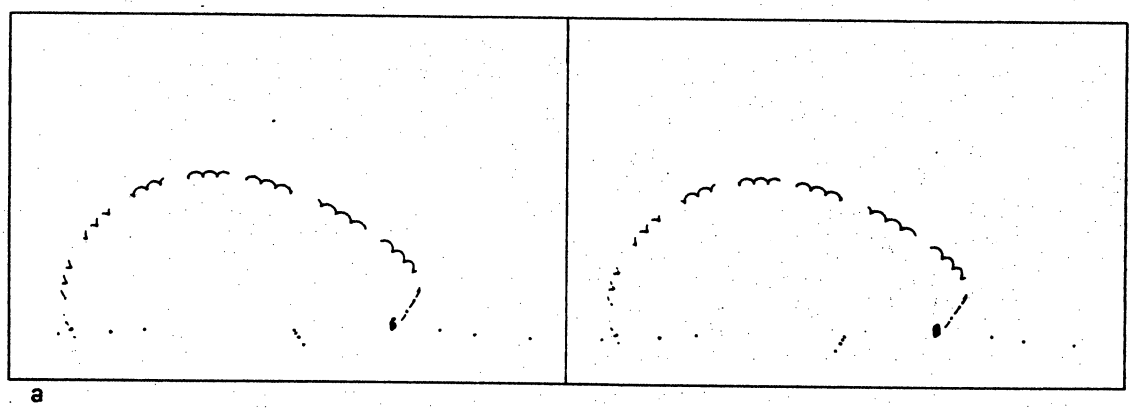

a

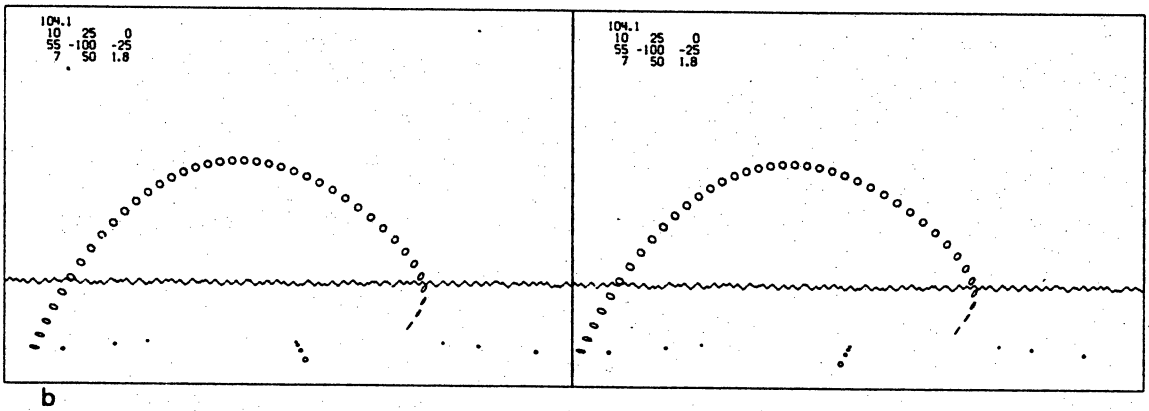

b

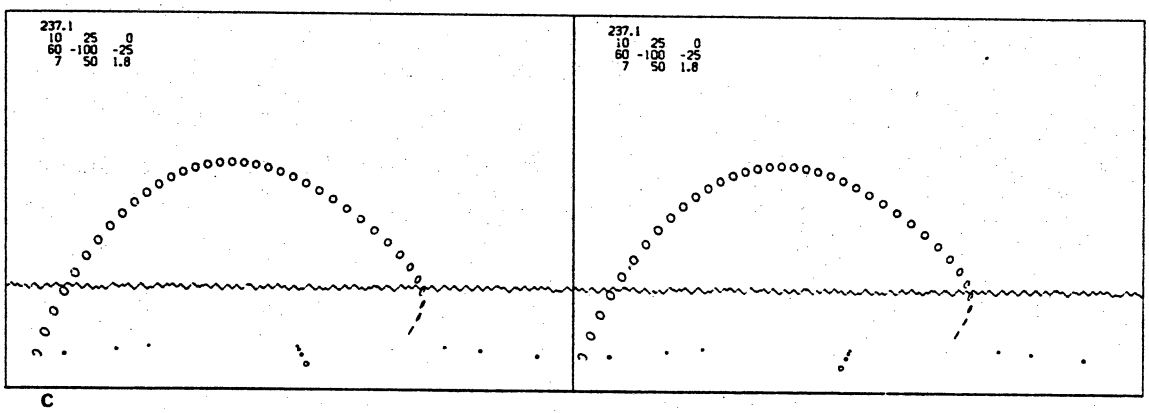

c

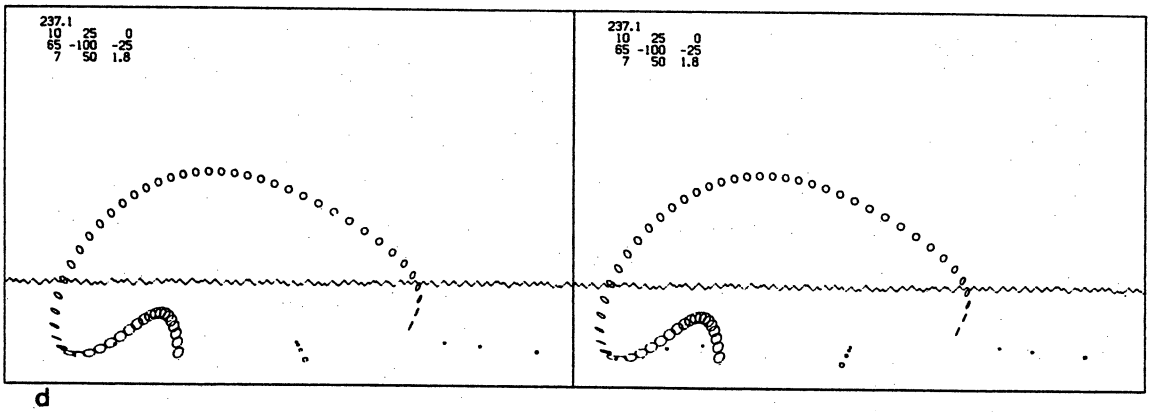

d

fig. 17.9. L4 plain. a: {1}, 8R24A/L24. b: {2}. c: {3}. d: {3}.

Level 1: boomerang picture in fig. 10.1, physical properties in table 10.1, more dimensions given in table 18.1.

Level 2: absent.

Level 3: boomerang nr. 245.1, see table 18.1.

Level 3': boomerang nr. 255.1.

arm	e	l	c_t	c_r	α_{ot}	α_{or}	dC_L	C_{L1}	C_{L2}	C_{L3}	C_{L4}	C_{Dm}	dC_D
1	+92	296	50	55	+3.0	+6.0	.09	-1.0	+1.8	-0.5	+0.8	.04	.03
	reversed profile				+1.0	+4.0	.10	-1.0	+2.4	-0.5	+0.8	.08	.03
2	-69	297	51	57	+1.0	+6.0	.09	-1.0	+1.8	-0.5	+0.8	.04	.03
	reversed profile				+3.0	+4.0	.10	-1.0	+2.4	-0.5	+0.8	.08	.03

table 18.1. Boomerang nr. 245 belonging to L5. a = 307. Lengths in mm, angles in degrees. See Part II, §22 for explanation.

List of flight path pictures for boomerang L5.

fig.	level	negatives or boomerang nr.	f_o	V_o	Ψ_o	ϑ_o	φ_o	ψ_o	X_o	Y_o	Z_o	β	W_o	W_1
18.1a	1	5R12A/L14A												
b,d	3	245.1	10	25	0	70	-150	-10	0	50	1.8	0	0	0
c	3'	255.1	10	25	0	70	-150	-10	0	50	1.8	0	0	0
18.2a	1	6R35/L34												
b,d	3	245.1	10	25	0	70	-180	-10	-10	50	1.8	0	0	0
c	3'	255.1	10	25	0	65	-180	-10	-10	50	1.8	0	0	0
18.3a	1	6R36/L34												
b,d	3	245.1	10	25	0	75	-180	-10	-10	50	1.8	0	0	0
c	3'	255.1	10	25	0	70	-180	-10	-10	50	1.8	0	0	0
18.4	1	6R9/L8												
b,d	3	245.1	10	25	0	75	-165	- 5	0	50	1.8	0	0	0
c	3'	255.1	10	25	0	70	-165	- 5	0	50	1.8	0	0	0
18.5a	1	5R14A/L16A												
b,d	3	245.1	10	25	0	55	-165	- 5	0	50	1.8	0	0	0
c	3'	255.1	10	25	0	55	-165	- 5	0	50	1.8	0	0	0
18.6a	1	5R17A/L19A												
b,d	3	245.1	10	25	0	75	-100	-20	14	50	1.8	0	0	0
c	3'	255.1	10	25	0	75	-100	-20	14	50	1.8	0	0	0
18.7a	1	5R18A/L20A												
b	1	6R2/L2												
c,d	3	245.1	10	25	0	70	-100	-10	14	50	1.8	0	0	0
18.8a	1	6R3/L3												
b,d	3	245.1	10	25	0	60	- 90	- 5	14	50	1.8	0	0	0
c	3'	255.1	10	25	0	60	- 90	- 5	14	50	1.8	0	0	0

fig.	level	negative or boomerang nr.	f_o	V_o	Ψ_o	ϑ_o	φ_o	ψ_o	X_o	Y_o	Z_o	β	W_o	W_l
18.9a	1	5R27A/L29A												
b,d	3	245.1	10	24	0	65	- 90	0	14	50	1.8	0	0	0
c	3'	255.1	10	24	0	65	- 90	0	14	50	1.8	0	0	0
18.10a	1	9R27A/L30A												
b,d	3	245.1	10	25	0	75	-175	-15	-12	50	1.8	310	1.3	.6
c	3'	255.1	10	25	0	75	-175	-15	-12	50	1.8	310	1.3	.6

Comment.

It is important to note that the level 3' model boomerang 255.1 has a status rather different from the level 3' boomerangs computed for the boomerangs L1, L4, L6, F18 and WU, for which level 2 results are available. In the latter case, the principal aim of the computation of the level 3 boomerangs was a good agreement with the measured aerodynamic forces (level 2) (see Part II, §31). The level 3' boomerangs, in this case, contain a correction for the contribution to the boomerang arms' angle of incidence due to precession (see §5). Therefore, level 3' flight paths could be expected to be more realistic than the corresponding level 3 paths. (Experimental forces corrected for precession are not available.) In the case of boomerang L5, however, the principal aim of the computation of the level 3 boomerang 245.1 was to obtain a good agreement with level 1 *flight paths*. Afterwards the corresponding level 3' boomerang 255.1 was computed. Hence, in this case, there is no ground for expecting the level 3' flight paths to be more realistic than the level 3 paths (It might have been better if we had reversed the procedure, and had first computed a level 3' boomerang aimed at agreement with level 1 flight paths.) The value of a comparison between level 3 paths and level 3' paths, in the present case, lies in showing the effect of the "precession correction" per se. As was explained in §5, this correction generally increases the torque component T_x and decreases the torque component T_y. This causes a decrease of the lying-down (= slower decrease of ϑ) of a boomerang in its flight. This in turn results in a somewhat less elevated flight path, and an increased tendency for the path to continue curving counterclockwise. Such effects can indeed be seen in the flight paths presented in this section. In three cases ϑ_o was taken 5° lower for boomerang 255.1 than for boomerang

245.1 in order to obtain flights of roughly the same elevation.

Boomerang L5 is the biggest and the heaviest of all the boomerangs used in the field experiments. Its flight paths are larger and more elongated than those of boomerangs L1 and L4. Often the farthest point is about 45 m distant from the launching point. This boomerang appears to return best in a light breeze, see fig. 18.11.

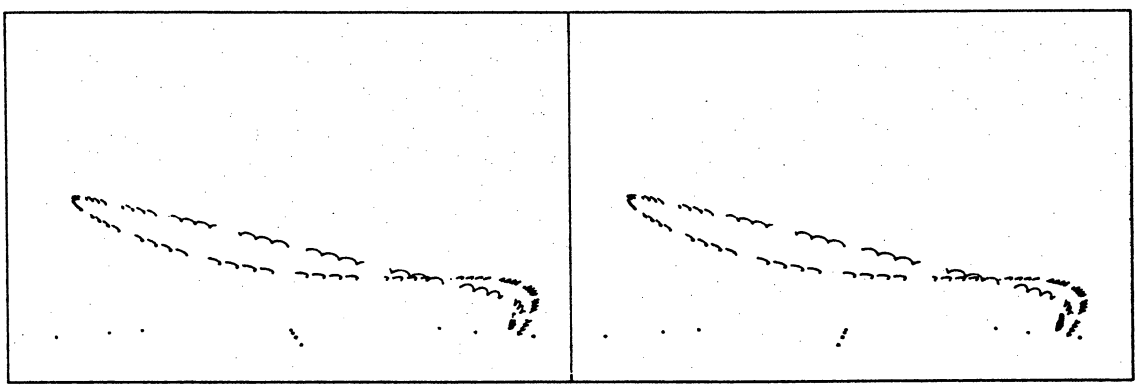

fig. 18.11. 9R33A/L36A, boomerang L5, {1}. Wind speed $\approx$ 1.6m/s, $\beta \approx 310°$.

About 20 usable flight paths of boomerang L5 were recorded under windy conditions (17-8-1973). It is rather unfortunate that no satisfcatory level 3 flights could be computed with the wind conditions chosen according to tabel 15.1. This failure may be due to the large fluctuations ($\approx$ .5m/s) in the actually prevailing wind.

The agreement between the level 1 and the level 3 paths presented here is rather good. A reasonable agreement was difficult to obtain for cases in which boomerang L5 was launched at $80° \lesssim \vartheta_o \lesssim 90°$, $-10° \lesssim \psi_o \lesssim 0°$. Figure 18.10 (with wind) shows a substantial difference in the initial conditions of the level 2 flight and the level 3 flight. In the photograph $\psi_o \approx -5°$, but at level 3 it was necessary to take $\psi_o \approx -15°$ in order to obtain a flight path with at least a global likeness. The effect of a change in φ_o can be seen by comparing fig. 18.1 with fig. 18.2, and the effect of a change in ϑ_o by comparing fig. 18.2 with fig. 18.3 and fig. 18.4 with fig. 18.5.

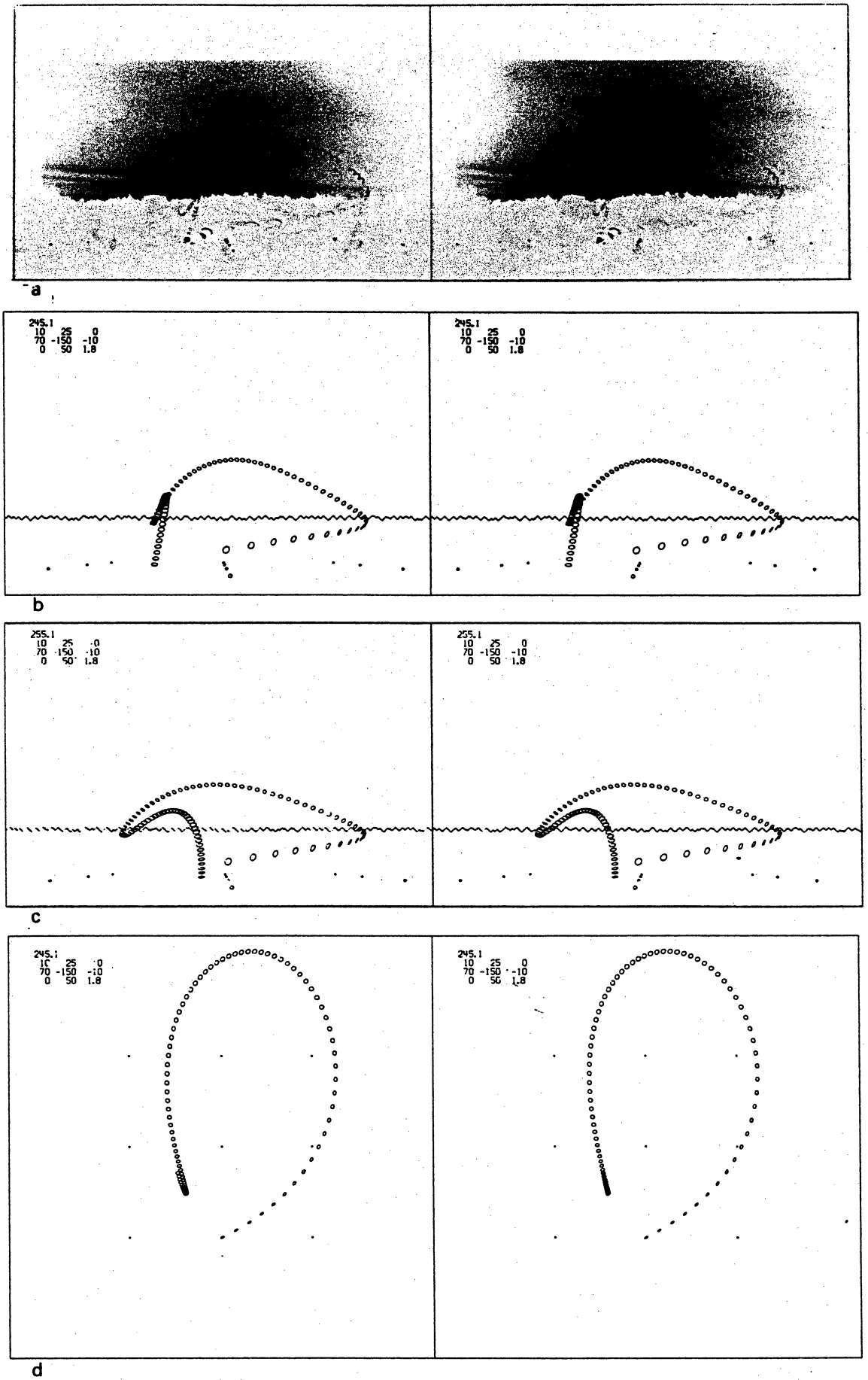

fig. 18.1. L5. a: {1}, 5R12A/L14A. b,d: {3}. c: {3'}.

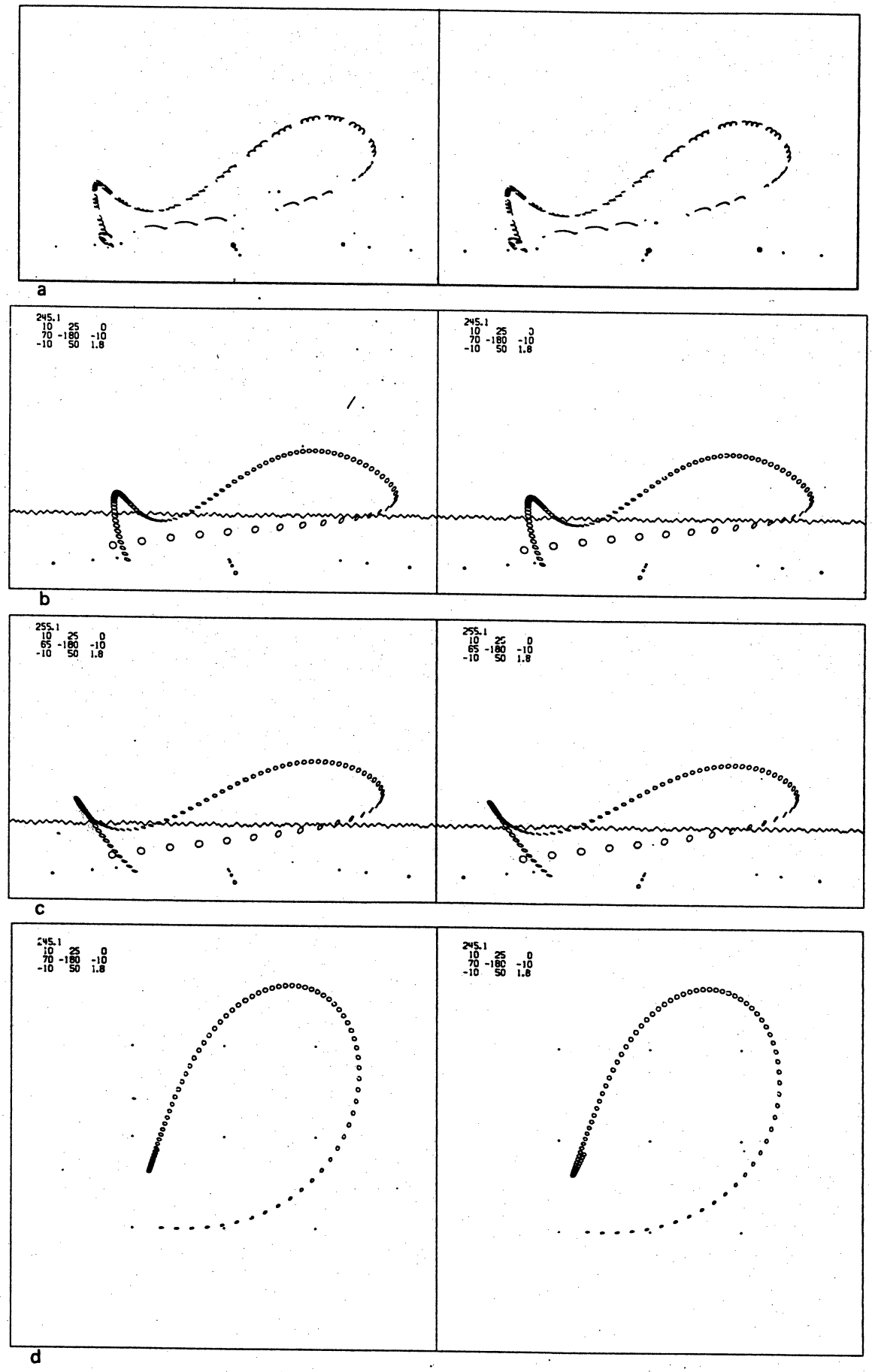

fig. 18.2. L5. a: {1}, 6R35/L34. b,d: {3}. c: {3'}.

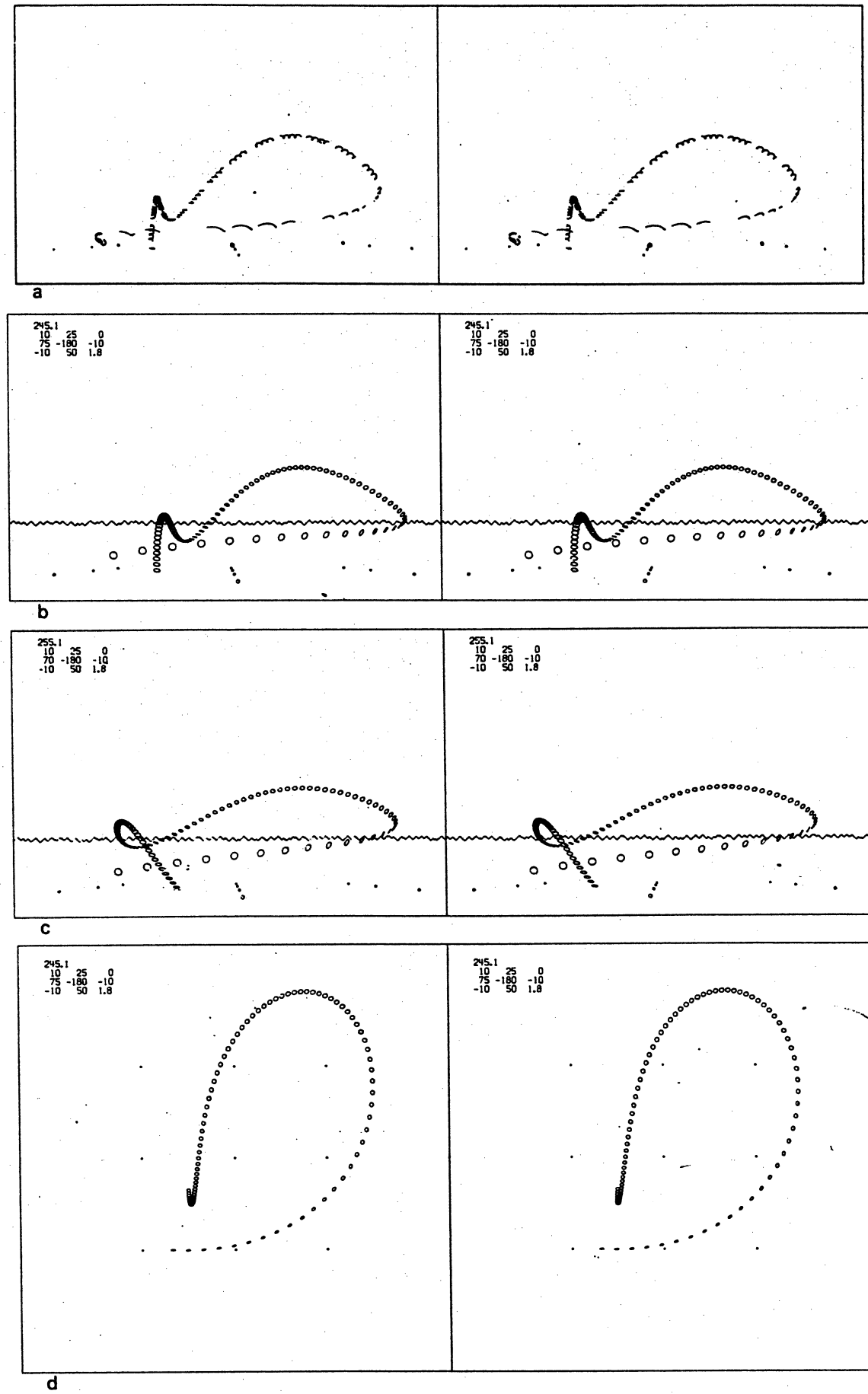

fig. 18.3. L5. a: {1}, 6R36/L35. b,d: {3}. c: {3'}.

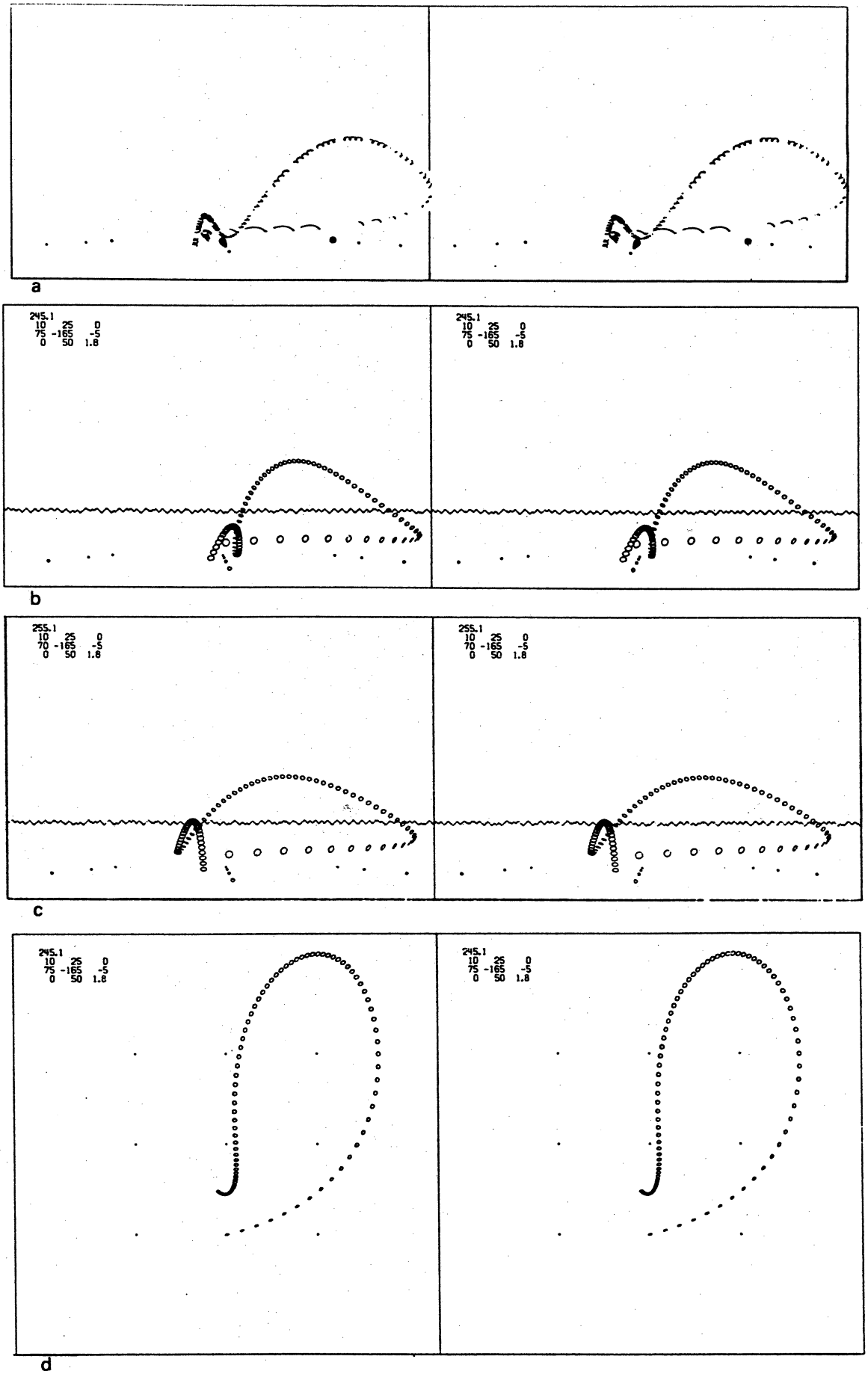

fig. 18.4. L5. a: {1}, 6R9/L8. b,d: {3}. c: {3'}.

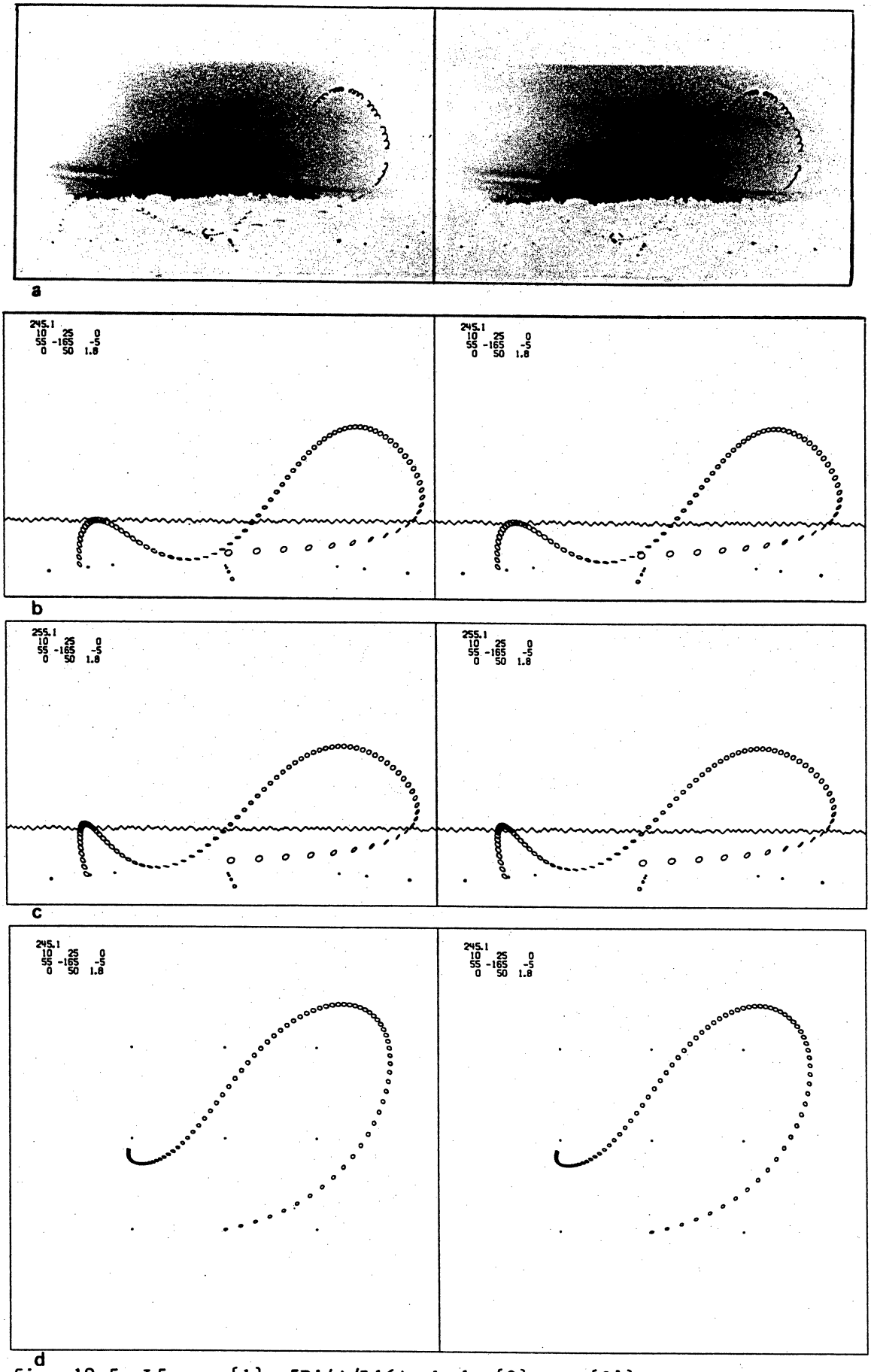

fig. 18.5. L5. a: {1}, 5R14A/L16A. b,d: {3}. c: {3'}.

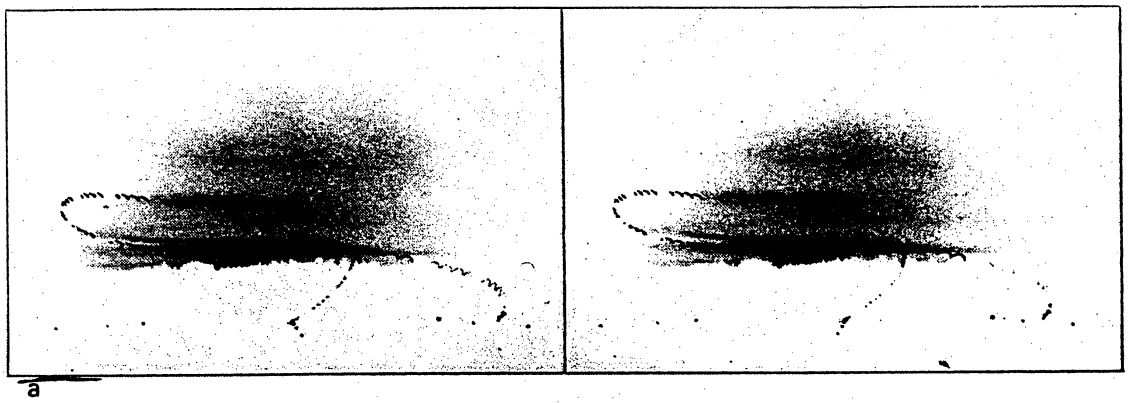

a

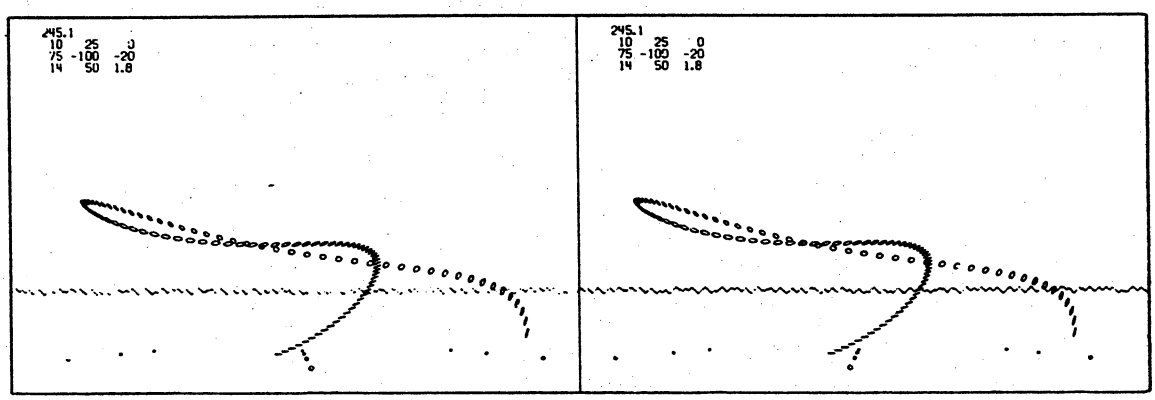

b

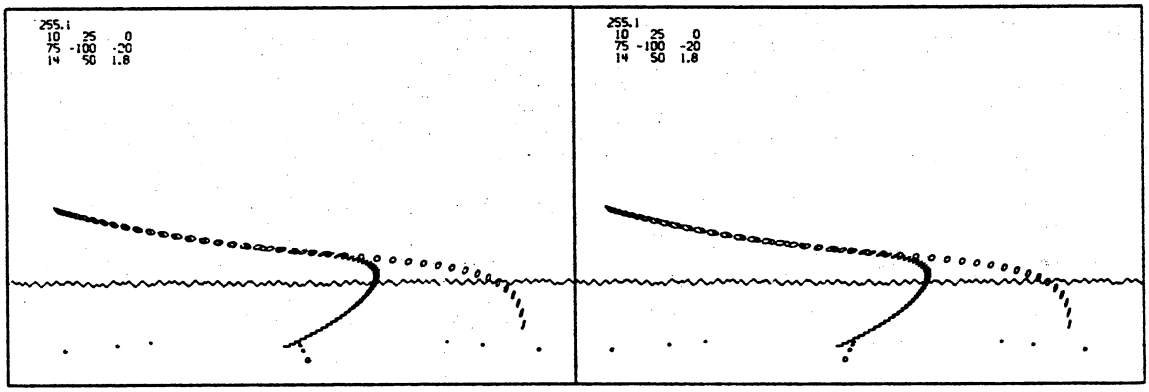

c

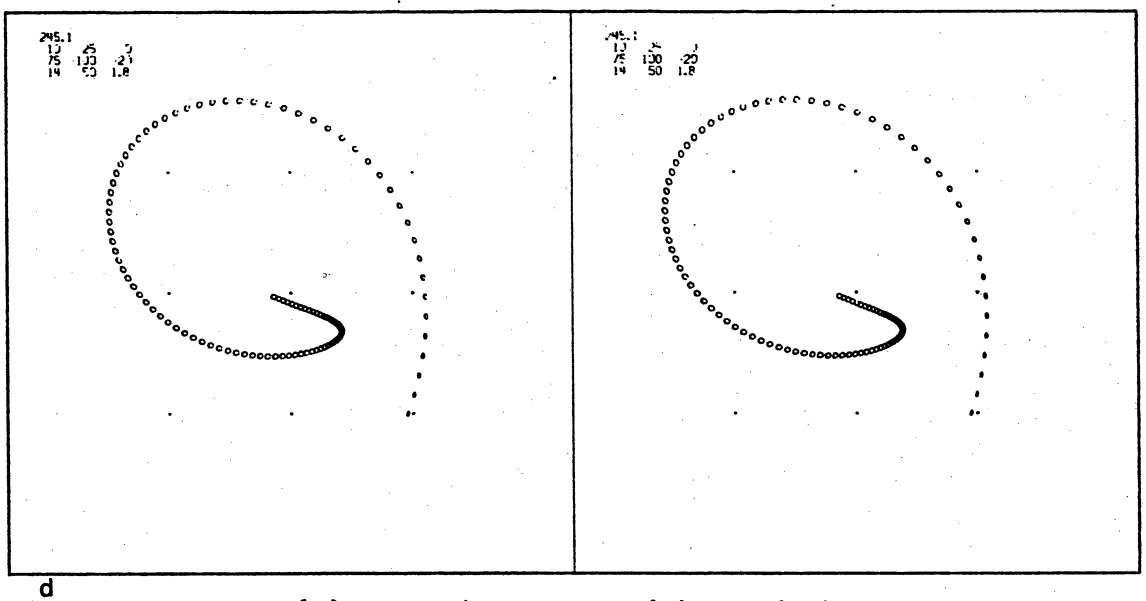

d

fig. 18.6. L5. a: {1}, 5R17A/L19A. b,d: {3}. c: {3'}.

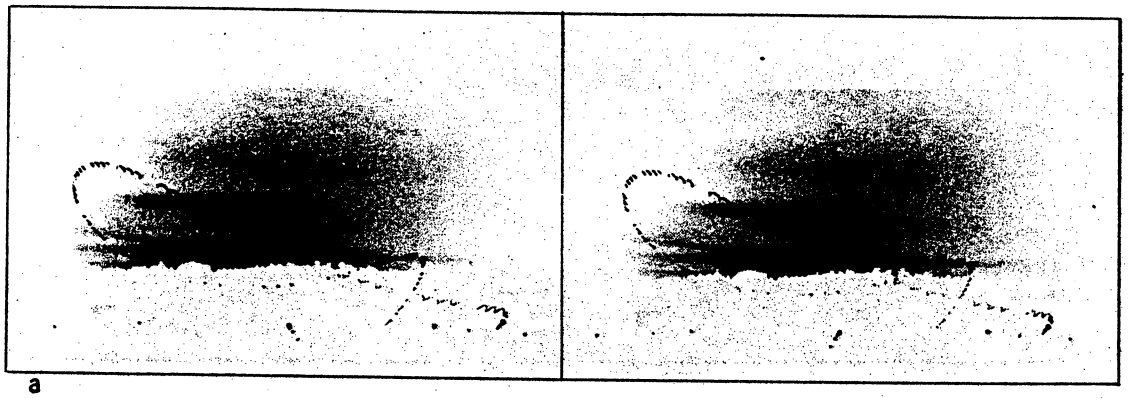

a

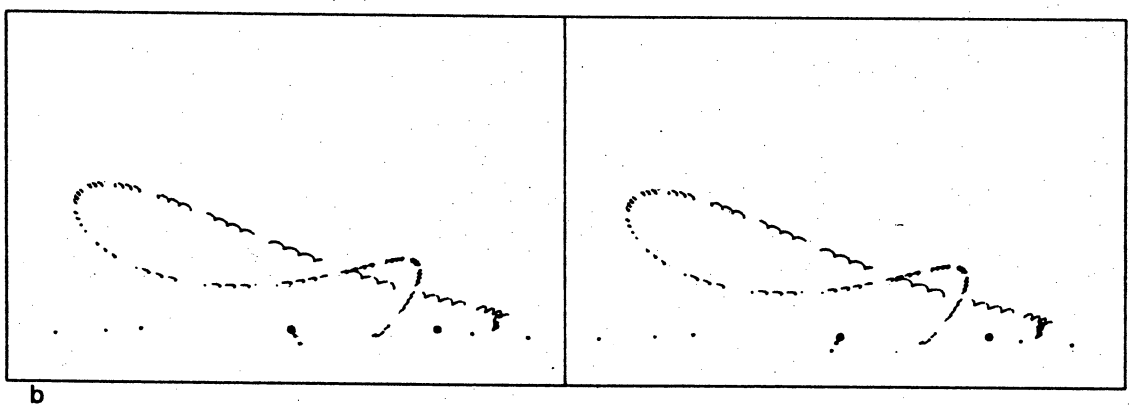

b

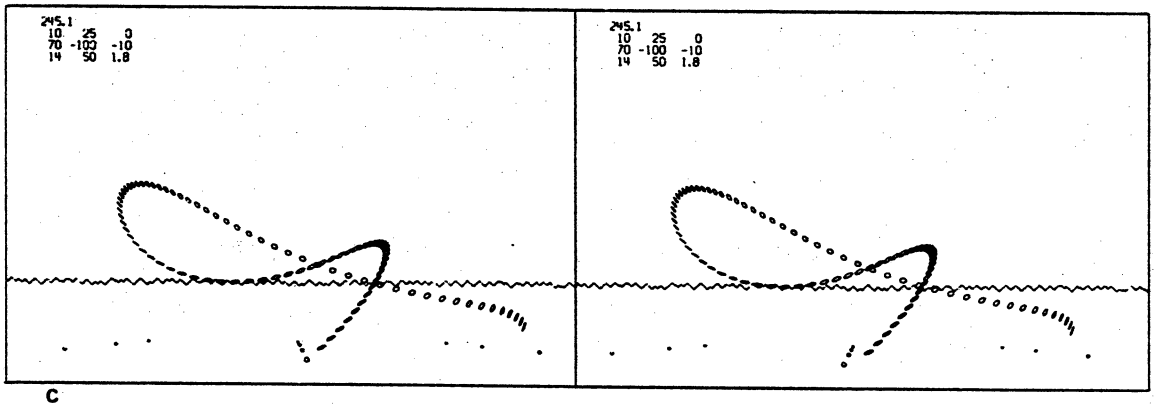

c

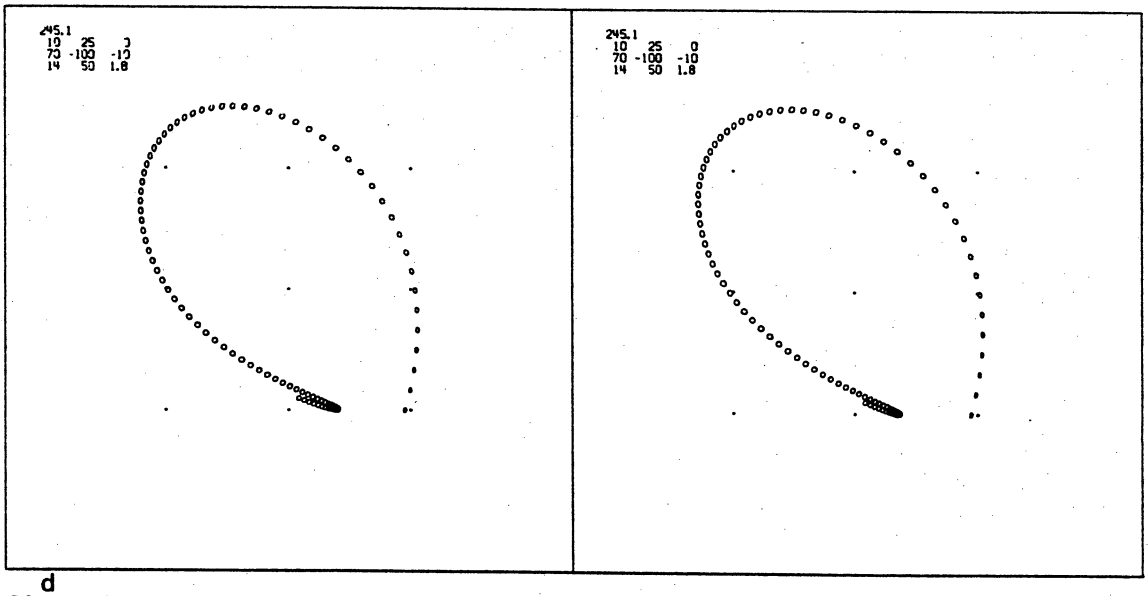

d

fig. 18.7. L5. a: {1}, 5R18A/L20A. b: {1}, 6R2/L2. c,d: {3}.

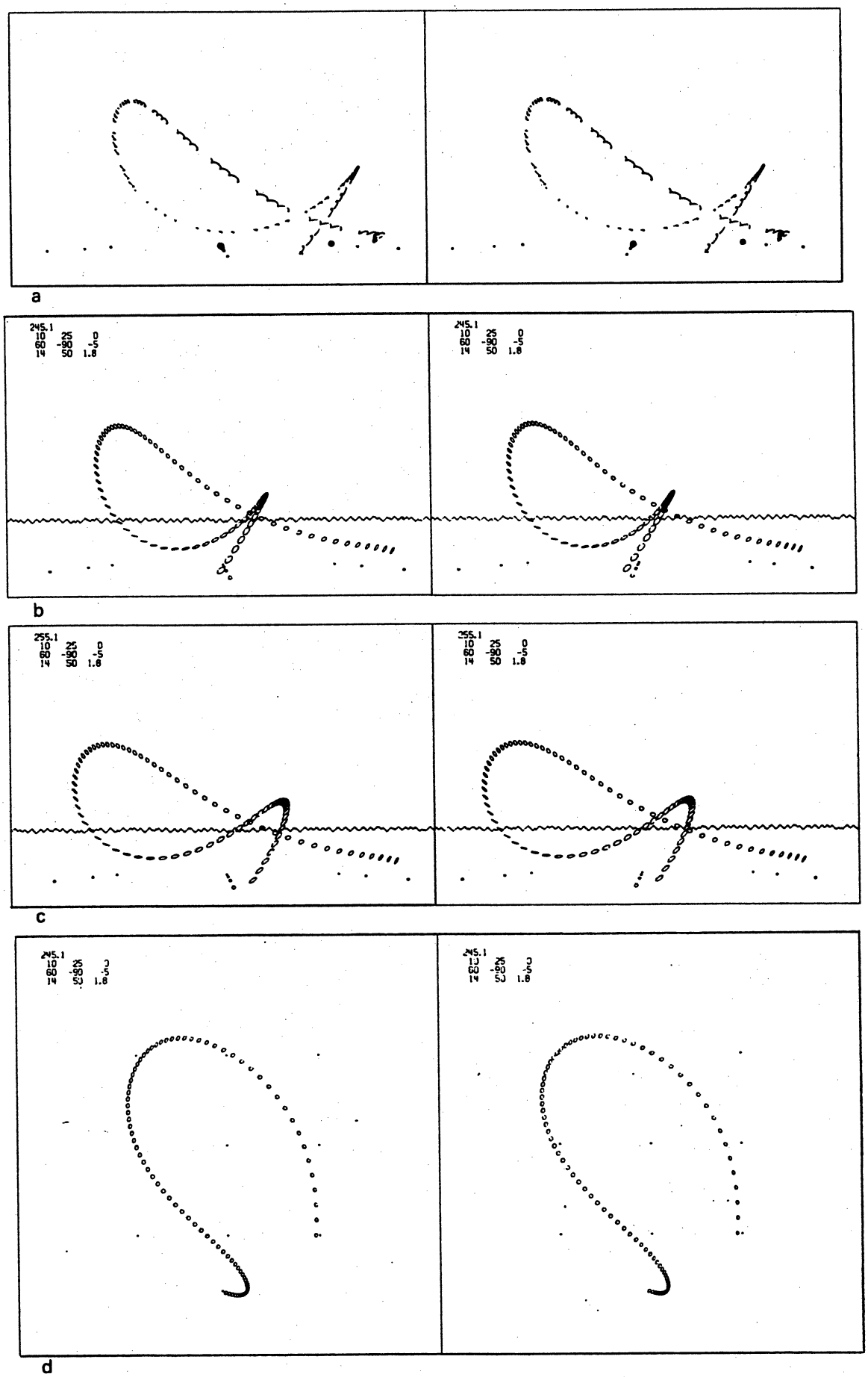

fig. 18.8. L5. a: {1}, 6R3/L3. b,d: {3}. c: {3'}.

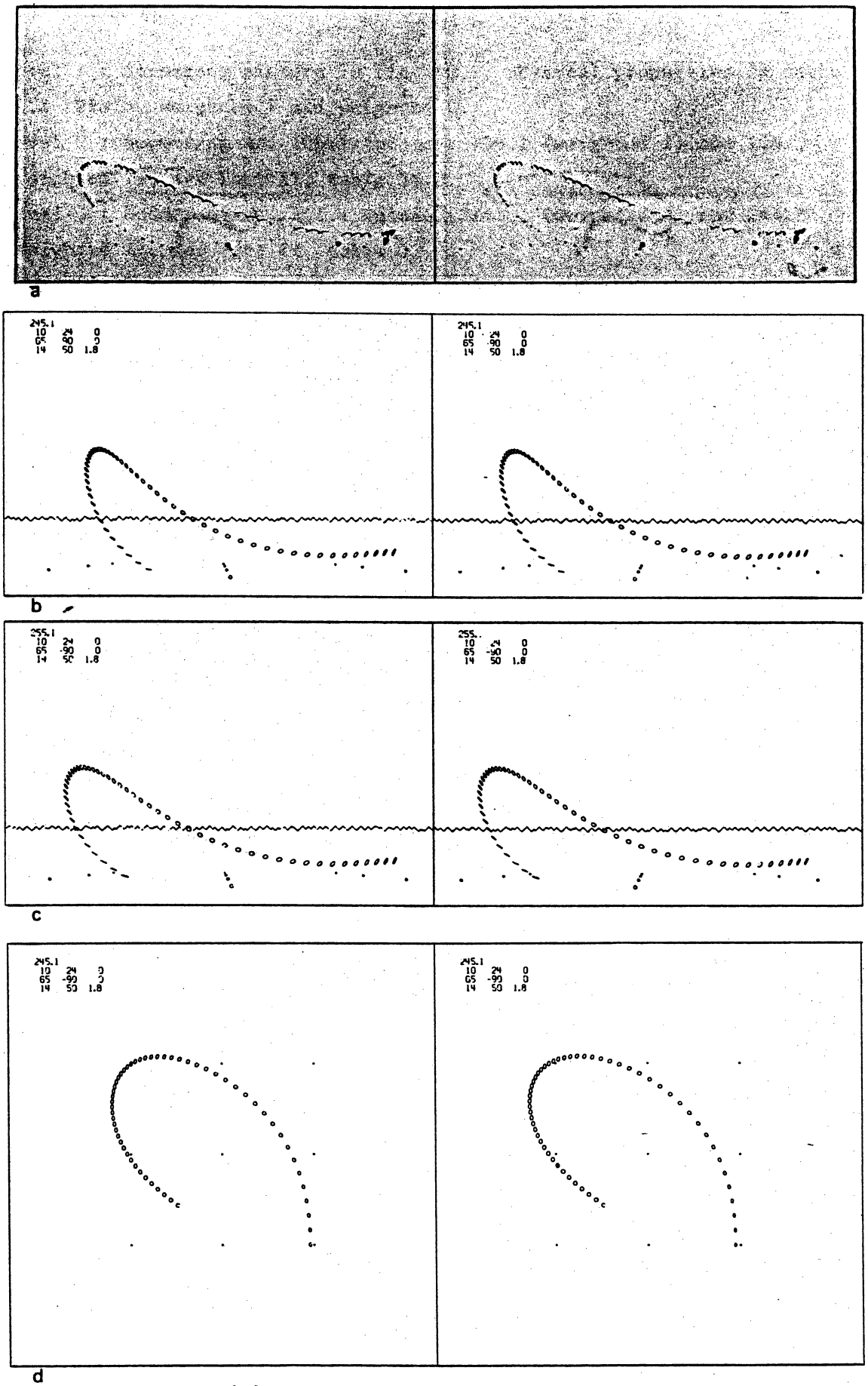

fig. 18.9. L5. a: {1}, 5R27A/L29A. b,d: {3}. c: {3'}.

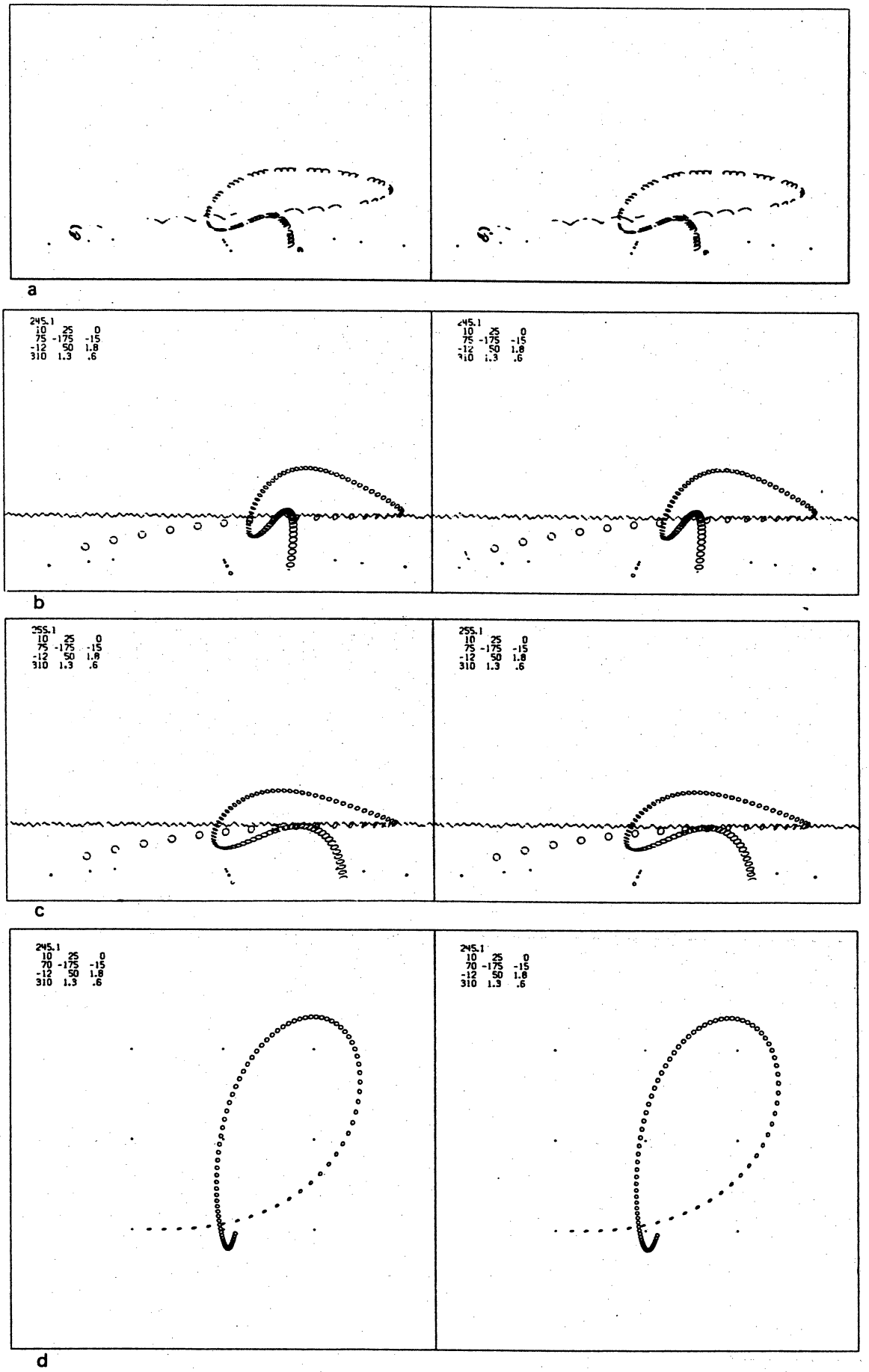

fig. 18.10. L5. a: {1}, 9R27A/L30A. b,d: {3}. c: {3'}.

§19 *Boomerang L6.*

Level 1 : boomerang picture in fig. 10.1, physical properties in table 10.1. Plain, weighted 1 and weighted 2.
Level 2 : boomerang nr. 106.1 (plain), 106.2 (weighted 1) and 106.3 (weighted 2), see Part II, table 31.3.
Level 3 : boomerang nr. 241.1 (plain), 241.2 (weighted 1) and 241.3 (weighted 2), see Part II, table 32.1.
Level 3': boomerang nr. 253.1 (plain), 254.2 (weighted 1) and 254.3 (weighted 2). No flight paths presented.
Level 2 and level 3 graphs of aerodynamic force components: Part II, fig. 31.19 through 31.24.
No flight paths are presented of the version "weighted 1".

In the case of boomerang L6 the level 2 flight paths poorly resemble the photographed ones, due to inaccurate measurements of the aerodynamic forces (see Part II, fig. 31.21). Rather surprisingly, it turns out that the level 2 model boomerang 108.1, belonging to boomerang F18, traverses flight paths very similar to those of boomerang L6. Therefore each flight path photograph of boomerang L6 is accompanied by a computed flight path of boomerang nr. 108.1, said to be of *level 2** in this case.

List of flight paths of boomerang L6 plain.

fig.	level	negatives or boomerang nr.	f_o	V_o	Ψ_o	ϑ_o	φ_o	ψ_o	X_o	Y_o	Z_o	β	W_o	W_1
19.1a	1	12R12/L19A												
b,d	2*	108.1	10	25	0	65	-165	-10	- 5	50	1.8	0	0	0
c	2	106.1	10	25	0	60	-165	-10	- 5	50	1.8	0	0	0
19.2a	1	12R29/L36A												
b,d	2*	108.1	10	25	0	70	-170	-10	- 7	50	1.8	0	0	0
c	3	241.1	10	25	0	70	-170	-10	- 7	50	1.8	0	0	0
19.3a	1	12R24/L31A												
b,d	2*	108.1	10	25	0	60	-180	- 5	-12	50	1.8	0	0	0
c	2	106.1	10	25	0	55	-180	- 5	-12	50	1.8	0	0	0
19.4a	1	14R5A/L5A												
b,d	2*	108.1	10	25	0	80	-160	- 5	-11	50	1.8	250	.5	.2
c	3	241.1	10	25	0	80	-160	- 5	-11	50	1.8	250	.5	.2
19.5a	1	12R30/L37A												
b,d	2*	108.1	10	25	0	60	-110	-10	12	50	1.8	0	0	0
c	2	106.1	10	25	0	55	-110	-10	12	50	1.8	0	0	0
19.6a	1	12R19/L26A												
b,d	2*	108.1	10	25	0	80	-100	-15	14	50	1.8	0	0	0
c	2	106.1	10	25	0	75	-100	-15	14	50	1.8	0	0	0

fig.	level	negatives or boomerang nr.	f_o	V_o	Ψ_o	ϑ_o	φ_o	ψ_o	X_o	Y_o	Z_o	β	W_o	W_1
19.7a	1	14R10A/L10A												
b,d	2*	108.1	10	25	0	70	-170	-15	-7	50	1.8	250	.5	.2
c	3	241.1	10	25	0	70	-170	-15	-7	50	1.8	250	.5	.2

List of flight path pictures for boomerang L6 weighted 2.

fig.	level	negatives or boomerang nr.	f_o	V_o	Ψ_o	ϑ_o	φ_o	ψ_o	X_o	Y_o	Z_o	β	W_o	W_1
19.8a	1	13R20/L19												
b,d	2*	108.1	10	25	0	65	-180	-15	-8	50	1.8	250	.5	.2
c	3	241.3	10	25	0	70	-180	-15	-8	50	1.8	250	.5	.2
19.9a	1	13R17/L16												
b,d	2*	108.1	10	25	0	70	-165	-20	-7	50	1.8	250	.5	.2
c	3	241.3	10	25	0	70	-165	-20	-7	50	1.8	250	.5	.2
19.10a	1	13R10/L9A												
b,d	2*	108.1	10	25	0	60	-110	-10	9	50	1.8	250	.5	.2
c	2	106.3	10	25	0	50	-110	-10	9	50	1.8	250	.5	.2
19.11a	1	13R22/L21												
b,d	2*	108.1	10	25	0	60	-110	-15	10	50	1.8	250	.5	.2
c	3	241.3	10	25	0	65	-110	-15	10	50	1.8	250	.5	.2

Comment.

Boomerang L6 traverses elongated loops, which have an appearance quite different from the more circular orbits traversed by the boomerangs L1 and L4. This indicates a strong tendency for the L6 to lie down. Probably the ratio T_y/T_x during the flights is greater for this boomerang than for boomerangs like L1, L4 and L5. The agreement between the photographed flight paths and the computed flights of boomerang 108.1 is striking. However, the level 2 (106.1 and 106.3) flights and the level 3 (241.1 and 241.3) flights agree only poorly with the field experiments. Evidently, the aerodynamic characteristics of boomerang 106 are wrong, and so are those of boomerang 241. Moreover, even when I tried to obtain a level 3 boomerang which was to reproduce the photographed flight paths rather than the measured aerodynamic forces for boomerang L6, I did not succeed. Relatively the best agreement between a level 1 path and a level 3 path is shown in fig. 19.11 for the weighted 2 version of boomerang L6.

In fig. 19.9a, level 1, the phenomenon of autorotation can be seen. Boomerang L6 initially spins at about $10\frac{1}{2}$ rev/s, at the highest point

of the flight the spin has decreased to 9 rev/s, and just before touch-down it has increased to almost 11 rev/s. In the accompanying level 2* flight of boomerang 108.1 the spin at the corresponding points has the values 10.0, 8.5 and 9.3 rev/s respectively.

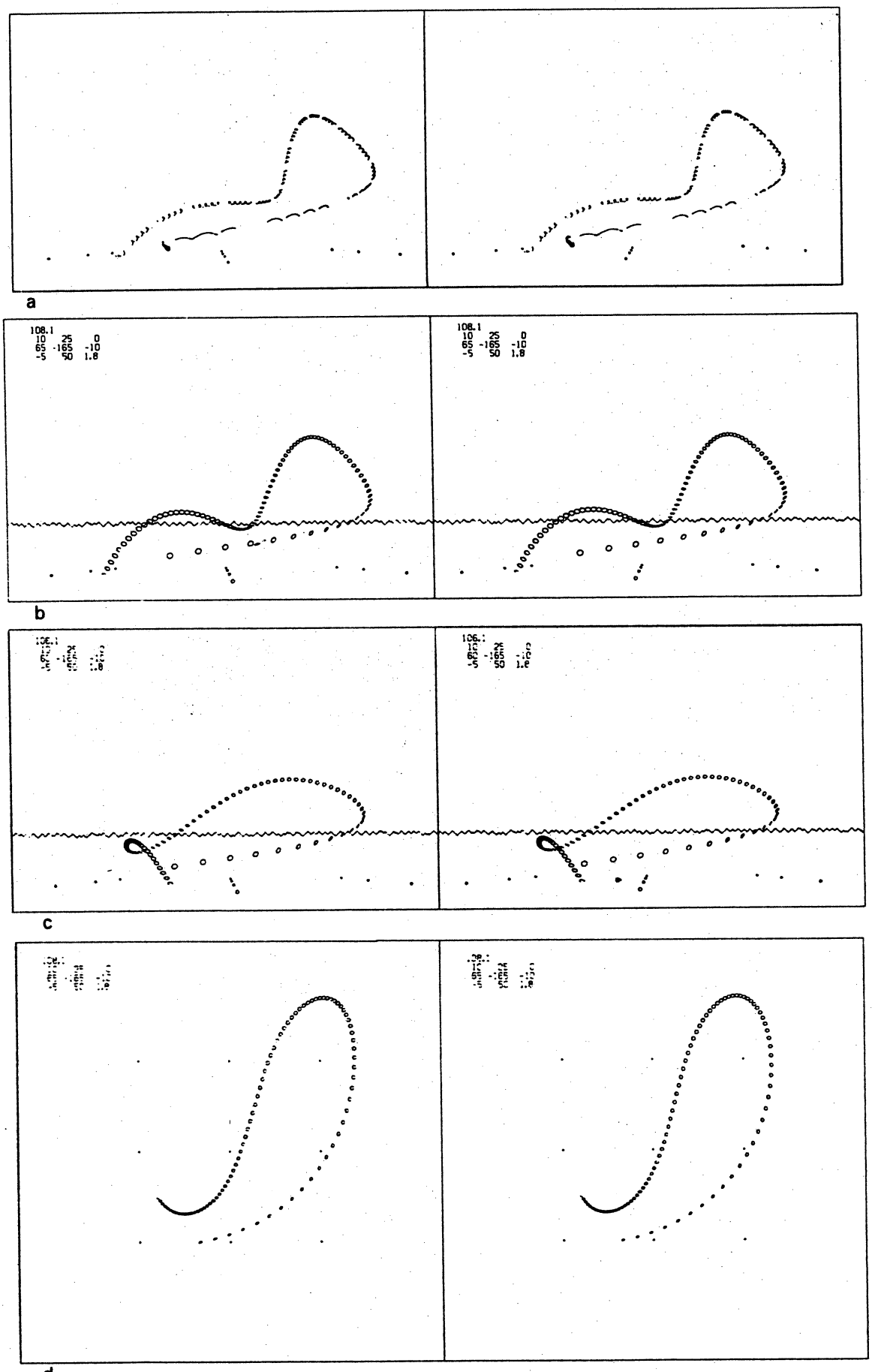

fig. 19.1. L6 plain. a: {1}, 12R12/L19A. b,d: {2*}. c: {2}.

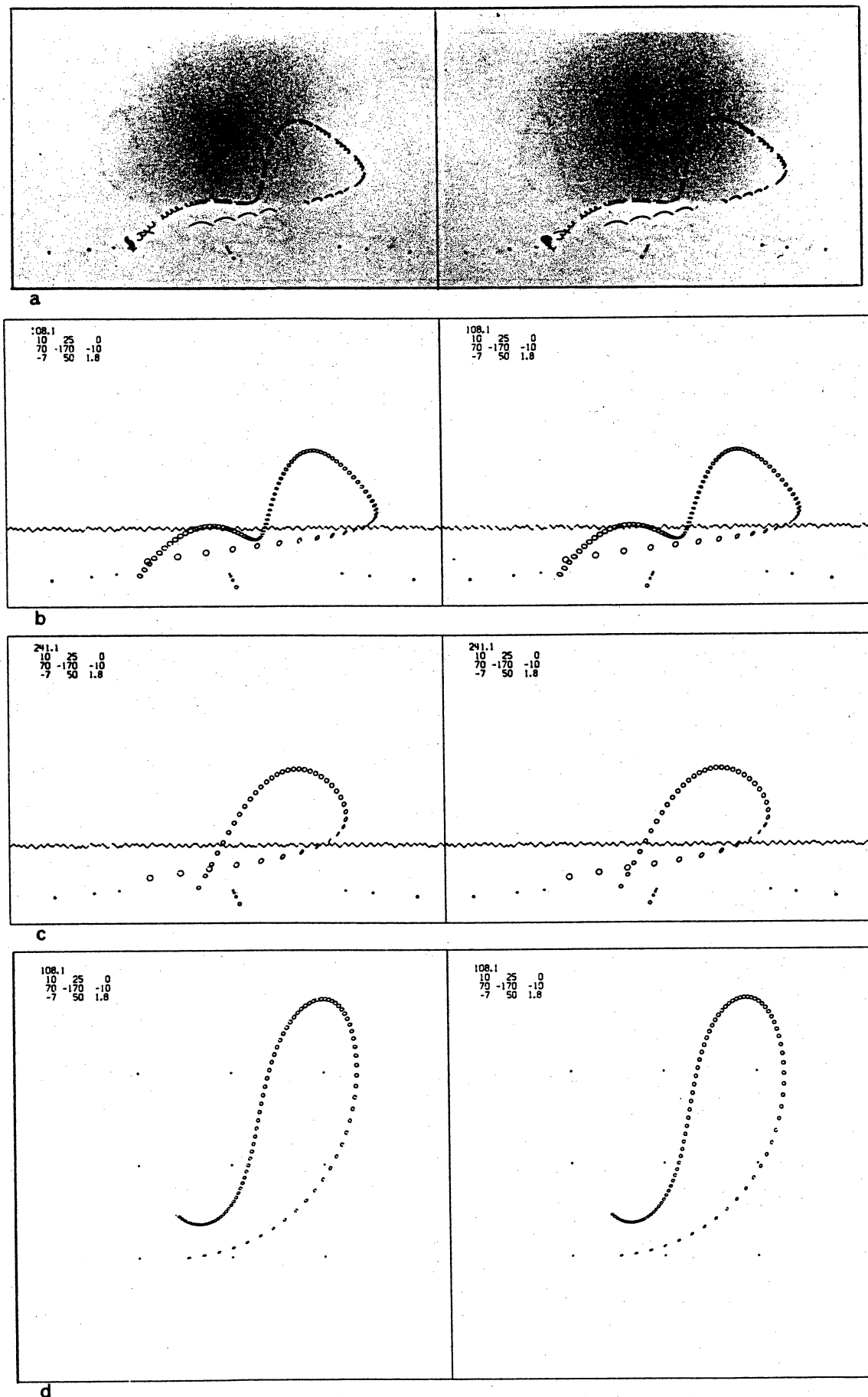

fig. 19.2. L6 plain. a: {1}, 12R29/L36A. b,d: {2*}, c: {3}.

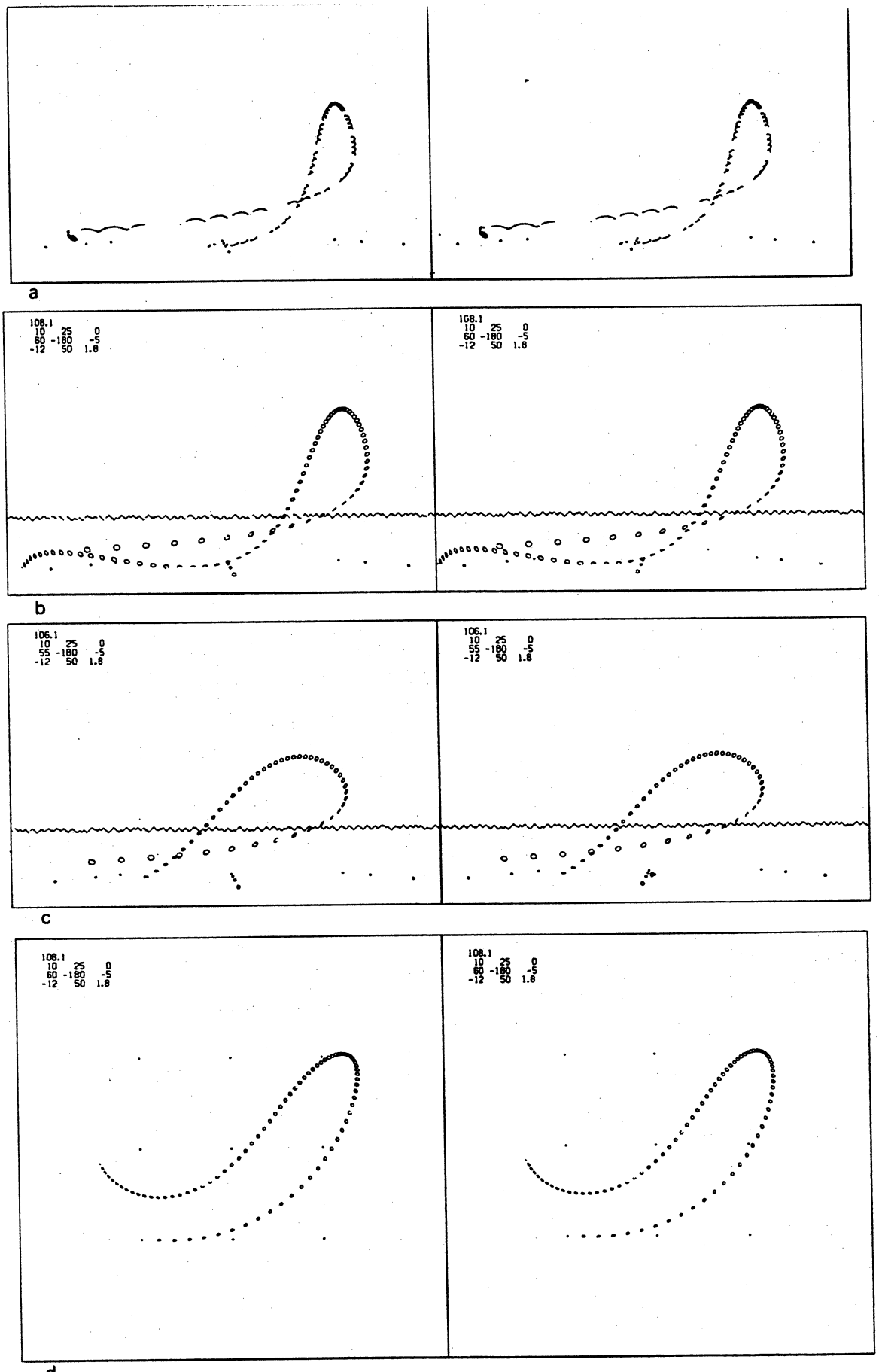

fig. 19.3. L6 plain. a: {1}, 12R24/L31A. b,d: {2*}. c: {2}.

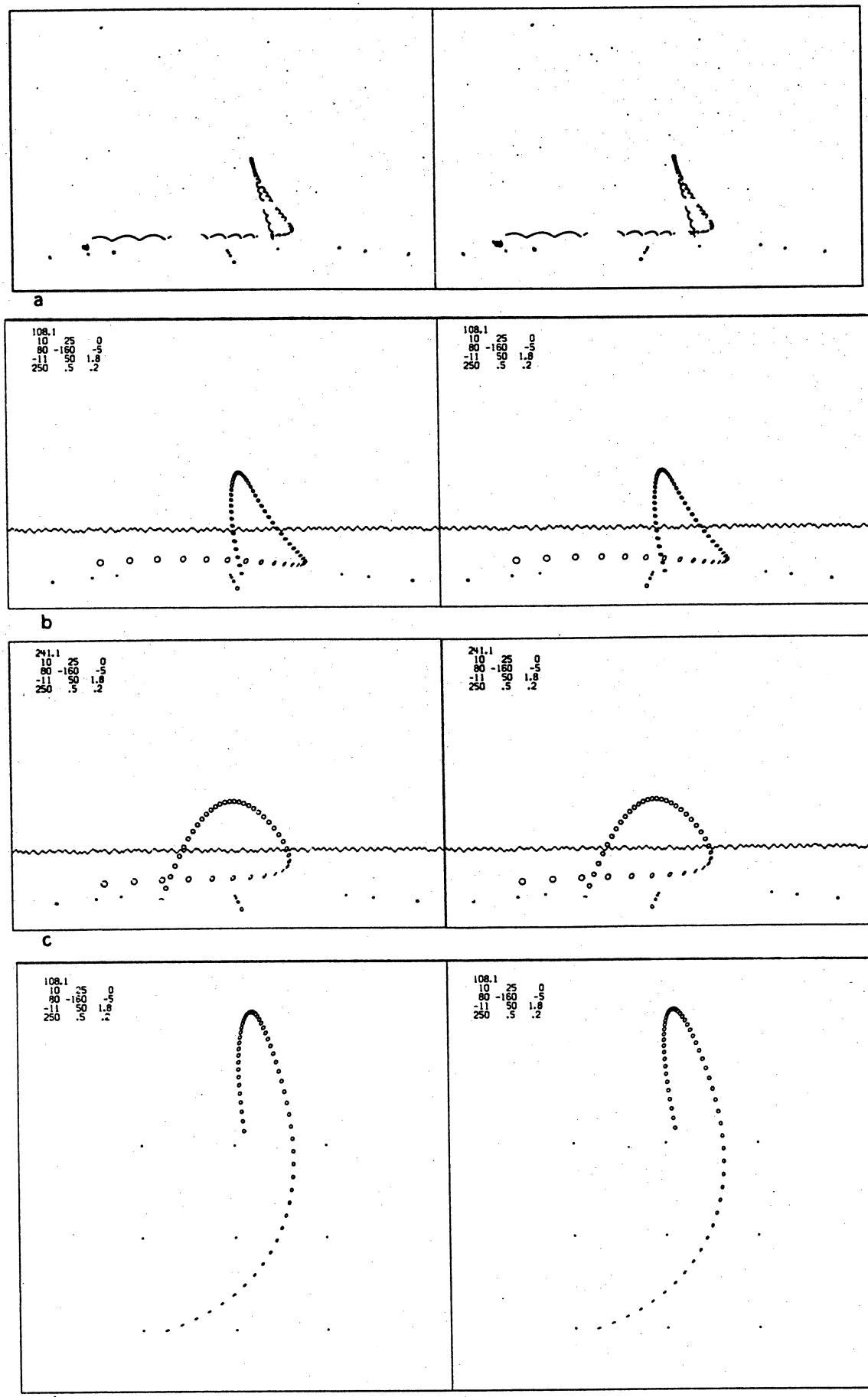

fig. 19.4. L6 plain. a: {1}, 14R5A/L5A. b,d: {2*}. c: {3}.

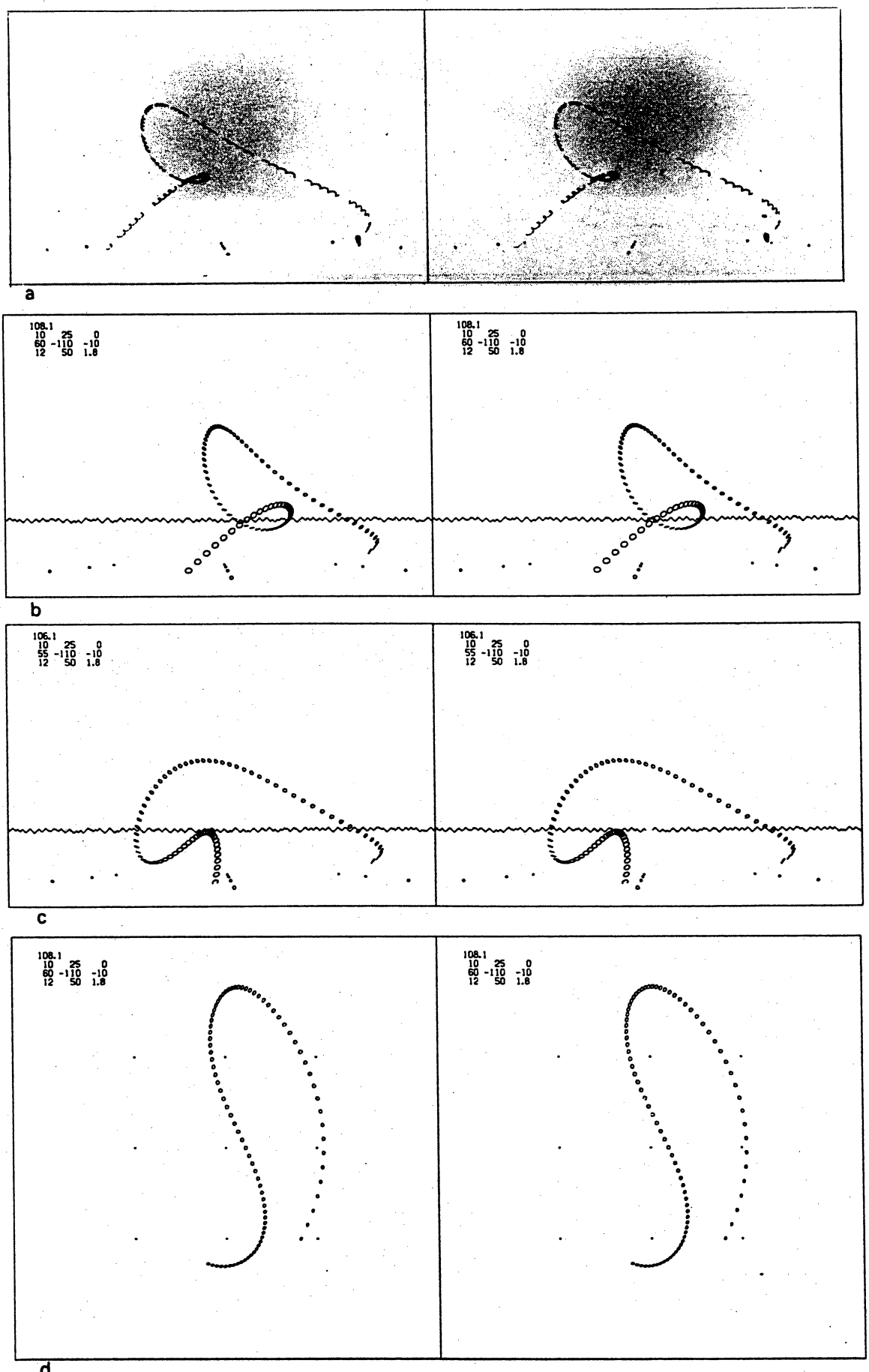

fig. 19.5. L6 plain. a: {1}, 12R30/L37A. b,d: {2*}. c: {2}.

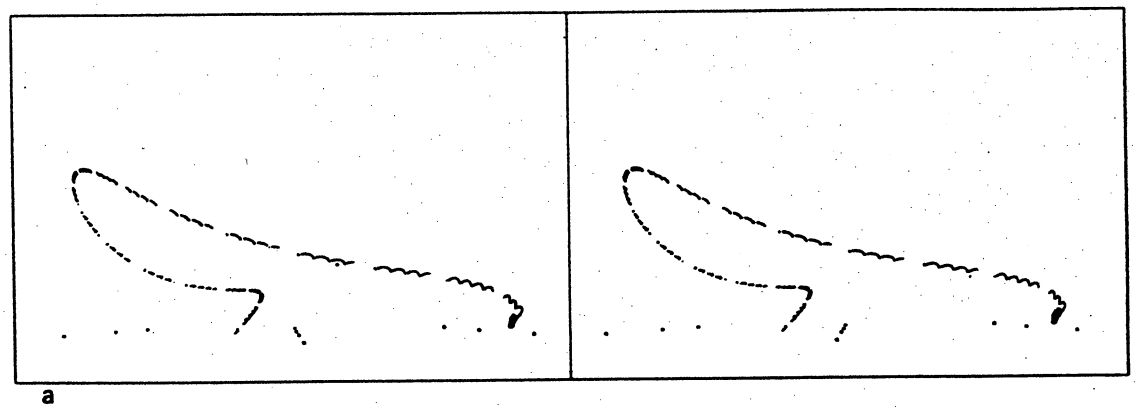

a

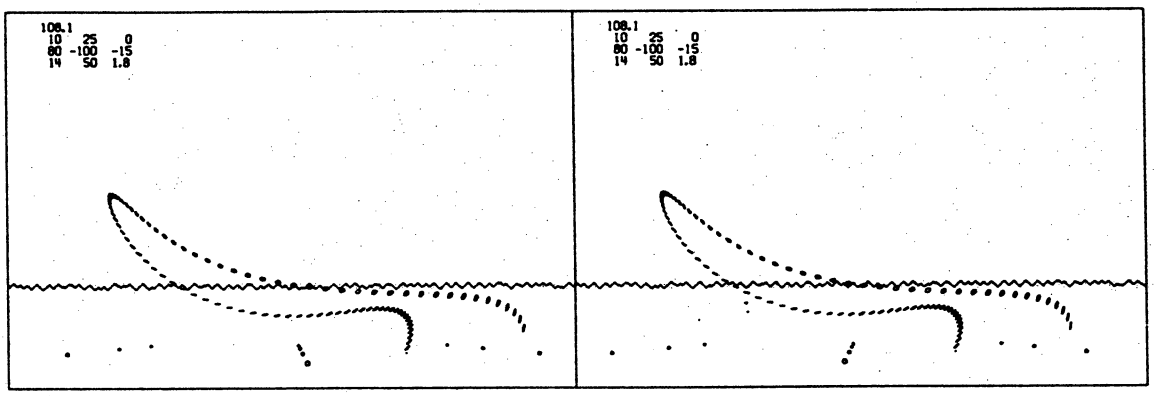

b

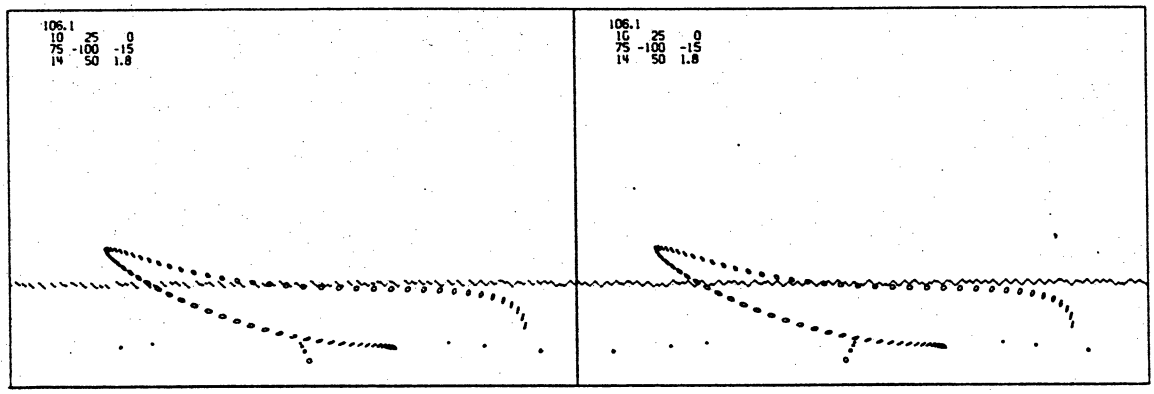

c

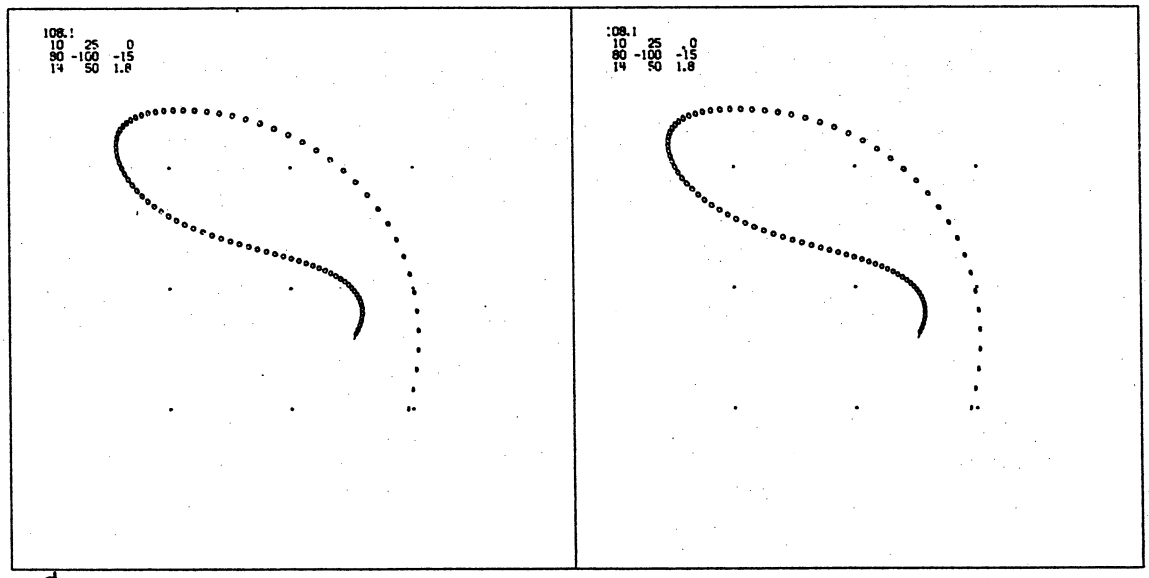

d

fig. 19.6. L6 plain. a: {1}, 12R19/L26A. b,d: {2*}. c: {2}.

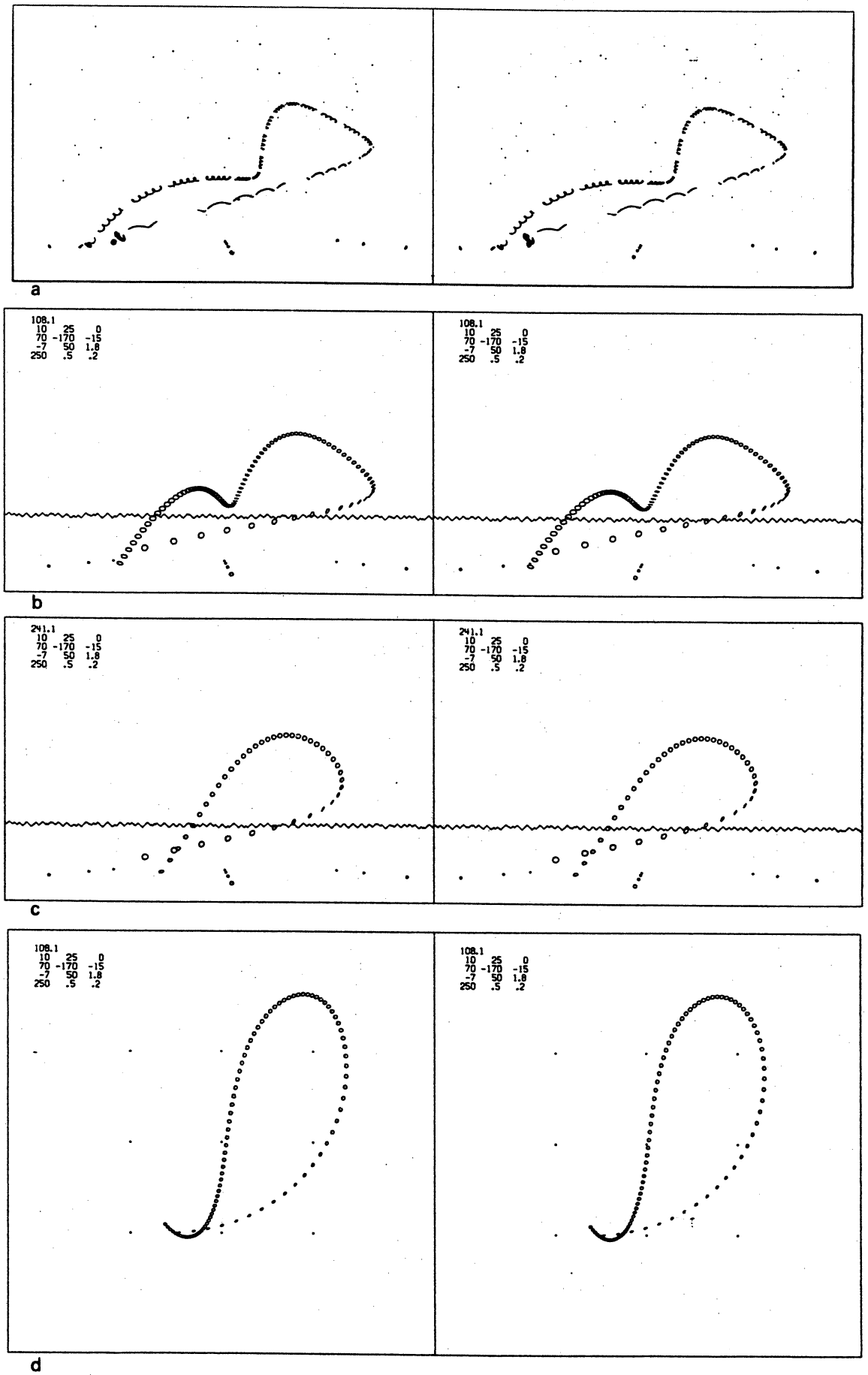

fig. 19.7. L6 plain. a: {1}, 14R10A/L10A. b,d: {2*}. c: {3}.

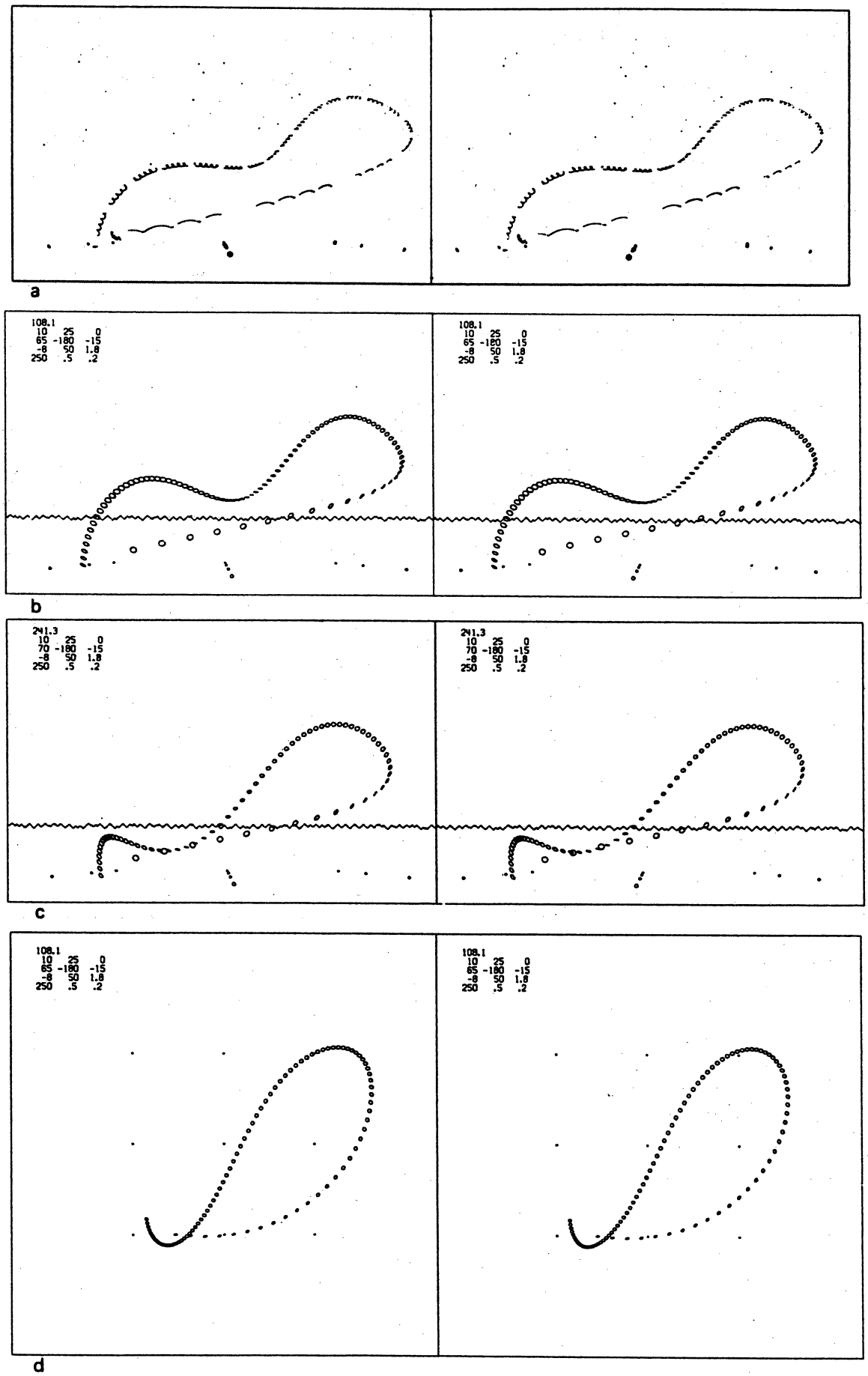

fig. 19.8. L6 weighted 2. a: {1}, 13R20/L19. b,d: {2*}. c: {3}.

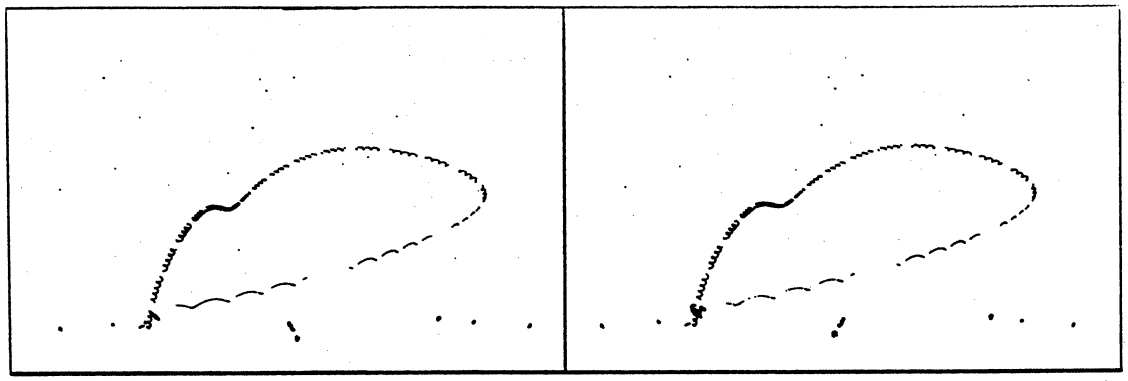

a

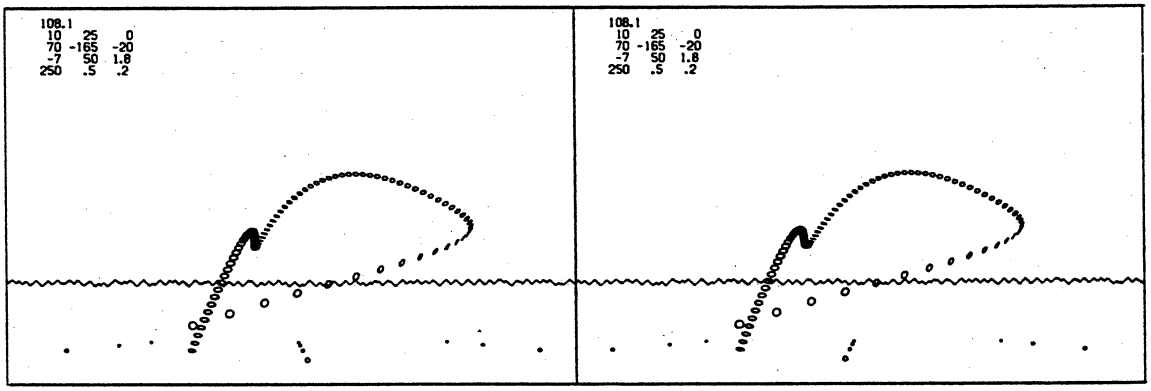

b

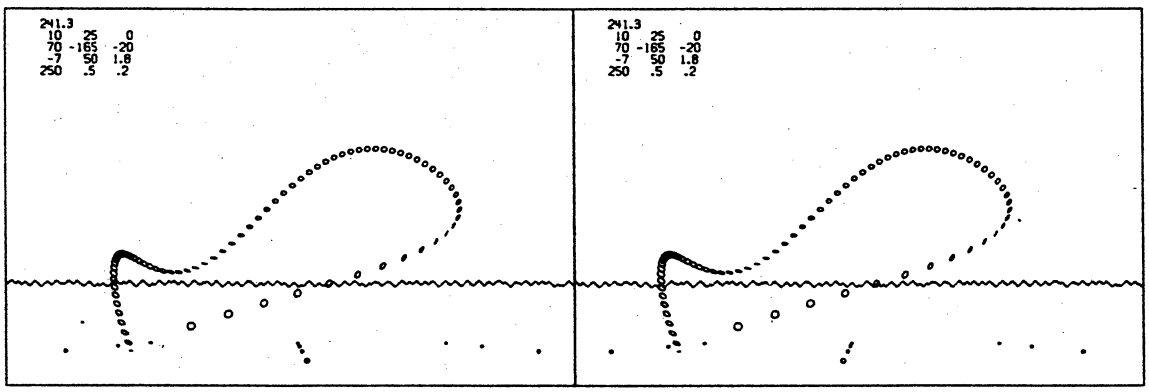

c

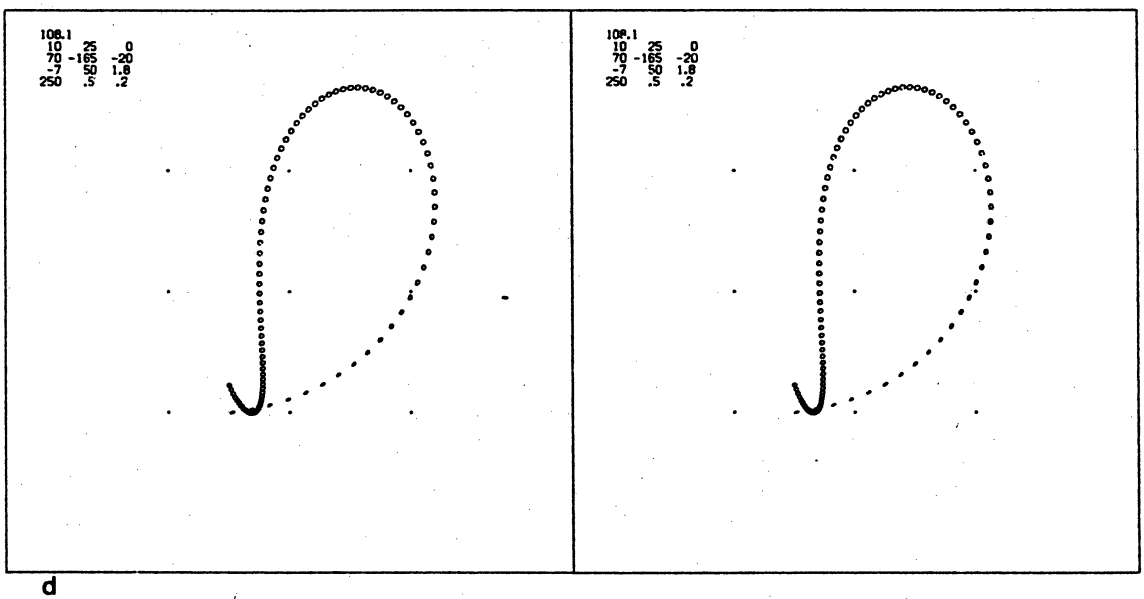

d

fig. 19.9. L6 weighted 2. a: {1}, 13R17/L16. b,d: {2*}. c: {3}.

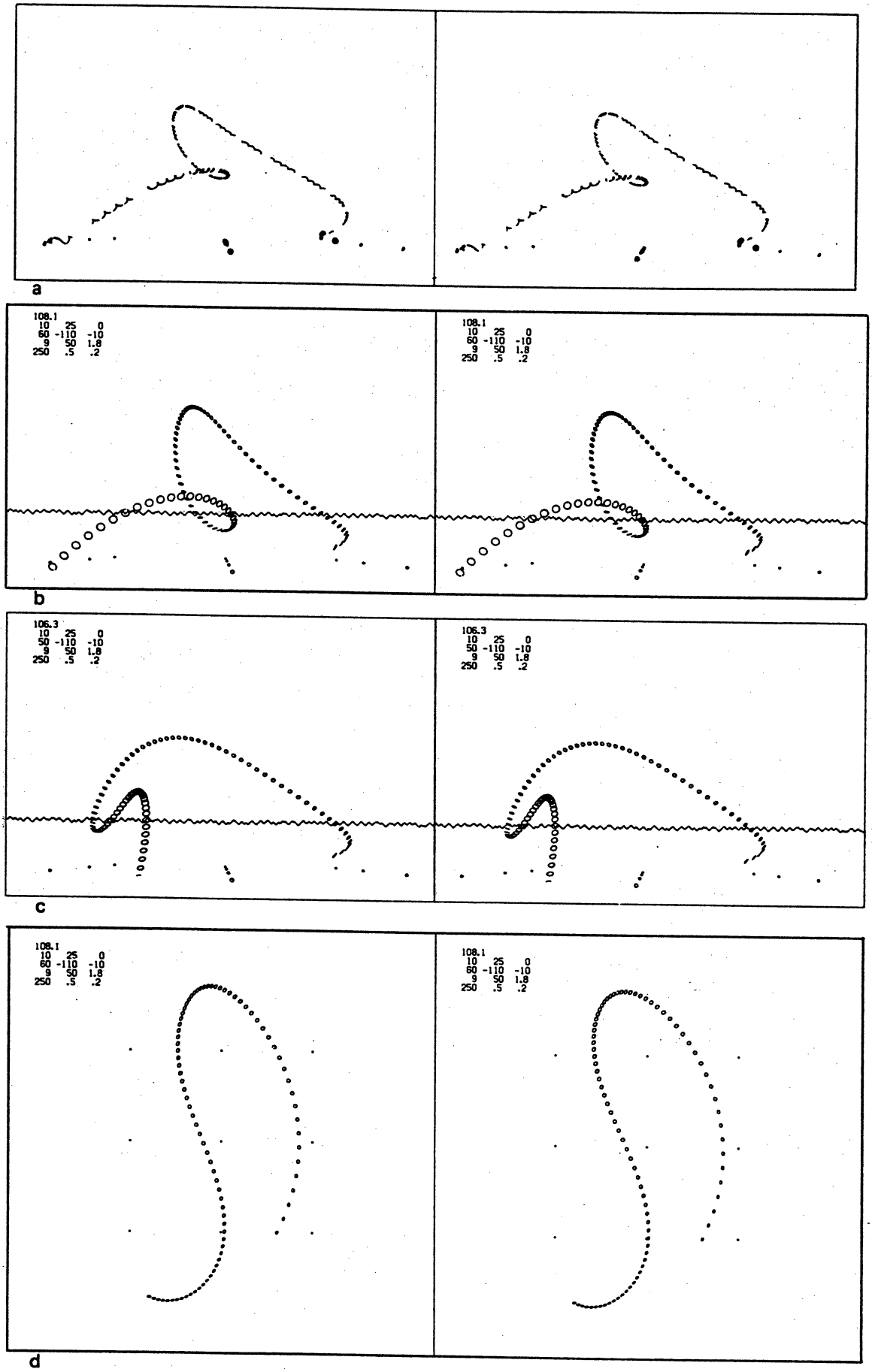

fig. 19.10. L6 weighted 2. a: {1}, 13R10/L9A. b,d: {2*}. c: {2}.

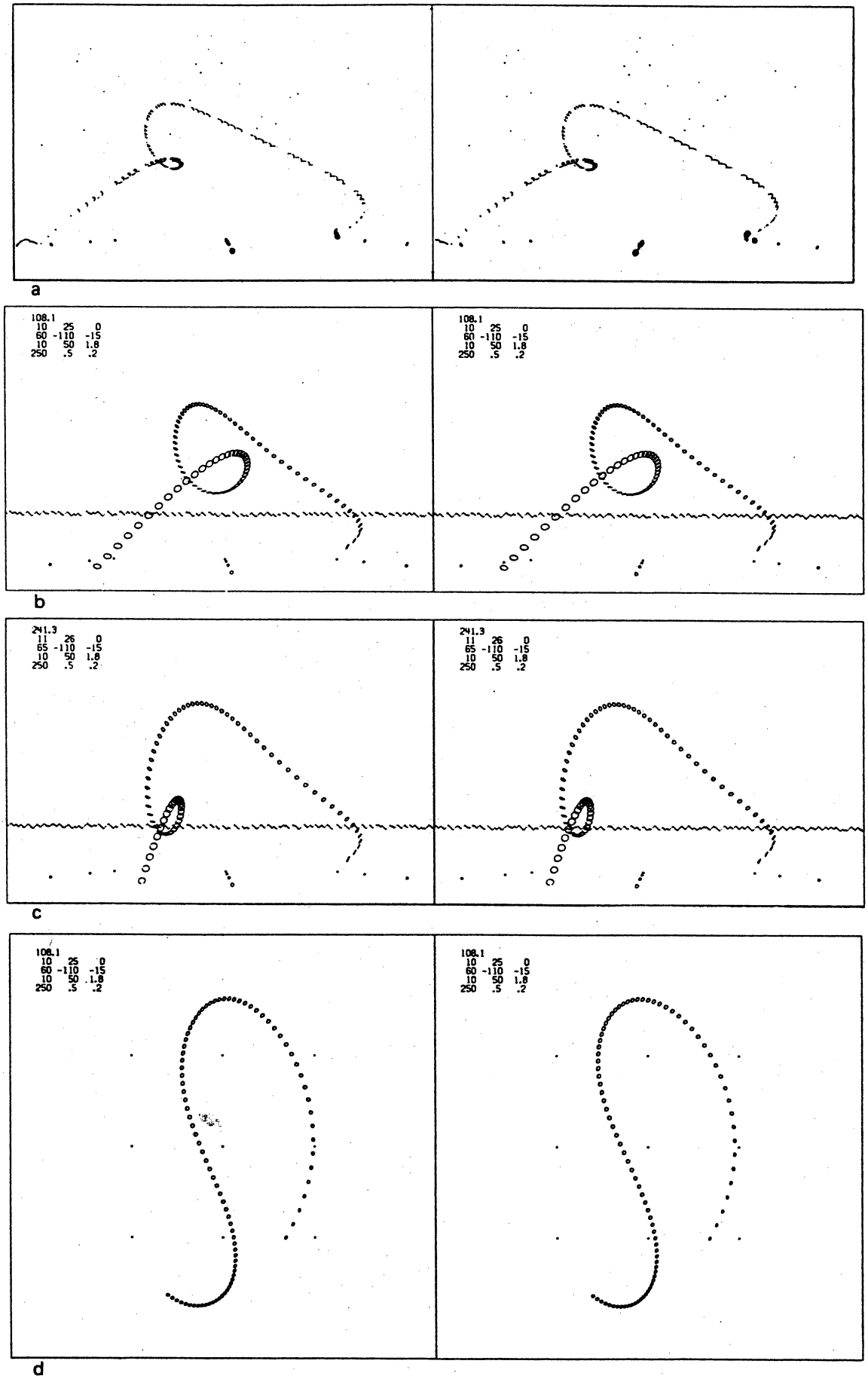

fig. 19.11. L6 weighted 2. a: {1}, 13R22/L21. b,d: {2*}. c: {3}.

§20 *Boomerang F18.*

Level 1 : boomerang picture in Part II, fig. 18.1, physical properties in table 10.1. No flight paths recorded.
Level 2 : boomerang nr. 108.1, see Part II, table 31.4.
Level 3 : boomerang nr. 242.1, see Part II, table 32.1.
Level 3': boomerang nr. 256.1. No flight paths presented.
Level 2 and level 3 graphs of aerodynamic force components: Part II, fig. 31.25 through 31.30.

Photographic stereograms are not available for boomerang F18, its level 1 paths have been witnessed by eye only. Fig. 20.1 offers a comparison between one level 2 flight and one level 3 flight. Three orthogonal projections are plotted, just like the example in fig. 9.1. The square surrounding the vertical projection on a horizontal plane has sides of 40 m, the maximum height above ground level contained within the lines of the horizontal projections is 20 m.

The level 2 path resembles the actual flight paths of boomerang F18. The level 3 path, however, is rather different, boomerang 242.1 does not lie down fast enough. This causes its flight path to be less elongated than it should be.

Eleven more flight paths of boomerang 108.1 are shown in the preceding section on boomerang L6.

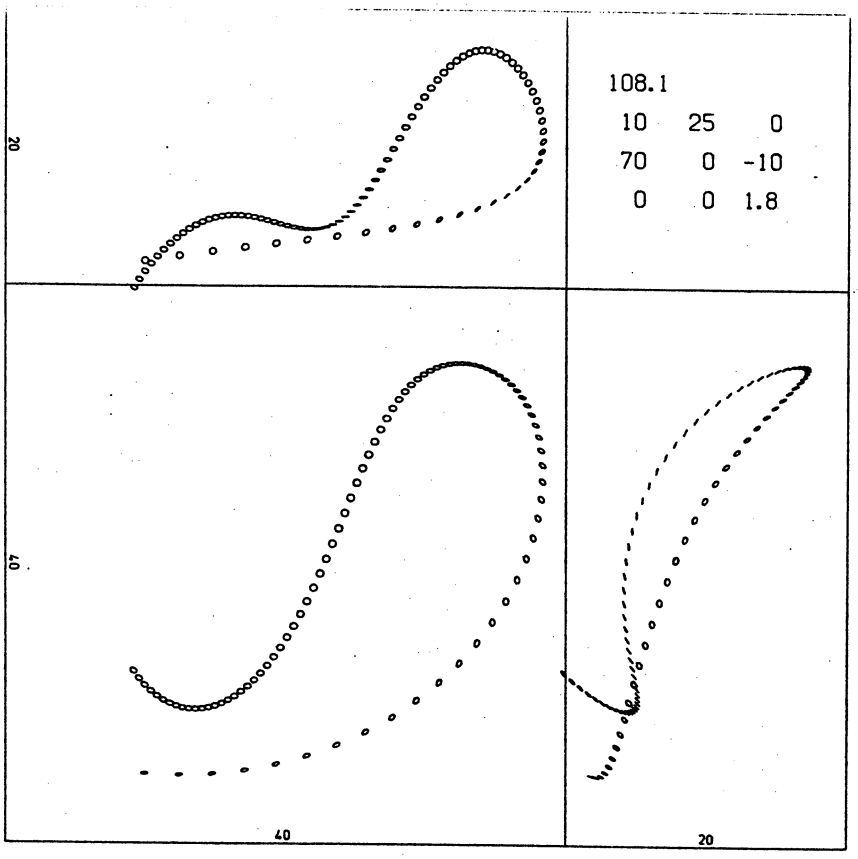

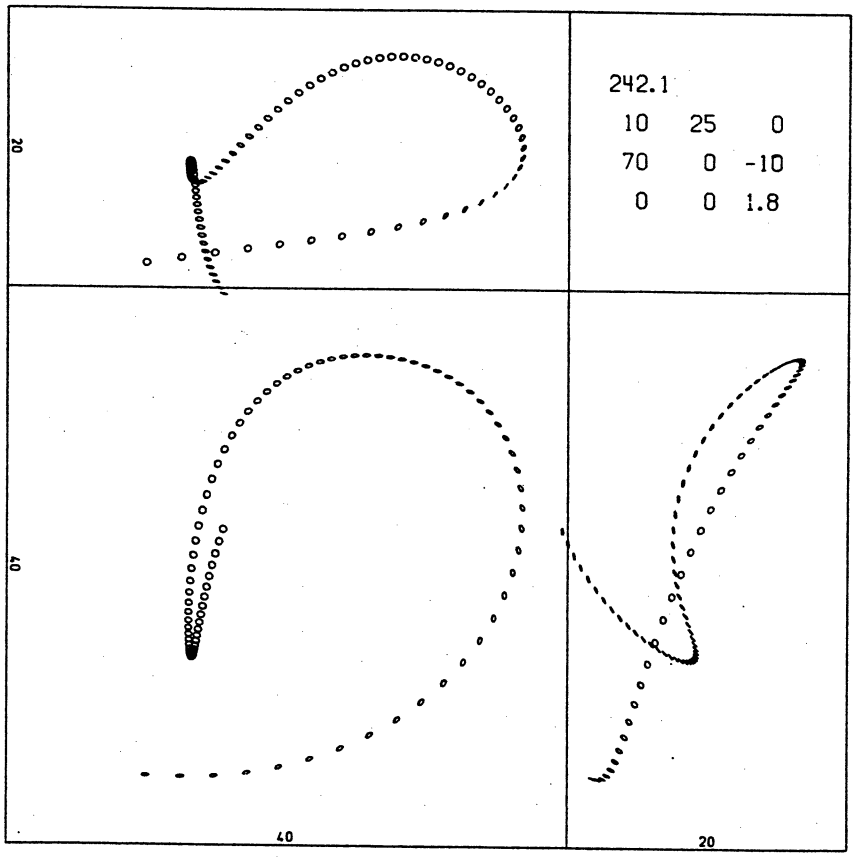

fig. 20.1
boomerang F18
a: {2}.
b: {3}.

§21 *Boomerang WU.*

Level 1 : boomerang picture in Part II, fig. 28.1, physical properties in table 10.1. No flight paths recorded.
Level 2 : boomerang nr. 109.1, see Part II, table 31.5.
Level 3 : boomerang nr. 239.1, see Part II, table 32.1.
Level 3': boomerang nr. 257.1. No flight paths presented.
Level 2 and level 3 graphs of aerodynamic force components: Part II, fig. 31.31 through 31.36.

The flights of the right-handed boomerang WU have been witnessed by eye only. It usually traverses rather low flight paths with a diameter of roughly 35 m. Fig. 21.1 presents orthogonal projections for one level 2 path and one level 3 path, in exactly the same way as fig. 20.1 does for boomerang F18. Both flight paths reasonably resemble actual flight paths of boomerang WU.

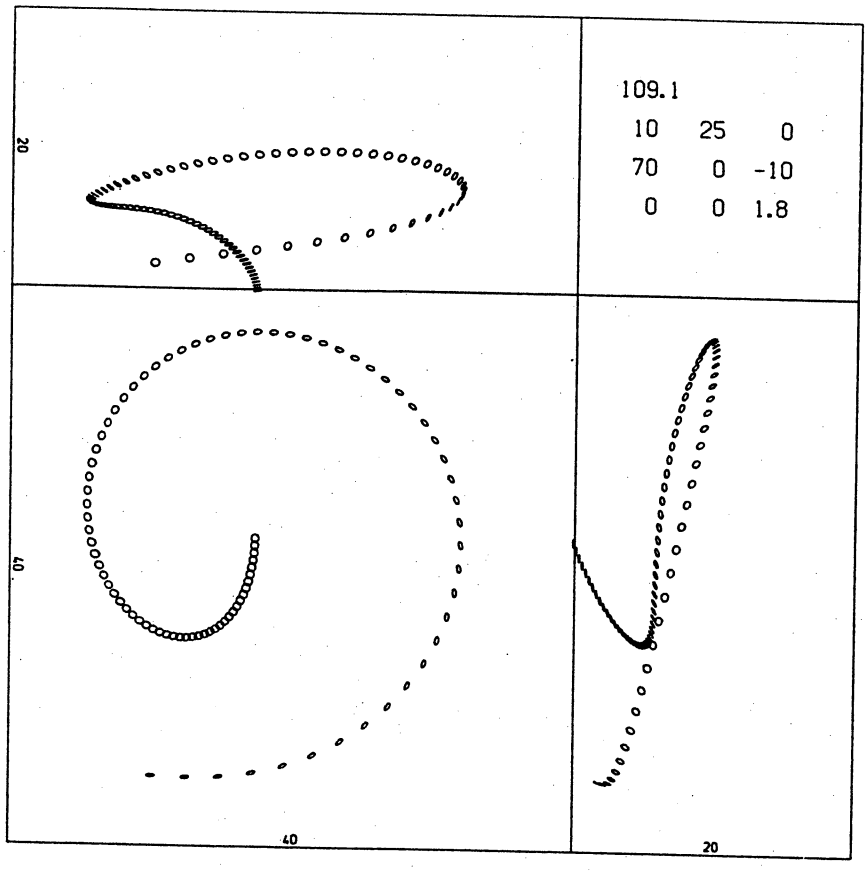

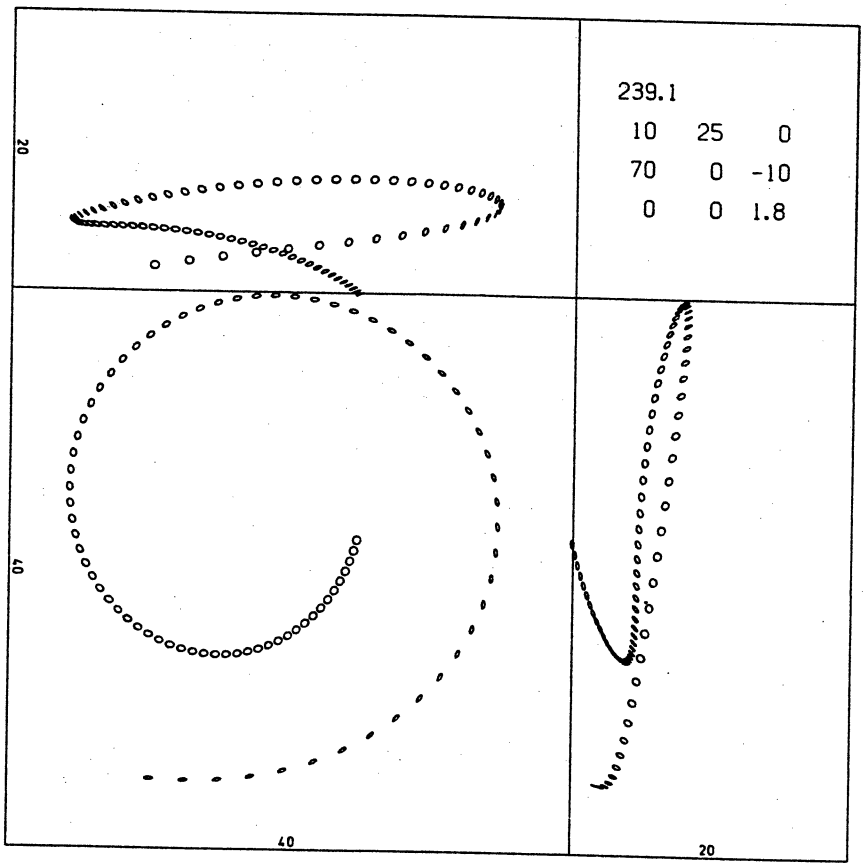

fig. 21.1
boomerang WU
a: {2}.
b: {3}.

§22 *Discussion of the results*

The preceding six sections with flight path stereograms offer a considerable amount of experimental and theoretical data. These provide qualitative, rather than precise quantitative, evidence to judge the validity of our boomerang theory. We did not attempt to extract precise measurements of the level 1 flight paths from the photographic stereograms. For this purpose photographs taken in perpendicular directions would be better suited and a boomerang-throwing machine would be indispensable. Lack of time and of equipment prevented us from carrying out more sophisticated field experiments. However, the experimental data presented in this chapter together with theoretical results are quite sufficient to reach some definite conclusions. In addition, the data allow the reader to form his or her own opinion.

At first glance there is a striking resemblance between photographed and computed flight paths. Such similarity can hardly be accidental. One should bear in mind that the calculated flight paths result from twice integrating the forces and torques acting on a model boomerang. After the first integration the boomerang's speed and spin are found, and after the second integration the boomerang's position (see equations (4.8), (4.9), (4.10)). Even a small deviation in the boomerang's angle of incidence Ψ during the motion may cause significant deviations in the course of the flight path. This difficulty was absent in the simple model of [Hess, 1968], where the angle Ψ was by assumption kept equal to zero, but in our present model - as in reality - the value of Ψ results from the opposing effects of transverse acceleration and precession, according to (6.1). A slight relative change in the rolling torque T_x with respect to the transverse force F_* may cause a substantial shift in the resulting value of Ψ, and hence in the curvature of the flight path. (This effect is discussed further down in this section.) It is therefore quite satisfactory that the dimensions of the computed flight paths correspond reasonably well to those of the real boomerang flight paths.

At second sight, one notices unmistakable differences between corresponding flight paths of the levels 1,2 and 3 or 3'. In some cases the differences are rather serious, particularly for boomerang L6. The deviations between the photographed and the computed flights may be due to one or more of the following three sources:
A) Uncertainties in the photographed flights. The unknown fluctuations of the wind during a flight may be important. Even the average wind velocity during a flight is not precisely known. The shape of the boomerangs during free flight may differ somewhat from that during the wind tunnel experiments. Moreover, the boomerangs may have suffered slight deformations (warp) in the course of the field experiments.
B) Inadequacies of our model for boomerang dynamics, developed in Chapter I. These might be due to the simplification of the equations of motion (see §3 and §5).
C) Errors in the aerodynamic forces acting on the model boomerangs. This means at level 2: errors in the measured force components (which are discussed in Part II, §29), and at levels 3 and 3': shortcomings of our winglet model (which are discussed in Part II, §33).

It is not easy to trace the deviations between flight paths of different levels to particular sources of errors with certainty. For instance, if one compares flight paths of level 1 with those of level 3', errors of types A, B and C all may be present simultaneously, and the available data may be insufficient to separate the effects due to each type of error. Let us nevertheless try to set a step in this direction. Our attempt is based on the assumption that the qualitative and quantitative agreement between the presented flight paths of different levels - as far as present - is not spurious, but should be considered as an indication of the (partial) validity of the underlying theoretical models.

Errors of type A can be present in all level 1 flight paths. Wind fluctuations are expected to cause random deviations, which probably differ from one experimental night to the other. Deformations of a boomerang from its expected shape may cause systematic deviations

in its flights.

In the theoretical results, the errors of type B and type C cannot be distinguished easily. While many of the computed flight paths look fairly realistic, there are some which poorly agree with the experiments. For instance, in the case of boomerang L1, the level 2 paths look particularly good, whereas in the case of boomerang L6 they look rather bad. It is plausible that here the poor quality is due to errors of type C. Indeed, probably there are substantial errors in the measured aerodynamic forces for boomerang L6 (see Part II, §33). Differences between flight paths of level 2 and flight paths of level 3 must be due to errors of type C. It is undeniable that these play a significant part: the graphs in Part II, §31 show - partially systematic - differences between level 2 and level 3 boomerangs, which, of course, give rise to differences between the level 2 and level 3 flight paths. We shall presently discuss this point in more detail.

Errors of type B would be recognisable as systematic deviations, occurring for all boomerangs, between level 1 flights on the one side, and level 2 and level 3(or 3') flights on the other side. We did not find clear-cut indications or such deviations, although their presence cannot be ruled out. For instance: generally the agreement between level 3 paths with experimental paths is least good for cases with $80° \lesssim \vartheta_o \leq 90°$, $-10° \lesssim \psi_o \lesssim 0°$, i.e. when the boomerang is launched in a nearly horizontal direction with its plane nearly vertical. It seems improbable that this would be caused by errors of type A.

It is surprising that level 3' flight paths invariably appear to be less, instead of more, realistic than level 3 paths. This definitely indicates a shortcoming of our aerodynamic model. For a discussion of the differences between flight paths of level 3 and level 3', see also §18. These differences are certainly not negligible, which suggests that a "precession correction" (see §5) would make sense, at least for a realistic aerodynamic boomerang model. In our winglet model, however, the "precession correction" only seems to bring out the model's shortcomings more clearly. Unfortunately, it is difficult

to obtain a valid "precession correction" for level 2 boomerangs. It would be interesting to see how realistic "level 2'" flight paths would look.

It seems likely that most of the deviations of the calculated flights from the photographed flights originate from errors in the aerodynamic forces used in the flight path computations. The available evidence strongly suggests that our theory of boomerang motion yields very good results, provided the aerodynamic forces are given correct values as functions of $\vec{\omega}$,V and Ψ. However, it is difficult to assess the actual accuracy of this theory per se, since this would require a much more precise knowledge of the aerodynamic forces on boomerangs than is available at present.

Let us now consider one case in more detail. It concerns the comparison between a level 2 flight and a level 3 flight for boomerang L1. See figure 16.2. Both model boomerangs, 101.1 and 195.1, are launched at the same initial conditions: f_o = 11 rev/s, V_o = 28 m/s $\Psi_o = 0°$, $\vartheta_o = 90°$, $\psi_o = -15°$. The bird's-eye views of the flight paths (fig. 16.2 e for 101.1, resp. f for 195.1) look rather different. Obviously, after flying for about one second, the path of boomerang 195.1 is more strongly curved than the path of boomerang 101.1. In the first part of the flight the 195.1 flies at a larger angle of incidence Ψ. This is borne out by fig. 22.1, which shows (Ψ,U)-diagrams for each of both flights. A (Ψ,U)-diagram is a path in (Ψ,U)-space traversed by the boomerang in the course of its flight. Both flights start at the point Ψ = 0, U = 1.36. The (Ψ,U)-trajectory proceeds mainly from upper left to lower right. In the case of boomerang 101.1 Ψ soon reaches a value of 8.6°, whereas in the case of boomerang 195.1 Ψ increases to 13.4°. A difference of this kind between boomerangs 101.1 and 195.1 occurs in all flight paths, but in the case considered at present it is particularly strong. It can be traced to a difference in the aerodynamic torque component T_x (see Part II, fig. 31.9). For $\Psi \gtrsim 10°$, T_{1x} is significantly larger for boomerang 195 than for boomerang 101. In fact it must be too large for boomerang 195, since most of the flight paths computed for boomerang 101.1 look very realistic.

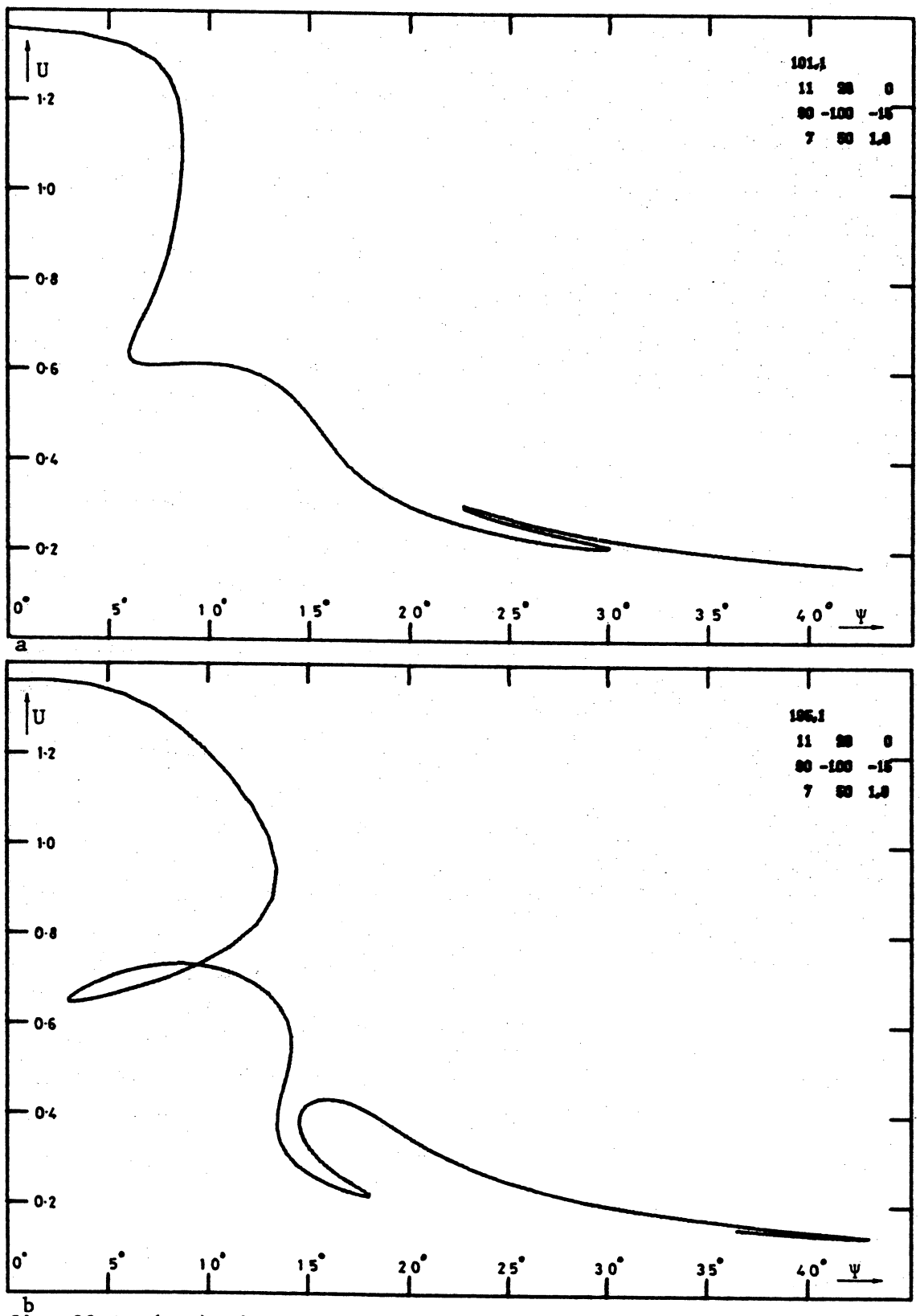

fig. 22.1 (Ψ,U)-diagrams a) a flight by boomerang 101.1. b) corresponding flight by boomerang 195.1.

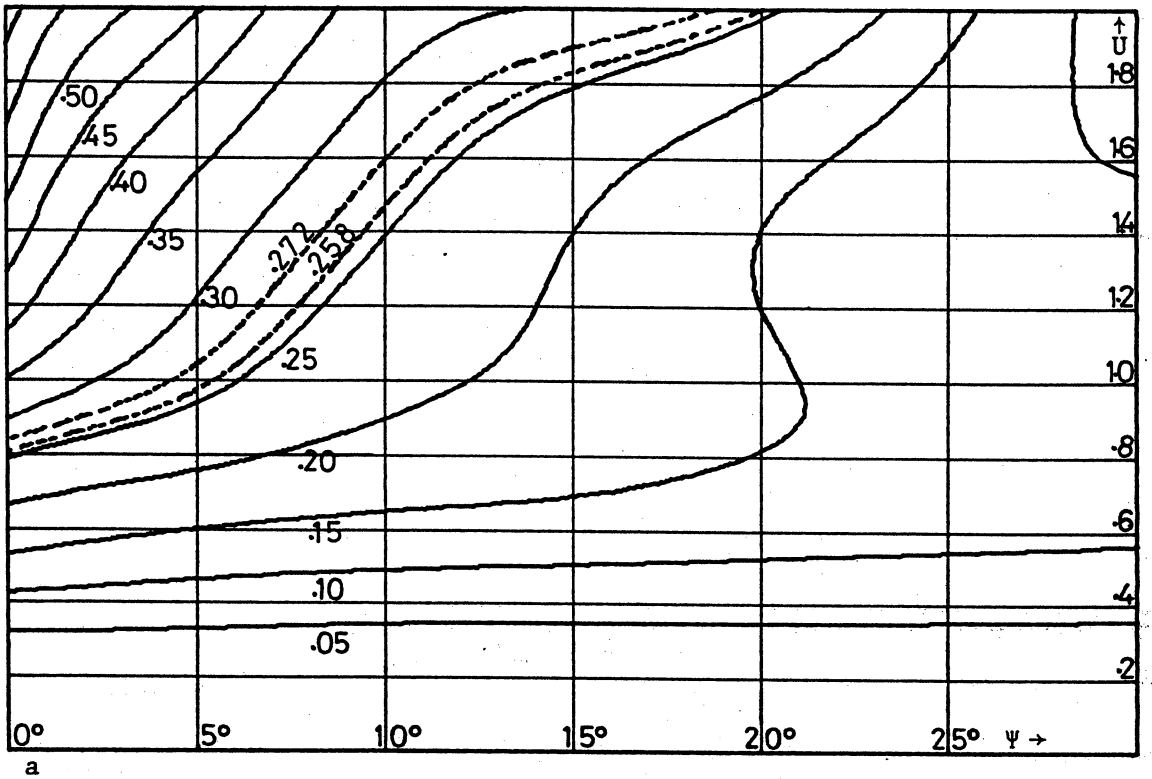

a

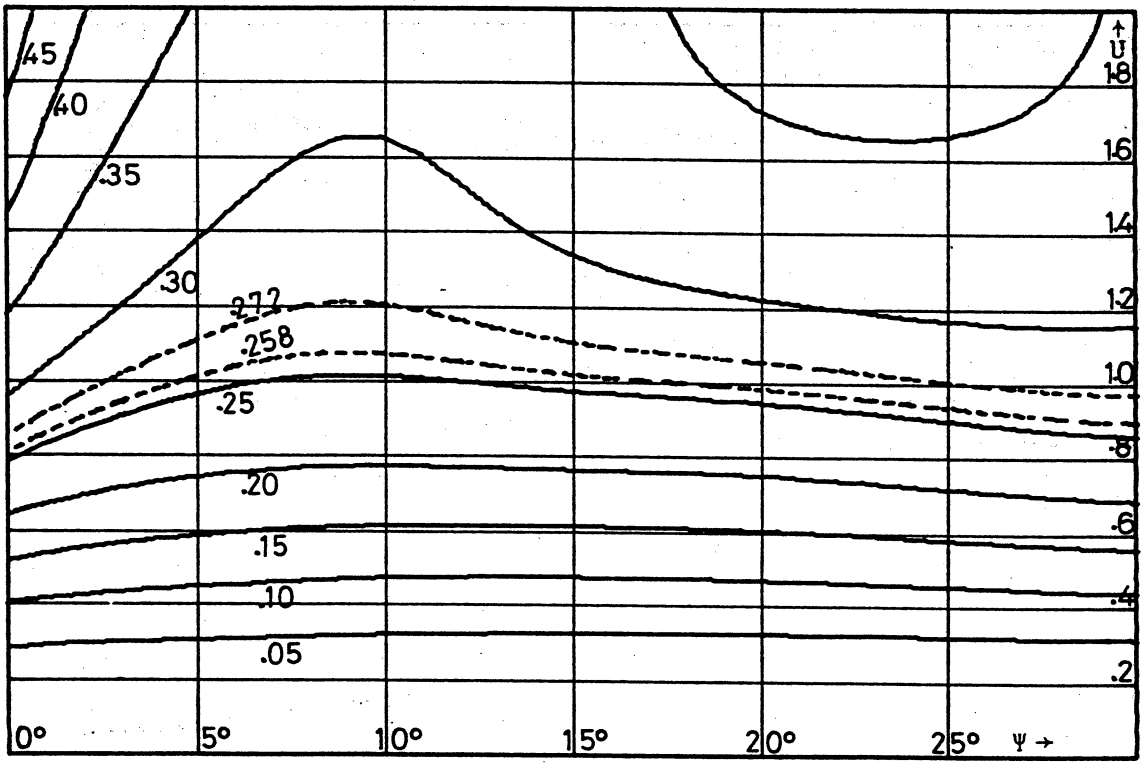

b

fig. 22.2 Contours of the function UT_{1x}/F_{1L} in the (Ψ,U)-plane. a) for boomerangs 101. b) for boomerangs 195. Dashed lines indicate where the function equals λ for the plain resp.weighted version of the boomerang.

than for boomerang 101.1. Although in the flights of fig. 16.2 the condition: $\vartheta \simeq \frac{1}{2}\pi$, $\Psi \approx 0$ does not hold, and the boomerang's weight enters in the problem, the above line of reasoning still has a qualitative validity, and explains much of the difference between the level 2(101.1) and the level 3(195.1) flight path.

It may be of interest to note that the path of a boomerang in the (Ψ,U)-plane, under the condition $\vartheta \simeq \frac{1}{2}\pi$, $\Psi = 0$, is determined by both $\dot{\Psi}$ and $\dot{U}$. It is easy to derive an equation, similar to (22.1), which gives a condition for stationary U, i.e. for $\dot{U} = 0$:

where:

$$\left.\begin{aligned} \frac{-UT_{1z}}{F_{1D}} &= \lambda \\ F_{1D} &= F_{1x}\cos\Psi + F_{1z}\sin\Psi \end{aligned}\right\} \quad (22.2)$$

It can also be shown that, for $F_{1D} > 0$, U decreases as long as $-UT_{1z}/F_{1D} < \lambda$. Contour maps for this function could be drawn similar to the ones shown in fig. 22.2, and similar dashed lines would indicate the points in the (Ψ,U)-plane for which $\dot{U} = 0$. If a point of stability exists, it lies on the intersection of the dashed lines corresponding to the conditions (22.1) and (22.2) respectively ($\dot{\Psi} = 0$, $\dot{U} = 0$).

level, boomerang	t sec.	f rev/s	V m/s	U	Ψ degr.	ϑ degr.	φ degr.	ψ degr.
all	0	11.0	28.0	1.36	0.0	90.0	-100.0	-15.0
{2} ,101.1	1.0	10.6	19.7	0.99	8.5	66.9	18.4	-15.4
{3} ,195.1	1.0	10.6	18.0	0.94	13.4	76.4	27.8	-18.7
{3'},250.1	1.0	10.9	18.7	0.92	13.1	79.2	30.4	- 9.3

table 22.1 Some values for the theoretical flights of fig. 16.2 at t = 0 and after 1 second.

It was shown in §6 that, for a boomerang flying at $\vartheta \approx 90°$, $\Psi \approx 0°$ the angle of incidence Ψ can only be stationary, i.e. $\dot{\Psi} = 0$, if

$$\left.\begin{aligned} \frac{U\, T_{1x}}{F_{1L}} &= \lambda \\ \text{where} \qquad F_{1L} &= F_{1z}\cos\Psi - F_{1x}\sin\Psi \end{aligned}\right\} \quad (22.1)$$

and $\lambda = I_3/ma^2$. This follows directly from (6.13). Figure 22.2 shows contours of the function UT_{1x}/F_{1L} of Ψ and U in a part of the (Ψ,U)-plane, for both boomerangs 101 and 195. Dashed lines with the values .258 and .272 denote respectively the points where the function equals λ for the plain and for the weighted version of boomerang L1. According to §6, as long as $UT_{1x}/F_{1L} > \lambda$ (and $F_{1L} > 0$), the boomerang has the tendency to increase Ψ and proceed to the right, "downhill", until it reaches a point where (22.1) is satisfied (on a dashed line). Here we suppose that we have a hypothetical case in which $\vartheta \approx \frac{1}{2}\pi$, $\Psi \approx 0$ throughout this first stage of the flight. Fig. 22.2 clearly indicates that, for high values of Ψ and high values of U, the function UT_{1x}/F_{1L} is greater for boomerangs 195 than for boomerangs 101. For equal values of U, higher than about 1.1, the dashed lines of the 195 deviate strongly from the corresponding lines of the 101. (At $\Psi \approx 6°$ the lines for both boomerangs agree). What is the effect of such a deviation? Immediately after the start, at $\Psi \approx 0°$ and $U \approx 1.3$ say, both boomerangs 101.1 and 195.1 proceed to the right in the (Ψ,U)-plane. In the meantime U varies also, usually it decreases because the speed V diminishes relatively more than the spin f (which may even increase by autorotation if Ψ becomes large enough). Hence, generally, the initial part of a boomerang's path in the (Ψ,U)-plane is toward increasing Ψ and decreasing U. Fig. 22.2b shows that boomerang 195.1 cannot reach its dashed line unless $U \lesssim 1.1$, whereas, according to fig. 22.2a, boomerang 101.1 reaches its dashed line at $\Psi < 10°$, even if U is as high as 1.4. Therefore it is plausible that Ψ reaches a higher value, and hence the flight path gets a stronger curvature, for boomerang 195.1.

Tables 22.1, 22.2 and 22.3 list some values characterizing the flight paths of the levels 2, 3 and 3' shown in fig. 16.2. Table 22.1 indicates that φ changes by about 120° (level 2) or 130° (levels 3 and 3') in the first second of the flight. As $\dot{\varphi} \approx \omega_y$ here, this corresponds to $\omega_y/\omega_z \approx .03$. The boomerang's speed V decreases very strongly directly after the start, the deceleration having a value of about 1g. Table 22.2 shows that a main difference between the flight path of the level 3 boomerang and that of the level 3' boomerang concerns the maximum elevation (Z_2). This is also evident from fig. 16.2.

level, boomerang	Z_2 m	D_2 m	D_1 m	f_2 rev/s	f_1 rev/s	V_1 m/s	Ψ_2 degr.	U_1
{2} ,101.1	10.2	23.6	1.3	11.0	9.1	3.0	42.5	0.17
{3} ,195.1	9.5	21.2	3.2	11.0	9.3	2.3	43.5	0.13
{3'},250.1	6.3	20.6	4.5	11.1	9.4	3.3	32.0	0.15

table 22.2. Some values for the theoretical flight paths of fig. 16.2. Z_2 = maximum height, D_2 = maximum horizontal distance. D_1 = minimum horizontal distance reached in coming back. f_2 and f_1 = maximum resp. minimum spin. V_1 = minimum speed, Ψ_2 = maximum angle of incidence, U_1 = minimum $V/2\pi fa$.

level, boomerang	t sec.	P m.	n rev.	D m.
{2} ,101.1	9.5	91.6	91.1	12.6
{3} ,195.1	9.2	92.6	89.9	12.5
{3'},250.1	8.2	92.6	82.0	12.5

table 22.3. Some values for the theoretical flight path of fig. 16.2 at the instant of touch-down. t = duration of flight, P = total path length, n = total number of revolutions, D = distance of landing point from launching point.

Finally, we note that in all computed flights the boomerangs' states of motion are confined to the part of the (Ψ,U)-plane for which:

$$U \sin \Psi \lesssim 0.15 \qquad (22.3)$$

This means that many of the values in the model boomerangs' aerodynamic tables (such as 31.1 through 31.5) are not used. For the purpose of flight path calculations, therefore, it is not necessary to compute, or to determine experimentally, the values in the upper right parts (high Ψ, high U) of such tables.

CHAPTER IV

TRENDS

§23 *Methods used.*

This chapter deals with changes in a boomerang's flight path due to certain variations in the initial conditions or in the boomerang's properties. Twelve sections each contain a theoretical investigation of one effect, and one section (§36) deals with an experimental investigation. As far as possible, the theoretical results are compared with experimental observations.

In §24 through §29 either the initial conditions are varied or the external conditions such as the presence of wind or the absence of gravity. Here, the model boomerang mostly used in the flight path calculations is level 2 boomerang 101.1, which belongs to boomerang L1 (see §16). The 101.1 has proved to possess a quite realistic flying behaviour, and the computed effects on its flight due to variations in certain conditions probably agree very well with reality.

In §30 through §35 the boomerang's aerodynamic and mechanical parameters are varied. Here we take level 3 boomerang 195.1 (which also belongs to boomerang L1, see §16) as a point of departure. Other model boomerangs can be derived from it by changing one or more parameters. Only in §32 boomerang 239.1 (belonging to boomerang WU) is taken as a reference. A serious lacuna in our knowledge of boomerangs concerns the relation between the detailed shape of a boomerang's cross sections and the boomerang's aerodynamic characteristics. Therefore we cannot generally answer questions like: If a certain boomerang does not perform satisfactorily, how must its cross sections be modified in order to improve its performance? Neither can we give designs for "optimum" boomerangs.

Many of the following sections contain tables in which values are listed for several quantities characterizing the computed flight paths. These quantities, and the units in which they are expressed, are respectively:

t (sec) = duration of flight,
P (m) = total path length,
n = total number of revolutions,
D (m) = distance of landing point from launching point,
Z_2 (m) = maximum elevation,
D_2 (m) = maximum horizontal distance before returning,
D_1 (m) = minimum horizontal distance reached in coming back,
f_2, f_1 (rev/s) = resp. maximum and minimum spin,
V_1 (m/s) = maximum speed,
Ψ_2 (degr) = maximum angle of incidence,
U_1 = minimum $V/2\pi fa$.

Most of the computed flight paths in this chapter are represented by computer plots which show three orthogonal projections, constructed as outlined in §9. Numbers with line segments indicate their lengths in metres.

There are trends of a very interesting kind, which we did not investigate. Suppose a certain boomerang, launched at certain initial conditions, returns perfectly. Now change one or more parameters, such as the boomerang's mass, the wind velocity, or the angle ϑ_o. How must the remaining initial conditions be modified in order to make the boomerang still return perfectly? In the absence of wind, there are five independent parameters determining the initial conditions: f_o, V_o, Ψ_o, ϑ_o, ψ_o (leaving Z_o out of consideration). The point of touch-down, i.e. the point (X,Y,o) at which the boomerang for the first time in its flight reaches the ground $Z = 0$, has two degrees of freedom. This suggests that there is a three-dimensional subset of initial conditions f_o, V_o, Ψ_o, ϑ_o, ψ_o, for which a given boomerang with fixed properties returns perfectly. In the presence of wind φ_o becomes relevant too, and the subset in this case will be four-dimensional. It would be interesting to investigate the shape of such "subsets of perfect return". One could start with a simple case like the following one for a given boomerang. U_o and Ψ_o are kept constant, so that only three independent variables remain: V_o, ϑ_o, ψ_o. The "subset of perfect return" should be one-dimensional in this case. It might consist of one or more curved line segments in

$(V_o, \vartheta_o, \psi_o)$-space, or it might be empty for some boomerangs. For example, for any value of ϑ_o, either we have one or perhaps more values of V_o and ψ_o with a perfect return, or the boomerang cannot return perfectly at all.

§24 *The angle between boomerang's plane and horizon, ϑ_o.*

The angle ϑ_o is among the launching parameters most easily varied by the thrower. Figure 24.1 shows a typical example of the influence of ϑ_o on the flight path's shape. (These pictures were published earlier in [Hess, 1968, p. 135].) In fig. 24.1a boomerang L1 is launched at $\vartheta_o \approx 85°$ and the flight path remains relatively low. In fig. 24.1b the same boomerang is launched at $\vartheta_o \approx 65°$; here the maximum elevation is significantly larger.

Figure 24.4 shows three level 1 stereograms of boomerang L6 weighted 2. From top to bottom the angle ϑ_o decreases (the angle ψ_o may also have been slighty varied). The smaller ϑ_o, the more the boomerang flight path tends to curve outward near the end. Fig. 24.2 and 24.3 offer a comparison between two flights differing in ϑ_o, for boomerang L1 plain at the levels 1, 2 and 3.

More systematic and quantitative data are provided by the 8 computed flight paths of boomerang 101.1 (level 2) shown in fig. 24.5 a through h. This boomerang is launched at the following initial conditions:
f_o = 10 rev/s, V_o = 25 m/s, Ψ_o = 0°,
ϑ_o = variable, φ_o = 0°, ψ_o = -10°,
X_o = 0 m, Y_o = 0 m, Z_o = 1.8 m,
no wind.
The values chosen for ϑ_o are respectively: 100°, 90°, 80°, 70°, 60°, 50°, 40°, 30°.

ϑ_o	t	P	n	D	Z_2	D_2	D_1	f_2	f_1	V_1	Ψ_2	U_1
100	7.1	75.7	66.2	8.9	7.5	24.5	6.2	10.0	8.7	1.9	82.6	.11
90	7.5	75.7	69.7	5.9	8.3	23.6	3.0	10.0	8.8	2.5	49.8	.15
80	7.7	76.9	70.9	7.7	9.9	22.4	1.7	10.0	8.7	2.8	39.3	.17
70	7.4	76.3	67.1	10.2	12.3	20.8	7.6	10.0	8.3	1.8	59.2	.11
60	7.1	76.5	63.0	16.9	14.8	19.0	13.5	10.0	7.9	1.8	33.4	.11
50	6.9	78.1	60.0	25.8	17.1	17.7	15.6	10.1	7.4	4.3	16.3	.27
40	4.4	55.2	39.0	13.1	18.9	15.0	13.1	10.2	7.4	5.1	13.5	.31
30	4.4	52.0	41.0	8.1	20.1	14.2	8.1	10.2	7.8	3.1	10.9	.18

Table 24.1. Some values for the flights of fig. 24.5. Symbols explained in §23.

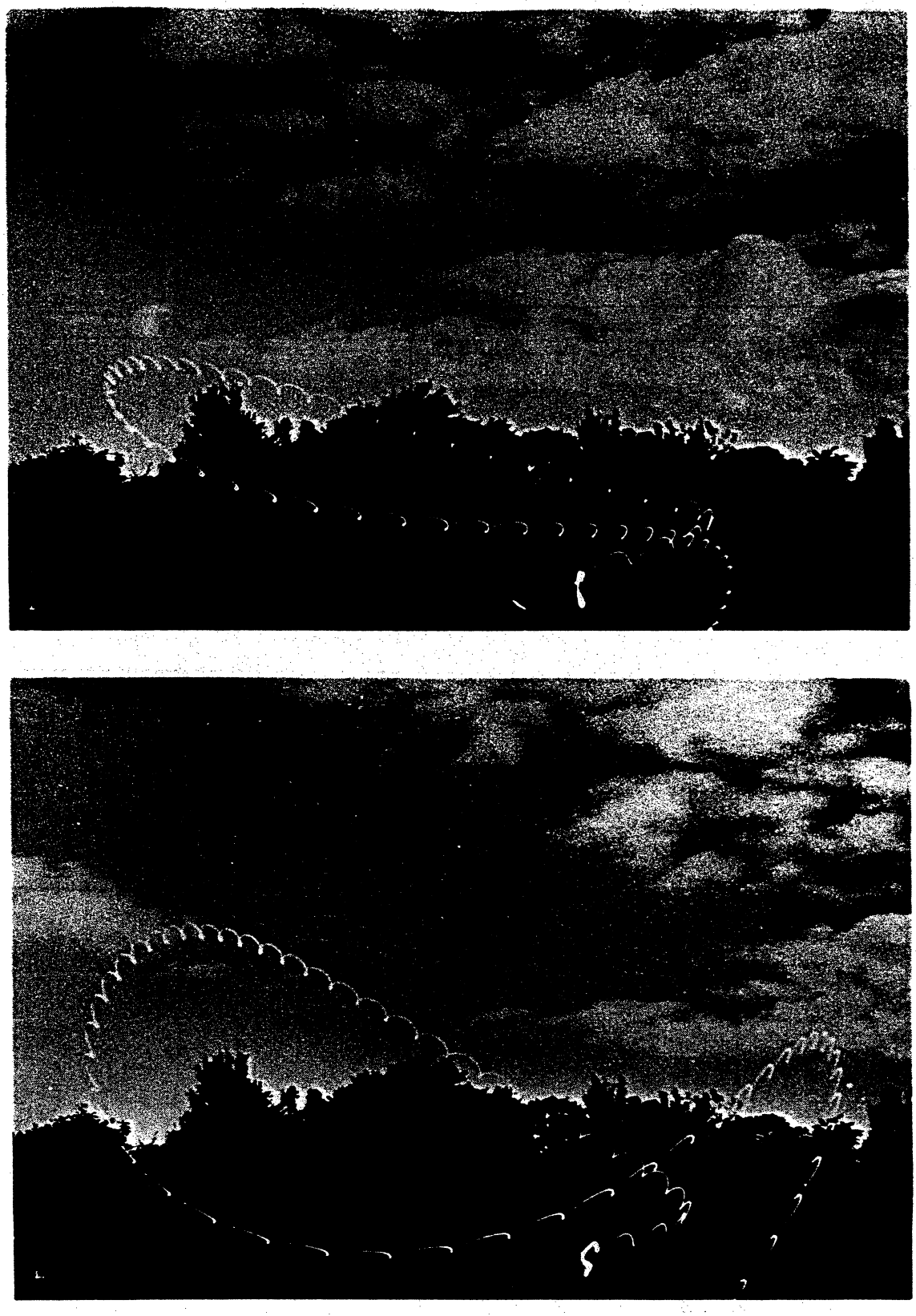

fig. 24.1. Boomerang L1 plain (Oct. 1967). a: photograph B11. b: photograph B15. Difference in flight paths mainly due to difference in ϑ_o.

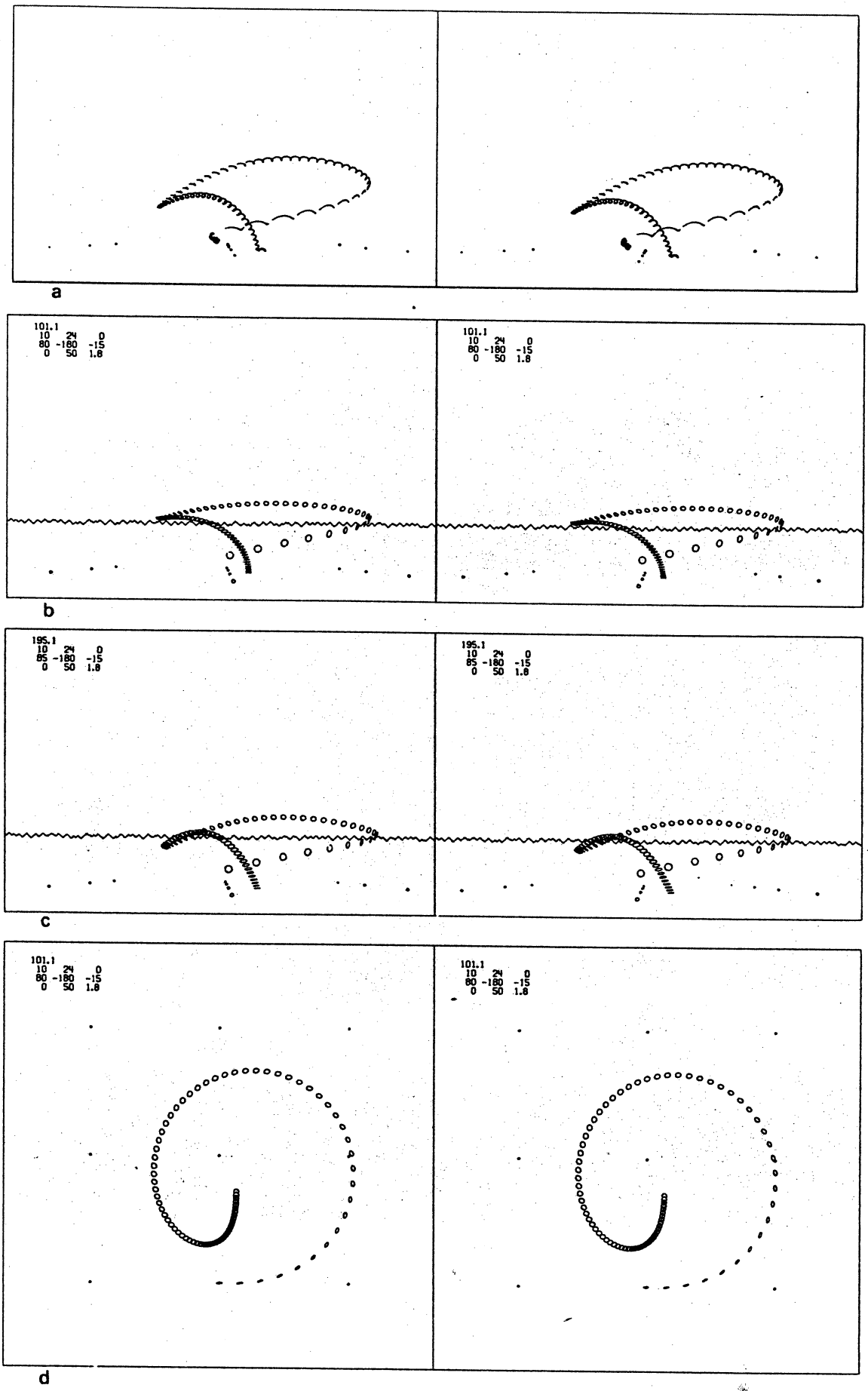

fig. 24.2. L1 plain: a: {1}, 7R5/L5A. b,d: {2}. c: {3}.

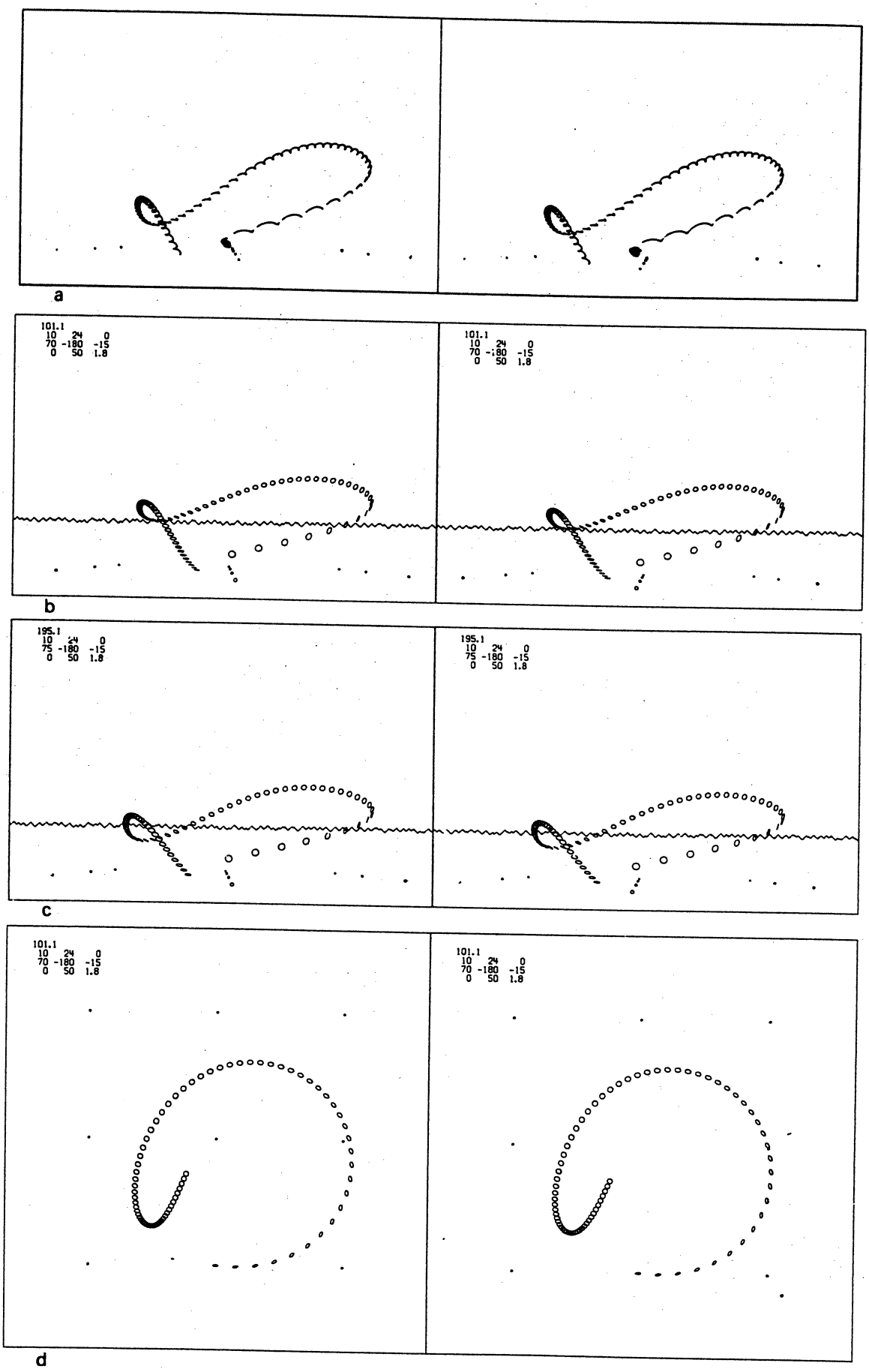

fig 24.3. L1 plain. a: {1}, 7R2/L2A. b,d: {2}. c: {3}.

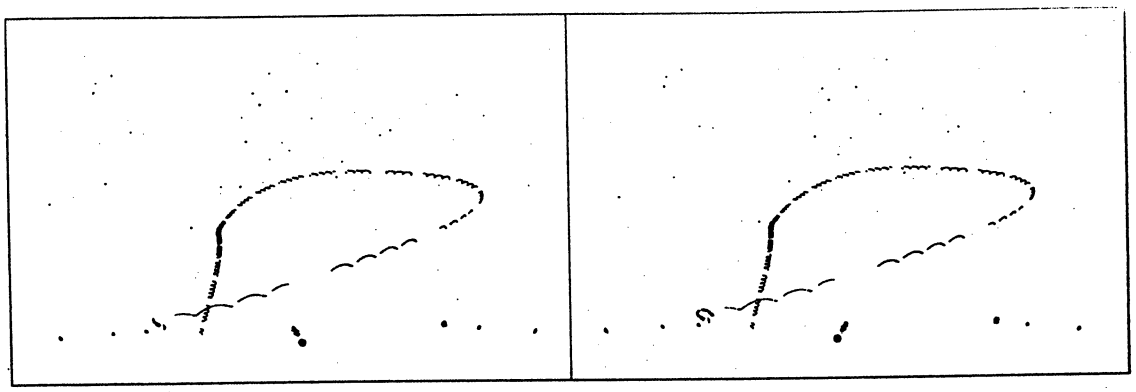

a

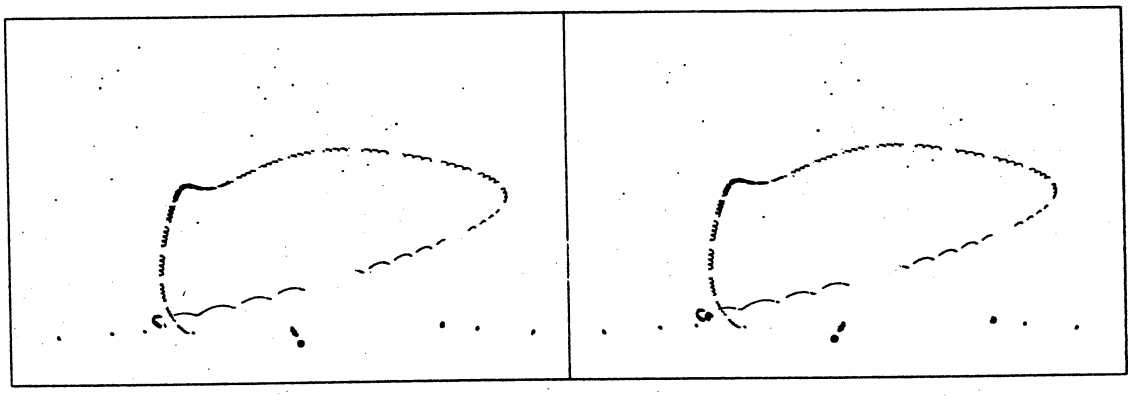

b

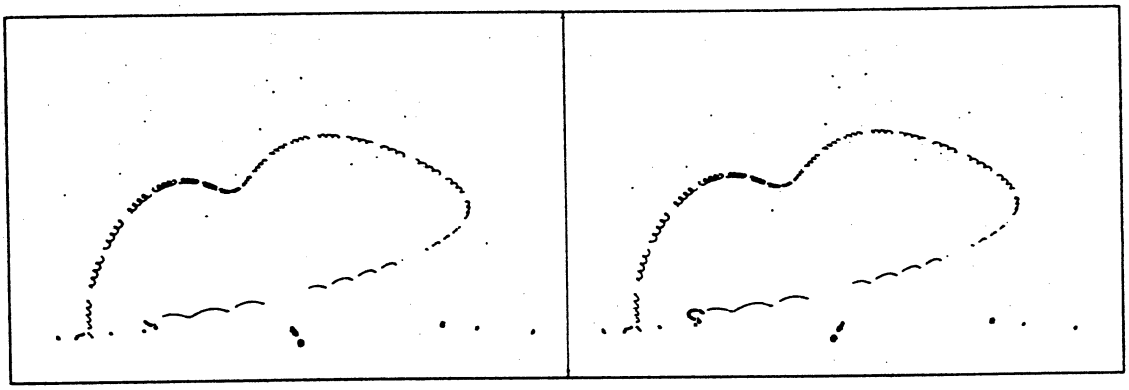

c

fig. 24.4. L6 weighted 2. Wind at Z ≈ 5 m: W ≈ 0.7 m/s, β ≈ 250°.
a: {1}, 13R21/L20. b: {1}, 13R18/L17. c: {1}, 13R15/L14.
Differences between a, b and c probably mainly caused by differences in ϑ_o, and, to a lesser extent, by differences in ψ_o.

Some numerical values for the 8 flights of fig. 24.5 are listed in table 24.1. Two obvious effects caused by varying ϑ_o are : 1^{o} the decrease with ϑ_o of the maximum elevation (Z_2), and 2^{o} the increase with ϑ_o of the maximum horizontal distance (D_2) reached before returning. Both effects are shown in the graph fig. 14.6. The same effects can also be observed in [Hess, 1968, p. 133] in flight paths computed on the basis of a very simple boomerang model.

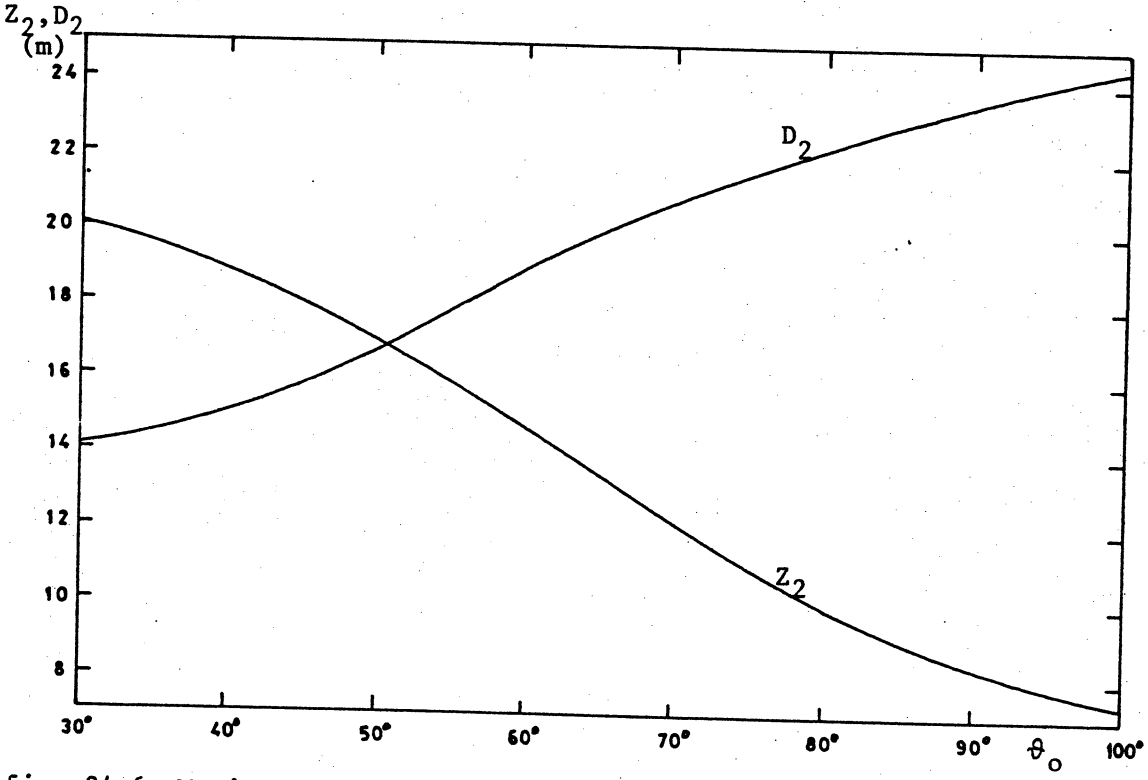

fig. 24.6. Maximum height (Z_2) and maximum horizontal distance before returning (D_2) vs. ϑ_o for the flight paths of fig. 24.5.

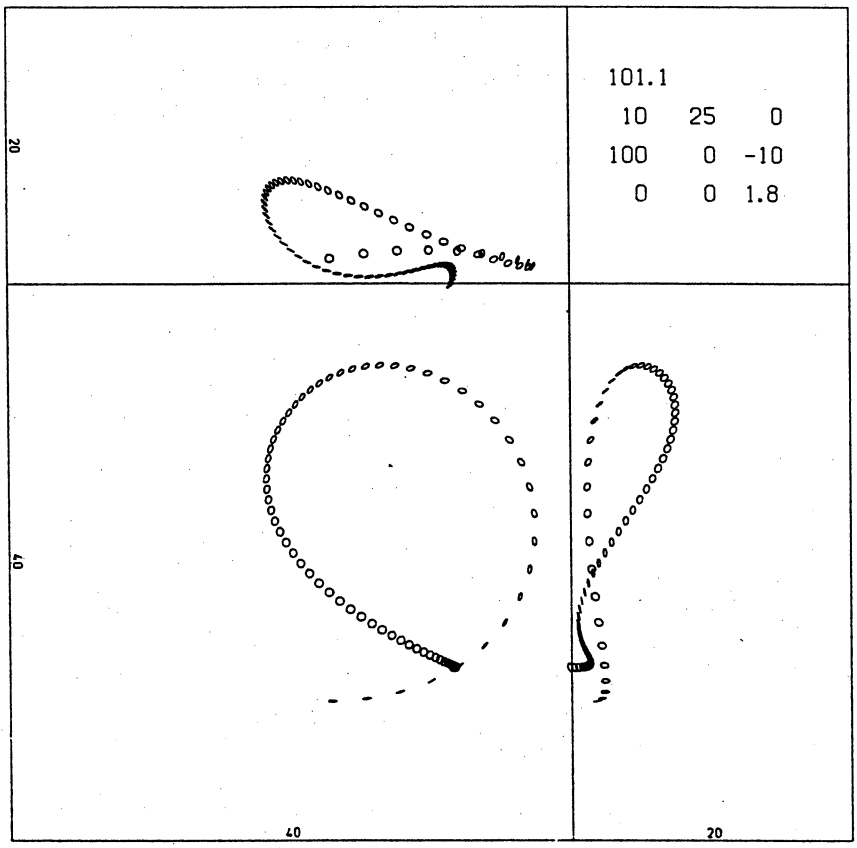

fig. 24.5a

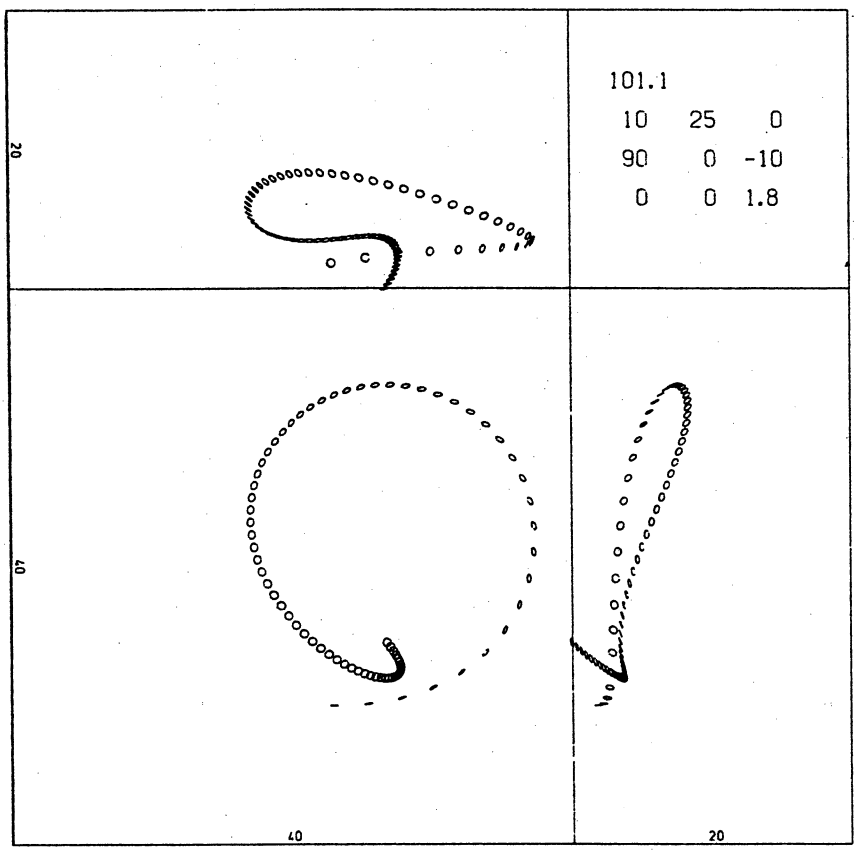

fig. 24.5b

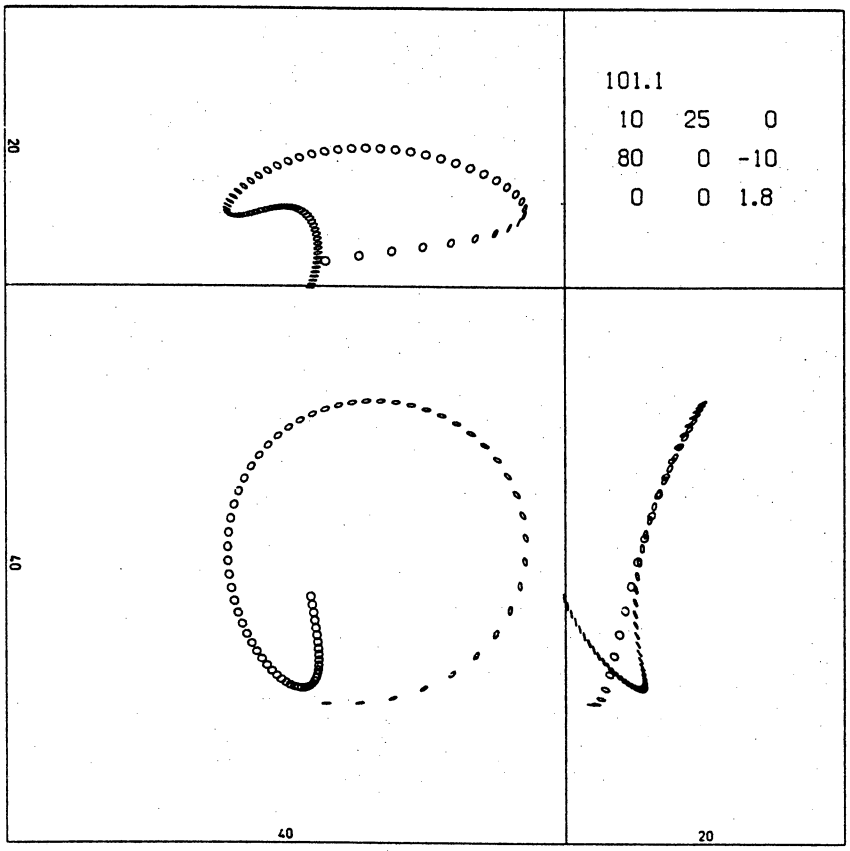

fig. 24.5c

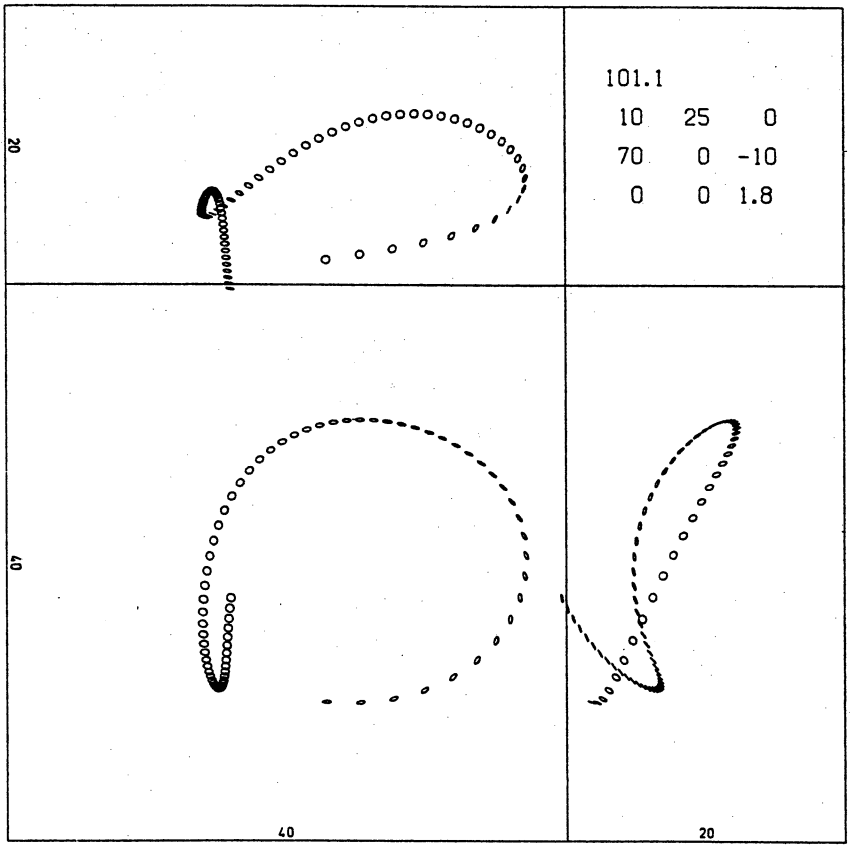

fig. 24.5d

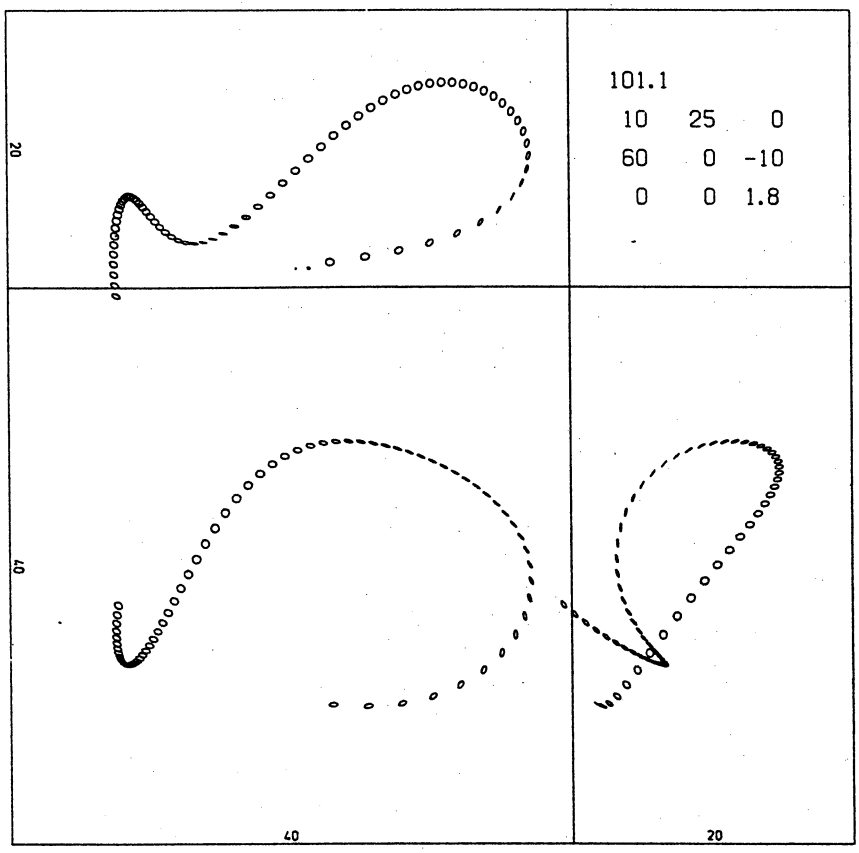

fig. 24.5e

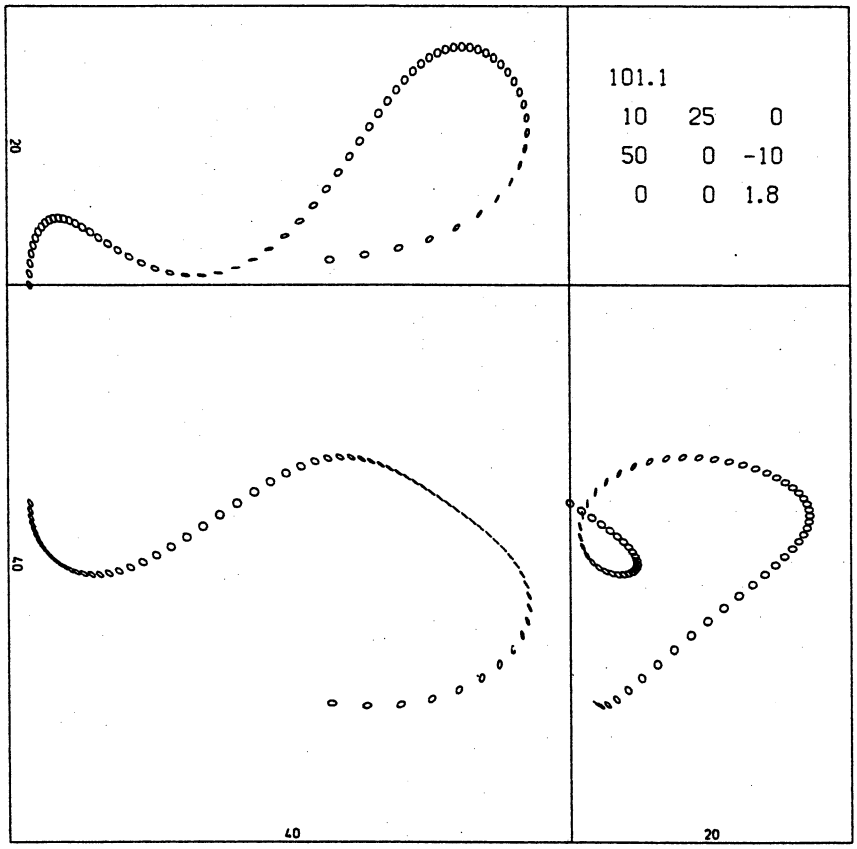

fig. 24.5f

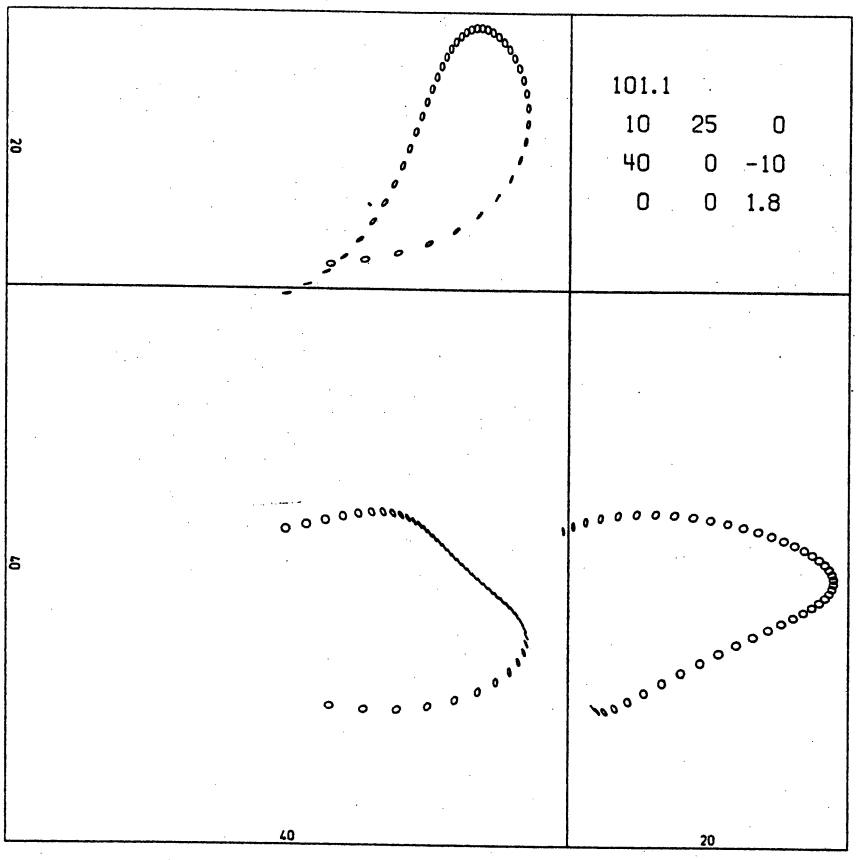

fig. 24.5g

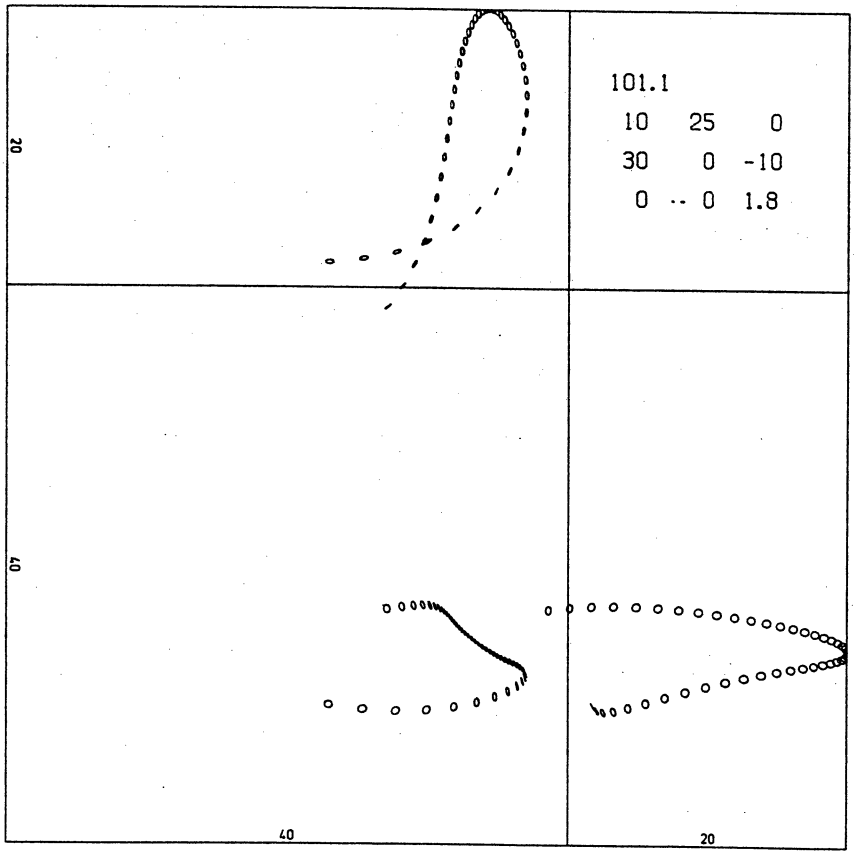

fig. 24.5h

§25 *The angle* ψ_o

Suppose that values have been selected for the angles ϑ_o and φ_o and that the boomerang is to be launched at $\Psi_o = 0$ (zero angle of incidence). Then the orientation of the boomerang's plane is determined, and the boomerang's initial velocity is parallel to this plane. By making a choise for ψ_o the direction of the velocity is completely determined. The definition of the angle ψ is such (see §4) that for $\vartheta > 0$, $\Psi = 0$ the boomerang ascends if $\sin\psi < 0$ and descends if $\sin\psi > 0$. In the cases presented in this section the boomerang is launched in a horizontal or upward direction.

Figure 25.1 a through f shows 6 flight paths computed for boomerang 101.1 (level 2). The initial conditions are chosen as follows:
$f_o = 10$ rev/s, $V_o = 25$ m/s, $\Psi_o = 0^o$
$\vartheta_o = 80°, \varphi_o = 0°$, ψ_o = variable
$X_o = 0$ m, $Y_o = 0$ m, $Z_o = 1.8$ m,
no wind.
The values chosen for ψ_o are respectively: 0°, -10°, -20°, -30°, -40°, -50°.
The flight paths are plotted on the same scale as those of fig. 24.5.

ψ_o	t	P	n	D	Z_2	D_2	D_1	f_2	f_1	V_1	Ψ_2	U_1
0	7.1	73.9	65.3	3.2	10.6	22.4	2.6	10.2	8.4	1.6	80.3	.09
-10	7.7	76.9	70.9	7.7	9.9	22.4	1.7	10.0	8.7	2.8	39.3	.17
-20	8.8	80.8	81.1	15.0	9.5	22.5	5.2	10.0	8.9	2.5	65.5	.14
-30	8.9	83.4	81.2	17.3	10.4	23.1	9.8	10.0	8.8	2.6	49.9	.15
-40	6.9	78.7	61.6	19.1	12.3	24.3	16.7	10.0	8.3	2.5	23.8	.15
-50	6.2	75.9	53.3	29.5	14.2	27.5	27.0	10.0	7.7	1.0	24.2	.06

Table 25.1. Some values for the flights of fig. 25.1. Symbols explained in §23.

Table 25.1 lists some values for the flights of fig. 25.1. A main effect, not indicated in table 25.1, is that for increasing values of $-\psi_o$, the boomerang reaches its maximum elevation (Z_2) earlier. This is shown in table 25.2. Thus: the more steeply upward a boomerang is launched, the earlier it begins to descend.

ψ_o	0°	-10°	-20°	-30°	-40°	-50°	
$t(Z = Z_2)$	2.4	2.3	1.9	1.4	1.3	1.3	seconds

Table 25.5. Time after which maximum height is reached for flights of fig. 25.1.

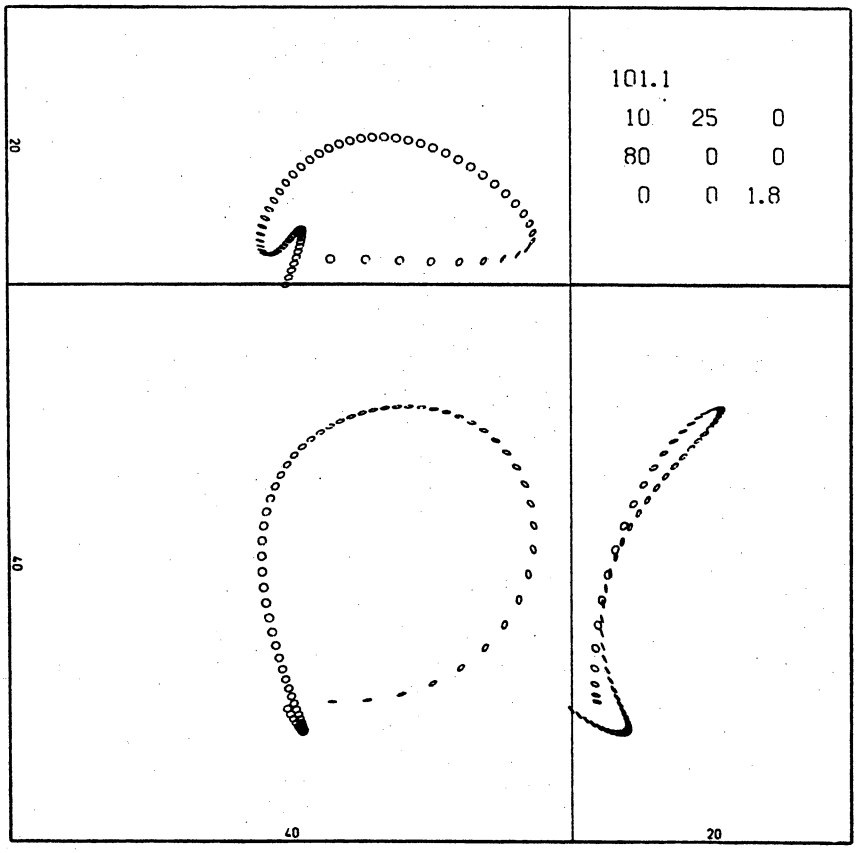

fig. 25.1a

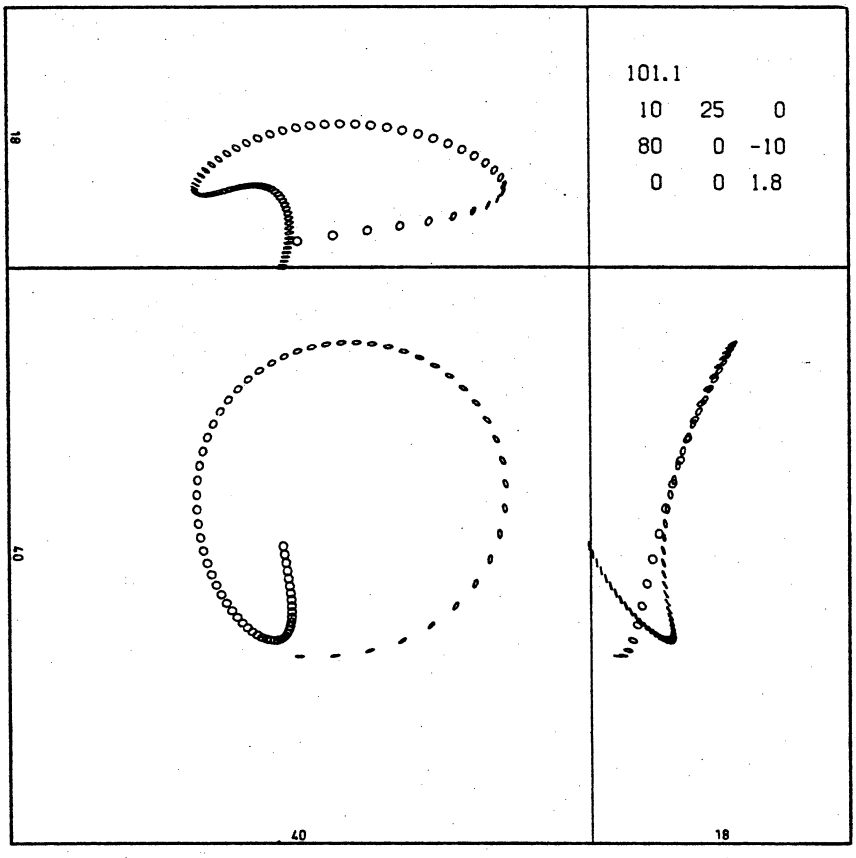

fig. 25.1b

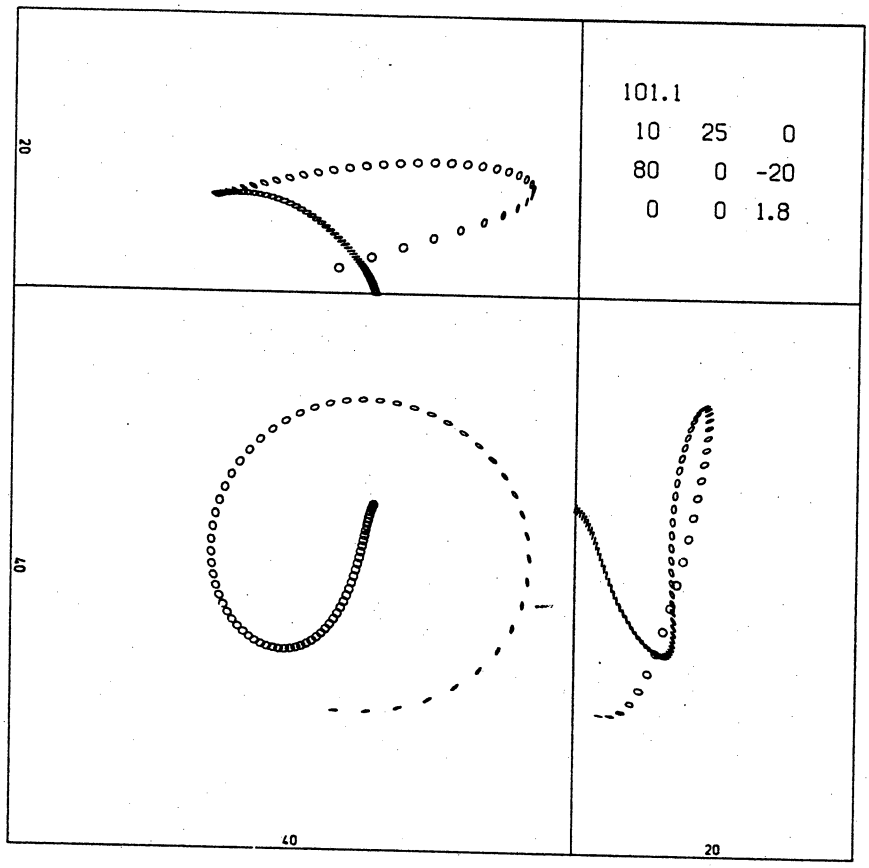

fig. 25.1c

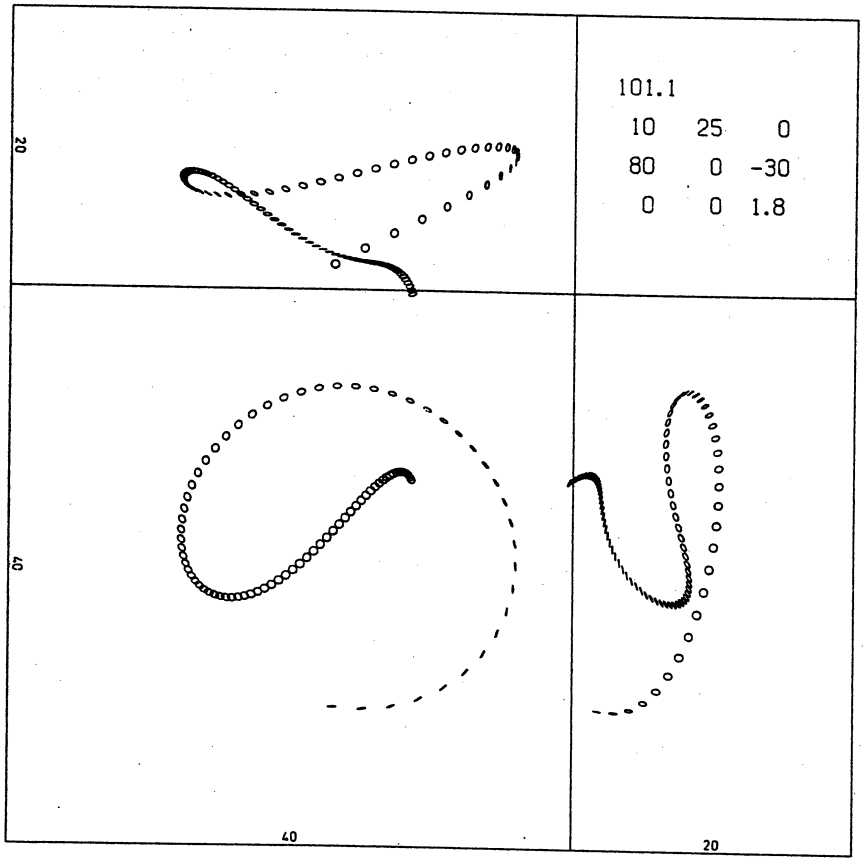

fig. 25.1d

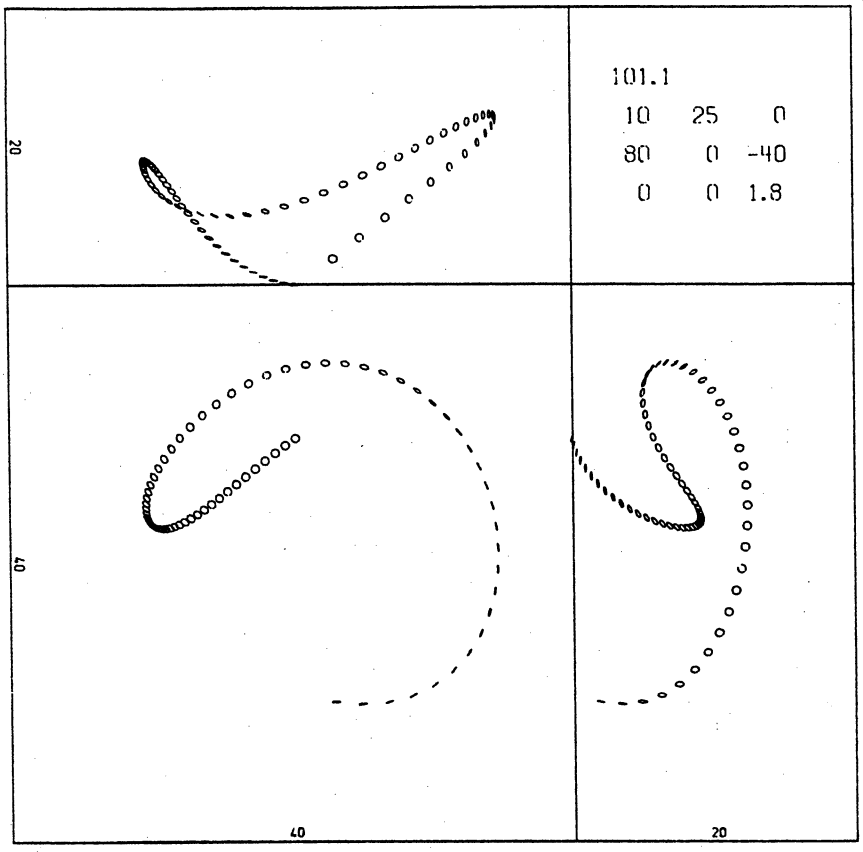

fig. 25.1e

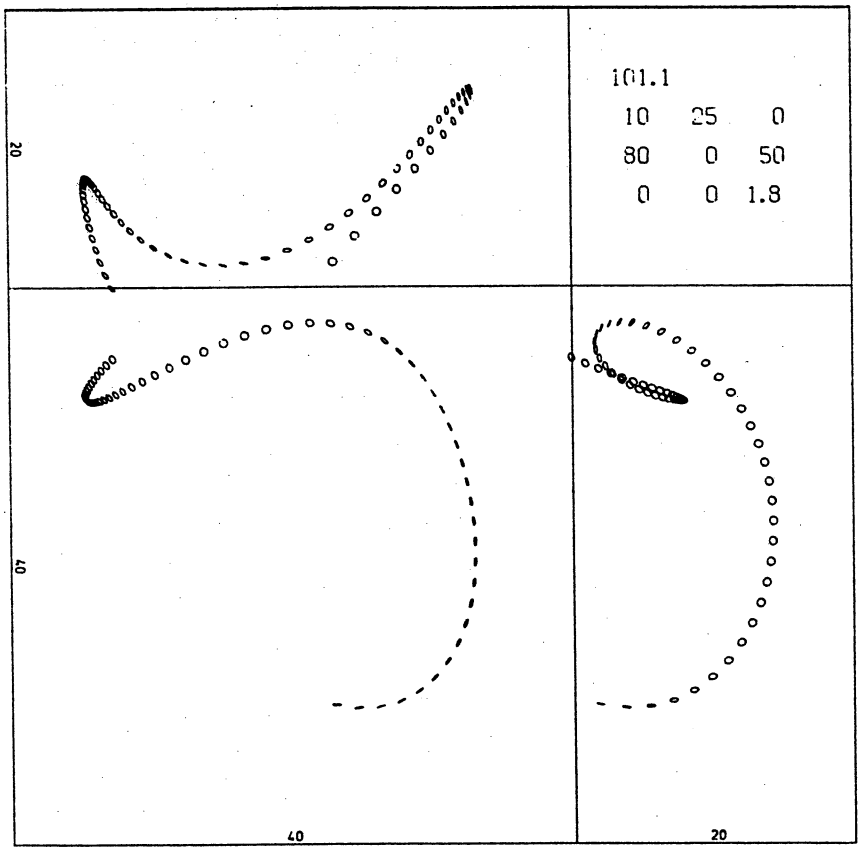

fig. 25.1f

§26 *Initial speed V_o and initial spin f_o.*

Everyone who has thrown returning boomerangs may have noticed the curious fact that the force with which a boomerang is launched has little influence on the diameter of the flight path. The main effect of a proportional increase of V_o and f_o is that the flight lasts longer, and that the boomerang may traverse a second loop before reaching the ground. If a boomerang is launched with too little speed and spin, it drops to the ground too early for it to complete a return flight.

In this section data are given for 5 computed flights of boomerang 101.1 (level 2). This boomerang is launched at the following initial conditions:

f_o = variable, V_o = variable, $\Psi_o = 0$,
$\vartheta_o = 80°$, $\varphi_o = 0°$, $\psi_o = -10°$,
$X_o = 0$ m, $Y_o = 0$ m, $Z_o = 1.8$ m,
no wind.

The initial values for f_o and V_o are chosen as follows:

case	f_o rev/s	V_o m/s	U_o
1	8	20	1.34
2	10	25	1.34
3	12	30	1.34
4	12	20	0.89
5	8	30	2.00

The corresponding flight paths are shown in fig. 26.1a through d, with the exception of case 3, for which pictures are presented in fig. 24.5c and fig. 25.1b. Some values for these five flights are listed in table 26.1.

f_o	V_o	t	P	n	D	Z_2	D_2	D_1	f_2	f_1	V_1	Ψ_2	U_1
8	20	6.0	57.0	50.5	4.0	5.7	21.5	4.0	9.0	7.8	2.6	58.4	.15
10	25	7.7	76.9	70.9	7.7	9.9	22.4	1.7	10.0	8.7	2.8	39.3	.17
12	30	10.2	104.0	98.4	15.5	13.9	22.3	2.7	12.0	9.0	2.6	30.9	.15
12	20	5.2	59.3	51.8	15.4	3.4	27.2	15.4	12.0	9.1	6.4	15.7	.37
8	30	7.1	85.4	58.9	18.2	17.4	16.8	11.3	9.3	7.3	2.4	17.2	.15

Table 26.1. Some values for the flights of fig. 26.1. Symbols explained in §23.

From the evidence presented here obviously two conclusions can be drawn: 1° The boomerang's maximum distance before returning (D_2), or rather its flight path curvature, is nearly independent of the initial velocity, provided that U_o is constant; and 2° D_2 increases for decreasing values of U_o. Hence if the boomerang is launched at a higher relative spin (lower advance ratio U_o), the flight path diameter is larger.

The first phenomenon was to be expected on the basis of the exposition in §7 after (7.15). It is one of the most characteristic properties of boomerang flights. The constancy of a boomerang's flight path diameter was also predicted by the simple model of [Hess, 1968] (see the computed flight paths in [Hess, 1968, p. 132]).

The second phenomenon can be explained on the basis of the exposition in the second half of §22 (see fig. 22.2a). If U_o is increased, the boomerang's angle of incidence Ψ increases to higher values, the aerodynamic forces increase, and the flight path becomes more strongly curved: D_2 decreases. This effect was not predicted by the simple model of [Hess, 1968], on the contrary: this model asserts that a boomerang's flight path diameter is independent of V_o and f_o separately, and hence independent of U_o.

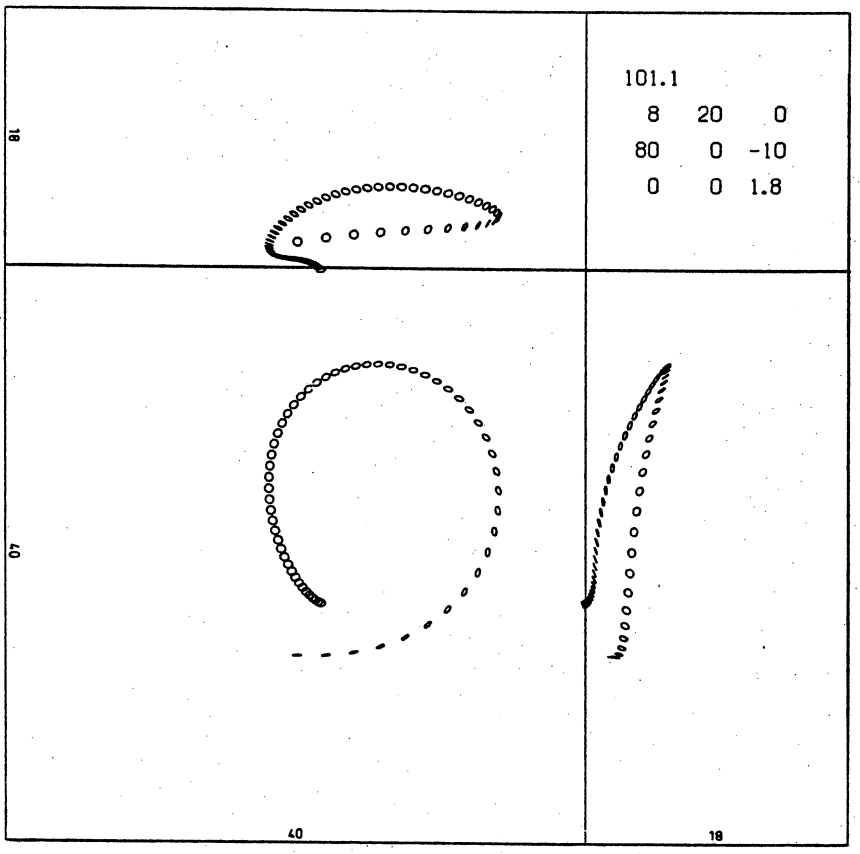

fig. 26.1a

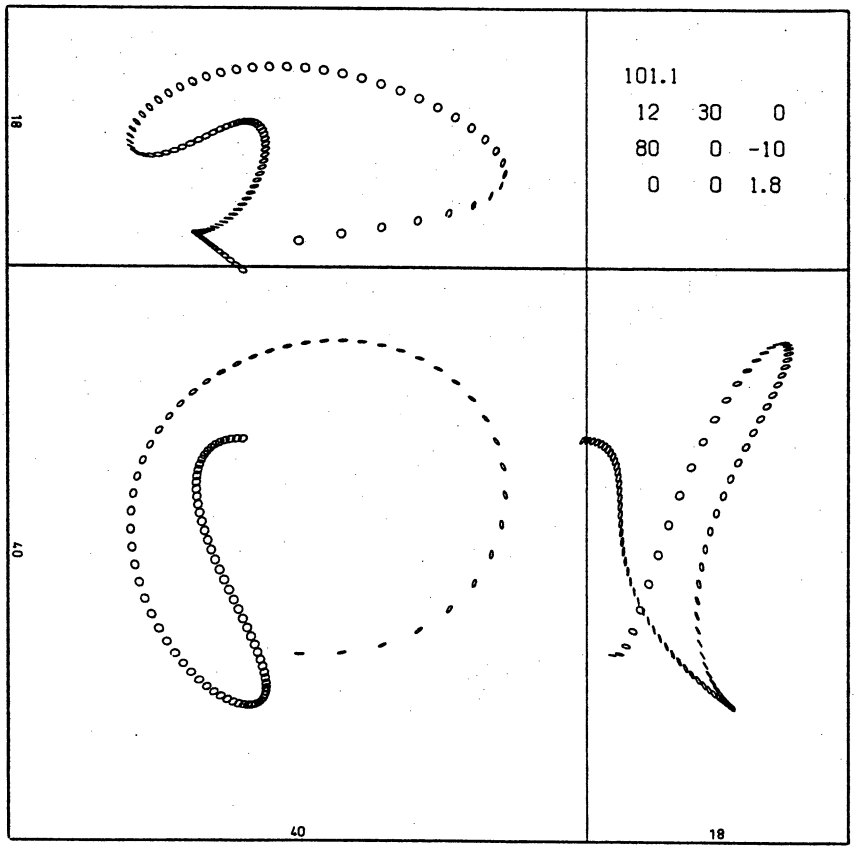

fig. 26.1b

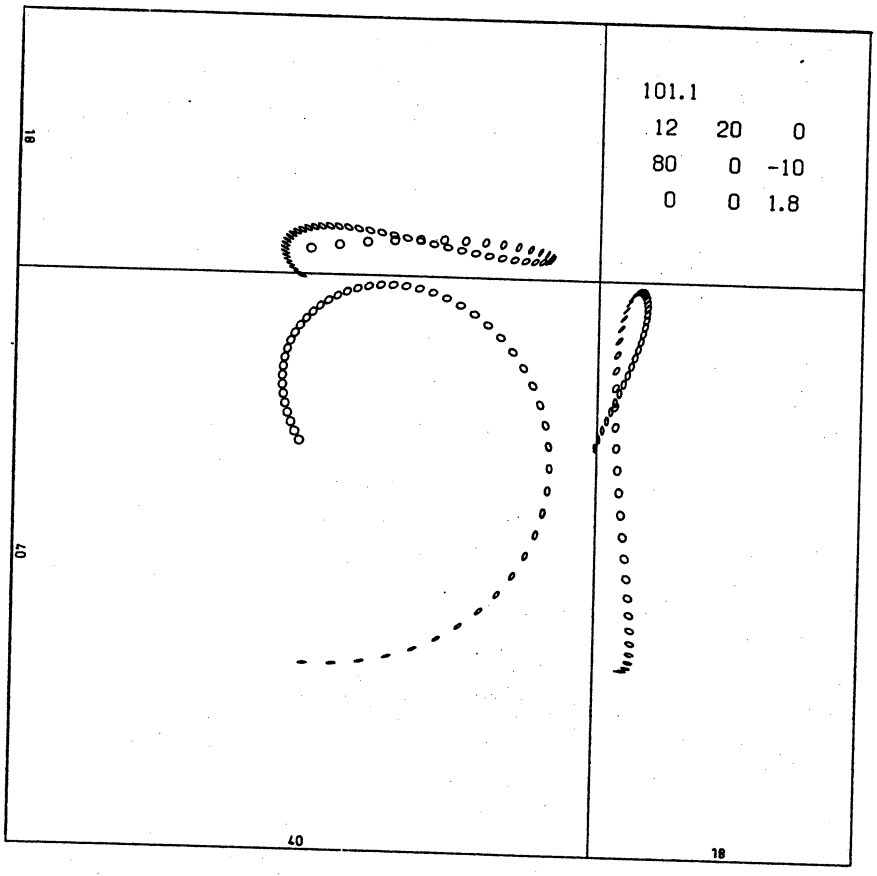

fig. 26.1c

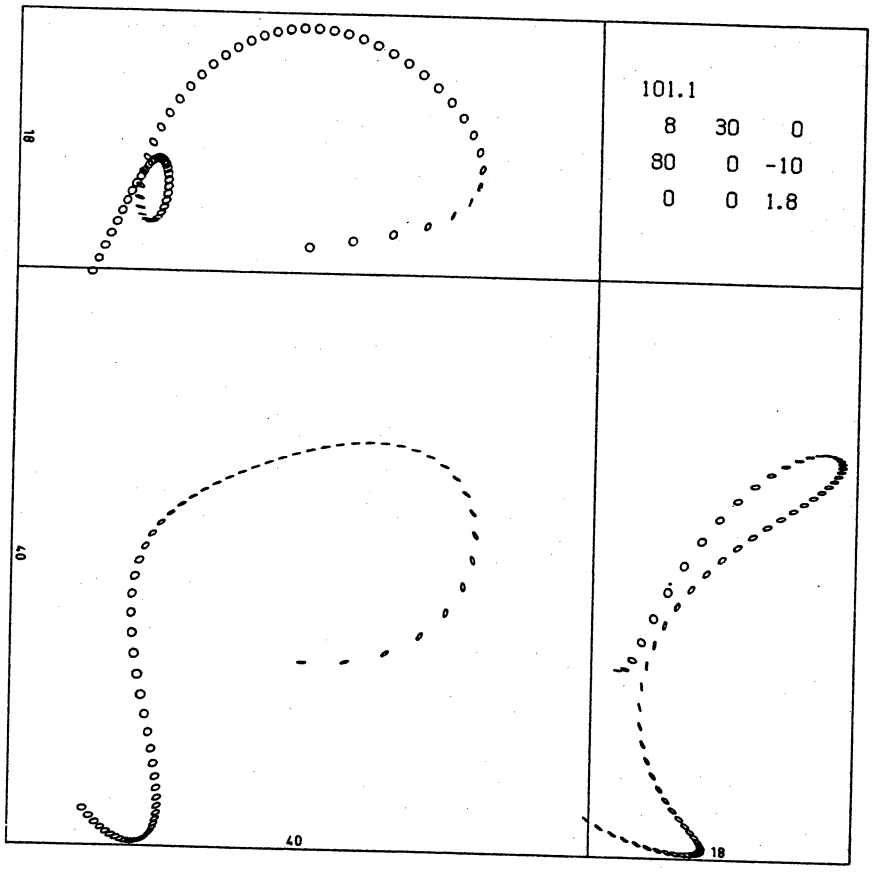

fig. 26.1d

§27 *The angle of incidence* Ψ_o.

It seems to be difficult for a human boomerang thrower to vary at will the initial angle of incidence Ψ_o. Usually this angle is not much different from zero, and probably $|\Psi_o| < 10°$ for most boomerang launchings. However, the precise value Ψ_o may depend on the throwing technique used.

In this section 4 flight paths are presented, computed for boomerang 101.1 (level 2), with the initial conditions:
f_o = 10 rev/s, V_o = 25 m/s, Ψ_o = variable,
ϑ_o = 80°, φ_o = 180°, ψ_o = -10°,
X_o = 0 m, Y_o = 50 m, Z_o = 1.8 m,
no wind.
The values chosen for Ψ_o are respectively: -5°, 0°, +5°, +10°.

The resulting flight paths are shown in a compound bird's-eye view stereogram, fig. 27.1, as continuous curves. (The simulated cameras' position, and the field of view are the same as for the bird's-eye view stereograms for boomerang 101.1 in §16, see §15.) Fig. 27.1 clearly brings out the differences between the flight paths. First, the lower

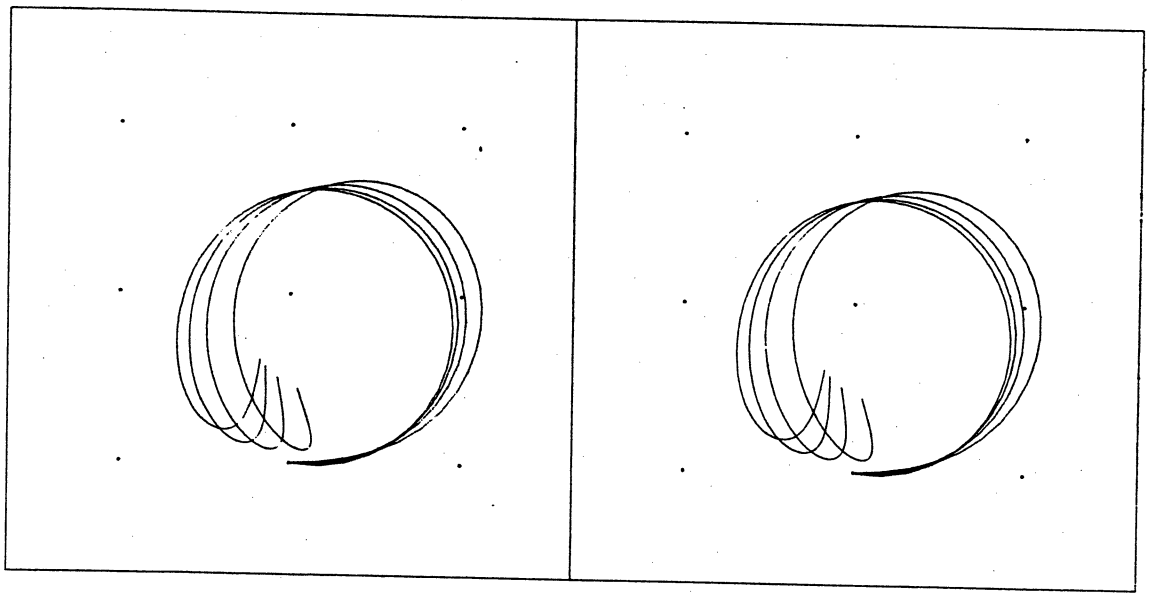

Fig. 27.1. Compound bird's-eye view stereogram of 4 flight paths differing in Ψ_o.

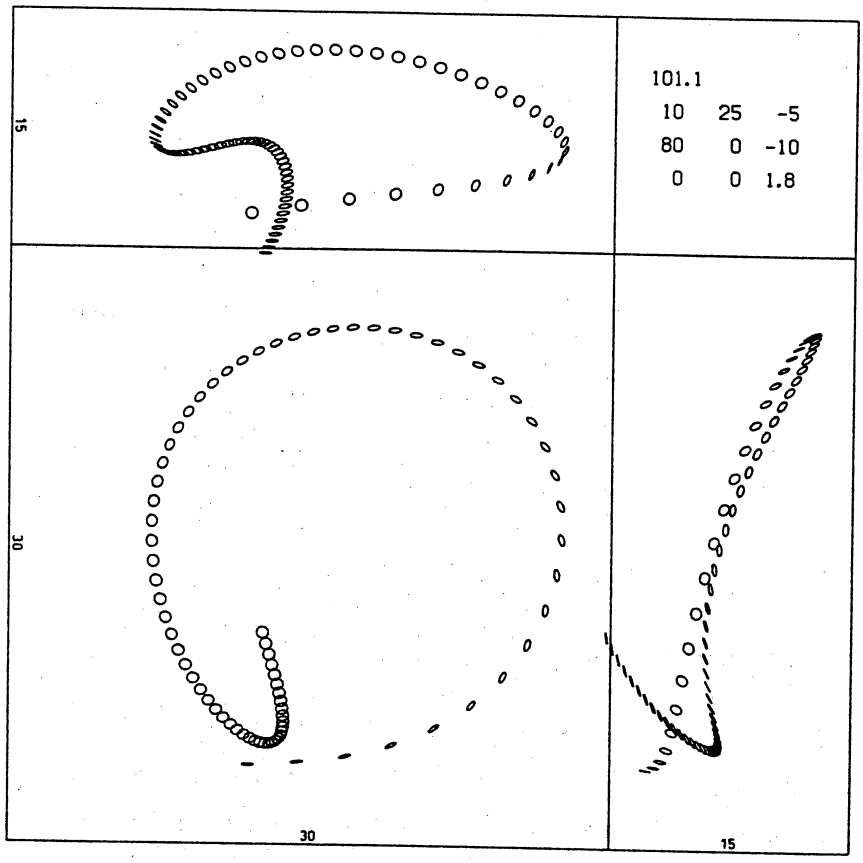

fig. 27.2a

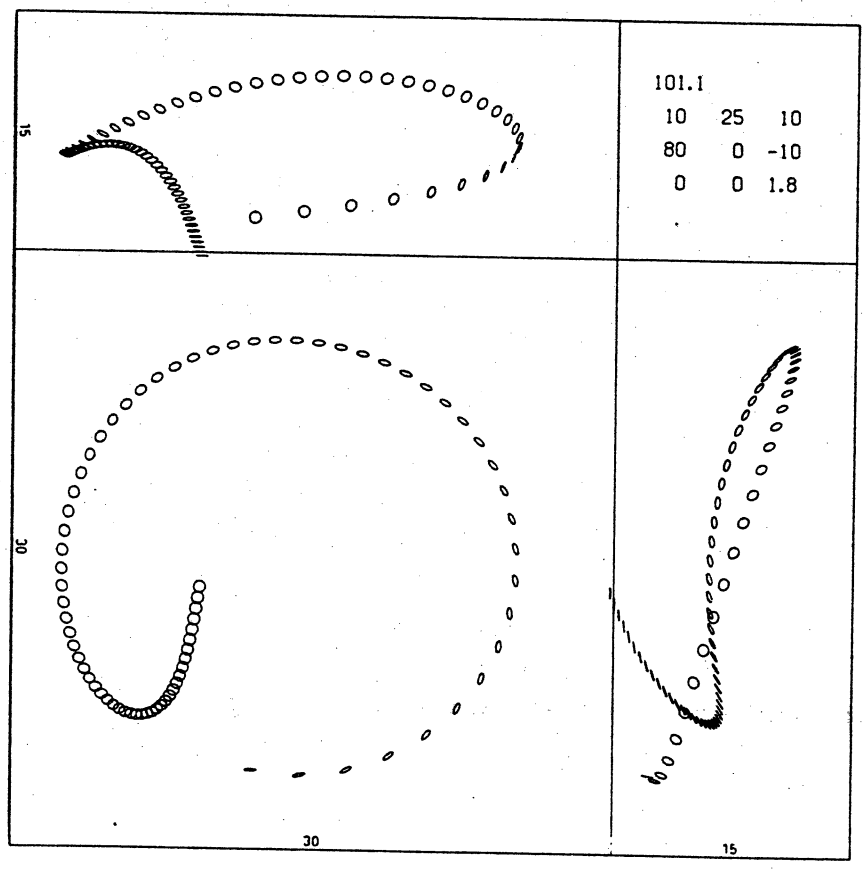

fig. 27.2b

Ψ_o the more the path curves inward near the end. Secondly, the higher Ψ_o, the stronger the initial curving of the path. Remember that the initial orientation of the boomerang's plane, being determined by ϑ_o and φ_o, is the same in all four cases. The direction of the boomerang's initial velocity, however, differs because of differences in Ψ_o. If the flight paths were slightly rotated with respect to each other so that their initial tangents would coincide, the differences in initial flight path curvature would be more obvious. The flight paths for which $\Psi_o = -5°$ and $+10°$ respectively, are separately shown in fig. 27.2.

Ψ_o	t	P	n	D	Z_2	D_2	D_1	f_2	f_1	V_1	Ψ_2	U_1
-5	7.7	77.3	70.3	6.7	10.1	23.3	1.3	10.0	8.6	2.6	45.7	.15
0	7.7	76.9	70.9	7.7	9.9	22.4	1.7	10.0	8.7	2.8	39.3	.17
5	7.7	76.2	71.5	8.9	9.6	21.9	3.6	10.1	8.8	3.0	35.6	.18
10	7.6	74.6	71.4	9.6	9.0	21.8	5.5	10.3	8.9	3.2	32.3	.19

Table 27.1. Some values for the flights discussed in this section.

Table 27.1 lists some values for the four computed flights. Additional data for one second after the start are given in table 27.2. Obviously: the higher Ψ_o, the more V and the less f is slowed down. Significant autorotation occurs for $\Psi_o = 10°$.

Ψ_o degr.	t sec.	Ψ degr.	U	f rev/s	V m/s.
all	0	var.	1.34	10.0	25.0
-5	1.0	9.7	1.00	9.6	18.0
0	1.0	9.2	0.94	9.9	17.4
5	1.0	8.7	0.89	10.1	16.9
10	1.0	8.1	0.85	10.3	16.4

Table 27.2. Some values for the flights at t = 1 sec.

Figure 27.3 contains superimposed (Ψ,U)-diagrams for the first parts of the four flights. The (Ψ,U)-tracks are seen to converge quickly to $\Psi \approx 9°$, $U \approx 1.1$. This can be explained on the basis of the exposition given in the second half of §22. The phenomenon exhibited by fig. 27.3 sheds light on the question of the "backward" instability of a

boomerang's motion, discussed at the end of §9. If a flight is computed backward in time, starting from an instant at which $\Psi \approx 9^\circ$, $U \approx 1.1$, small numerical errors may soon result in substantial deviations. Considered in reversed time, the curves in fig. 27.3 diverge very rapidly for $U \gtrsim 1.3$.

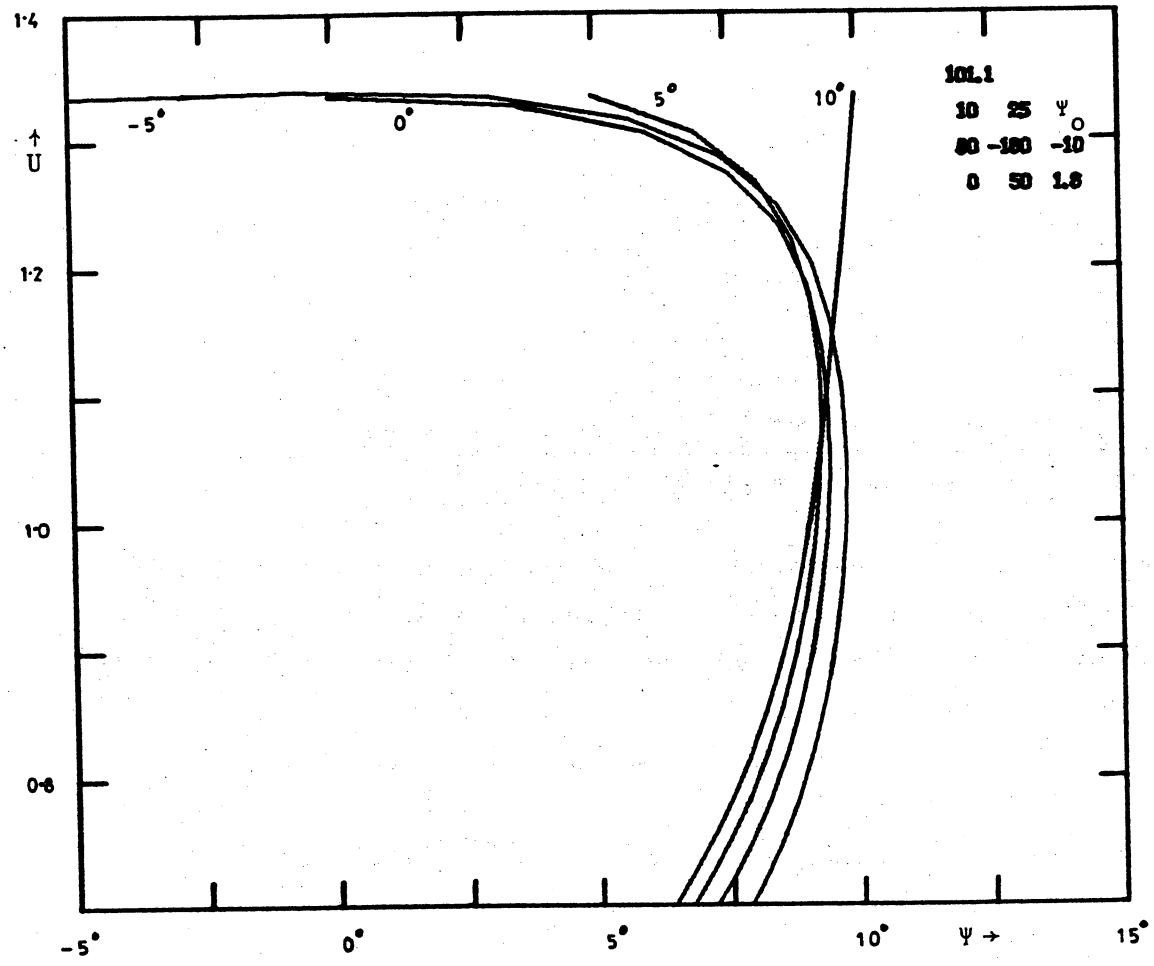

Fig. 27.3. Superimposed (Ψ,U)-diagrams for the first parts of the four flights discussed in this section. Boomerang 101.1 is launched at resp. $\Psi_o = -5°$, 0°, 5°, 10° and U = 1.34.

§28 *A boomerang's final state of motion.*

What happens when a boomerang is launched at great height? Or, how would the flight path continue if no ground would be present to stop the boomerang's motion? Figures 28.1 and 28.2 show that the boomerang would end up travelling along a helical path, clockwise as seen from above, and spiral down on and on.

The flight path shown here is computed for boomerang 101.1 (level 2) with the initial conditions:

f_o = 10 rev/s, V_o = 25 m/s, Ψ_o = 0,
ϑ_o = 80°, φ_o = 180°, ψ_o = -10°,
X_o = 0 m, Y_o = 45 m, Z_o = 1.8 m,
no wind.

The computations are ended when the boomerang drops below the level Z = -100 m, this happens 32.2 sec. after the start.

Figure 28.1 shows a bird's-eye stereogram (simulated cameras' positions at (±3, 50, 80) m, field of view at Z = 0: -20 m $\leq$ X $\leq$ 25 m, 40 m $\leq$ Y $\leq$ 85 m), and fig. 28.2 presents two orthogonal projections in the X-and Y-directions respectively. A (Ψ,U)-diagram for this flight is given in fig. 28.3.

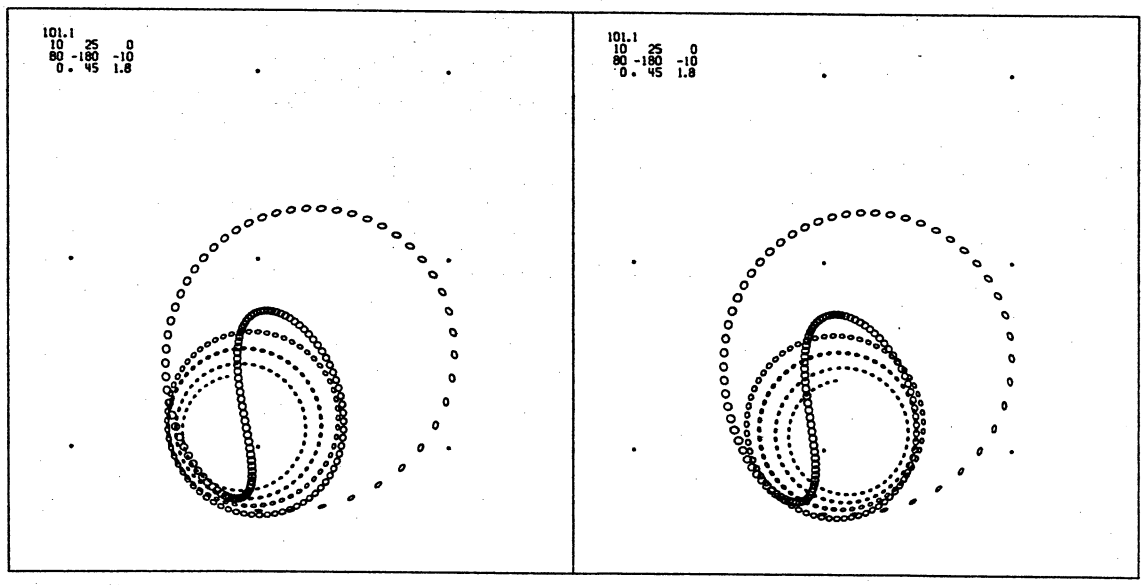

fig. 28.1. Bird's-eye view stereogram of boomerang flight ending 100 m below ground level.

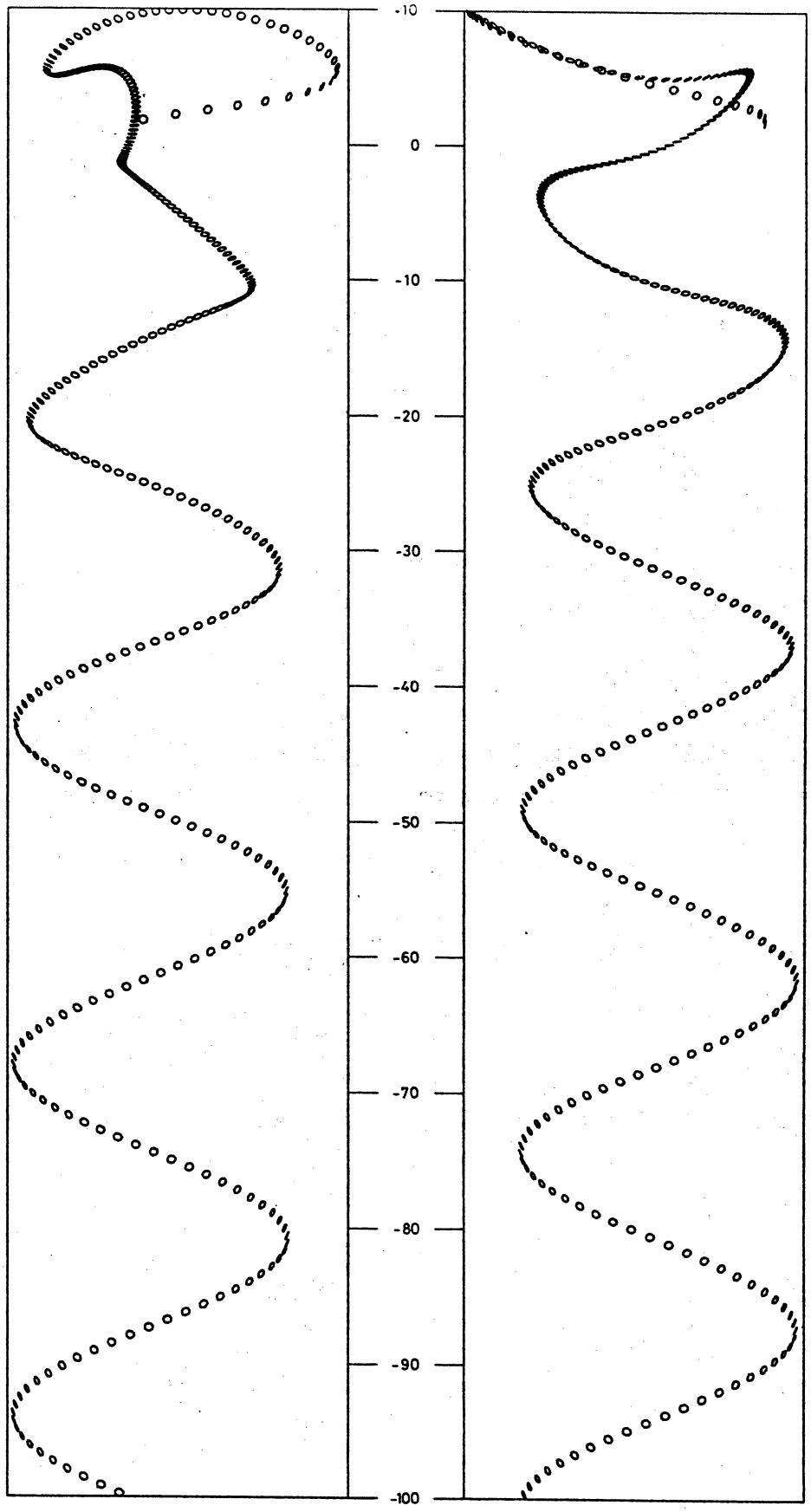

fig. 28.2.
(X,Z) and (Y,Z)-
projections
of flight path
ending at
Z = -100 m.

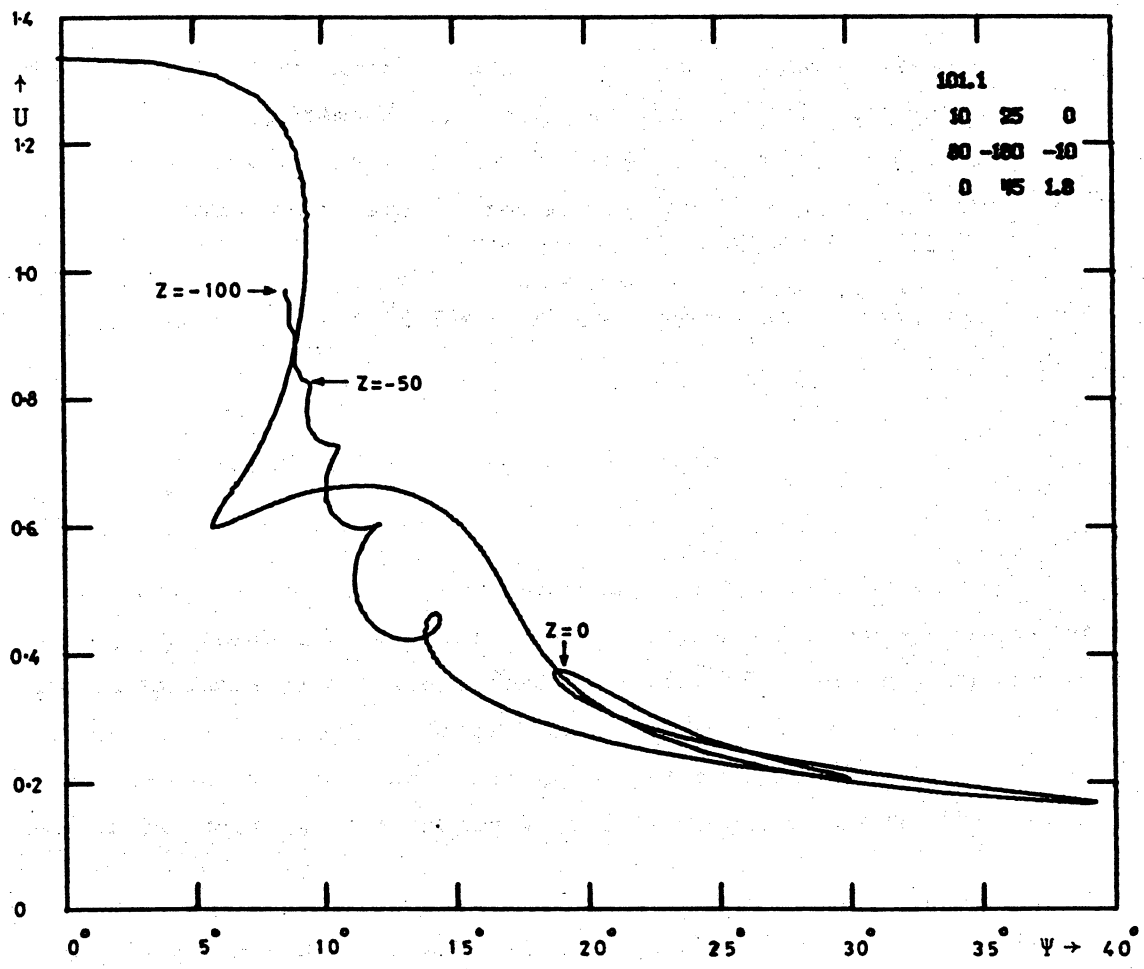

fig. 28.3. (Ψ,U)-diagram for the flight ending at Z = -100 m.

The state of motion finally reached by boomerang 101.1 is characterized by:

$$f = 8.5 \text{ rev/s},\ V = 15.4 \text{ m/s},\ U = 0.97,\ \Psi = 8.6°,\ \vartheta = 68°,\ \psi = 159°.$$

The helical path is characterized by:

$$\phi = 20.2 \text{ m},\ \Delta Z = 26.3 \text{ m},\ \Delta t = 4.6 \text{ sec.}$$

where ϕ is the diameter of the path's vertical projection (which has a circular shape), ΔZ is the difference in height and Δt the time interval between two points of the flight for which φ differs by 2π. Although the numerical calculations indicate that the boomerang's state of motion has not yet become quite constant at Z = -100 m, the values given above probably are very close to the values characterizing the final state of motion for boomerang 101.1. The same values were obtained for flight